Using Smoothed Particle Radiation Magnetohydrodynamics to Explore How Protostars are Formed

---

There is no easy route from the Earth to the Stars

Benjamin Tomos Lewis

Submitted by Benjamin Tomos Lewis to the University of Exeter as a thesis for the degree of Doctor of Philosophy in Physics, Wednesday, 31st. May, 2017.

The Abstract

The properties which define a molecular cloud core — the evolutionary phase bridging between a molecular cloud and a protostar — are extensive. These properties include the initial density profile; velocity field; and magnetic field strength and geometry (and the alignment of this with other fields). These properties have a major effect on the nature of the protostar or protostars ultimately produced when the core collapses.

We present a series of calculations using smoothed particle radiation magneto-hydrodynamics of the collapse of a molecular cloud core to the first hydrostatic core phase. Before this, we describe and analyse our numerical method, including exploring historical difficulties and the limits of the stability.

We explore the role of the geometry of the magnetic field, and showing that the nature of any outflows produced from a first hydrostatic core is closely related to the inclination angle of the field. We continue this analysis into the role of the field strength and geometry. We find that highly misaligned fields do not form bipolar outflows and discuss the cause of this, and additionally find that the angular momentum transport in weak field calculations is insufficient to prevent fragmentation and the formation of binary systems. When an outflow is formed, even in the most idealised initial conditions, the velocity is never $|v_z| > 10\,\mathrm{km \cdot s^{-1}}$.

We consider next the role of turbulent and rotational kinetic energy, and find that transonic turbulence can prevent the formation of an outflow unless a critical ratio of rotation to turbulent energy is exceeded. Even so, we observe that outflows produced in non–laminar calculations are slower ($|v_z| \sim 1\,\mathrm{km \cdot s^{-1}}$) than those from laminar configurations. We then show that a Bonnor–Ebert density profile can produce a stable binary system with a helical outflow without the prolific fragmentation seen in fast rotating uniform density distributions.

DVI file compiled from the LaTeX source files on Tuesday, 15th. August, 2017 at 7.40 p.m. G.M.T.

For Grandad, my guide and counsel.

Requiem æternam dona eis, Domine :
et lux perpetua luceat eis.

. . .

In memoria æterna erit iustus,
ab auditione mala non timebit.

The Table of Contents

The List of Figures

The List of Tables

The Declaration

Portions of this thesis have been published in peer–reviewed papers or conference proceedings, or are being prepared for publication.

Section III.1 of chapter III is derived from the proceedings paper 'Smoothed Particle Magnetohydrodynamics: A State of the Union' (Lewis, Bate, and Tricco 2016) published in the proceedings of the *11th. international S.P.H.E.R.I.C. workshop* held at the *Technische Universität München* in June 2016.

Section III.3 is derived from the proceedings paper 'Stable smoothed particle magnetohydrodynamics in very steep density gradients' (Lewis *et al.* 2015) published in the proceedings of the *10th. international S.P.H.E.R.I.C. workshop* held at the *Università degli Studi di Parma* in June 2015; however, the calculations have been re–run and reanalysed compared to those in the published paper.

Chapter IV and section III.2 of chapter III are based on the paper 'Smoothed particle magnetohydrodynamic simulations of protostellar outflows with misaligned magnetic field and rotation axes' (Lewis, Bate, and D. J. Price 2015) published in volume 451 (pages 4,807–4,818) of the *Monthly Notices of the Royal Astronomical Society* in July 2015 and on the 'Erratum and Addendum' (Lewis, Bate, and D. J. Price 2017) to that paper published in volume 464 (pages 2,499–2,501) in January 2017. However, like section III.3 the calculations have been re–run and re–analysed without the issues identified in the Erratum.

Chapter V has been published as 'The dependence of protostar formation on the geometry and strength of the initial magnetic field' (Lewis and Bate 2017) in volume 467 (pages 3,324–3,337) of the *Monthly Notices of the Royal Astronomical Society* in May 2017.

Chapter VI is being readied for submission as a paper, and chapter VII as a letter, to the *Monthly Notices of the Royal Astronomical Society*.

In all of the above, the author of this thesis was also the lead author of the paper or conference proceedings. The author was lead author on all the published papers and performed all of the analysis and write–up presented in those papers.

The Table of Definitions

Throughout this work, unless the context otherwise requires, we represent various physical and mathematical properties by the symbols in table A.

We use Einstein's index notation to represent vectors and tensors, where repeated indicies imply summation, throughout for clarity. To avoid confusion with S.P.H. particle indicies, the letters i, j, k, *etc.* as superscripts are used exclusively for vector indicies, and the letters a, b, c, *etc.* as subscripts exclusively for S.P.H. particles.

Table A. Symbol definitions.

Operators		
∇^i	nabla (del)	
D_t	convective (total) derivative	$\mathrm{D}_t = v^i \nabla^i + \partial_t$
∂_t	partial derivative with respect to t	
$\triangle$	the Laplacian	*i.e.* $\triangle \equiv \nabla^2$
Physical Fields		
ρ	fluid density	
v^i	fluid velocity	
u	specific internal energy	
B^i	magnetic field	
J^i	current density	$J^i = \epsilon^{ijk} \nabla^j B^k$
p	fluid (hydrodynamic) pressure	(occasionally p_{hyd} for clarity)
ϕ	self-gravitational potential	
$\mathscr{F}^i$	radiative flux	
$\mathscr{E}$	radiation energy density	
P^{ij}	radiation pressure tensor	
Other physical quantities		
σ^{ij}	Maxwell's stress tensor	
r^i	radius vector	
c_{s}	sound speed	

Table A. Symbol definitions (continued).

$c_{\rm a}$	Alfvén speed	$c_{\rm a} = {}^{B}/\sqrt{\mu_{\rm o}\rho}$
$c_{\rm c}$	speed of the hyperbolic cleaning wave	$c_{\rm c}^2 = c_{\rm s}^2 + c_{\rm a}^a$
$\mathscr{M}$	Mach number	$\left\|v^i\right\| = \mathscr{M} c_{\rm s}$
$p_{\rm mag}$	magnetic pressure	$p_{\rm mag} = {}^{B^2}/_{2\mu_{\rm o}}$
$\ell_{\mathscr{J}}$	Jeans length	
κ	fluid opacity	
$\mu_{\rm mol}$	(mean) molecular weight	
$T_{\rm fl}$	fluid temperature	
$T_{\rm rad}$	radiation temperature	
f^{ij}	Eddington tensor	
$f\,(\mathscr{E})$	Eddington factor function	
$B\,(T_{\rm fl})$	Planck function	
$E_{\rm kin}$	kinetic, *etc.*, energy	
$\eta_{\rm v}$, $\eta_{\rm R}$, ...	viscous, magnetic, *etc.* diffusivities	
Dimensionless ratios		
β	'plasma beta'	$\beta = {}^{p_{\rm hyd}}/_{p_{\rm mag}}$
$\beta_{\rm rot}$	ratio of rotational (*etc.*) to gravitational potential energy	
$\beta_{\rm tot}$	ratio of all 'supportive' forces to gravitational energy	
ε	ratio of turbulent and rotational energy	$\varepsilon = {}^{\beta_{\rm turb}}/_{\beta_{\rm rot}} = {}^{E_{\rm turb}}/_{E_{\rm rot}}$
$\mathscr{R}$	Reynold's number	$\mathscr{R} = {}^{v\ell}/_{\eta_{\rm v}}$
$\mathscr{R}_{\rm m}$	'magnetic' Reynold's number	$\mathscr{R}_{\rm m} = {}^{v\ell}/_{\eta_{\rm R}}$
μ	mass–to–flux ratio (in terms of the critical ratio)	$\mu = {}^{\varpi_{\rm core}}/_{\varpi_{\rm critical}}$
ϖ	mass–to–flux ratio	$\varpi \propto {}^{M}/_{\Phi}$
γ	adiabatic index	
S.P.H. quantities		
ρ_a,v_a^i, ...	density, *etc.*, of some S.P.H. particle a	
$W_{ab}\,(h_a)$	smoothing kernel for particle a at b	$W_{ab}\,(h_a) = W\left(r_a^i - r_b^i, h_a\right)$
h_a	smoothing length of particle	
m_a	mass of particle	
η	h, in terms of the 'mean particle separation'	$\eta = h\sqrt[\nu]{{}^{\rho}/_{m}}$
$N_{\rm ngh}$	number of neighbour particles	

Table A. Symbol definitions (continued).

α_{AV}	artificial viscosity switch	
α_{AR}	artificial resistivity switch	
$\varrho_{\mathrm{m,a}}$	magnetic 'charge density' (monopole term)	$\varrho_{\mathrm{m,a}} = \nabla^i_a B^i_a$
Constants and mathematical symbols		
δ^{ij}	Kroencker delta tensor	
ϵ^{ijk}	Levi–Civita symbol	
μ_{o}	permeability of free-space	$\mu_{\mathrm{o}} = 4\pi \times 10^{-7}\ \mathrm{H \cdot m^{-1}}$ (s.i.)
c	speed of light in vacuo	$c = 2.998 \times 10^{10}\ \mathrm{cm \cdot s^{-1}}$
G	universal gravitational constant	$G = 6.672{,}6 \times 10^{-8}\ \mathrm{dyn \cdot cm^2 \cdot g^{-2}}$
N_{A}	Avogadro's number	$N_{\mathrm{A}} = 6.022{,}140{,}857 \times 10^{23}\ \mathrm{mol^{-1}}$
k_{B}	Boltzmann's constant	$k_{\mathrm{B}} = 1.380{,}7 \times 10^{-16}\ \mathrm{erg \cdot K^{-1}}$
$\mathscr{R}_g$	the universal gas constant	$\mathscr{R}_g = N_{\mathrm{A}} k_{\mathrm{B}} = 8.3145 \times 10^7\ \mathrm{erg \cdot K^{-1} \cdot mol^{-1}}$
σ_{B}	Stefan-Boltzmann constant	$\sigma_{\mathrm{B}} = 5.670{,}5 \times 10^{-5}\ \mathrm{erg \cdot cm^{-2} \cdot s^{-1} \cdot K^{-4}}$
au	the astronomical unit	1 au = 14,959,787,070,000 cm
pc	parsec	$1\ \mathrm{pc} = 3.086 \times 10^{18}\ \mathrm{cm}$
a	one year	1 a $\stackrel{\mathrm{def}}{=}$ 365 1/4 days
$\mathrm{M}_\odot$	solar mass	$1\ \mathrm{M}_\odot \stackrel{\mathrm{def}}{=} 1.996 \times 10^{33}\ \mathrm{g}$
Da	unified atomic mass unit / Dalton	$1\ \mathrm{Da} \simeq 1.660{,}539{,}040 \times 10^{-24}\ \mathrm{g}$
ν	number of spatial dimensions	invariably $\nu = 3$

Physical constants are taken (in general) from E. R. Cohen and Taylor (1987), with certain astrophysical constants from Luzum *et al.* (2011) (which became Resolution B1 of the XXVIII$^{\mathrm{th.}}$ General Assembly of the International Astronomical Union) and from Resolution B3 of the XXIX$^{\mathrm{th.}}$ General Assembly of the International Astronomical Union.

We use the centimetre–gramme–second system of units, using electro–static units (*i.e.* where co–efficent in Coulomb's Force Law[1] is exactly unity) throughout.

1. *vide* de Coulomb (1785)

The Acknowledgements

It is no understatement to say that this thesis could not have happened without my supervisor, Professor Matthew R. Bate, who among other things showed me that magnetic fields are not actually terrifying, and allowed me to dismantle and reassemble sphNG. I am additionally grateful for the support and guidance of Professor Joe Monaghan (the spiritual grandfather of S.P.H.), Dr. Daniel Price (perhaps the grandfather of S.P.M.H.D.), Dr. James Wurster, Professor Tim Naylor, Dr. Terrence Tricco, and Dr. Matthew Browning.

I must thank: Felix for putting up with me through two offices — and keeping my MacBook ineptitude under control; Tom W., Tom G., Tom C., Tom E., Elisabeth, Ahmad, Ben D., Jess, Freddy, Maria, Sam, the G27 coterie and everyone I've inevitably forgotten for the non–M.H.D. and non–S.P.H. side to Exeter (*ne quid nimis*, after all); and Michael for (when I can find you) explaining how radiation works. Also Emma, who by some magic has kept my chronic disorganisation from becoming a complete disaster!

The understanding of my campaign team in Croesyceiliog (particularly Lawrence and Shannon) was exemplary. Having your candidate vanish mid–campaign several times to sort out dissertational matters is rather sub–optimal — and we still managed a better showing than *anyone* would ever have expected.

It almost goes without saying that I would also like to thank my family in South Wales for putting up with me whilst I wrote this monograph. Normal service will now resume.

Finally, Aric (for psephology), Hannah (for, *inter alia*, inventing movie night), Calum (for æroplanes), Dr. Alistair Edge (for the M.Phys. that preceded this degree), the late Eva Schumaker–Reid (for advice never forgotten), Sue and Dave (for Australia), Martyn (for computing), Becca (for the Latin and Ancient Greek), and Emma B. (you know why).

The above notwithstanding, this thesis would almost certainly never have been finished without that *triumvirate* of Taylor, Fladgate, & Yeatman.

Benjamin T. Lewis
Exeter, Devon, The United Kingdom,
Wednesday, 31st. May 2017

CHAPTER I

The Introduction

Omnium rerum principia parva sunt.

Liber v, Capitulum lviii,
De Finibus Bonorum et Malorum, Marcus Tullius Cicero (*ca.* 45 B.C.)

Poca favilla gran fiamma seconda.

Canto i, Paradiso, Dante Alighieri (1320)

The Hellenic astronomers believed the fixed stars were immutable and unchanging, set in a grand crystalline sphere around the Earth — as recounted by Hipparchus (*ca.* 160–120 B.C.) and more completely by Ptolemy (*ca.* 150–170 A.D.). Modern astronomy has shown this to be far from correct, beginning with the observation that S.N. 1572 had no (observable) parallax and therefore could not be an atmospheric effect by Brahe (1573) and the similar discovery for S.N. 1604 by Kepler (1606). Rather than being permanent and static objects, we find that stars are dynamic and variable entities, with the formation of new stars (Robitaille and Whitney 2010) — and the death of older ones (S. P. Reynolds *et al.* 2008) — occurring regularly in both our own galaxy and throughout the Universe. Notwithstanding the advances in astronomical thinking since the time of Eudoxus' Φαινόμενα and today, many questions about how stars form remain; and solutions to these questions directly affect how we understand the Sun formed, and ultimately the Earth. However, the time scales — and the quite literally 'astronomical' distances — over which these processes occur prevent simple observation being used alone. Instead we turn to analytical and numerical models, the latter almost invariably performed on high–performance computers, to make predictions about the way a disparate, though bound, cloud of gas and dust produces a star.

In this work, we consider a comparatively short evolutionary epoch: how a bound 'core' in a molecular cloud collapses to form a pre–stellar object. Although only lasting *ca.* 30,000 years, this process marks the transition from a large low density cloud to a very compact dense object — a pre–stellar core — which after further evolution would become a (proto–)star. Although short, how this process proceeds has a marked effect on what the resultant protostar or protostars look like. For example, we find that changes in the primordial magnetic field threaded through the collapsing core can produce an array of different structures at the centre.

Short though this process is, it presents unique computational challenges. The initial density of a molecular cloud core is approximately $10^{-18}\,\mathrm{g}\cdot\mathrm{cm}^{-3}$, which is equivalent to about six million hydrogen atoms per cubic centimeter; the first stall phase (the formation of a first hydrostatic core) occurs at $10^{-10}\,\mathrm{g}\cdot\mathrm{cm}^{-3}$, eight orders of magnitude later (and about the same density as ten human red blood cells per cubic centimeter). In a few calculations, we proceed further to $10^{-5}\,\mathrm{g}\cdot\mathrm{cm}^{-3}$ to capture the second collapse phase. Stable hydrodynamics across eight or thirteen orders of magnitude presents many challenges, although smoothed particle hydrodynamics (S.P.H.), being mesh-free and able to automatically adjust the resolution as the density changes, is very capable. However, the addition of magnetism presents particular difficulties: magnetohydrodynamics are challenging even with simpler problems, and eight orders of magnitude of variation require a careful numerical approach. Consequently, on the way to considering how stars form we also consider potential improvements to our radiation magnetohydrodynamical method and, importantly, the limits of the state of the art.

In this chapter we begin with a review of the process of star formation in section I.1,

covering the evolutionary epoch captured by the numerical calculations in this thesis, and also including a summary of both earlier and later processes for context. Since magnetic effects form such an integral part of this work, we then devote section I.2 to a review of magnetised astrophysical fluids and ways these can be observed. We then include a brief overview of computational fluid dynamics, and in particular magnetohydrodynamics, in section I.3 to provide a contextual background to our numerical method and to our work on improvements thereto. Finally, in section I.4 we review the work contained in chapters III to VII. A complete discussion and review of our numerical method is presented in chapter II.

I.1 The Formation of the Fixed Stars

Stars are, compared to almost any other region of space, extremely dense. The process of turning space, where the mean density can be less than one particle per cubic centimetre into a star, where densities are many orders–of–magnitude higher, therefore requires several stages. The first is the formation of galaxies from the initial anisotropy of the distribution of matter in the universe and then the collapse of filamentary or other structures (either in a 'top down' fashion, as originally proposed by Eggen, Lynden–Bell, and Sandage 1962; Searle and Zinn 1978; or a 'bottom up' fashion, *e.g.* White and Rees 1978) followed by subsequent galactic mergers (Barnes 1992; Barnes and Hernquist 1992, 1996) and related processes[1]. A discussion of this is outwith the scope of this thesis.

Once a galaxy has formed, by whatever formation process, the gas within it will inevitably be turbulent and chaotic (Roberts 1969), as well as being denser than the intergalactic medium — the diffuse interstellar medium has a density of approximately one hydrogen atom per cubic centimetre (Ferrière 2001). Regions of this turbulent low density fluid then coalesce. These regions make up a comparably small fraction of the total volume of a 'typical' galaxy, *e.g.* the Milky Way and comprise about $1/100^{\text{th}}$. of the overall volume but in the region of $1/2^{\text{th}}$. of the total mass. In a spiral galaxy, these regions are correlated with the spiral arm structures (R. S. Cohen *et al.* 1980; Dame *et al.* 1987). These regions are termed giant molecular clouds (G.M.C.) and contain the regions — sometimes called 'stellar nurseries', as seen in the constellation of Orion (Kanipe 1989) — where new stars are formed (see, *e.g.* Sargent 1977, 1979). Smaller molecular clouds, sometimes termed 'Bok globules' (after Bok and Reilly 1947), also exist and these also contain regions of active star formation (*e.g.* Reipurth, Heathcote, and Vrba 1992). However, in this thesis we concentrate solely on star formation processes as they descend from a G.M.C., and we discuss how these clouds evolve and develop in sub–section I.1.1 *infra*.

However, a G.M.C. only has a density on the order of thirty particles per cubic cen-

1. we note that these mergers are often the cause of intense bursts of star formation (Hibbard 1997), *e.g.* as seen in the merging complex of NGC 4038 and NGC 4039 (Neff and Ulvestad 2000) (see also Hernquist 1989)

timetre (see, *e.g.* Gillmon and Shull 2006), so a further evolutionary stage is necessary before the star formation process can begin. This is the formation of a dense molecular cloud 'core' by some process, *e.g.* turbulence, a supernova shockwave, filamentary accretion, *etc.* (Ballesteros–Paredes *et al.* 2007). When a sufficiently compact object is formed, the self–gravitational forces within the object can exceed the ability of the gas pressure to prevent a gravitational collapse. This process is called the Jeans instability, after Jeans (1902), and we discuss this important phenomenon in more detail in sub–section I.1.2 *infra*. A molecular cloud core collapsing under its own gravity will eventually form one or more compact objects at the centre. In addition, a larger core may itself fragment into small cores as sub–regions themselves exceed the Jeans mass. The collapse will continue, with the gas density increasing (and a corresponding increase in the gas pressure since, all things being equal, $p \propto 1/V^{\gamma}$, where p and V represent the pressure and volume and γ is the adiabatic index) and ultimately with an increase in the gas temperature — at 'high' densities the assumption that the astrophysical plasma is an isothermal[2] ideal gas ceases to apply. Isothermality will be maintained for as long as the core can radiate away the graviational potential energy liberated as it collapses. If the core becomes opaque, which it does at densities of $\rho \sim 1 \times 10^{-13} \mathrm{g} \cdot \mathrm{cm}^{-3}$ (about sixty–thousand million protons per cubic centimetre), then the gravitational potential energy will instead act to heat the gas and increase the pressure faster than possible in a purely isothermal system. This acts to eventually stall the collapse, forming the first hydrostatic core (Larson 1969), which is the evolutionary epoch this thesis examines. These two processes are discussed in sub–sections I.1.3 and I.1.4.

Although the numerical calculations in this thesis do not continue beyond the first hydrostatic core phase, it is important to consider how the results obtained here fit into the subsequent picture. A first hydrostatic core forms when $\rho \gtrsim 1 \times 10^{-10}\,\mathrm{g} \cdot \mathrm{cm}^{-3}$. Once the temperature of this object exceeds the disassociation energy for diatomic hydrogen (H_2) additional liberated gravitational potential energy will act to dissociate these diatomic molecules. Thereafter, this newly separated hydrogen will be rapidly ionized, removing further gravitational energy. After $\rho \gtrsim 1 \times 10^{-8}\,\mathrm{g} \cdot \mathrm{cm}^{-3}$ the second collapse phase is fully underway. This process continues, as discussed in sub–section I.1.5, until the gas densities and temperatures can realise a sufficient gas pressure — which occurs when dissociation is essentially complete — to prevent further gravitational collapse and a protostar is formed.

The resulting protostar will continue to accrete gas from the surrounding area, including from any circumstellar disc or similar, and will ultimately begin generating thermal energy from nuclear fusion reactions instead of gravitational collapse. This pre–main–sequence star will then continue to evolve, and eventually become a main–sequence star after proceeding along a Hayashi track (Hayashi 1961; Hayashi and Hoshi 1961).

2. so the equation of state is exactly $p\left(\rho\right) = \left(\gamma - 1\right)\rho\epsilon$ or $p\left(\rho\right) = 2/3\rho\epsilon$ for monatomic hydrogen

I.1.1 The Evolution of Giant Molecular Clouds

Giant molecular clouds are dense regions of the interstellar medium. These regions have a sufficent density to attenuate ionizing cosmic ray flux (and any other source of ionization) so that molecular hydrogen[3] can form, hence the name. In spiral galaxies, these clouds appear to correlate with the spiral structures (there is essentially no molecular fluid in the inter–arm regions of the Milky Way, Digel *et al.* 1996), which implies a 'short' lifetime (in galactic terms) of $< 10\,\mathrm{Ma}$ (see Williams, Blitz, and McKee 2000). As noted above, the fluid which comprises the majority of the volume of a galaxy is turbulent, consequently molecular clouds are themselves turbulent. This turbulent motion drives the evolution of the cloud itself. Clearly, the clouds are broadly gravitationally bound (although, see Elmegreen 1993b) but not excessively so. If molecular clouds were very gravitationally supercritical, they would take on a more centrally condensed nature.

Instead, the turbulent and other motion within them causes the density structure to be very anisotropic (*e.g.*, as seen in the calculations performed by Bate 2009, 2012; Federrath and Klessen 2012; Padoan and Nordlund 2002). However, the stars that these clouds produce seem to follow a broadly consistent pattern notwithstanding the progenitor cloud. This pattern is termed the initial mass function[4] (I.M.F.) and observationally appears to be consistent both within the Milky Way and in other galaxies. Why this is so consistent (*e.g.* Bastian, Covey, and Meyer 2010) (and whether there are any exceptions, *e.g.* Geha *et al.* 2013) is an area of active observational and theoretical research.

I.1.2 The Jeans Instability

Ignoring any potential velocity or magnetic fields, the only forces acting on a sphere of gas are the gravitational self–potential of the fluid and the hydrodynamic fluid pressure. These two forces act in opposing directions, consequently a sphere where the self–gravity exceeds the fluid pressure will collapse. Conversely, a sphere where these two forces are the same will sit in equilibrium. As originally derived by Jeans (1902), this was approched by considering a density perturbation in an infinite uniform density medium. A slightly simpler way to imagine a gaseous sphere (analogous to a molecular cloud core) of radius r_{core} within which is contained some mass M_{core}, in which the only forces are self–gravity and fluid pressure, then there are two characteristic time scales. The first is the 'sound crossing time', *i.e.* the time taken for a sound wave (either a rarefaction or compression wave) to cross the sphere, given by

$$t_{\mathrm{s}} = \frac{r_{\mathrm{core}}}{c_{\mathrm{s}}}, \tag{I.1}$$

3. indeed, any molecules

4. *cf.* Chabrier (2003), Kroupa (2001), and Salpeter (1955)

where c_s is the sound speed of the fluid within the sphere. The second is simply the gravitational free–fall time (which is the minimum time the sphere would take to collapse so that $r_{core} \rightarrow 0$ assuming no other forces are present) given by

$$t_{ff} = \frac{1}{\sqrt{G\rho}}, \tag{I.2}$$

where ρ is the density of the fluid and G is the universal gravitational constant. If

$$t_{ff} < t_s \tag{I.3}$$

then any perturbation to the the sphere will collape it before a pressure wave has time to reach the perturbation and restore the original radius. By imagining a sphere which is exactly in equilibrium where equations I.1 and I.2 are exactly equal we obtain an expression for the Jeans length,

$$\ell_{\mathcal{J}} = \frac{c_s}{\sqrt{G\rho}}, \tag{I.4}$$

and the related Jeans mass (simply the mass contained within a sphere of exactly one Jeans length), *viz.*

$$M_{\mathcal{J}} = \int_{\phi=0}^{\phi=2\pi} \int_{\theta=0}^{\theta=\pi} \int_{r=0}^{r=1/2\,\ell_{\mathcal{J}}} \rho r^2 \sin\theta \mathrm{d}r\mathrm{d}\theta\mathrm{d}\phi = \frac{1}{6}\pi\rho\ell_{\mathcal{J}}^3. \tag{I.5}$$

If the fluid contained within the sphere is an ideal gas, then equation I.4 can be rewritten as

$$\ell_{\mathcal{J}} = \sqrt{\frac{\gamma \mathscr{R}_g T_{fl}}{\mu_{mol} G\rho}}, \tag{I.6}$$

where μ_{mol} is the mean molecular weight of the fluid. Considering the Jeans length in this manner is expedient because astrophysical plasmas are *very* close to ideal gases in the regime where the Jeans instability is likely. Consequently, if we know the spatial extent, average temperature and density of a region we can predict whether it is stable. However, as we hinted at the start of this sub–section, if additional sources of support in addition to the fluid pressure are present it would be possible for a region where $M > M_{\mathcal{J}}$ to remain uncollapsed.

An interesting effect is that the equation of state (and the adiabatic index) can influence whether or not the collapse fragments into sub–collapses. This phenomena was first noted by Hoyle (1953), although with a slightly more expansive treatment including cooling and related concepts. In effect, if the fluid pressure increases more rapidly as the fluid density rises than the self–potential does then increasing the density will operate to increase the Jeans length; conversely, if the self–gravity increases more rapidly then an elevated density will produce a reduced Jeans length. In the latter regime, a sphere undergoing a Jeans collapse will develop regions *within the sphere* which are themselves Jeans

unstable, and these may fragment and collapse themselves. This phenomenon, though unimportant in the calculations performed in this thesis is necessary when considering the formation of stellar clusters and related matters. It transpires that, in practice, for axisymmetric density distributions without a significant degree of rotation this fragmentation mode is unlikely.

I.1.3 Collapse of a Magnetised Molecular Cloud Core

The instability discussed in the preceding sub–section is the proximate reason why regions of an otherwise globally gravitationally stable G.M.C. collapse. However, before we consider the process of the collapse we first need to incorporate the effect of magnetic fields. Radiation and comparable effects principally operate to adjust $T_{\rm fl}$ and are therefore naturally incorporated[5] into equation I.6. The way to incorporate this is to first imagine a sphere in virial equilibrium (Clausius 1870), *i.e.* one where

$$2\mathcal{T} = -\mathcal{V}, \tag{I.7}$$

where $\mathcal{T}$ and $\mathcal{V}$ are the kinetic and potential energies. More comprehensively, this could be written as

$$2\mathcal{T} + 3\left(\gamma - 1\right)\mathcal{U} + \mathcal{H} = -\mathcal{V}, \tag{I.8}$$

where the additional terms $\mathcal{U}$ and $\mathcal{H}$ represent the contribution from thermal and magnetic sources (as done, *e.g.*, by Chandrasekhar and Fermi 1953b). This could be imagined as (for a simple astrophysical plasma where $\mathcal{T} = \mathcal{H} = 0$)

$$\frac{3}{2}\frac{\mathscr{R}_g T_{\rm fl}}{\mu_{\rm mol}} = \alpha\frac{GM_{\rm core}^2}{r_{\rm core}}, \tag{I.9}$$

where α is some order unity constant related to the internal density distribution (*e.g.* $\alpha = 3/5$ for a uniform density sphere, per *ibid.*). For magnetic effects to support this core against gravitational collapse, we can imagine the limit whereby instead $\mathcal{T} = \mathcal{U} = 0$, and

$$\mathcal{H} = \oiint_S r^j \sigma^{ij} \mathrm{d}S^i, \tag{I.10}$$

where σ^{ij} is the Maxwell stress tensor (see section II.2) and r^i is a position vector. This integral approximately evaluates to

$$\mathcal{H} \approx \frac{1}{6}B^2 r_{\rm core}^3, \tag{I.11}$$

5. although radiation *pressure* is a little more complicated, it is a 'small' effect compared to thermal and magnetic support

which follows from making the assumption that only an isotropic pressure $^1/_2 B^2$ component of σ^{ij} exists and that this is spatially invariant, therefore

$$\oiint_S r^j \, \sigma^{ij}\big|_{\rm iso} \, \mathrm{d}S^i \rightarrow \iiint_V r^j \delta^{ij} \, \sigma^{ij}\big|_{\rm iso} \, \mathrm{d}V \rightarrow \frac{1}{2}\frac{1}{4\pi} \iiint_V B^2 \mathrm{d}V, \tag{I.12}$$

$$\frac{1}{8\pi} \iiint_V B^2 \mathrm{d}V = \frac{1}{8\pi} B^2 \iiint_V r^2 \sin\theta \mathrm{d}r\mathrm{d}\theta\mathrm{d}\phi = \frac{1}{6} r^3 B^2. \tag{I.13}$$

Equivalently in terms of the magnetic flux through the surface of the sphere defined by $r^2_{\rm core}$,

$$\Phi = \pi B r^2_{\rm core}, \tag{I.14}$$

$$\mathscr{H} \approx \frac{\Phi^2}{6\pi^2 r_{\rm core}}. \tag{I.15}$$

Therefore, in much the same way that exactly one Jeans length is exactly in equilibrium (equation I.6) if

$$\frac{\Phi^2}{6\pi^2 r_{\rm core}} = -\mathscr{V} = \frac{3}{5}\frac{G M^2_{\rm core}}{r_{\rm core}}, \tag{I.16}$$

we can obtain the critical mass which will exactly balance the forces from magnetic flux through a sphere of that mass, *i.e.*

$$M_{\mathscr{B}} = \sqrt{\frac{5}{18\pi^2 G}}\Phi^2. \tag{I.17}$$

This represents a gravitational analogue to the Jeans mass (equation I.5) discussed in the preceding sub–section. For completeness, we note that the co–efficents in all these virial equations vary depending on the assumptions used. An example of this is shown by the earlier analysis of Nakano and Nakamura (1978) who obtain

$$M_{\mathscr{B}} = \sqrt{\frac{1}{4\pi^2 G}}\Phi^2, \tag{I.18}$$

which differs in effect by a factor of $\sqrt{9/10}$ from equation I.17.

Throughout this we have assumed that the 'ideal' magnetohydrodynamics approximation holds[6]. This explains the lack of any dependence on the radius in equation I.17 (or indeed equation I.18) — the critical mass for stability against magnetic forces is a function only of the field strength itself. In practice this means that for any core where $M_{\rm core} < M_{\mathscr{B}}$ (which we term a sub–critical core) will not collapse and will reach a finite non–zero ra-

6. sometimes expressed as the flux being 'frozen in' to the fluid

dius (and *vice versa* for a super–critical core with $M_{\rm core} > M_{\mathscr{B}}$). In practice, as noted in chapter IV, the exact calculation of equation I.17 should take account of somewhat more physics than this idealised scenario, however, the mass–to–flux ratio in terms of the critical ratio (however computed) can be imagined as

$$\mu = \frac{M_{\rm core}}{M_{\mathscr{B}}}. \tag{I.19}$$

The only mechanism by which a core with $\mu < 1$ can collapse is if some process, *e.g.* ambipolar diffusion (Simon 1955), can operate to rearrange the magnetic field and reduce the supporting flux.

Until now we have avoided considering the velocity field throughout the core. In reality, the turbulent motion present in the progenitor G.M.C. will cause any condensing sub–region to also have a velocity field. Considering again the virial thoeorem (equation I.7) but with

$$\mathscr{T} = \frac{1}{2} M_{\rm core} \left\langle v^2 \right\rangle \tag{I.20}$$

we can obtain the relation

$$-\mathscr{V} = 2\mathscr{T} = \frac{3}{5}\frac{GM_{\rm core}}{r_{\rm core}} = \frac{1}{2}\left\langle v^2 \right\rangle. \tag{I.21}$$

If we neglect the $3/5$ co–efficent on $\mathscr{V}$ this is simply a statement that if the kinetic energy exceeds the potential energy the core will unbind. We denote this ratio with

$$\beta_{\rm kin} = \frac{E_{\rm kin}}{E_{\rm grav}}. \tag{I.22}$$

For a core which is only rotating, this can be slightly simplified to

$$\beta_{\rm rot} = \frac{E_{\rm rot}}{E_{\rm grav}}, \tag{I.23}$$

with

$$E_{\rm rot} = \frac{1}{2} I \Omega^2 = \frac{1}{5} M_{\rm core} r_{\rm core}^2 \Omega^2 \tag{I.24}$$

where I is the moment of inertia and Ω is the angular velocity of the core. On the right–hand side we have assumed the moment of inertia associated with a uniform sphere, *i.e.* $I = 2/5 M_{\rm core} r_{\rm core}^2$. If $\beta \gtrsim 1$ the core will unbind and *vice versa*. Since this is only an approximate relation, in reality $\beta = 1$ is not an exact equilibrium point (and, indeed, for a turbulent velocity field much would depend on the precise distribution of the velocities).

If we obtain a Jeans unstable core, with $\mu > 1$ and $\beta < 1$, then it will collapse under its own gravity. All the initial conditions we use are designed so that this is true. In the limiting case where $\mu = \infty$ and $\beta = 0$ the time–scale for the core to collapse would be the

free–fall time (equation I.2), outside of this limit the collapse will take somewhat longer. In practice we find that changing μ so long as[7] $\mu \geq 5$ only causes small changes in the collapse time compared to moving from $\beta = 0.005$ to $\beta \approx 0.9$. The free–fall time for a core with $M_{\text{core}} = \text{M}_\odot$ is $t_{\text{ff}} \approx 25{,}000\,\text{a}$ so this process proceeds, compared to the timescales involved in the generation and evolution of galaxies and a G.M.C. exceedingly rapidly.

I.1.4 The First Hydrostatic Core

As the core collapses the fluid density will necessarily increase — no mass is being lost, so a reduction in the volume must increase the density. This will necessarily increase the pressure of the fluid (via the Boyle–Mariotte law, Boyle 1662; Mariotte 1679), however, the assumption that the fluid can be treated isothermally will hold until quite late in the collapse. Isothermality can only be maintained when the core can radiate away liberated gravitational potential energy. If the core were to cease to be transparent to the radiation flux carrying away this energy then the fluid would increase in temperature. Since, by the ideal gas law (Calpeyron 1834) an increase in fluid temperature will cause an increase in the fluid pressure at a given volume (and molar quantity of fluid), *i.e.*

$$\frac{V}{n} = R\frac{T}{P}, \tag{I.25}$$

this implies there will be an equilibrium radius at which the collapse will stop. The calculations by Larson (1969)[8] find that the opacity of the core becomes non–negligible at about a fluid density of $\rho = 1 \times 10^{-13}\,\text{g}\cdot\text{cm}^{-3}$. This was obtained by assuming a *constant* Rosseland (1924) mean opacity of $\kappa = 0.15\,\text{cm}^2\cdot\text{g}^{-1}$, although as many other discussions of circumstellar and interstellar dust have noted (*inter alia* Gaustad 1963; Guertler, Henning, and Dorschner 1989; Mathis, Rumpl, and Nordsieck 1977; Pollack, McKay, and Christofferson 1985), the real picture is much more complicated. Above this density, the temperature of the fluid *increases* as noted above instead of remaining constant. Larson (1969) then find that the equilibrium point at which the collapse ceases occurs at a radius of $r = 6 \times 10^{13}\,\text{cm} = 4\,\text{au}$ (corresponding to a volume of $V = 9 \times 10^{41}\,\text{cm}^3$) containing a mass of $1 \times 10^{31}\,\text{g} = 0.005\,\text{M}_\odot$ (which gives a fluid density of $2 \times 10^{-10}\,\text{g}\cdot\text{cm}^{-3}$ and, by applying a form of equation I.25 a fluid temperature of about $T = 170\,\text{K}$. These quanities, which define the first hydrostatic core regime, are also used to set the conditions of our 'inner boundary' conditions, *e.g.* the sink particles as discussed in section II.5.

Infalling material from the remainder of the (still isothermal and still almost free–falling) core will continue to accreted onto the hydrostatic core in the centre. A shock front

7. we avoid $1 < \mu < 5$: although these cores are super–critical the effects of ambipolar diffusion would become increasing important so the ideal M.H.D. approximation would not be a suitable assumption

8. Although these are for a non–rotating, non–magnetized, core and adopt several other simplifying assumptions, these calculation provide a remarkably robust description of how a molecular cloud core produces a protostar.

forms when this material is suddenly stopped as it reaches the core boundary, and any material added to the core will increase the mass. This alone would increase the core temperature and density, however, in addition the outer regions of the hydrostatic core radiate energy away. Consequently the core both *increases* in mass whilst concurrently *decreasing* in volume — which necessarily precipitates a large increase in density and temperature.

In reality, the progenitor molecular cloud core which went on to produce a first hydrostatic core will possess a non–negligible quantity of angular momentum (produced ultimately from the turbulence in the antecedent G.M.C., Fleck and Clark 1981). This will cause the infalling material to form a disc around the hydrostatic core. We recognise two morphological types of these discs: in Lewis and Bate (2017) we defined a pseudo–disc as a flattened disc–like structure, rotating around the hydrostatic core but with a non–negligible radial velocity towards the core (and hence a sub–Keplerian rotation profile) which is nonetheless pressure supported against further gravitational collapse perpendicular to the disc plane. This earlier, and larger, structure is ultimately replaced by a true accretion disc at a later evolutionary epoch.

A serious problem emerges, however. The total angular momentum observed in molecular cloud cores is markedly higher than either that seen in more evolved stars and that which would destroy the stellar system. This problem was termed the 'angular momentum catastrophe'. The effect of the magnetic field, including the production of any bipolar outflow and the resolution of this 'catastrophe', will be discussed in the next section.

I.1.5 The Second Collapse Phase

The process of decreasing in volume whilst increasing in mass due to accretion and radiation noted at the end of the previous sub–section will continue until some change in the properties of the fluid occurs. The first of these would be a change in the nature of the opacity causing dust — here Larson (1969) made the assumption that all dust evaporates at $T = 1{,}400\,\mathrm{K}$. As before, the actual picture is more complicated this, and different species of interstellar dust will sublimate at different temperatures (see, *e.g.*, Salpeter 1977). More importantly, once a temperature of about $T = 2{,}000\,\mathrm{K}$ is reached the diatomic hydrogen in the hydrostatic core will begin to dissociate into monatomic hydrogen (again, this is a simplification of an otherwise complex process, see *e.g.*, Dalgarno and Roberge 1979; Lepp and Shull 1983). This process of changing H_2 into H atoms will cause a second collapse phase to occur. Effectively all the gravitational energy liberated by this reduction in radius will be used to dissociate H_2, and thence to ionize it and other gases present in the fluid. Consequently the overall temperature of the core will not appreciably increase.

Of interest to us is the point at which this process begins. Although we do not actually follow this second collapse numerically, we do need to ensure that when we apply an inner boundary condition this is done correctly. One way to do this is to ensure that the region in question is clearly in the process of collapsing beyond a first hydrostatic

core. Larson (1969) found that a two–fold increase in the mass within and a two–fold decrease in the radius of the hydrostatic core marked the beginning of this phase, which ultimately terminates when $\rho \approx 1 \times 10^{-2}\,\mathrm{g \cdot cm^{-3}}$. Numerically following the collapse to this density would be unfeasible[9], and is also unnecessary. Consequently, we define $\rho = 1 \times 10^{-5}\,\mathrm{g \cdot cm^{-3}}$ as the fluid density at which a core is clearly in the second collapse phase.

After a new, significantly smaller, dense core is formed by this process, the protostar continues to evolve to ultimately form a star. This dense core is often termed (by observational classification) a 'Class 0' young stellar object (Y.S.O.). As these objects progessively blow away their circumstellar material, beginning first by eliminating material not contained within the accretion or protoplanetary disc and ultimately all circumstellar gas, they evolve into 'Class I', 'Class II', and 'Class III' Y.S.O. s (F. C. Adams, Lada, and Shu 1987).

I.2 On the Magnetic Field in Astrophysical Fluids

The preceding section only included a discussion of magnetic fields insofar as these affect the stability of a molecular cloud core. In this section we discuss these fields in more detail. The majority of the baryonic matter in the universe exists as a plasma, a fluid phase which is an admixture of negatively charged electrons and positively charged ions. The resulting fluid is highly sensitive to electromagnetic fields due to the approximately free motion of positive and negative charges relative to each other.

Observations (*e.g.* Caswell 1976; Ellis and Hamilton 1966) and theoretical calculations (*e.g.* the two–phase model of Field, Goldsmith, and Habing 1969 and the three–phase model of McKee and J. P. Ostriker 1977) of the interstellar medium indicate that a significant fraction is comprised of ionized hydrogen gas. Similarly, molecular clouds contain magnetic fields (Crutcher and Kazes 1983; Crutcher *et al.* 1993; Crutcher, Troland, and Heiles 1981; Crutcher, Troland, and Kazes 1987) even though a large fraction of the mass therein is in a gaseous molecular phase not an ionized plasma phase. All of this indicates that a magnetohydrodynamical treatment of the evolution of astrophysical fluids is necessary.

Even at some of the largest scales, *i.e.* galaxies, the magnetic field present throughout the astrophysical plasma affects the evolution of the fluid. Observations of galaxies *without* the traditional 'grand design' spiral arms still find spiral 'magnetic arms' in the plane of the galactic disc (Beck 2005), and in grand design galaxies these correlate with the optical spiral arms (Neininger 1992). The obvious candidate to explain these fields, which are observed to be reasonably strong, is a galactic dynamo, as proposed by Parker (1970, 1971a,b). These magnetic fields may then influence the formation of a G.M.C., via

9. the high densities involved require a very short time–step to simulate

one or more instabilities (*e.g.* Parker 1966, the M.R.I., Kim, E. C. Ostriker, and Stone 2003, or that proposed by Elmegreen 1987).

We noted in sub–section I.1.1 *supra* that a G.M.C. is comprised of turbulent fluid. This turbulent motion naturally creates and drives the formation of magnetic fields, which in turn influence the evolution of the cloud (Heiles *et al.* 1993). Importantly, it appears that all G.M.C.s are sufficently massive that magnetic effects can not support them against gravity (*i.e.* they are supercritical in the same sense as a supercritical molecular cloud core discussed in sub–section I.1.3) (*e.g.* Crutcher 1999; McKee 1989). However, the magnetised turbulent motions within these clouds will produce a complicated magnetic field structure. This will have two overall effects: firstly it will change how the filamentary structure of the cloud evolves (and hence where are the overdensities that lead to the Jeans instability, *vide* sub–section I.1.2) by providing both additional magnetic pressure and also regions parallel to the field lines where fluid flow is enhanced. Secondly, it will affect the initial conditions for a molecular core collapse. It is this second effect we concentrate on in this thesis.

I.2.1 The Initial Magnetic Field in a Core

The stability analysis in sub–section I.1.3 assumed a uniform magnetic field. A common additional assumption (although unimportant for that analysis) is that this field is also aligned to the rotation axis of the core. This simplifying assumption makes analytical and numerical studies of molecular cloud cores more tractable, but is unlikely to be true in a real core. The velocity field of a molecular cloud core (which will provide the rotation) is provided from the progenitor molecular cloud along with the magnetic field (*e.g.* Hennebelle and Falgarone 2012; Vázquez-Semadeni *et al.* 2005). The turbulent motions in molecular clouds will produce filamentary structures; however, it has been observed that the magnetic field strength does not appear (at least on large scales in 'lower' density regions) to scale with column density (see, *inter alia*, Planck Collaboration *et al.* 2016a). At higher densities, the situation may well be more complicated (and a scaling between column density and field strength is observed) (*e.g.* Chapman *et al.* 2011; Santos *et al.* 2014). Either of these configurations imply that the magnetic field and any rotational velocity field are unlikely to be completely in alignment, and may well be considerably misaligned. This supposition is confirmed by observations of clouds and cores, *e.g.* the structure of L1544, L183, and L43 observed by Ward-Thompson *et al.* (2000) and L1642 by Malinen *et al.* (2016).

The earliest theoretical work assumed an aligned magnetic field and rotation axis (and a laminar velocity profile). From this the characteristic evolutionary process, whereby a spherical core becomes collapses, becomes oblate and ultimately forms a disc structure and an outflow closely aligned with rotation axis was determined (Banerjee and Pudritz 2006; Bate, Tricco, and D. J. Price 2014; Hennebelle and Fromang 2008; Machida, Inutsuka, and Matsumoto 2006, 2008; D. J. Price, Tricco, and Bate 2012; Tomida *et al.* 2013). The

change from a spherical core (which is itself a simplifying assumption) to an oblate core is seen even in rotating non–magnetised calculations (Nejad-Asghar 2010), however, increasing the magnetic field strength causes enhanced oblateness (Matsumoto and Hanawa 2011). The cause of the this identical to the way a magnetic field aligned with a turbulent filament causes enhanced accretion: there is no magnetic pressure *parallel* to the magnetic field lines and therefore when these are aligned with the rotation axis the result is an oblate core. Clearly the situation will be more complicated when the magnetic field and rotation axis are not aligned, as evidenced by earlier work by D. J. Price and Bate (2007) and Ciardi and Hennebelle (2010).

Once the molecular core has collapsed and begun the process of forming a first hydrostatic core, a disc forms around it. This is a natural consequence of the conservation of angular momentum in the system. Unlike a circumstellar disc, these discs are very large (often on the order of 100 au) and sub–Keplerian. This latter property may be a product of magnetic braking effects (Armitage 2011; Rappaport, Verbunt, and Joss 1983, *cf.* a comparable effect in neutron stars, Ghosh and Lamb 1978) — rather than viscous drag or other magnetohydrodynamic effects such as the magnetorotational instability (M.R.I.) — and this magnetic braking may be essential for the evolution of the protostar (Basu and Mouschovias 1994). The comparably rapid motion of this disc then drives more complicated M.H.D. processes. It has been argued that this magnetic braking is actually *too* efficent and is unable to ever produce a Keplerian accretion disc (Allen, Li, and Shu 2003; Galli *et al.* 2006; Mellon and Li 2008). Recent work has avoided this problem either by noting that turbulence will reduce the braking efficency (*e.g.* Seifried *et al.* 2012) or by invoking non–ideal M.H.D. effects (*e.g.* Wurster, D. J. Price, and Bate 2016) or both.

I.2.2 Bipolar Jets and Outflows

The most dramatic of the magnetic effects seen around protostars and their antecedent hydrostatic cores are bipolar jets. These are the ultimate causes of the Herbig–Haro objects (Burnham 1890; Haro 1952; Herbig 1951) which are indicative of star formation. Our understanding of the precise formation mechanism for these jets is still somewhat incomplete. However, what is clear is that they are formed by the rotating disc which surrounds either a first hydrostatic core or a stellar core. D. J. Price, Pringle, and King (2003) showed that the maximum velocity of an outflow from an accretion disc is related to the maximum Keplerian velocity in the disc — in effect the minimum radius. This allows us to divide protostellar outflows into two groups: 'slow' outflows produced from the region around a first hydrostatic core; and 'fast' outflows from more evolved objects. The latter have velocities in the region of $10\,\mathrm{km}\cdot\mathrm{s}^{-1} < |v| < 30\,\mathrm{km}\cdot\mathrm{s}^{-1}$ as found numerically by Banerjee and Pudritz (2006), Bate, Tricco, and D. J. Price (2014), and Machida, Inutsuka, and Matsumoto (2006, 2008) and observationaly *e.g.* in BHR 71 by Bourke *et al.* (2017). The velocities of the slower jets are $|v| \leq 10\,\mathrm{km}\cdot\mathrm{s}^{-1}$, limited by the first hydrostatic core radius of $r \simeq 4\,\mathrm{au}$.

The 'standard model' for how these jets are formed is that originally proposed by Blandford and Payne (1982) (see also Lynden–Bell 1996). In this model, the interplay between the toroidal and poloidal components of the magnetic field are considered separately. The former acts to collimate the jet and thereby transport angular momentum away. The latter — coupled with any thermal pressure — is required to first move fluid out of the plane of the disc and thereby create an outflow at all. These collimated outflows are important parts of the star formation process since they very efficently transport angular momentum away from the disc. This avoids the overly prolific fragmentation seen in purely hydrodynamic calculations and also helps explain the observed 'low' angular momentum in the solar system compared to that expected for a molecular cloud core. Some observational evidence for this poloidal–toroidal formation was found in NGC 1333 IRAS 4A by Ching *et al.* (2016).

The preceding paragraph implicitly assumes an aligned system. The situation is similar but more complicated once the effects of misalignment and turbulence are considered. Observational evidence for this exists, *e.g.* Hull *et al.* (2013a) and Hull *et al.* (2013b) noted misalignements between the velocity vector of an outflow and magnetic field vector in the system[10]. An obvious cause of this would be the magnetic field and angular momentum vectors being misaligned: the magnetic field will attempt to put any accretion disc perpendicular to the field lines, and *vice versa* for the rotational velocity field. Any disruption to the disc as the result of these misalignments would also reduce the efficency of the acceleration processes which drive the outflow (*cf.* Bogovalov and Tsinganos 1999) and consequently produce slower outflows.

Numerical calculations, for example those performed by (Ciardi and Hennebelle 2010) and by us (see both this thesis and also Lewis and Bate 2017; Lewis, Bate, and D. J. Price 2015), indicate that a misalignment between the rotation and magnetic field axes can indeed produce effects of this nature. Additionally, it may be possible for the 'slow' jet to orient close to, *e.g.*, the magnetic field axis and then the 'fast' jet to switch and be more closely oriented to the angular momentum vector of the system.

I.2.3 Observing Magnetic Fields

It is not possible to directly measure the magnetic field in the astrophysical plasma — one can not insert a Hall probe or some other magnetometer into a molecular cloud and measure the magnetic flux. Consequently indirect methods must be used. One such method is to look at the polarization of dust particles by the field. Alone, this would not provide any information about the strength of the field — although it would certainly be useful for determining the geometry, as done by Planck Collaboration *et al.* (2016b). However, it is possible to draw interferences from the *statistical distribution* of this polarization. If

10. the contrary configuration has also been observed, *e.g.* in IRAS 18089-1732 by Beuther *et al.* (2010) although in this system the turbulence present may complicate matters

we assume that the astrophysical plasma is completely turbulent (*i.e.* that there are no non–random velocity field sources) then we can use the Chandrasekhar and Fermi (1953a) method to estimate the magnitude of the field. This works by noting that the perturbation of the polarization vectors will be higher for weaker fields and *vice versa*. The caveat with this approach is that if the fluid contains non–turbulent motion the perturbations will be over–estimated and a consequently over–weak field will be estimated. This approach has been successfully used to estimate the fields present in molecular clouds, *e.g.* as in Sandstrom and Goodman (2001), however, even with various corrective approaches (*e.g.* Hildebrand *et al.* 2009; Houde *et al.* 2011, 2009) this method is only accurate down to about a factor of two (Crutcher 2012). Provided that a grain size approximately the same as the desired wavelength of light to be polarized can be observed then this technique can probe the magnetic field even in dense cloud cores (Cho and Lazarian 2005).

If the column density of the cloud is sufficently low, *e.g.* at the cloud edges, then it should be possible to use background stars to probe the field strengths using this method. Surveys using this technique, as opposed to light from *within* the cloud, have been performed, *e.g.* for Perseus, Taurus, and Ophiuchus by Goodman *et al.* (1990). This method is by definition restricted to the line–of–sight field and consequently may miss three–dimensional field structures. There are also complexities due to uncertainties in the geometry of the cloud itself. From within the cloud, attempts have been made to use thermal emission from within the cloud to measure the polarization vectors. This was first performed for M42 and W51A in a balloon detector survey by Cudlip *et al.* (1982).

An alternative — and somewhat more direct — approach is to use the Zeeman (1897) effect. This is only feasible for certain molecules due to the specific energy levels required, however it has been observed for H I, OH, and CN lines[11] in molecular clouds. The underlying principle behind this is that in the presence of a magnetic field, the magnetic moment of an atom produces a separation in energy levels given by

$$\Delta E = m_l \mu_B B = m_l \frac{e\hbar}{2m_e} B, \tag{I.26}$$

where the magnetic quantum number is given by $m_l = 2l + 1$, e is the elementary charge, m_e the electron mass, the reduced Planck constant (the Dirac constant) $\hbar = {}^{h}/_{2\pi}$, and μ_B is the Bohr magneton[12] as usual. In terms of frequencies, this produces three frequency shifts: when $m_l = 0$, $\Delta r = 0$ and the original line frequency is recovered, and (assuming $\ell = 1$) the two shifted frequencies are given by

$$\Delta r = \pm \frac{e}{2m_e} B. \tag{I.27}$$

11. these latter two exhibiting what was historically known as the 'anomalous' Zeeman effect

12. *cf.* Procopiu (1913)

The situation is slightly more complex in non–singlet states but the underlying principle remains. Therefore, if we can measure Δv accurately for a particular spectral line we have a direct measure of B (given certain assumptions about the field geometry). This technique has been used (on the OH line) by Crutcher *et al.* (1993) to find that — overall — molecular clouds appear to be in an approximate magnetic virial equilibrium, for the Ophiuchus cloud by Goodman and Heiles (1994), and the use of the Square Kilometre Array for more detailed studies has been proposed (Robishaw *et al.* 2015). However, this technique remains time consuming compared to other methods (Crutcher and Troland 2008).

By performing a Bayesian analysis of several surveys using these techniques (*viz.* Crutcher 1999, Falgarone *et al.* 2008, Troland and Crutcher 2008) Crutcher, Hakobian, and Troland (2010) (see also Crutcher 2012) showed that molecular cloud cores are most likely to be super–critical. However, since an average mass–to–flux ratio in the region of $\mu \approx 2 \sim 3$ is also found by this (and other) analyses, this implies that *some* cores are close to critial or even sub–critical. This provides a motivation for consider a range of initial magnetic field strengths. Further, this indicates that the initial magnetic field strength in a molecular core varies significantly between cores which will then influence the subsequent evolution.

I.3 Fluid Dynamics

In the preceding section we noted that the astrophysical plasma is a fluid. This means a natural way to study it is to use fluid dynamics. In the next chapter we cover our numerical method in detail, in this section we instead cover the overarching concepts. In much the same way as some of the first recorded thoughts on the nature of the fixed stars date from the Hellenic astronomers, the earliest musings on the dynamics of fluids may have been by Archimedes of Syracuse (*ca.* 250 B.C.). Modern fluid dynamics owes much to improvements and discoveries in the nineteeth century. In this thesis, we use fluid dynamics to study how astrophysical fluids evolve. The underlying assumption in fluid dynamics is that the fluid is continous and as a result the motion of individual particles is unimportant. This is an essential for even a simple problem (since tracking individual atoms or molecules is completely intractable) and even for *very* low density fluids[13] is a very accuarate approximation.

Since we don't follow our calculations to very *high* densities, we are able to make a series of assumptions. Firstly we assume that the astrophysical plasma is compressible. Although incompressibility can simplify analytical approaches to fluid dynamics, it transpires that it actually significantly increases the complexity of using our S.P.H. method. Secondly, we assume that the astrophysical plasma is inviscid[14]. Using this, the compress-

13. far lower than the lowest densities in our calculations

14. neglecting the artificial S.P.H. viscosity applied to prevent numerical artefacts, *vide infra* sub–section II.1.4

ible Navier–Stokes (Navier 1823; Stokes 1854) momentum equation,

$$\mathrm{D}_t v^i = -\frac{1}{\rho}\nabla^i p + \eta_\mathrm{v}\triangle v^i + \frac{1}{3}\eta_\mathrm{v}\nabla^i\nabla^j v^j + g^i, \tag{I.28}$$

becomes

$$\mathrm{D}_t v^i = -\frac{1}{\rho}\nabla^i p + g^i. \tag{I.29}$$

This statement that $\eta_\mathrm{v} = 0$ is equivalent to saying that our fluid has an infinite Reynolds number (O. Reynolds 1883; Stokes 1851), *i.e.*

$$\mathscr{R} = \frac{v\ell}{\eta_\mathrm{v}} = \infty. \tag{I.30}$$

If the fluid had been incompressible, this equation would also slightly simplify in the presence of viscosity since an incompressible fluid guarantees a solenoidal velocity field (*i.e.* $\nabla^i v^i = 0$). Equation I.29, once discretised as detailed in section II.1, forms the basis of our numerical method. Since we assume that our fluid is compressible throughout, and we are careful to set the boundaries so that the fluid is contained, we do not need to deal with the complexities for solid boundaries and the like.

Numerical simulations of astrophysical phenomena have a long history. Arguably, this began with the simple 'N–body' experiment performed by Holmberg (1941). This used light bulbs — since luminous flux follows the same inverse square law as a gravitational potential — as a proxy for gravity. In this way, an otherwise impossible calculation, using only seventy–four stars in two galaxies which would require 5,476 calculations per time–step, became tractable. The advent of the computer age allows this same principle to be applied to fluids. Modern computers can perform millions of calculations per second, which allows for a fluid with significantly higher resolution (or equivalently an N–body calculation with more stars) to be performed in a reasonable length of time. However, even with the earliest computers, significant results were obtained, albeit generally at lower numerical resolution. For example, the original S.P.H. paper, Lucy (1977), had a resolution of only sixty S.P.H. particles (effectively sixty interpolation points).

With modern computational technology, resolutions easily in excess of a million particles are tractable. At the most extreme, a small number of calculations have used over a thousand–million particles (Schaye *et al.* 2015). This prodigious increase in resolution since both the early work of Holmberg (1941) and of Lucy (1977) has opened up a wide range of astrophysical problems to theoretical work. Low resolution calculations will, for example, be unable to effectively model turbulent effects which are smaller than the minimum resolution. It is important to note, though, that as well as any numerical limitations caused by various assumptions made, the fundamentally finite resolution used is a limitation.

I.3.1 (Ideal) Magnetohydrodynamics

All of the calculations performed in this thesis consider the evolution of a magnetised fluid. Therefore we need to extend the technique discussed above to include magnetic fields. We are aided in this endeavour by the fact that the plasma can be imagined as a fluid (meaning we can use a modified form of the non–magnetic equations above); that a form of Ohm's Law for a plasma can be obtained (*i.e.* there is a simple relation between the electric and magnetic fields); and that the fluid is electrically neutral. We also continue the assumption of a single species fluid. The Ohm Law[15] for a plasma is given by

$$J^i = \sigma \left(E^i + \frac{1}{c} \epsilon^{ijk} v^j B^k \right), \tag{I.31}$$

or equivalently, by noting that the resistivity of the fluid $\eta = 1/\sigma$,

$$E^i = \eta J^i - \frac{1}{c} \epsilon^{ijk} v^j B^k, \tag{I.32}$$

The Maxwell–Faraday Law (Maxwell's IIIrd. Equation) (*cf.* Faraday 1832) is given by

$$\partial_t B^i = -c \epsilon^{ijk} \nabla^j E^k, \tag{I.33}$$

which if we substitute in the Ohm Law given by equation I.32 into equation I.33 gives an equation for the change in the magnetic field over time,

$$\partial_t B^i = \epsilon^{ijk} \nabla^j \epsilon^{klm} v^l B^m - \eta c \epsilon^{ijk} \nabla^j J^k. \tag{I.34}$$

In a perfectly conducting fluid there is no resistivity by definition, so if we consider this equation in the limit where $\eta = 0$ we obtain the ideal M.H.D. induction equation, *viz.*

$$\partial_t B^i = \epsilon^{ijk} \nabla^j \epsilon^{klm} v^l B^m. \tag{I.35}$$

Given that a divergence of the curl of a vector is exactly zero, this also provides the link between M.H.D. and Gauss' Law for magnetism, *viz.* that

$$\partial_t \nabla^i B^i = 0. \tag{I.36}$$

Importantly, this constraint implies that any numerical scheme which directly evolves equation I.35 must take care to maintain equation I.36 since the solenoidal constraint does not enter these equations in any other way. It will become clear in chapter II and especially in chapter III that this presents several difficulties. These equations describe how

15. *cf.* Ohm (1827) for the linear relation

the magnetic field evolves in the fluid.

We now need to modify equation I.29 to include this additional field. We begin with the Lorentz force law (Heaviside 1889; Lorentz 1892),

$$F^i = q\left(E + \frac{1}{c}\epsilon^{ijk}v^j B^k\right). \tag{I.37}$$

However, written in this form (which is for the motion of individual point charges) it is not directly useful for a fluid — where we explicitly wish to ignore the motion of *individual* particles. Instead, we can consider the force density, defined so that

$$f^i = n_q q\left(E + \frac{1}{c}\epsilon^{ijk}v_q^j B^k\right), \tag{I.38}$$

where n_q is the number density of charged particles (*i.e.* so that $\varrho_q = n_q q$ is the charge density) and v_q^j is the velocity field of those particles. A plasma consists of a mixture of two species of charges: negatively charged electrons with a charge of $q = -e$ and with a number density n_e and positively charged ions with $q = +e$ with a corresponding density n_i . The motion of each species produces a force density, and the total force is the combination of these, *i.e.*

$$f^i = f^i_{v_\mathrm{i}} + f^i_{v_\mathrm{e}}, \tag{I.39}$$

$$f^i = n_\mathrm{i} e\left(E + \frac{1}{c}\epsilon^{ijk}v_\mathrm{i}^j B^k\right) - n_\mathrm{e} e\left(E + \frac{1}{c}\epsilon^{ijk}v_\mathrm{e}^j B^k\right). \tag{I.40}$$

Re–arranging this equation, we obtain

$$f^i = eE\left(n_\mathrm{i} - n_\mathrm{e}\right) + \frac{e}{c}\left(n_\mathrm{i}\epsilon^{ijk}v_\mathrm{i}^j B^k - n_\mathrm{e}\epsilon^{ijk}v_\mathrm{e}^j B^k\right). \tag{I.41}$$

A fluid with an equal balace of electrons and ions, *i.e.* one which is charge neutral, will have $n_\mathrm{i} - n_\mathrm{e} = 0$ and consequently the first term on the right–hand side is zero. Therefore, the force density is given by

$$f^i = \frac{1}{c}\epsilon^{ijk}\left(e n_\mathrm{i} v_\mathrm{i}^j - e n_\mathrm{e} v_\mathrm{e}^j\right) B^k. \tag{I.42}$$

By definition, a current density is defined as

$$J^i = \varrho_q v_q^i = q n_q v_q^i, \tag{I.43}$$

and therefore the force density can be written as

$$f^i = \frac{1}{c}\epsilon^{ijk} J^j B^k. \tag{I.44}$$

We now note that a force density can be represented as the divergence of a stress tensor, *viz.*

$$\nabla^i \sigma^{ij} = \frac{1}{c}\epsilon^{ijk} J^j B^k. \tag{I.45}$$

If we can obtain an expression for the current density, J^j, we will have a useful force density equation which we can combine with equation I.29.

To obtain this, we consider the Maxwell–Ampère Law (Maxwell 1861),

$$\epsilon^{ijk}\nabla^j B^k = \frac{4\pi}{c} J^i + \frac{1}{c}\partial_t E^i, \tag{I.46}$$

which for an charge neutral fluid gives an expression for the current density[16], *viz.*

$$J^i = \frac{c}{4\pi}\epsilon^{ijk}\nabla^j B^k. \tag{I.47}$$

Substituting equation I.47 into equation I.45 we obtain the M.H.D. force density (and implicitly the M.H.D. stress tensor),

$$\nabla^i \sigma^{ij} = \frac{1}{4\pi}\frac{1}{\rho}\epsilon^{ijk}\left(\epsilon^{jlm}\nabla^l B^m\right) B^k. \tag{I.48}$$

From this we obtain a force equation for M.H.D. (both ideal and non–ideal M.H.D. have the same expression for the force):

$$\mathrm{D}_t v^i = -\frac{1}{\rho}\nabla^i p + \frac{1}{4\pi}\frac{1}{\rho}\epsilon^{ijk}\left(\epsilon^{jlm}\nabla^l B^m\right) B^k + g^i. \tag{I.49}$$

although in practice (as we note in chapter II) we generally write this and equation I.35 not in terms of curl operations in computational schemes.

I.3.2 Non–Ideal Magnetohydrodynamics

Although in this thesis we restrict ourselves to the ideal M.H.D. approximation only, we include a brief summary of the three non–ideal M.H.D. effects for completeness. Importantly, furture work on the evolution of molecular cloud cores will need to include some or all of these effects, and significant progress is being made in this arena. The three non–ideal effects are Ohmic resistivity (sometimes Ohmic dissipation or Ohmic diffusion), ambipolar diffusion, and the Hall effect. We will briefly consider each of these in turn and then produce a full non–ideal M.H.D. induction equation. As noted in the preceding sub–section all three of these phenomena only involve modifications to the induction equation. In addition to being simply diffusive, a resistive M.H.D. implementation could allow for

16. an interesting side–note here is that because the divergence of a curl is zero, this *also* implies that the current density field is solenoidal in ideal M.H.D.

some process of magnetic reconnection (perhaps caused by turbulence) to be simulated (Santos-Lima, de Gouveia Dal Pino, and Lazarian 2012), although reconnection may in practice require a more advanced plasma physics scheme.

If we imagine that the plasma *does* contain an electric field, perhaps called $\tilde{E}^i$, and that the approximation

$$J^i = \sigma \tilde{E}^i \tag{I.50}$$

is valid, then we can write

$$\tilde{E}^i = \frac{c}{4\pi\sigma}\epsilon^{ijk}\nabla^j B^k, \tag{I.51}$$

and substitute this into equation I.31 so that we obtain an expression of the form

$$\frac{1}{c}\epsilon^{ijk}v^j B^k - \frac{c}{4\pi\sigma}\epsilon^{ijk}\nabla^j B^k = E^i, \tag{I.52}$$

which when inserted into equation I.33 produces

$$\partial_t B^i = \epsilon^{ijk}\nabla^j \left(\epsilon^{klm}v^l B^m - \frac{c^2}{4\pi\sigma}\epsilon^{klm}\nabla^l B^m\right). \tag{I.53}$$

If σ is constant across the fluid, *i.e.* $\nabla^i \sigma \left(r^i\right) = 0 \, \forall r^i$, then by the vector identity

$$\epsilon^{ijk}\nabla^j \epsilon^{klm}\nabla^l B^m \equiv \nabla^i \nabla^j B^j - \triangle B^i \tag{I.54}$$

and using the constraint that $\nabla^j B^j = 0$, this can be written as a diffusion equation,

$$\partial_t B^i = \epsilon^{ijk}\nabla^j \epsilon^{klm} v^l B^m + \eta_R \triangle B^i. \tag{I.55}$$

where the magnetic (resistive) diffusivity (analogous to diffusion in fluids more generally),

$$\eta_R = \frac{c^2}{4\pi\sigma}. \tag{I.56}$$

Early we noted the existence of a dimensionless number, the Reynolds number, which related the viscosity of a fluid to its motion. An analogus number can be constructed for M.H.D. with resistivity, *viz.* the magnetic Reynolds number,

$$\mathscr{R}_m = \frac{v\ell}{\eta_R}, \tag{I.57}$$

As before, when $R_m = \infty$ the fluid is non–resitive (and the ideal M.H.D. approximation applies). We note in passing that when $\mathscr{R}_m \ll 1$ the advective term (the first term in equation I.55) can be neglected and the field evolution treated simply as the diffusion of the initial field (or a boundary, or both) over time.

Until now, as well as the consistent assumption of a single species fluid, we have

also assumed that the relative motion of electrons (v_e), ions (v_i), and neutrals (v_n) can also be neglected. If this isn't true then the induction equation also needs to take account of this relative motion. This can be divided into two forms: ambipolar diffusion, thought of as either the motion of the ions relative to the bulk fluid of the motion of (neutral) fluid; and the Hall effect, which is the relative motion of electrons and ions. This produces a pair of velocities, the ambipolar drift velocity

$$v^i_\mathrm{ambipolar} = v^i_\mathrm{i} - v^i_\mathrm{fluid} = \frac{m_\mathrm{n} m_\mathrm{e}}{4\pi\gamma n_\mathrm{n} n_\mathrm{e}} \epsilon^{ijm} \left(\epsilon^{jkl} \nabla^k B^l\right) B^m, \tag{I.58}$$

and the Hall drift velocity,

$$v^i_\mathrm{Hall} = v^i_\mathrm{e} - v^i_\mathrm{i} = -\frac{c}{4\pi e n_\mathrm{e}} \epsilon^{ijk} \nabla^j B^k, \tag{I.59}$$

where n_e and m_e represent the number and masses of each component, and γ is the 'friction' of the fluid. If we then note that the velocity in equation I.35 is *actually* the composite of the motion of the whole fluid and these two drift velocities — $v^i = v^i_\mathrm{fluid} + v^i_\mathrm{ambipolar} + v^i_\mathrm{Hall}$ — then (along with the Ohmic resistivity), we have

$$\partial_t B^i = \epsilon^{ijk} \nabla^j \left[\epsilon^{klm} \left(v^l + v^l_\mathrm{ambipolar} + v^l_\mathrm{Hall}\right) B^m - \eta_\mathrm{R} \epsilon^{klm} \nabla^l B^m\right], \tag{I.60}$$

$$\begin{aligned}
\partial_t B^i = {} & \epsilon^{ijk} \nabla^j \left(\epsilon^{klm} v^l B^m\right) + && \Big\} \text{ ideal} \\
& \epsilon^{ijk} \nabla^j \left(\eta_\mathrm{R} \epsilon^{klm} \nabla^l B^m\right) + && \Big\} \text{ resistivity} \\
& \epsilon^{ijk} \nabla^j \left\{\epsilon^{klm} \left[\epsilon^{lnp} \left(\eta_\mathrm{A} \epsilon^{nrs} \nabla^r B^s\right) B^p\right] B^m\right\} + && \Big\} \text{ ambipolar diffusion} \\
& \epsilon^{ijk} \nabla^j \left[\epsilon^{klm} \left(\eta_\mathrm{H} \epsilon^{lnp} \nabla^n B^p\right) B^m\right] && \Big\} \text{ Hall effect}
\end{aligned} \tag{I.61}$$

A comprehensive description of non–ideal magnetohydrodynamics and the derivation thereof (which is outwith the scope of this thesis) can be found in, *inter alia*, Balbus and Terquem (2001), Pandey and Wardle (2008), Wardle (2007), and Wardle and Ng (1999). These effects are beginning to be incorporated into calculations of collapsing molecular cores and of protoplanetary discs, *e.g.* by Bai and Stone (2017), Hennebelle *et al.* (2016), Masson *et al.* (2016), Wurster, D. J. Price, and Ayliffe (2014), and Wurster, D. J. Price, and Bate (2016, 2017).

I.4 This Thesis

In chapter III we present the first part of our work. We begin this chapter by discussing two underlying deficencies in our numerical method, both related to the difficulty in keep-

ing the magnetic field solenoidal. This has been an issue in computational magneto-hydrodynamics since its invention. We show that mitigating non–solenoidality caused by floating–point truncation error alone is insufficent to keep our M.H.D. method stable. The cause of this is the approximate nature of the derivative operators used. The S.P.H. method used particles which have no inherent order. When this 'lattice' of particles becomes highly irregular — disordered — the S.P.M.H.D. force equation produces a spurious force parallel to the magnetic field lines . Although corrective methods for this have been proposed since the invention of S.P.H., they all result in a loss of perfect momentum conservation because the resulting force equation is no longer derived from a Lagrangian. We then show that this loss of momentum conservation is proportional to the lattice disorder it is trying to mitigate. We then conclude that for any current S.P.M.H.D. method derived from a Lagrangian it is possible to either have a correct method *or* a conservative one. We also confirm the existing analysis that at least insofar as $\beta > 1$ can be guaranteed, a stable S.P.M.H.D. is possible.

We then continue by discussing a now deprecated modification to S.P.M.H.D. called the 'average h' method and the reasons — a particularly pernicious bug in our numerical integrator — that led to the invention of this method. This scheme utilised an average within the S.P.H. interpolation kernel, and this led to a consideration of the effects of different averages in S.P.H.. We present this as the final part of chapter III since it will still be useful for S.P.H. schemes which use averages as a way to implement variable resolution, even though our method (set out in chapter II) does not.

Each of the subsequent chapters considers the evolution of a molecular cloud core to a first hydrostatic core. As we discussed earlier in this chapter, a fairly large set of initial conditions are possible — we focus primarily on the initial velocity, and magnetic fields, and to a lesser extent on the equation of state and initial density field. In order to keep the analysis tractable, in each chapter we only adjust one or two input parameters at a time. In chapter IV we consider the effect of varying the geometry of the magnetic field (*i.e.* the inclination angle between the magnetic field and rotation axes) alone; then in chapter V we consider the interplay betwen the field *strength* and *geometry*. We find that the inclination angle, which denote with ϑ, between the two axes has a significant effect on the evolution of the core. Initially the field geometry causes the core to collapse in an oblate, triaxial, or prolate manner depending on ϑ so that the semi–minor axis of the ellipsoid is aligned with ϑ (not with the angular momentum vector). We then find in chapter IV that inclinations of $\vartheta \geq 60^\circ$ do not form a bipolar outflow. When $\vartheta \leq 45^\circ$ an outflow is formed but the outflow is slower and less collimated as ϑ increases. We also find that the jet — if one is present — aligns closer to the magnetic field axis than the rotation axis.

In chapter V we then vary the field strength, defined as mentioned earlier in this chapter I by way of the mass–to–flux ratio μ. By comparing the evolution of cores with differing geometries and field strengths, we find that the oblateness/triaxiality/*etc.* of the collapsing core is proportional to both the geometry and field strength as expected.

We also find that when $\mu \geq 10$ although the outflow on larger scales orients parallel to the magnetic field axis (and the pseudo–disc orients perpendicularly), on smaller scales the inner pseudo–disc re–orients perpendicular to the rotation axis as the influence of angular momentum begins to dominate over magnetic effects. This causes the jet to also re–orient so that it remains perpendicular to the disc which generates it. We then perform a poloidal–toroidal decomposition to analyse how the jet and outflow is formed. We also find that for $\mu = 20$ the magnetic braking present — and the lack of an outflow (caused by an insufficent poloidal field) — is transports insufficent angular momentum and the disc fragments into a binary or ternary system.

Chapter VI first considers changing from a barotropic equation of state (*i.e.* a purely magnetohydrodynamic numerical method) to a radiative equation of state (which requires a radiative transfer scheme) and we find that the latter is necessary to fully model the pseudo–disc around a first hydrostatic core. We then use this radiation magnetohydrodynamic method to examine the interaction between differing amounts of turbulence (*i.e.* increasing the magnitude of the velocity field) and the magnetic field strength; and then finally consider the interaction between the turbulent and rotational components of the velocity field (holding the magnetic field constant). We first show that increasing the turbulent Mach number from $\mathscr{M} = 1/10$ to $\mathscr{M} = 1$ (from sub–sonic to transonic turbulence) distrupts the formation of a pseudo–disc so that outflow formation is supressed and we show this is due to the elimination of a poloidal field component. We then continue by increasing the initial rotation rate of a transonic core and show that when the ratio of rotational to turbulent kinetic energy exceeds unity a pseudo–disc is formed and this disc produces an outflow.

Finally in chapter VII we switch from an initially uniform density field to a centrally condensed one and examine how increasing the rotational component of the velocity field alone change the evolution of the system. A centrally condensed density profile — a Bonnor–Ebert sphere density profile — is more resistent to spurious fragmentation at higher rotation rates. This allows a significantly elevated rotation rate to be probed with an R.M.H.D. scheme and we show that rotation rates where the effective solid body rotation timescale significantly exceeds the free–fall timescale stable binary systems with moderate separations are produced. In addition, unlike the binaries produced when $\mu = 20$ these systems produce helical outflows which transport angular momentum out of the binary pair.

We then summarise and conclude the thesis in chapter VIII. In chapter IX we outline some potential further work, for example incorporating the non–ideal M.H.D. effects introduced in sub–section I.3.2.

CHAPTER II

The Smoothed Particle Radiation Magnetohydrodynamics Method

Omnis ars naturæ imitatio est.

Epistula LXV, Epistulæ Morales ad Lucilium,
Lucius Annæus Seneca 'the Younger' (*ca.* A.D. 65)

Numerical calculations of fluid dynamics problems can be divided into two general approaches: those which use a grid and calculate how the fluid moves between grid cells, and those which employ 'particles' and move these to represent the motion of the fluid. Smoothed particle hydrodynamics (S.P.H.) is, as the name suggests, of the second kind. Formally, it can be described as a (D. J. Price 2012)

lagrangian particle method for solving the equations of hydrodynamics.

A fluid consists of an effectively infinite number of (to all intents and purposes) infinitesimal particles — this is the continuum limit. Obviously this would be impossible to calculate on any computer, so in S.P.H. each 'particle' represents a (large) quantity of fluid particles and properties are then interpolated over a region around each S.P.H. particle (*i.e.* 'smoothed'). In this way a continous fluid can be represented by a — comparatively limited — finite number of computational elements, making computations feasible. Every S.P.H. particle can move independently and as a result the method is ideally suited to highly non–symmetric problems, unlike grids which naturally favour a symmetry along the grid axes[1].

As testament to its utility, the originally fully compressible S.P.H. described in section II.1 has subsequently been extended into incompressible (I.–S.P.H.) (*e.g.* Lo and Shao 2002) and the closely related weakly–compressible (W.C.–S.P.H.) methods (*e.g.* Dalrymple and Rogers 2006). This latter approach is adopted to avoid certain difficulties regarding the requirement that the velocity field is solenoidal[2] in an incompressible fluid. Additionally, further expansions have included free-surface flows which require an understanding of how an incompressible fluid and what is in effect a completely empty space interact (for a comprehensive review, see Colagrossi, Antuono, and Le Touzé 2009), the mechanics of solid objects and material strength problems (Libersky and Petschek 1990).

In section II.1 we describe the fundamental structure of the S.P.H. method, then in sections II.2 and II.3 we show how this simple hydrodynamic method can be extended first to include magnetism, producing smoothed particle magnetohydrodynamcs (S.P.M.H.D.) and also radiation and hence smoothed particle radiation magnetohydrodynamics (S.P.R.-M.H.D.). We then continue, incorporating gravity in section II.4 to produce a smoothed particle radiation quasi–ideal magnetohydrodynamics with self–gravity scheme, and then conclude by introducing sink particles (a necessary computational efficency) in section II.5 and then discussing our overall computational method in section II.6. All numerical schemes have limitations, which range from simply having a finite resolution to more fundamental issues such as the well studied (for a comprehensive discussion, see Dehnen and Aly 2012) 'pairing instability' in S.P.H.. We discuss the limitations of M.H.D. in S.P.H.

1. Although recent work using moving or deformable meshes, *e.g.* `AREPO` (Springel 2011) and `GIZMO` (Hopkins 2015), which sit between a purely grid based or particle based scheme, have produced some interesting results in this regard.

2. This difficultly is somewhat similar to our own battle with Gauss' Law for Magnetism.

in the following chapter (chapter III), along with some further observations on how S.P.-M.H.D. works in extreme circumstances.

II.1 Hydrodynamics

When Wellington thrashed Bonaparte,
As every child can tell,
The House of Peers, throughout the war,
Did nothing in particular,
And did it very well:
Yet Britain set the world ablaze
In good King George's glorious days!

The Earl of Mountararat in 'Iolanthe' (or 'the Peer and the Peri'),
W.S. Gilbert (1882)

To calculate the evolution of a fluid, four equations must be solved, *viz.* the continuity equation which describes the conservation of mass in the fluid,

$$\partial_t \rho + \nabla^i \rho v^i = 0, \tag{II.1}$$

the momentum equation, which describes evolution of the velocity field here written in the form given by Cauchy (1827), and where g^i represents *all* external forces,

$$\mathrm{D}_t v^i = \frac{1}{\rho} \nabla^i \sigma^{ij} + g^i, \tag{II.2}$$

an equation describing the evolution of the energy of the fluid here given in terms of the specific internal energy,

$$\mathrm{D}_t \varepsilon = \nabla^j v^i \sigma^{ij}, \tag{II.3}$$

and an equation of state — usually a function of the form $p = p\left(\rho\right)$. In these equations, and throughout this thesis, the symbols ρ, v^i, ε, and p represent the density, velocity, specific internal energy and pressure fields respectively. We use ε rather than u to represent the specific internal energy to avoid confusion with the use of u as a velocity in some texts. For a purely hydrodynamical system, the stress–tensor is simply

$$\sigma^{ij} = -p\delta^{ij}, \tag{II.4}$$

and therefore equation II.2 becomes the familiar

$$\mathrm{D}_t v^i = \frac{1}{\rho} \nabla^i p, \tag{II.5}$$

but these four equations can be easily extended into more advances regimes by suitable modifications to σ^{ij} and the addition of further evolution equations as required. These

are a system of non–linear coupled equations and are extremely resistant to analytical solutions for all but the most trivial cases (non–linearity being an inherent property of almost *any* interesting fluid flow). Consequently we need a numerical approach to solve these equations.

II.1.1 S.P.H. Fundamentals

S.P.H. relies on kernel interpolation theory – the idea that a property at a point in space, which often is but need not be[3] on an S.P.H. particle itself, can be computed as a form of weighted average over some or all of the other particles in the ensemble. In other words, although particles exist as infinitesimal points they represent the fluid over a wider spatial area, approximating the continuum. Fundamentally, the kernel interpolant for some arbitrary continous property $F\left(r^i\right)$ is given by the integral

$$F\left(r^i\right) = \int_{-\infty}^{+\infty}\int_{-\infty}^{+\infty}\int_{-\infty}^{+\infty} F\left(r'^i\right) W\left(r^i - r'^i, h\right) \mathrm{d}^3 r'^i, \tag{II.6}$$

or equivalently (this form is useful because it makes equation II.9 take it's usual form)

$$F\left(r^i\right) = \int_{-\infty}^{+\infty}\int_{-\infty}^{+\infty}\int_{-\infty}^{+\infty} \frac{F\left(r'^i\right)}{\rho\left(r'^i\right)} W\left(r^i - r'^i, h\right) \rho\left(r'^i\right) \mathrm{d}^3 r'^i. \tag{II.7}$$

We use the notation $\mathrm{d}^3 r'^i$ to denote integration over three three spatial dimensions, which for Cartesian co–ordinates and spherical polar co–ordinates would be $\mathrm{d}^3 r'^i \equiv \mathrm{d}x\mathrm{d}y\mathrm{d}z$ and $\mathrm{d}^3 r'^i \equiv r\sin\theta \mathrm{d}r\mathrm{d}\theta\mathrm{d}\phi$ (with the appropriate changes to the integration limits) respectively. More exotic choices of co–ordinate system also exist. For a finite number of interpolation points, this becomes

$$F\left(r^i\right) \approx \widetilde{F}\left(r^i\right) = \sum_b^N m_b \frac{F_b}{\rho_b} W\left(r^i - r_b^i, h\right), \tag{II.8}$$

where $\widetilde{F}\left(r^i\right)$ represents the estimate of F obtained from the set of interpolation points N. From this it is simple to obtain the well-known S.P.H. density interpolant (see, *e.g.*, Gingold and Monaghan 1982; Monaghan 1988; Nagasawa and Miyama 1987) by setting $F = \rho$ in equation II.8

$$\rho_a = \sum_b^N m_b W_{ab}\left(h\right), \tag{II.9}$$

3. *e.g.* when producing rendered figures for display, centreing the interpolation on a pixel or comparable display element may be more natural.

where we have used the shorthand $\rho_a \equiv \rho\left(r_a^i\right)$ and $W_{ab}(h) \equiv W\left(r_a^i - r_b^i, h\right)$. In all of these equations, W is some arbitrary weighting function that controls how much influence an S.P.H. particle has over distance, the intention being that at large radii the effect of the particle on the interpolated density will be small compared to very small radii. Although the choice of W is arbitrary, clearly it should be a function that tends to zero as $r \to \infty$. In addition, because we require mass to be conserved,

$$\int_{-\infty}^{+\infty}\int_{-\infty}^{+\infty}\int_{-\infty}^{+\infty}\rho\left(r^i\right)\mathrm{d}^3r'^i = M_{\mathrm{tot}} \equiv \sum_b^N m_b, \tag{II.10}$$

this (and also the observation that the left-hand side of equation II.9 contains no terms other than the density and the kernel function) naturally implies that the kernel is normalised such that

$$\int_{-\infty}^{+\infty}\int_{-\infty}^{+\infty}\int_{-\infty}^{+\infty} W d^3r^i = 1. \tag{II.11}$$

D. J. Price (2012) also note that the kernel must be always positive and monotonically decreasing as r^i increases, is symmetrical and has a 'flat' central portion so that numerical noise is not produced by the motion of very close neighbours. Additionally, we also note the constraint

$$\lim_{h\to\infty} W_{ab}(h) = \delta\left(r_a^i - r_b^i\right). \tag{II.12}$$

As W rapidly becomes very small for even intermediate values of $r^i = r_a^i - r_b^i$, a significant computation efficiency can be obtained by producing a kernel where $W = 0 \,\forall\, r^i > R$, where R is a maximum or 'compact support' radius. This allows the set of neighbour particles N to be reduced to a limited set N_{ngh}, although small values of R (and hence small N_{ngh} sets) introduce additional numerical noise.

From this, an extraordinary array of potential kernel functions have been proposed. These range from the simple Gaussian for which $N_{\mathrm{ngh}} = N$ and $R = \infty$,

$$W\left(r^i, h\right) = \frac{\mathcal{A}}{h^\nu}\exp\left(-\left[\frac{r^i}{h}\right]^2\right), \tag{II.13}$$

where ν is the number of spatial dimensions and $\mathcal{A}$ is a normalisation constant to ensure the constraint in equation II.11 is satisfied, functions such as the B–splines, where the cubic spline M_4 has $R = 2h$ and the quintic M_6 has $R = 3h$ to the Wendland (1995) kernels. Choosing a kernel with compact support is a balance between a function with a large R (and hence large set N_{ngh}) and run time. The computational models we use have a very large number of particles, therefore we use the M_4 kernel which has an extremely small

support radius and $N_{\mathrm{ngh}} \approx 50$. This is a function of the form

$$w(q) = \begin{cases} 1/4\left(2-q\right)^3 - \left(1-q\right)^3, & 0 \leq q < 1, \\ 1/4\left(2-q\right)^3, & 1 \leq q < 2, \\ 0, & \text{elsewhere}, \end{cases} \tag{II.14}$$

where we have used the shorthand

$$q = \frac{|r^i - r'^i|}{h}. \tag{II.15}$$

This can then be turned into a normalised interpolating kernel by writing

$$W\left(q\right) = \frac{\mathcal{N}}{h^\nu} w\left(q\right), \tag{II.16}$$

where again ν is the number of spatial dimensions and the normalisation constant has values of

$$\mathcal{N} = \begin{cases} 2/3, & \nu = 1, \\ 10/7\pi, & \nu = 2, \\ 1/\pi, & \nu = 3. \end{cases} \tag{II.17}$$

Equation II.14 is differentiable (although the second derivative of this and many other kernels present some difficulties), which means that we simply write

$$\partial_q w(q) = \begin{cases} 9/4q^2 - 3q, & 0 \leq q < 1, \\ -3/4\left(2-q\right)^2, & 1 \leq q < 2, \\ 0, & \text{elsewhere}, \end{cases} \tag{II.18}$$

and can then obtain

$$\nabla^i W\left(q\right) = \frac{\mathcal{N}}{h^\nu} \partial_q w\left(q\right) \hat{r}^i, \tag{II.19}$$

where the unit vector pointing between r^i and r'^i is given by

$$\hat{r}^i = \frac{r^i - r'^i}{|r^i - r'^i|}, \tag{II.20}$$

as the gradient of the interpolation kernel. We observe here that equation II.14 is positive definite and that equation II.18 is negative definite. The second derivative poses a challenge because it exhibits a change of sign (this is true for *all* kernel functions for which

$w(q)$ is monotonically decreasing and where $\partial_q w(q)$ is zero at R) at $q = 2/3$,

$$\partial_q^2 w(q) = \begin{cases} 9/2q - 3, & 0 \leq q < 1, \\ 3 - 3/2q, & 1 \leq q < 2, \\ 0, & \text{elsewhere,} \end{cases} \tag{II.21}$$

meaning that the Laplacian of the interpolation kernel is given by

$$\triangle W\left(q\right) = \frac{\lambda}{h^{\nu}} \partial_q^2 w\left(q\right) \hat{r}^i. \tag{II.22}$$

This derivative is particularly bad for the cubic B-spline (which only has a non-constant derivative up to ∂_q^2) and a smoother second derivative can be obtained for the higher order functions.

We can combine equation II.8 and equation II.19 to obtain an interpolation for the gradient of some arbitrary field F,

$$\nabla^i F\left(r^i\right) \approx \sum_b^N m_b \frac{F_b}{\rho_b} \nabla^i W\left(r^i - r_b^i, h\right), \tag{II.23}$$

and similarly for an arbitrary vector field[4] F^j we can obtain interpolations for the divergence (which produces a scalar), curl (a vector) and gradient (a rank–2 tensor), as

$$\nabla^j F^j\left(r^i\right) \approx \sum_b^N m_b \frac{F_b^j}{\rho_b} \nabla^j W\left(r^i - r_b^i, h\right), \tag{II.24}$$

$$\epsilon^{ijk} \nabla^j F^k\left(r^i\right) \approx \sum_b^N \epsilon^{ijk} m_b \frac{F_b^k}{\rho_b} \nabla^j W\left(r^i - r_b^i, h\right), \tag{II.25}$$

$$\nabla^j F^i\left(r^i\right) \approx \sum_b^N m_b \frac{F_b^i}{\rho_b} \nabla^j W\left(r^i - r_b^i, h\right). \tag{II.26}$$

The Laplacian operator could also be interpolated as

$$\triangle F^i\left(r^i\right) \approx \sum_b^N m_b \frac{F_b^i}{\rho_b} \triangle W\left(r^i - r_b^i, h\right). \tag{II.27}$$

In principle, these are sufficient to discretise any system of first-order differential equation; in practice as D. J. Price and Monaghan (2004a) observe equations II.23 to II.26 become increasingly incorrect as the distribution of particles becomes disordered. This presages a more fundamental issue which we will explore further whereby particle disorder is source

4. *i.e.* a rank–1 tensor

of many S.P.M.H.D./S.P.R.M.H.D. related difficulties. Before this, we first switch notation slighty: hitherto we have considered all interpolations at some arbitrary point in space, r^i. In practice, it is more useful to interpolate properties so that these can be used to evolve an S.P.H. particle, which we denote as a (and then $b \in N_{\rm ngh}$ is one of the neighbour particles of a, *i.e.* those particles which have $|r_a^i - r_b^i| < R$).

As is more fully explored in D. J. Price (2012) two approaches can be used to reduce this error (fully eliminating it requires that $N_{\rm ngh} \rightarrow \infty$ which would return us to the continuum and hence integrals not summations, *cf.* equation II.7). The first is the 'anti-symmetric' derivative, formed by subtracting off the first-order error term,

$$\nabla^j F^i \left(r^i\right) \approx \sum_b^N m_b \frac{F_b^i - F_a^i}{\rho_b} \nabla^j W \left(r^i - r_b^i, h\right). \tag{II.28}$$

The alternative is the 'symmetric' derivative, obtained from deriving the S.P.H. equations of motions directly from the Lagrangian, whereby

$$\nabla^j F^i \left(r^i\right) \approx \sum_b^N \rho_a m_b \left(\frac{F_a^i}{\rho_a^2} + \frac{F_b^i}{\rho_b^2}\right) \nabla^j W \left(r^i - r_b^i, h\right). \tag{II.29}$$

The complete derivation of equations II.28 and II.29 can be found in D. J. Price (*ibid.*). One observation that will become important later is that equation II.29 is not invariant to the addition of a constant offset, *e.g.* a modification to the field of the form $F'_{\{a,b\}} = F_{\{a,b\}} + f$. Additionally it is sensitive to particle disorder (although less so than the bare derivative given by equation II.26) and in particular has an error term of the form (obtained by taking a Taylor expansion of equation II.29)

$$\sum_b^N F_a \rho_a m_b \left(\frac{1}{\rho_a^2} + \frac{1}{\rho_b^2}\right) \nabla^j W \left(r^i - r_b^i, h\right). \tag{II.30}$$

As discussed in Tricco and D. J. Price (2012) the use of pairs of conjugate operators — of which equations II.28 and II.29 comprise such a pair — is necessary to ensure momentum and energy conservation. Consequently it is not possible to use the arguably superior anti–symmetric derivative everywhere. This also implies that it is not possible to simply subtract equation II.30 and still maintain exact momentum conservation, which will *also* become important later.

II.1.2 Self–consistent Adaptive Resolution

Throughout this sub–section we have assumed a spatially constant h, i.e. that $\nabla^i h = 0$ everywhere (a temporally variable h, *i.e.* $\partial_t h \neq 0$, requires no modifications to any of the S.P.H. interpolation equations). However, a more optimal use of computational resources is to vary h across the whole computational domain so that additional resolution is pro-

vided in areas of high complexity and *vice versa*. One way to do this, first proposed by D. J. Price and Monaghan (2004b) is to maintain an approximately constant number density under the smoothing kernel (or alternatively phrased, within the smoothing sphere), in effect that

$$h_a \propto \sqrt[\nu]{\frac{1}{n_a}}, \tag{II.31}$$

or the comparable statement that

$$\rho h^{\nu} \tag{II.32}$$

is constant. If $m_a = m \; \forall \; a \in N$ (that particles have equal mass) becomes the familiar

$$h_a \propto \sqrt[\nu]{\frac{1}{\rho_a}}. \tag{II.33}$$

This leads to self-consistently setting the smoothing length using

$$h_a = \eta \sqrt[\nu]{\frac{m_a}{\rho_a}}, \tag{II.34}$$

and equation II.9, and to the important observation that h and ρ are different manifestations of the same numerical parameter – *i.e.* that fluid density and resolution are identical concepts. An observation which (*again*) will become important later, is that this scheme neither guarantees a spatially invariant N_{ngh} nor an identical mass in each smoothing sphere. To do so would require stretching the kernel support radius, with the attendant particle pairing due to putting particles within the $q \leq 2/3$ regime of the $\partial_q^2 w(q)$ function. We are instead enforcing a constant average N_{ngh} — for the cubic spline that $\langle N_{\text{ngh}} \rangle = 57.3$. Formally, whilst $N_{\text{ngh},a} \in \mathbb{Z} \; \forall \; a \in N$, $\langle N_{\text{ngh}} \rangle \notin \mathbb{Z}$ in general, where N represents the set of *all* particles in the calculation, which clearly implies that this scheme will not produce a constant neighbour count.

The optimum value of η is a property of the kernel choice, so for the cubic B–spline it is 1.2. Values above the optimum are susceptible to particle pairing, conversely values below it are unconverged. A thorough discussion of this concept can be found in D. J. Price (2004).

The pair of equations II.9 and II.34 need to be solved iteratively. We use the Newton–Raphson (Newton 1669; Raphson 1690) method to do this (with a nominal fall-back to the bisection method if this technique fails to converge), given in its usual form by

$$\rho_{n+1} = \rho_n + \frac{h\left(\rho_n\right)}{\partial_\rho h\left(\rho_n\right)}, \tag{II.35}$$

where naively we would write

$$\partial_\rho h\left(\rho_n\right) = -\frac{1}{\nu\rho} \sqrt[\nu]{\frac{m}{\rho}} \equiv -\frac{h}{\nu\rho}. \tag{II.36}$$

However, this neglects the changes to equation II.9 caused by h no longer being spatially constant. If $h_a = h$ is constant $\forall\ r_a$, then

$$\mathrm{D}_t \rho_a = \sum_b^N m_b \left(v_a^i - v_b^i \right) \nabla_a^i W_{ab}\left(h\right). \tag{II.37}$$

This is not true for the case where $h_a \neq h_b$ in general; here we instead obtain

$$\mathrm{D}_t \rho_a = \sum_b^N m_b \left(v_a^i - v_b^i \right) \nabla_a^i W_{ab}\left(h_a\right) + \sum_b^N m_b \partial_{h_a} W_{ab}\left(h_a\right) \partial_t h_a \tag{II.38}$$

from the chain rule. The important 'sleight–of–hand' here is to notice that

$$\partial_t h_a = \partial_{\rho_a} h_a \partial_t \rho_a, \tag{II.39}$$

and we have an expression for $\partial_\rho h$ from equation II.36 giving

$$\partial_t h_a = -\frac{h_a}{\nu \rho_a} \mathrm{D}_t \rho_a. \tag{II.40}$$

Inserting this into equation II.38 we can write the continuity equation as (with the addition of a new parameter Ω_a)

$$\mathrm{D}_t \rho_a = \frac{1}{\Omega_a} \sum_b^N m_b \left(v_a^i - v_b^i \right) \nabla_a^i W_{ab}\left(h_a\right). \tag{II.41}$$

Ω_a is a term which 'takes account' of the new spatial variation in h. Whilst often small, the contribution provided by this term is necessary for a complete and correct S.P.H. method. The usual form of this term is[5]

$$\Omega_a = 1 - \partial_{\rho_a} h_a \sum_b^N m_b \partial_h W_{ab}\left(h_a\right), \tag{II.42}$$

$$\Omega_a = 1 + \frac{h_a}{\nu \rho_a} \sum_b^N m_b \partial_h W_{ab}\left(h_a\right). \tag{II.43}$$

Following a similar approach, the symmetric and anti-symmetric derivatives given by equations II.28 and II.29 then become

$$\nabla^j F^i \left(r^i \right) \approx \sum_b^N m_b \left(\frac{1}{\Omega_a} \frac{F_a^i}{\rho_a^2} \nabla_a^j W_{ab}\left(h_a\right) + \frac{1}{\Omega_b} \frac{F_b^i}{\rho_a^2} \nabla_b^j W_{ab}\left(h_b\right) \right), \tag{II.44}$$

5. We include the traditional cautionary observation here that the form of this term as first presented in D. J. Price and Monaghan (2004b) is *very* incorrect.

$$\nabla^j F^i\left(r^i\right) \approx \frac{1}{\Omega_a \rho_a^2} \sum_b^N m_b \left(F_a^i - F_b^i\right) \nabla_a^j W_{ab}\left(h_a\right). \tag{II.45}$$

This is a complete adaptive S.P.H. scheme, which we now apply to hydrodynamics.

II.1.3 Hydrodynamics

D. J. Price and Monaghan (2004b) use a Lagrangian approach to obtain the S.P.H. equations of motion self-consistently. This leads to several important conclusions about the correct choice of kernel (the kernel used to evaluate derivatives *must* be the same as the one use in the density summation) and more importantly that the only S.P.H. operators that can maintain perfect momentum and energy conservation are also the conjugate pairs given by equations II.28 and II.29.

Instead of repeating that analysis, here we will simply apply the operators obtained to the relevant parts of equations II.1 to II.3 to obtain a system of discrete hydrodynamics equations. In principle, we could evolve the fluid density using the continuity equation, *via* something like[6]

$$\mathrm{D}_t \rho_a = \frac{1}{\Omega_a} \sum_b^N m_b \left(v_a^i - v_b^i\right) \nabla_a^i W_{ab}\left(h_a\right), \tag{II.46}$$

which is simply the first derivative of the standard S.P.H. density interpolant equation II.9. In practice, simply using equation II.9 directly avoids the errors inherent in S.P.H. derivatives and therefore we calculate the density field of the fluid explicitly each time step. One potential use for equation II.46 (although not one we use) is to provide the initial guess for the Newton–Raphson solver to iterate equation II.34; however, this is often unnecessary since the rate of change of ρ and h is sufficiently small to allow the solver to be started from the previous values and still converge. We add as an aside that because of the construction of equation II.9, mass conservation in S.P.H. (even with quite advanced schemes, *e.g.* Vacondio *et al.* 2013) is exact[7] unlike many Eulerian grid methods.

The S.P.H. momentum equation is then given by

$$\mathrm{D}_t v_a^i = -\sum_b^N m_b \left(\frac{1}{\Omega_a} \frac{\sigma_a^{ij}}{\rho_a^2} \nabla_a^j W_{ab}\left(h_a\right) + \frac{1}{\Omega_b} \frac{\sigma_b^{ij}}{\rho_b^2} \nabla_a^j W_{ab}\left(h_b\right)\right), \tag{II.47}$$

$$\mathrm{D}_t v_a^i = -\sum_b^N m_b \left(\frac{1}{\Omega_a} \frac{p_a}{\rho_a^2} \nabla_a^j W_{ab}\left(h_a\right) + \frac{1}{\Omega_b} \frac{p_b}{\rho_b^2} \nabla_a^j W_{ab}\left(h_b\right)\right), \tag{II.48}$$

where we have used the symmetric first derivative operator as derived and applied by D. J.

6. This is also given in equation II.41.

7. Notable exceptions to this include incompressible S.P.H. schemes which solve a Poisson equation for the pressure, *e.g.* an equation of the form $\triangle p = f\left(v^i\right)$.

Price and Monaghan (2004a) (*cf.* equation II.45). Similarly, although using the conjugate anti–symmetric operator (*cf.* equation II.44), we can write the S.P.H. total energy equation as

$$\mathrm{D}_t \varepsilon_a = \frac{p_a}{\Omega_a \rho_a^2} \sum_b^N m_b \left(v_a^j - v_b^j \right) \nabla_a^j W_{ab}\left(h_a\right). \tag{II.49}$$

These provide discrete solutions to equations II.2 and II.5 and combined with the adaptive smoothing length technique obviating the need for a continuity equation are the essential ingredients of an S.P.H. scheme. They are, however, incorrect in the presence of strong shocks where inter–particle penetration can occur.

II.1.4 Artificial Viscosity

The correction for this is provided by an 'artificial' viscosity which operates to decelerate converging particle flows, and thus maintain the structure of the fluid. Numerous methods of producing this viscosity term have been proposed, but all are coupled to equations II.48 and II.49 by simply adding the viscous contribution on to the 'Lagrangian' part[8], so that

$$\mathrm{D}_t v_a^i = \mathrm{D}_t v_a^i|_{\text{ideal}} + \mathrm{D}_t v_a^i|_{\text{artificial}} = \mathrm{D}_t v_a^i|_{\text{ideal}} - \sum_b^N m_b \Pi_{ab} \nabla_a^i \overline{W}_{ab}, \tag{II.50}$$

$$\mathrm{D}_t \varepsilon_a = \mathrm{D}_t \varepsilon_a|_{\text{ideal}} + \mathrm{D}_t \varepsilon_a|_{\text{artificial}} = \mathrm{D}_t \varepsilon_a|_{\text{ideal}} + \sum_b^N m_b \Xi_{ab} \left(v_a^j - v_b^j \right) \nabla^j \overline{W}_{ab}. \tag{II.51}$$

If, and only if, Π_{ab} (and Ξ_{ab}) operates pairwise on particles (which all useful S.P.H. viscosities do) this will maintain energy and momentum conservation in the Lagrangian. If spatially constant smoothing lengths are used this is obtained with no further work, however, in equations II.50 and II.51 we have written $\overline{W}_{ab}$. This is an average of the two smoothing kernels, given by

$$\overline{W}_{ab} = \frac{1}{2}\left[W_{ab}\left(h_a\right) + W_{ab}\left(h_b\right)\right], \tag{II.52}$$

and is required to maintain this pairwise operation, and hence conservation of momentum and energy when $\nabla^i h \neq 0$.

Many potential choices of Π exist. All of these attempt to apply as little false viscosity as possible, while still keeping the fluid structure intact at the shock boundary. Two principle considerations apply: first that the viscous term should be of as low a magnitude as possible (and proportional to the converging flow velocity), and secondly that the viscosity should only be applied *very* close to the problematic shock. The latter consideration is provided in the form of a 'switch' — an additional fluid parameter which is

8. Formally, the modification to equation II.49 is required only to maintain energy conservation, not stability. It would clearly need to be omitted for an isothermal equation of state, for instance.

evolved alongside the usual ones — and which disables the viscosity when it is unnecessary. Here we describe first the 'traditional' Morris and Monaghan (1997) viscosity and the more modern Riemann–solver based method used in this work.

In the Morris and Monaghan (*ibid.*) scheme we have[9]

$$\Pi_{ab} = -\frac{\alpha \overline{c}_{ab} \mu_{ab} + \beta \mu_{ab}^2}{\overline{\rho}_{ab}}, \tag{II.53}$$

where $\overline{c}_{ab}$ and $\overline{\rho}_{ab}$ are average sound speeds and fluid densities respectively, and

$$\mu_{ab} = \frac{\overline{h}_{ab} \left(v_a^i - v_b^i \right) \left(r_a^i - r_b^i \right)}{r^2 + \varepsilon}. \tag{II.54}$$

ε is a 'small' number to avoid numerical singularities as $r \to 0$. α and β are order unity parameters, conventionally set so that

$$\alpha \sim 1, \tag{II.55}$$

$$\beta \sim 2. \tag{II.56}$$

To prevent spurious viscosity being applied to diverging flows, $\Pi = 0$ if $\nabla^i v^i > 0$.

This viscosity term is sufficient insofar as it prevents deleterious deterioration of the fluid structure, and it contains a 'classical' von Neumann and Richtmyer (1950) viscosity term (the $\beta \mu^2$ component). It is also pairwise and hence a conservative modification to the S.P.H. Lagrangian. However, it neither contains an effective switch (α and β are temporally invariant) nor is it clear how to extend it to magnetised or relativistic problems.

We use the Riemann solver (*cf.* Godunov 1959) based viscosity derived by Chow and Monaghan (1997) (following Monaghan 1997), *viz.*[10]

$$\Pi_{ab} = -\frac{\alpha_{\mathrm{AV}} v_{\mathrm{sig},ab}}{2\rho_{ab} \left(v_a^i - v_b^i \right) \left(\hat{r}_a^i - \hat{r}_b^i \right)}, \tag{II.57}$$

where v_{sig} is the signal velocity, *i.e.* the maximum speed at which information can be exchanged between two particles. In a stationary medium this would be the sound speed, for a moving flow it is given by

$$v_{\mathrm{sig}} = c - \beta v^i \hat{r}^i, \tag{II.58}$$

where β is some order unity parameter (invariably $1 \leq \beta \leq 2$). A slight complexity whereby the sound speeds for two particles within the same smoothing sphere may differ

9. In this scheme, $\Pi = \Xi$.

10. We write α_{AV} in this scheme to avoid confusion with the switch for artificial magnetic resistivity discussed in sub–section II.2.2.

is avoiding by taking an average, so that

$$v_{\rm sig} = \frac{1}{2}\left(c_a + c_b\right) - \beta\left(v_a^i - v_b^i\right)\left(\hat{r}_a^i - \hat{r}_b^i\right). \tag{II.59}$$

Unlike the Morris and Monaghan (1997) scheme, this method has a different Ξ term, given by

$$\Xi_{ab} = -\frac{\alpha_{\rm AV} v_{{\rm sig},ab}}{2\overline{\rho_{ab}}\tilde{\epsilon}_{ab}\hat{r}_{ab}^i}, \tag{II.60}$$

where the difference in energies (in a hydrodynamic calculation essentially the difference in kinetic energies) given by

$$\tilde{\epsilon}_{ab} = \frac{1}{2}\left[\left(v_a^i \hat{r}_{ab}^i\right)^2 - \left(v_b^i \hat{r}_{ab}^i\right)^2\right]. \tag{II.61}$$

An important advantage of this is that changes in the magnetic energy can be relatively easily incorporated, and this technique can also be used to provide an artificial magnetic 'viscosity' (*i.e.* a resistivity).

The $\alpha_{\rm AV}$ parameter in equation II.57 is neither spatially nor temporally invariant. Instead this parameter is evolved in time. This is a much more subtle approach than the simpler method of merely switching the whole term off in the presence of a diverging flow. Like viscosity schemes, many switches exist although all follow a similar premise: the amount of dissipation added should be scaled by how quickly a shock is growing and its magnitude.

We use the conceptually simple switch proposed by Morris and Monaghan (*ibid.*). In this two extrema are defined, $\alpha_{\rm min}$ and $\alpha_{\rm max}$ (although approaches without an $\alpha_{\rm max}$ can be constructed). $\alpha_{{\rm AV},a}$ is then evolved according to an equation of the form

$$\partial_t \alpha_{{\rm AV},a} = -\frac{\alpha_{{\rm AV},a} - \alpha_{\rm min}}{\tau_a} + \mathcal{S}_a, \tag{II.62}$$

where τ_a is some decay time and $\mathcal{S}_a$ is a source term which operates to increase $\alpha_{{\rm AV},a}$ at a shock front. The optimum expressions to determine τ_a and $\mathcal{S}_a$ are difficult to determine *a priori* and vary depending on the computational problem. We use a decay timescale given by an expression of the form

$$\tau_a = \frac{h_a}{\mathscr{C}_\tau v_{\rm sig}}, \tag{II.63}$$

with $0.1 < \mathscr{C}_\tau < 0.2$, and a source term of the form

$$\mathcal{S}_a = \max\left(-\nabla^i v^i\left(\alpha_{\rm max} - \alpha\right), 0\right). \tag{II.64}$$

Similarly, the correct choices of $\alpha_{\rm min}$ and $\alpha_{\rm max}$ vary between problems, in particular how low the minimum can be set to is related to how well particle order is maintained away from shock fronts.

Using the above provides a complete, stable, and conservative adaptive resolution smoothed particle hydrodynamics scheme. We now extend this to include magnetism.

II.2 Magnetohydrodynamics

> His third great discovery is the Magnetization of Light, which I should liken to the Weisshorn among mountains — high, beautiful, and alone.
>
> Faraday as a discoverer, John Tyndall (1894)

Astrophysical plasmas are magnetised — as indeed are many other fluids — consequently a purely hydrodynamical treatment is unsatisfactory. Adding magnetohydrodynamics into S.P.H. is tantalizingly simple, comprising a modification to the stress tensor which now becomes (in the centimetre–gramme–second unit system)

$$\sigma^{ij} = -\left(p + \frac{1}{8\pi}B^2\right)\delta^{ij} + \frac{1}{4\pi}B^iB^j, \tag{II.65}$$

and adding the induction equation. This can be obtained by considering the Maxwell–Faraday Law (Maxwell's III$^{\text{rd.}}$ Law) in a frame co–moving with the fluid. This transforms

$$\epsilon^{ijk}\nabla^j E^k = -\partial_t B^i \tag{II.66}$$

into the usual ideal M.H.D. induction equation

$$\partial_t B^i = \epsilon^{ijk} v^j B^k. \tag{II.67}$$

Here, as usual, B^i and E^i represent the magnetic[11] and the electric fields.

Expanding the right–hand side of equation II.67 produces a volume weighted induction equation, *viz.*

$$\mathrm{D}_t B^i = B^j\nabla^j v^i - B^i\nabla^i v^i, \tag{II.68}$$

where the third term from the expansion, $v^j\nabla^j B^i$, has been subsumed into the D_t operator. Combining this with the continuity equation produces a mass–weighted equivalent, sometimes called Walén's equation (Işık, Schmitt, and Schüssler 2011),

$$\mathrm{D}_t\frac{B^i}{\rho} = \left(\frac{B^j}{\rho}\nabla^j\right)v^i. \tag{II.69}$$

However, like the fruit and water which taunted fallen Tantulus eternally in Tartarus [12], a stable and conservative M.H.D. formalism in S.P.H. has proved quite evasive.

---

11. or, equivalently, the magnetic flux density

12. *cf.* Apollodorus (*ca.* 100–200 B.C.) and Diodorus Siculus (*ca.* 36 B.C.)

In this section we discuss how M.H.D. is implemented in S.P.H., and the corrective measures applied to produce a useful S.P.M.H.D. method. Chapter III then contains a more thorough discussion of the *limitations* of those corrections.

In S.P.M.H.D., and following D. J. Price (2012) and D. J. Price and Monaghan (2004a, 2005) the induction becomes either (by discretising equation II.69)

$$\mathrm{D}_t \frac{B_a^i}{\rho_a} = -\sum_b^N \frac{m_b}{\Omega_a \rho_a^2} \left(v_a^i - v_b^i\right) B_a^j \nabla_a^j W_{ab}\left(h_a\right), \tag{II.70}$$

or by discretising equation II.68

$$\mathrm{D}_t B_a^i = \frac{1}{\Omega_a} \frac{1}{\rho_a^2} \sum_b^N m_b \left(B_a^j v_a^j - B_b^j v_b^j\right) \nabla_a^i W_{ab}\left(h_a\right). \tag{II.71}$$

We note here that these are anti–symmetric derivatives, conjugate to the derivative operator used to evaluate the momentum equation, which is required to maintain conservation properties.

Substituting equation II.65 into the general S.P.H. momentum equation given in equation II.47 produces the S.P.M.H.D. momentum equation

$$\begin{aligned}
\mathrm{D}_t v_a^i = &-\sum_b^N m_b \left(\frac{1}{\Omega_a}\frac{p_a}{\rho_a^2}\delta^{ij}\nabla_a^j W_{ab}\left(h_a\right) + \frac{1}{\Omega_b}\frac{p_b}{\rho_b^2}\delta^{ij}\nabla_a^j W_{ab}\left(h_b\right)\right) \\
&- \frac{1}{8\pi}\sum_b^N m_b \left(\frac{1}{\Omega_a}\frac{B_a^2}{\rho_a^2}\delta^{ij}\nabla_a^j W_{ab}\left(h_a\right) + \frac{1}{\Omega_b}\frac{B_a^2}{\rho_b^2}\delta^{ij}\nabla_a^j W_{ab}\left(h_b\right)\right) \\
&+ \frac{1}{4\pi}\sum_b^N m_b \left(\frac{1}{\Omega_a}\frac{B_a^i B_a^j}{\rho_a^2}\nabla_a^j W_{ab}\left(h_a\right) + \frac{1}{\Omega_b}\frac{B_b^i B_b^j}{\rho_b^2}\nabla_a^j W_{ab}\left(h_b\right)\right)
\end{aligned} \tag{II.72}$$

Although this is not the most compact way to write this equation — and computationally it is invariably separated simply into an isotropic and an anisotropic part — it allows the interaction between terms (which also should include an artificial viscosity) to be seen. In many practical codes, we instead evaluate a pairs of equations derived from separating

this out according to

$$\mathrm{D}_t v_a^i = -\sum_b^N m_b \left(\frac{1}{\Omega_a} \frac{p_a + {}^1/_{8\pi} B_a^2}{\rho_a^2} \delta^{ij} \nabla_a^j W_{ab}(h_a) + \frac{1}{\Omega_b} \frac{p_b + {}^1/_{8\pi} B_b^2}{\rho_b^2} \delta^{ij} \nabla_a^j W_{ab}(h_b) \right) + \frac{1}{4\pi} \sum_b^N m_b \left(\frac{1}{\Omega_a} \frac{B_a^i B_a^j}{\rho_a^2} \nabla_a^j W_{ab}(h_a) + \frac{1}{\Omega_b} \frac{B_b^i B_b^j}{\rho_b^2} \nabla_a^j W_{ab}(h_b) \right) \tag{II.73}$$

and exploit the fact that the B^2 term is all–but a pressure term to reduce the number of calculations performed and thus speed up the calculation. We also note that considering the equations in this manner — as an isotropic pressure and an anisotropic tensor term — aids the understanding of how S.P.M.H.D. works.

The B^2 and $B^i B^j$ components of the stress tensor interact so that the force parallel to the field lines is exactly zero. This absence of magnetic pressure along the field lines produces the characteristic preferential direction of fluid flow in highly magnetised plasmas. However, even by simple inspection a problem with equation II.72 can be seen: if the magnetic pressure is greater than the fluid pressure this may no longer be true. This will supply a spurious *attractive* force (from the $B^i B^j$ terms) along the field lines, rapidly destroying the calculation. This is an identical effect to that observed when S.P.H. is applied to solids with external stresses, whereby if the external stress term overhauls the internal 'support' pressure (recalling that in a solid the particle separation should be constant) the object rapidly collapses. Due to this heritage, this instability in S.P.H. is termed the 'tensile instability'.[13] A calculation failing due to this instability has the peculier property that momentum and energy conservation remain exact and the density estimator (and hence the smoothing length) remain correct. That this is the case is obvious given the derivation of these equations directly from the M.H.D. Lagrangian, *etc.*, but it does highlight an important 'feature' of M.H.D. in S.P.H.: perfect conservation properties are not sufficent for a correct formalism.

Clearly this must be corrected for, otherwise S.P.M.H.D. would be restricted to regimes where the plasma β is greater than unity. In chapter III we provide a comprehensive review of various schemes and an analysis of the fundamental issue with the S.P.M.H.D. momentum equation as derived from the Lagrangian, and restrict ourselves in this chapter to describing the method applied to make our calculations tractable.

Børve, Omang, and Trulsen (2001) proposed subtracting a source term from equa-

13. Or sometimes 'tensile pairing', but this invites confusion with the somewhat less common pairing instability caused by stretching the compact support radius of the kernel.

tion II.72. Qualitatively this involves taking an S.P.H. estimation of the local magnetic divergence, then subtracting that from the momentum equation. This is in principle an effective correction because the magnetic field should be divergence free, and therefore in the continuum limit this correction is otiose.

We calculate the magnetic divergence in S.P.H. as

$$\nabla_a^i B_a^i = \frac{1}{4\pi} \sum_b^N m_b \left(\frac{1}{\Omega_a} \frac{B_a^i}{\rho_a^2} \nabla_a^i W_{ab}(h_a) + \frac{1}{\Omega_b} \frac{B_b^i}{\rho_b^2} \nabla_a^i W_{ab}(h_b) \right) (= \varrho_a) . \tag{II.74}$$

We use the symbol ϱ as a short-hand for the magnetic charge density, which is analogous to the electric charge density seen in electrodynamics and in Gauss' Law (Maxwell's first equation). From this we obtain a modified momentum equation, where

$$\begin{aligned} \mathrm{D}_t v_a^i = &- \sum_b^N m_b \left(\frac{1}{\Omega_a} \frac{p_a}{\rho_a^2} \delta^{ij} \nabla_a^j W_{ab}(h_a) + \frac{1}{\Omega_b} \frac{p_b}{\rho_b^2} \delta^{ij} \nabla_a^j W_{ab}(h_b) \right) \\ &- \frac{1}{8\pi} \sum_b^N m_b \left(\frac{1}{\Omega_a} \frac{B_a^2}{\rho_a^2} \delta^{ij} \nabla_a^j W_{ab}(h_a) + \frac{1}{\Omega_b} \frac{B_b^2}{\rho_b^2} \delta^{ij} \nabla_a^j W_{ab}(h_b) \right) \\ &+ \frac{1}{4\pi} \sum_b^N m_b \left(\frac{1}{\Omega_a} \frac{B_a^i B_a^j}{\rho_a^2} \nabla_a^j W_{ab}(h_a) + \frac{1}{\Omega_b} \frac{B_b^i B_b^j}{\rho_b^2} \nabla_a^j W_{ab}(h_b) \right) \\ &- \chi \frac{1}{4\pi} B_a^i \sum_b^N m_b \left(\frac{1}{\Omega_a} \frac{B_a^j}{\rho_a^2} \nabla_a^j W_{ab}(h_a) + \frac{1}{\Omega_b} \frac{B_b^j}{\rho_b^2} \nabla_a^j W_{ab}(h_b) \right) . \end{aligned} \tag{II.75}$$

χ is a parameter to control the amount of correction applied: in principle $\chi = 1/2$ should be sufficent (due to the $1/2 \cdot 1/4\pi \equiv 1/8\pi$ co-efficent in the isotropic stress tensor), however, empirical tests indicate that setting $\chi = 1$ is better. The important caveat here is that the operator provided by equation II.74 clearly does not operate pairwise on the particles (because the local magnetic divergence is not a pairwise force like a viscosity) and consequently this modification to the momentum equation violates conservation of linear momentum. This does place real limitations on calculations, however, the choice is in essence one between a *conservative* force and a *correct* one. Later, we will show that *any* attempt to take the M.H.D. momentum equation from the Lagrangian, and then stabilise it against a non–vanishing numerical monopole term is inherently unconservative.

In the case $\chi = 1$, we can slightly simplify equation II.75 (if only as a computational

efficiency) to

$$\begin{aligned} \mathrm{D}_t v_a^i = &- \sum_b^N m_b \left(\frac{1}{\Omega_a} \frac{p_a}{\rho_a^2} \delta^{ij} \nabla_a^j W_{ab}(h_a) + \frac{1}{\Omega_b} \frac{p_b}{\rho_b^2} \delta^{ij} \nabla_a^j W_{ab}(h_b) \right) \\ &- \frac{1}{8\pi} \sum_b^N m_b \left(\frac{1}{\Omega_a} \frac{B_a^2}{\rho_a^2} \delta^{ij} \nabla_a^j W_{ab}(h_a) + \frac{1}{\Omega_b} \frac{B_b^2}{\rho_b^2} \delta^{ij} \nabla_a^j W_{ab}(h_b) \right) \\ &+ \frac{1}{4\pi} \sum_b^N m_b \left(\frac{1}{\Omega_b} \frac{B_b^i B_b^j}{\rho_b^2} \nabla_a^j W_{ab}(h_b) + \frac{1}{\Omega_b} \frac{B_a^i B_b^j}{\rho_b^2} \nabla_a^j W_{ab}(h_b) \right), \end{aligned} \tag{II.76}$$

which as noted above would almost certainly be implemented in any practical code by folding the pressure–like terms together.

II.2.1 Divergence Cleaning

Until now we have avoided mentioning the solenoidal constraint, *viz.* that Gauss' law for magnetism (Maxwell's second equation) provides that

$$\nabla^i B^i = 0 \tag{II.77}$$

everywhere. We instead treated the tensile instability as an issue caused by a bad S.P.H. estimate of the operator $\nabla_a^i B_a^i B_a^j$. Although this *looks like* the production of a false magnetic charge density, in reality it is simply an artefact of the noisy symmetric derivative operator. However, the conjugate operator used in the induction equation, the anti-symmetric derivative, is much less sensitive to particle disorder and consequently *is* affected by the difficulties in maintaining a solenoidal field.

The fundamental issue is that there is no explicit or implicit constraint that $\nabla^i B^i = 0$ in any of our S.P.M.H.D. equations. Instead we (should) enforce this constraint when setting the initial field, and then rely on how well our computational method can maintain

$$\partial_t \nabla^i B^i = 0. \tag{II.78}$$

Due to truncation error, $\partial_t \nabla^i B^i$ is inevitably non-zero, and consequently our induction equation will produce an ever more unphysical field.

To correct for this, we use the constrained hyperbolic divergence cleaning method originally derived by Tricco and D. J. Price (2012), based on the earlier method from grid codes proposed by Dedner *et al.* (2002). Qualitatively this involves coupling a scalar field to the induction equation, into which we place any magnetic charge density, which is then propagated as a wave and damped over a 'few' smoothing lengths. Because this neither creates nor destroys field directly, instead smoothing it out into the larger scale magnetic field, it maintains both exact conservation of energy and momentum (*cf.* Tricco and D. J.

Price 2012)[14].

Recently, Tricco, D. J. Price, and Bate (2016) have proposed an improvement to the original scheme which is correct for a spatially varying cleaning wave speed. We describe both schemes below (which differ only slightly) as, depending on when they were performed, the calculations in this thesis use either scheme.

To implement both schemes, we modify equations II.68 and II.69 by coupling the additional field so that

$$\mathrm{D}_t B^i = \mathrm{D}_t B^i|_{\mathrm{ideal}} - \nabla^i \psi = \mathrm{D}_t B^i|_{\mathrm{ideal}} + \mathrm{D}_t B^i|_{\mathrm{cleaning}}, \tag{II.79}$$

where $\mathrm{D}_t B^i|_{\mathrm{ideal}}$ represents the original, unmodified (and hence ideal M.H.D.), induction equation used. We then evolve ψ according to the damped wave equation given by (for the Tricco and D. J. Price 2012, scheme)

$$\mathrm{D}_t \psi = -c_{\mathrm{c}}^2 \nabla^i B^i - \frac{\psi}{\tau} - \frac{1}{2}\psi \nabla^i v^i, \tag{II.80}$$

or (for the Tricco, D. J. Price, and Bate 2016, scheme)

$$\mathrm{D}_t \frac{\psi}{c_{\mathrm{c}}} = -c_{\mathrm{c}} \nabla^i B^i - \frac{\psi}{c_{\mathrm{c}} \tau} - \frac{1}{2}\frac{\psi}{c_{\mathrm{c}}} \nabla^i v^i. \tag{II.81}$$

The implementation of equation II.79 and either equation II.80 or equation II.81 in S.P.H. is reasonably simple[15].

Finding the gradient of the ψ field is achieved by simply applying the symmetric derivative operator to obtain

$$\nabla_a^i \psi_a = -\sum_b^N m_b \left(\frac{\psi_a}{\Omega_a \rho_a^2} \nabla_a^i W_{ab}(h_a) + \frac{\psi_b}{\Omega_b \rho_b^2} \nabla_a^i W_{ab}(h_b) \right). \tag{II.82}$$

There is a requirement to use a pair of conjugate operators to evaluate the source term in the wave equation ($\nabla^i B^i$) and the gradient of the consequent field. The observation earlier that the anti-symmetric derivative is insensitive to the addition of a constant would seem to imply that using a symmetric derivative to calculate $\nabla^i B^i$ would be useful — if only by virtue of sampling the particle disorder more sensitively. However, empirical tests indicate that this approach produces numerical artefacts, almost certainly a result of the same phenomena of a spurious magnetic charge density seen for the (necessrily symmetric) momentum equation. We note that this aside, there is no requirement that

14. Though we add the cautionary observation that the consequent magnetic field, whilst solenoidal, is not necessarily the *correct* magnetic field; this error, however, should be *de minimis* compared to the overall field.

15. Modifying an existing code to switch from the equation II.80 to equation II.81 is *extraordinarily* simple, and the benefits well outweigh the small amount of time required to make this switch.

the operator used to evaluate $\nabla^i\psi$ match that used for $\mathrm{D}_t B^i|_{\mathrm{ideal}}$. We also use an anti-symmetric operator for the $\nabla^i v^i$ term for consistency with the continuity equation (and because this quantity is invariably calculated in codes in this manner already). The S.P.H. equation for the damped cleaning wave (for ψ/c_{c}) is

$$\mathrm{D}_t \frac{\psi_a}{c_{\mathrm{c},a}} = \frac{c_{\mathrm{c},a}}{\Omega_a \rho_a} \sum_b^N m_b \left(B_a^i - B_b^i\right) \nabla_a^j W_{ab}\left(h_a\right) - \frac{\psi_a}{c_{\mathrm{c},a}\tau_a} + \frac{1}{2}\frac{\psi_a}{c_{\mathrm{c},a}} \sum_b^N m_b \left(v_a^i - v_b^i\right) \nabla_a^j W_{ab}\left(h_a\right). \tag{II.83}$$

Converting this for the original ψ scheme simply involves multiplying through by $c_{\mathrm{c},a}$. The cleaning wave speed is set to the velocity of the fastest magnetosonic wave speed in the medium, *i.e.*

$$c_{\mathrm{c},a}^2 = c_{\mathrm{s},a}^2 + c_{\mathrm{a},a}^2, \tag{II.84}$$

where $c_{\mathrm{a},a}$ is the Alfvén speed. The Alfvén speed (named in honour of Alfvén 1942) is fastest M.H.D. wave speed in the fluid, and is given by

$$c_{\mathrm{a}} = \frac{B}{\sqrt{4\pi\rho}}. \tag{II.85}$$

In principle, this might be improved by adding a velocity divergence term, turning the cleaning wave speed into a signal velocity. However, before the derivation of the ψ/c_{c} scheme this had the potential to cause numerical issues and has therefore not been explored in great detail. In any case, this is unlikely to cause any issues except in, for example, a very rapidly rotating fluid.

The choice of the damping timescale is important, and is conventionally set according to an equation of the form

$$\tau = \frac{h}{\varsigma c_{\mathrm{c}}}, \tag{II.86}$$

so that the damping is controlled by the dimensionless parameter ς. Empirically, setting $\varsigma = 4/5$ has been observed to work well in real and test problems, and we adopt that value.

II.2.2 Artificial Resistivity

Similar to the hydrodynamical equations, the equations of ideal S.P.M.H.D. as formulated above are unable to accurately handle discontinuities (*i.e.* shocks) in the magnetic field. Consequently we add an artificial resistivity, akin to an artificial magnetic 'viscosity', to smear out the magnetic discontinuity over several smoothing lengths. This also requires a modification to the Ξ_{ab} term to take account of the thermalisation of magnetic energy and hence energy conservation. We use the term 'quasi-ideal' magnetohydrodynamics to describe this formalism since the assumption that the magnetic flux is 'frozen-in' to the fluid is no longer strictly true.

Like the energy equation (equation II.51), we add a term to the induction equation

so that[16]

$$\mathrm{D}_t B^i = \mathrm{D}_t B^i|_{\mathrm{ideal}} + \mathrm{D}_t B^i|_{\mathrm{cleaning}} + \sum_b^N m_b \Gamma_{ab} \left(B_a^i - B_b^i \right) \hat{r}_{ab}^j \nabla_a^j \overline{W}_{ab}. \tag{II.87}$$

As for the artificial viscosity, the choice of Γ_{ab} is in principle arbitrary (although it must be some form of pair-wise operation to avoid conservation violations). An obvious choice is a Riemann solver–esque method as used for the viscosity. Therefore, we set

$$\Gamma_{ab} = \frac{\alpha_{\mathrm{AR},a} v_{\mathrm{sig}}}{\overline{\rho_{ab}^2}}. \tag{II.88}$$

The 'correct' signal velocity to use in this equation presents a challenge, which we will return to. As usual, we set the α_{AR} parameter using a switch. The obvious approach would be to use a source term approach as used for the artificial viscosity, perhaps with (D. J. Price and Monaghan 2005)

$$\mathscr{S} = \frac{1}{\sqrt{4\pi\rho}} \max \left(|\nabla^i B^i|, |\epsilon^{ijk} \nabla^j B^k| \right). \tag{II.89}$$

We use the switch proposed by Tricco and D. J. Price (2013b) which applies less viscosity than the preceding method, and which has been observed to improve results in both test problems (Tricco and D. J. Price 2013a,b) and real calculations (Bate, *priv. comm.*). This switch does not involve a source and decay term at all, and instead sets

$$\alpha_{\mathrm{AR}} = h \left| \frac{\nabla^i B^j}{B^i} \right|. \tag{II.90}$$

Use of an artificial resistivity requires an equivalent modification to the ratio of specific energies in Ω_{ab} (*cf.* equation II.51) to include the magnetic energies. We replace the simple definition of $\tilde{\epsilon}_{ab}$ with

$$\tilde{\epsilon}_{ab} \equiv \tilde{\epsilon}_a + \tilde{\epsilon}_b, \tag{II.91}$$

we then use (D. J. Price and Monaghan 2004a, 2005)

$$\tilde{\epsilon}_a = \frac{1}{2} \left(v_a^i \hat{r}_{ab}^i \right)^2 + \frac{1}{8\pi\bar{\rho}_{ab}} \left[B_a^2 - \left(B_a^i \hat{r}_{ab}^i \right)^2 \right] \tag{II.92}$$

and similarly for $\tilde{\epsilon}_b$.

At least three choices of signal velocity exist for use in the artificial resistivity term.

16. See equation II.52 for the definition of the average kernel $\overline{W}_{ab}$

We again use a term of the form

$$v_{\rm sig} = \frac{1}{2}\left(c_a + c_b\right) - \beta\left(v_a^i - v_b^i\right)\hat{r}_{ab}^i, \tag{II.93}$$

but with the two sound speeds replaced with magnetosonic wave speeds according to (originally proposed by D. J. Price and Monaghan 2004a)

$$c = \frac{1}{2}\sqrt{c_s^2 + \frac{B^2}{4\pi\rho} \pm \frac{2cB^i\hat{r}_{ab}^i}{\sqrt{4\pi\rho}}}, \tag{II.94}$$

which is a hybrid between simply taking the maximum magnetosonic wave speed (as for the divergence cleaning) and a term which incorporates the orientation of the interacting M.H.D. waves. Anecdotal evidence indicates this is neither better nor worse than simply taking the maximum wave speed, given by

$$c^2 = c_{\rm s}^2 + \frac{B^2}{4\pi\rho}. \tag{II.95}$$

Alternatively one could take the positive root from

$$c^2 = \frac{1}{2}\left[c_{\rm s}^2 + \frac{B^2}{4\pi\rho} \pm \sqrt{\left(c_{\rm s}^2 + \frac{B^2}{4\pi\rho}\right)^2 - \frac{c_{\rm s}^2 B^2}{\pi\rho}\cos^2\theta}\right], \tag{II.96}$$

which does incorporate the wave orientation, θ. Again, anecdotal evidence indicates that the additional complexity created by this approach is of limited to no benefit.

Using these equations we have a complete and (generally) stable smoothed particle quasi-ideal magnetohydrodynamics scheme. In their fullest form, these equations are

$$\begin{aligned}
{\rm D}_t v_a^i = &-\sum_b^N m_b\left(\frac{1}{\Omega_a}\frac{p_a}{\rho_a^2}\delta^{ij}\nabla_a^j W_{ab}(h_a) + \frac{1}{\Omega_b}\frac{p_b}{\rho_b^2}\delta^{ij}\nabla_a^j W_{ab}(h_b)\right) && \Big\}\ \text{fluid pressure}\\
&-\frac{1}{8\pi}\sum_b^N m_b\left(\frac{1}{\Omega_a}\frac{B_a^2}{\rho_a^2}\delta^{ij}\nabla_a^j W_{ab}(h_a) + \frac{1}{\Omega_b}\frac{B_b^2}{\rho_b^2}\delta^{ij}\nabla_a^j W_{ab}(h_b)\right)\Big\}\ \text{magnetic pressure}\\
&+\frac{1}{4\pi}\sum_b^N m_b\left(\frac{1}{\Omega_a}\frac{B_a^i B_a^j}{\rho_a^2}\nabla_a^j W_{ab}(h_a) + \frac{1}{\Omega_b}\frac{B_b^i B_b^j}{\rho_b^2}\nabla_a^j W_{ab}(h_b)\right)\Big\}\quad \text{"}\quad \text{tension} \qquad \text{(II.97)}\\
&-\chi\frac{1}{4\pi}B_a^i\sum_b^N m_b\left(\frac{1}{\Omega_a}\frac{B_a^j}{\rho_a^2}\nabla_a^j W_{ab}(h_a) + \frac{1}{\Omega_b}\frac{B_b^j}{\rho_b^2}\nabla_a^j W_{ab}(h_b)\right)\Big\}\ \text{tensile instability correction}\\
&-\sum_b^N m_b\Pi_{ab}\nabla_a^i\overline{W}_{ab} \qquad\qquad \Big\}\ \text{artificial viscosity},
\end{aligned}$$

$$
\begin{aligned}
\mathrm{D}_t \frac{B_a^i}{\rho_a} = &- \sum_b^N \frac{m_b}{\Omega_a \rho_a^2} \left(v_a^i - v_b^i \right) B_a^j \nabla_a^j W_{ab}\left(h_a\right) && \Big\} \text{ ideal ind. equation} \\
&- \sum_b^N m_b \left(\frac{1}{\Omega_a} \frac{\psi_a}{\rho_a^2} \nabla_a^i W_{ab}\left(h_a\right) + \frac{1}{\Omega_b} \frac{\psi_b}{\rho_b^2} \nabla_a^i W_{ab}\left(h_b\right) \right) \Big\} && \text{divergence cleaning} \\
&+ \sum_b^N m_b \Gamma_{ab} \left(B_a^i - B_b^i \right) \hat{r}_{ab}^j \nabla_a^j \overline{W}_{ab} && \Big\} \text{ artificial resistivity,}
\end{aligned} \tag{II.98}
$$

in addition to the usual density interpolant and the same energy equation (equation II.49) as before. We note here that for the rest of this thesis we use the mass-weighted version of the induction equation exclusively.

II.3 Radiative Transfer

> Forthwith Light
> Ethereal, first of things, quintessence pure
> Sprung from the Deep, and from her Native East
> To journie through the airie gloom began,
> Sphear'd in a radiant Cloud, for yet the Sun
> Was not.
>
> Book vii, Paradise Lost, John Milton (1667 & 1674)

In the same way that astrophysical plasmas are magnestised, the fluid that makes up those plasmas transfers thermal energy by radiation. Consequently, for some calculations we also use a flux limited diffusion (F.L.D.) radiative transfer (R.T.) scheme to incorporate this physical process into our simulations. Rather than ray tracing, we use a system whereby we treat the radiative flux as a property of the fluid which can then be diffused through the medium. This provides considerable computational advantages, for example it obviates the need for a Monte Carlo (Richtmyer, Pasta, and Ulam 1947) scheme (*e.g.* as originally proposed by Lucy 1999) to evaluate the radiative terms.

Similar to adding magnetism to S.P.H., this principally involves adding a term to the momentum equation and adding an additional evolution equation. Radiation will change the fluid temperature and consequently a modification to the energy equation will also be necessary (and obviously this is incompatible with an isothermal equation of state). The momentum equation for radiation hydrodynamics (R.H.D.) is given by

$$
\mathrm{D}_t v^i = -\frac{1}{\rho} \nabla^i p + \frac{\kappa}{c} \mathscr{F}^i, \tag{II.99}
$$

or equivalently written by modifying the stress tensor so that

$$
\sigma^{ij} = \left(-p + \Lambda \mathscr{E} \right) \delta^{ij}, \tag{II.100}
$$

where $\mathscr{F}^i$ and $\mathscr{E}$ are the radiation flux and radiation energy density fields and Λ is some flux limiter function (discussed below). The evolution equation for the radiation energy density — the R.H.D. cousin of the M.H.D. induction equation — is provided by

$$\mathrm{D}_t \frac{\mathscr{E}}{\rho} = -\frac{1}{\rho}\nabla^i \mathscr{F}^i - \frac{1}{\rho}\nabla^i v^j P^{ij} + 4\pi\kappa B\left(T_{\mathrm{fl}}\right) - c\kappa\mathscr{E}, \tag{II.101}$$

and the energy equation is modified to become

$$\mathrm{D}_t \varepsilon = -\frac{p}{\rho}\nabla^i v^i - 4\pi\kappa B\left(T_{\mathrm{fl}}\right) + c\kappa\mathscr{E}, \tag{II.102}$$

where κ is the opacity of the fluid.

Although a complicated addition to the hydrodynamical equations, the equations of smoothed particle (F.L.D.) radiation hydrodynamics (S.P.R.H.D.) have the advantage over the equations of S.P.M.H.D. in that they are very stable and are principally limited only by computational time not algorithmic utility.

An important assumption is that the fluid is always in a local thermodynamic equilibrium, which it transpires is a reasonable assumption for astrophysical plasmas. Due to this, we can use the Planck function (*cf.* Planck 1914)

$$B\left(T_{\mathrm{fl}}\right) = \frac{\sigma_{\mathrm{B}}}{\pi} T_{\mathrm{fl}}^4, \tag{II.103}$$

which has no dependence on ν, the frequency of the radiation, and therefore we assume all radiation is 'grey'. $\sigma_{\mathrm{B}} = 5.670{,}5\times10^{-5}\,\mathrm{erg\cdot cm^{-2}\cdot s^{-1}\cdot K^{-4}}$ is the Stefan–Boltzmann constant and T_{fl} is the fluid temperature. A second temperature also exists, *viz.* the temperature of the radiative flux, T_{rad}. This is linked to the radiation energy density by

$$\mathscr{E}(T_{\mathrm{rad}}) = \frac{4\sigma_{\mathrm{B}}}{c} T_{\mathrm{rad}}^4. \tag{II.104}$$

The radiative flux is simply the gradient of the energy density. However, taking this gradient directly can result in unphysically rapid diffusion of radiation energy through the fluid, particularly in regions with a low fluid density. We therefore use a flux limiter, so the radiation flux becomes

$$\mathscr{F}^i = -\Lambda\nabla^i\mathscr{E} = -\frac{c\lambda\left(R\right)}{\kappa\rho}\nabla^i\mathscr{E} \tag{II.105}$$

where $\lambda\left(R\right)$ is the flux limiter. In essence, this is a form of the first diffusion law proposed by Fick (1855). In this work we use the limiter derived by Levermore and Pomraning (1981) which has

$$\lambda\left(R\right) = \frac{2+R}{6+3R+R^2}, \tag{II.106}$$

with the R parameter defined by

$$R\left(\mathscr{E}\right) = \left|\frac{\nabla^i E}{\kappa\rho\mathscr{E}}\right|. \tag{II.107}$$

From this the effect of radiative flux on the velocity field of the fluid can be computed. To calculate the change in the radiative energy density field one additional parameter is required: *viz.* the radiation pressure. This is a tensor, in general not isotropic, denoted by P^{ij} which couples the radiative energy density field to the shape of the radiation (flux) field. We obtain this by combining the energy density field with an Eddington tensor, such that

$$P^{ij} = f^{ij}\mathscr{E}, \tag{II.108}$$

where

$$f^{ij} = \frac{1}{2}\left[1 - f\left(\mathscr{E}\right)\right]\delta^{ij} + \frac{1}{2}\left[3f\left(\mathscr{E}\right) - 1\right]\hat{n}^i\hat{n}^j. \tag{II.109}$$

This contains an 'Eddington factor function', which is linked back to the flux limiter function and the R term *via*[17]

$$f\left(\mathscr{E}\right) = \lambda \circ R(\mathscr{E}) + \lambda^2 \circ R(\mathscr{E}) \cdot R^2(\mathscr{E}). \tag{II.110}$$

The intrinsically coupled nature of all these components makes an explicit numerical integration scheme computationally intractable. Consequently we evolve these equations in time using an implicit integration system, for the details of which see Whitehouse and Bate (2004, 2006) and Whitehouse, Bate, and Monaghan (2005). The values of $\mathscr{E}$ and $B\left(T_{\rm fl}\right)$ produced by the implicit solver are then added to the usual S.P.H. equations, with $\mathscr{F}^i$ produced from $\mathscr{E}$ by way of the usual S.P.H. operators.

If these R.H.D. equations are combined with the M.H.D. equations derived in section II.3, a complete system of smoothed particle radiation quasi-ideal magnetohydro-

17. where the notation $f \circ g$ represents the composition of two functions f and g

dynamics is obtained, *viz.* the full momentum equation for S.P.R.M.H.D. is

$$
\begin{aligned}
\mathrm{D}_t v_a^i = &- \sum_b^N m_b \left(\frac{1}{\Omega_a} \frac{p_a}{\rho_a^2} \delta^{ij} \nabla_a^j W_{ab}(h_a) + \frac{1}{\Omega_b} \frac{p_b}{\rho_b^2} \delta^{ij} \nabla_a^j W_{ab}(h_b) \right) && \Big\} \text{ fluid pressure} \\
&- \frac{1}{8\pi} \sum_b^N m_b \left(\frac{1}{\Omega_a} \frac{B_a^2}{\rho_a^2} \delta^{ij} \nabla_a^j W_{ab}(h_a) + \frac{1}{\Omega_b} \frac{B_b^2}{\rho_b^2} \delta^{ij} \nabla_a^j W_{ab}(h_b) \right) \Big\} && \text{magnetic pressure} \\
&+ \frac{1}{4\pi} \sum_b^N m_b \left(\frac{1}{\Omega_a} \frac{B_a^i B_a^j}{\rho_a^2} \nabla_a^j W_{ab}(h_a) + \frac{1}{\Omega_b} \frac{B_b^i B_b^j}{\rho_b^2} \nabla_a^j W_{ab}(h_b) \right) \Big\} && \text{" tension} \\
&- \chi \frac{1}{4\pi} B_a^i \sum_b^N m_b \left(\frac{1}{\Omega_a} \frac{B_a^j}{\rho_a^2} \nabla_a^j W_{ab}(h_a) + \frac{1}{\Omega_b} \frac{B_b^j}{\rho_b^2} \nabla_a^j W_{ab}(h_b) \right) \Big\} && \text{inst. corr.} \qquad \text{(II.111)} \\
&+ \sum_b^N m_b \left(\frac{\lambda(R_a)}{\Omega_a} \frac{\mathscr{E}_a}{\rho_a^2} \nabla_a^i W_{ab}(h_a) + \frac{\lambda(R_b)}{\Omega_b} \frac{\mathscr{E}_b}{\rho_b^2} \nabla_a^i W_{ab}(h_b) \right) && \Big\} \text{ radiative flux} \\
&- \sum_b^N m_b \Pi_{ab} \nabla_a^i \overline{W}_{ab} && \Big\} \text{ artificial viscosity.}
\end{aligned}
$$

The modification to the energy equation is much simpler since neither of the new terms involve an S.P.H. derivative operator.

II.4 Gravity

> What is there in places empty of matter? and Whence is it that the sun and planets gravitate toward one another without dense matter between them? Whence is it that Nature doth nothing in vain?
>
> Query XXVIII, Book III,
> Opticks: Or, a Treatise of the Reflexions,
> Refractions, Inflexions and Colours of Light,
> Sir Isaac Newton (1704—1718)

If magnetism and radiation are common in the universe then gravity is omnipresent. Gravity appears in our hydrodynamical equations as the canonical 'external force' — g^i in equation II.2, or equivalently (in terms of the self-gravitational potential ϕ)

$$\mathrm{D}_t v^i = -\frac{1}{\rho} \nabla^i p + \nabla^i \phi. \qquad \text{(II.112)}$$

Unlike the physical processes described in sections II.2 and II.3, this is the *only* modification required to add self–gravity to S.P.H.— provided ϕ can be calculated. The Poisson equation,

$$\triangle \phi = 4\pi G \rho, \qquad \text{(II.113)}$$

provides the general form of this self-potential. In reality, since S.P.H. is a particulate scheme calculating the gravitational potential is not dissimilar from an N–body code. In principle, every S.P.H. particle in the entire simulation provides a gravitational contribution to every other particle, and *vice versa*. If we could guarantee a collisionless fluid, then we can obtain an exact gravitational force at all length scales. However, although S.P.H. particles are prevented from agglomeration by the artifical viscosity terms, in shocks and density gradients particles will often pass close together. We therefore need to soften the gravitational potential, sacrificing absolute accuracy on very short length scales in exchange for overall numerical stability. Both methods provide exact conservation of momentum and energy.

In an N-body code a softening scheme would need to be selected. S.P.H. effectively provides one for free, since the smoothing kernel is *by its very nature* a softening function. A kernel with compact support has the additional advantage that outside of the compact support radius (*i.e.* for the overwhelming majority of the spatial extent of the calculation) of a particle the softening is zero and therefore the force is exact.

The general form of Newton's Universal Gravitational Law (Newton 1687) is an equation of the form

$$F^i\left(r^i\right) = -\frac{Gm_1m_2}{r^2}\hat{r}^i. \tag{II.114}$$

Exceptionally in this section, the sub–scripted m_1 and m_2 represent arbitrary point–masses not S.P.H. particles (though as will become clear, there is no difference in practice). This equation presents an issue due to a singularity:

$$\lim_{r\to\infty} F^i\left(r^i\right) = -Gm_1m_2\hat{r}^i \lim_{r\to\infty} \frac{1}{r^2} = \infty, \tag{II.115}$$

which is the cause of the need for a softened potential discussed above. The classic way of doing this is to use a Plummer (1911) potential, which replaces the r^2 term in equation II.114 with

$$r'^2 = r^2 + r_{\min}^2, \tag{II.116}$$

where $r_{\min}$ is some small 'minimum' radius. Whilst effective at preventing the singularity, this has the disadvantage that it affects the whole calculation (it is, in effect, always switched on). Instead, following D. J. Price and Monaghan (2007) we use the S.P.H. smoothing kernel in a softening kernel approach (see also Dehnen 2001; Dyer and Ip 1993).

To do this we first take the gravitational potential to be given by

$$\Phi\left(r^i\right) = -G\sum_c^N m_c \Upsilon\left(|r^i - r_c^i|, h\right), \tag{II.117}$$

where $\Upsilon\left(|r^i - r_c^i|, h\right)$ is the softening kernel (we derive this from the S.P.H. smoothing kernel below). We then obtain a gravitational force — which we need to couple the gravitational self–potential, equation II.113, into the momentum equation, equation II.2 — by

noting that

$$F_{\text{grav}}\left(r^i\right) = -\nabla^i \Phi\left(r^i\right), \tag{II.118}$$

so

$$F_{\text{grav}}\left(r^i\right) = -G\sum_c^N m_c \nabla^i Y\left(|r^i - r_c^i|, h\right). \tag{II.119}$$

An important sleight of hand now happens. We observe that Poisson's equation implies that

$$\rho\left(r^i\right) = \frac{1}{4\pi G}\triangle\Phi\left(r^i\right), \tag{II.120}$$

so we can then write

$$\rho\left(r^i\right) = \frac{1}{4\pi G}\nabla^i\left(-G\sum_c^N m_c \nabla^i Y\left(|r^i - r_c^i|, h\right)\right), \tag{II.121}$$

$$\rho\left(r^i\right) = -\frac{1}{4\pi}\left(\sum_c^N m_c \triangle Y\left(|r^i - r_c^i|, h\right)\right), \tag{II.122}$$

which looks similar to the usual S.P.H. density interpolant. This similarity can be more readily exposed if we define

$$Y\left(|r^i - r_c^i|, h\right) = -\frac{1}{4\pi}\int_0^\infty \int_0^\infty W\left(|r^i - r_c^i|, h\right) \mathrm{d}^2 r^i. \tag{II.123}$$

This allows the same kernel function, appropriately integrated, to be used for *both* the equations of fluid dynamics and also an N–body gravity. This also sidesteps the question of what the correct softening length *is* (*cf.* Athanassoula *et al.* 2000; Merritt 1996; Rodionov and Sotnikova 2005, *etc.*), since the S.P.H. smoothing length naturally answers that question (see also Bate and Burkert 1997). For completeness, we note that the softening kernel, Y, and its first derivative are defined such that

$$Y\left(q\right) = \frac{\lambda}{h^\nu} y\left(q\right), \tag{II.124}$$

and

$$\nabla^i Y\left(q\right) = \frac{\lambda}{h^\nu}\hat{r}\partial_r y\left(q\right). \tag{II.125}$$

The two integrated spline functions, $y\left(q\right)$ and $\partial_q y\left(q\right)$ are then defined as (for a cubic B–spline)

$$\int_\infty^\infty \int_\infty^\infty w(q)\mathrm{d}q = y(q)\begin{cases} 2/3\, q^2 - 3/10\, q^4 + 1/10\, q^5 - 7/5, & 0 \le q < 1, \\ 4/3\, q^2 - q^3 + 3/10\, q^4 - 1/30\, q^5 + 1/15q - 8/5, & 1 \le q < 2, \\ 0, & \text{elsewhere}, \end{cases} \tag{II.126}$$

$$\int_{\infty}^{\infty} w(q)\mathrm{d}q = \partial_q y(q) = \begin{cases} 4/3\, q - 6/5\, q^3 + 1/2\, q^4, & 0 \leq q < 1, \\ 8/3\, q - 3q^2 + 6/5\, q^3 - 1/6\, q^4 - 1/15 q^2, & 1 \leq q < 2, \\ 0, & \text{elsewhere.} \end{cases} \tag{II.127}$$

We require that outside of the compact support radius, R, the softening kernel behave like the usual inverse square law gravitational potential. Consequently, we set the constraint that (for a cubic B–spline) when $q > 2$, $y\left(q\right) = -1/r$ and $\partial_q y\left(q\right) = 1/r^2$.

D. J. Price and Monaghan (2007) then use a variational approach to obtain the correct momentum equation using this softening kernel constructed from the S.P.H. smoothing kernel. Briefly, they first take the gravitational Lagrangian,

$$\mathscr{L} = -\sum_{b}^{N} m_c \Phi_c, \tag{II.128}$$

noting that here $N \supseteq N_{\mathrm{ngh}}$ since a gravitational force is provided by *all* particles on *all* particles. By substitution, this becomes

$$\mathscr{L} = -\frac{1}{2} G \sum_{c}^{N} \sum_{d}^{N} m_c m_d Y_{cd}\left(h_c\right), \tag{II.129}$$

$$\mathscr{L} = -\frac{1}{2} G \sum_{c}^{N} \sum_{d}^{N} \frac{1}{2} m_c m_d \left[Y_{cd}\left(h_c\right) + Y_{dc}\left(h_d\right)\right], \tag{II.130}$$

when $h_c \neq h_d$ in general[18]. As D. J. Price and Monaghan (*ibid.*) observe, the derivative of this produces two terms when h is not spatially constant, and both are required for exact conservation. In a system with a spatially fixed resolution, the second term is necessarily zero and we would recover the 'obvious' form of the equation. So

$$\begin{aligned} \nabla_c^i \mathscr{L} = -\frac{1}{2} \sum_{c}^{N} \sum_{d}^{N} m_c m_d \Bigg\{ & \frac{1}{2} \nabla_c^i \left[Y_{cd}\left(h_c\right) + Y_{dc}\left(h_d\right)\right] \\ & + \frac{1}{2} \left[\nabla_c^i h_c \partial_{h_c} Y_{cd}\left(h_c\right) + \nabla_d^i h_d \partial_{h_d} Y_{dc}\left(h_d\right)\right] \Bigg\}. \end{aligned} \tag{II.131}$$

The second term is clearly analogous to the ∇h terms in the ordinary S.P.H. fluid equations. Using this, and some algebraic manipulation (*cf. ibid.*) we obtain the following force

18. Which is the case for any non–trivial compressible fluid.

equation,

$$\begin{aligned} \mathrm{D}_t v_a^i|_{\mathrm{grav}} = &-\frac{1}{2} G \sum_b^N m_b \left(\nabla_a^i Y_{ab}(h_a) + \nabla_a^i Y_{ab}(h_b) \right) \\ &- \frac{1}{2} G \sum_b^N m_b \left(\frac{\Theta_a}{\Omega_a} \nabla_a^i W_{ab}(h_a) + \frac{\Theta_b}{\Omega_b} \nabla_a^i W_{ab}(h_b) \right), \end{aligned} \tag{II.132}$$

which when added on to the S.P.H. momentum equation provides self–gravity in S.P.H.. The Ω term is as derived in section II.2 and the markedly similar Θ term is given by

$$\Theta_a = \partial_{\rho_a} h_a \sum_b^N m_b \partial_{h_a} Y_{ab}(h_a). \tag{II.133}$$

From this we can obtain the full momentum equation for smoothed particle flux–limited diffusion radiation quasi-ideal magnetohydrodynamics with self gravity, given by

$$\begin{aligned} \mathrm{D}_t v_a^i = &- \sum_b^N m_b \left(\frac{1}{\Omega_a} \frac{p_a}{\rho_a^2} \delta^{ij} \nabla_a^j W_{ab}(h_a) + \frac{1}{\Omega_b} \frac{p_b}{\rho_b^2} \delta^{ij} \nabla_a^j W_{ab}(h_b) \right) && \Big\} \text{ fluid pressure} \\ &- \frac{1}{8\pi} \sum_b^N m_b \left(\frac{1}{\Omega_a} \frac{B_a^2}{\rho_a^2} \delta^{ij} \nabla_a^j W_{ab}(h_a) + \frac{1}{\Omega_b} \frac{B_b^2}{\rho_b^2} \delta^{ij} \nabla_a^j W_{ab}(h_b) \right) && \Big\} \text{ magnetic pressure} \\ &+ \frac{1}{4\pi} \sum_b^N m_b \left(\frac{1}{\Omega_a} \frac{B_a^i B_a^j}{\rho_a^2} \nabla_a^j W_{ab}(h_a) + \frac{1}{\Omega_b} \frac{B_b^i B_b^j}{\rho_b^2} \nabla_a^j W_{ab}(h_b) \right) && \Big\} \quad " \quad \text{tension} \\ &- \chi \frac{1}{4\pi} B_a^i \sum_b^N m_b \left(\frac{1}{\Omega_a} \frac{B_a^j}{\rho_a^2} \nabla_a^j W_{ab}(h_a) + \frac{1}{\Omega_b} \frac{B_b^j}{\rho_b^2} \nabla_a^j W_{ab}(h_b) \right) && \Big\} \text{ inst. corr.} \\ &+ \sum_b^N m_b \left(\frac{\lambda(R_a)}{\Omega_a} \frac{\mathscr{E}_a}{\rho_a^2} \nabla_a^i W_{ab}(h_a) + \frac{\lambda(R_b)}{\Omega_b} \frac{\mathscr{E}_b}{\rho_b^2} \nabla_a^i W_{ab}(h_b) \right) && \Big\} \text{ radiative flux} \\ &- \frac{1}{2} G \sum_b^N m_b \left(\nabla_a^i Y_{ab}(h_a) + \nabla_a^i Y_{ab}(h_b) \right) && \Big\} \text{ self–gravity} \\ &- \frac{1}{2} G \sum_b^N m_b \left(\frac{\Theta_a}{\Omega_a} \nabla_a^i W_{ab}(h_a) + \frac{\Theta_b}{\Omega_b} \nabla_a^i W_{ab}(h_b) \right) && \Big\} \text{ energy cons.} \\ &- \sum_b^N m_b \Pi_{ab} \nabla_a^i \overline{W}_{ab} && \Big\} \text{ artificial viscosity.} \end{aligned} \tag{II.134}$$

Aside from the artificial viscosity term[19], we make the salient observation here that as predicted in sub–section II.1.1 every derivative term in equation II.134 *supra* is in the symmetric form. This is essential to maintain momentum and energy conservation and is a result of obtaining each term from a Lagrangian.

Unlike the fluid dynamics terms in S.P.H., these summations still operate over all N, not a restricted neighbour set N_{ngh}. In a very small calculation this may be acceptable, however, performing N loops over N individual particles is clearly inefficient. Neighbour finding can be done on a tree, and tree–gravity methods are also well studied. We can use this synergy to make a significant computational improvement: the same tree needed to compute gravity (which is all–but an unavoidable necessity) can be used to significantly optimize neighbour finding (or, conversely, if one has a code which already uses a tree to find neighbour particles, that tree can be recycled for gravitational use, see Freitag and Benz 2001). It is the ability to make this pairing that makes high–resolution S.P.H. calculations with gravity particularly efficient even over large spatial scales. We note, however, the slight loss in accuracy caused by the use of a tree as opposed to a direct summation, which is related to the analogy we made in the opening paragraph of this section about when can an extended mass be approximated by a point–mass.

II.5 Sink Particles

In this thesis we follow our calculations through many orders–of–magnitude of density, length, and other physical properties. We start with a reasonably sparse cloud core, and finish up with what is almost a protostar. However, in nature this continues: protostars have internal structure, with convective zones, radiative zones, and interactions between accreting material and the stellar surface[20]. To have a tractable calculation we need a way to neglect these internal dynamics. Our time–step begins (in the cloud core phase) as being $\Delta t > 120$ a and approaches $\Delta t \approx 7,000$ s as a first hydrostatic core is formed. If we did not leave out physical processes present sub–astronomical unit length–scales, Δt will rapidly approach $\Delta t = 1$ s, *i.e.* real–time (which effect was observed towards the end of the calculations presented in Bate, Tricco, and D. J. Price 2014). We do this by means of the 'sink particle'[21]. A sink particle is an inner boundary condition whereby material which passes within some radius r_{acc} of the particle is 'accreted' if certain tests are passed. Accreted material is added to the mass of the sink, which interacts with the continuing calculation solely via gravity.

19. which is closer in form to a second derivative in any case

20. And beneath *this* structure still more physical processes occur

21. Sometimes called a 'point–mass particle', although this invites confusion with various unrelated gravitational concepts.

II.5.1 Creation

Sink particles are inserted when the density of the calculation at a particular particle exceeds a pre–determined critical density. In addition, in non–radiative transfer calculations a series of tests are used to verify that the region around the proposed sink is properly bound and not a transient over–density. These tests are more complex in a radiative calculation, where we instead simply raise the critical density by a few orders of magnitude (which, by definition, any correctly bound region will reach within a reasonably short time scale). For example, whereas we would normally set the critical density to 10^{-10} g $\cdot$ cm^{-3} (on the assumption that a region which exceeds this density and passes the tests will inevitably form a protostar) in a radiative transfer calculation we raise this 10^{-5} g$\cdot$cm^{-3}, well into the second collapse phase.

The tests mentioned above are as follows Bate, Bonnell, and N. M. Price (1995). Firstly, the particle with the highest density in the calculation which exceeds the critical density is identified. The first test (which also applies to radiative transfer calculations) is then to ensure that the smoothing length of this particle is such that

$$h_a < \frac{1}{2} r_{\rm crit}, \tag{II.135}$$

to guarantee that the new sink particle will begin with a mass of

$$m_{\rm sink} \approx N_{\rm ngh} m_a, \tag{II.136}$$

(assuming, as is invariably the case, equal mass S.P.H. gas particles). We now need to verify that the region into which the sink will be inserted is bound. Having ascertained the $\approx$ 50 S.P.H. gas particles we calculate $E_{\rm therm}$, $E_{\rm rot}$, and $E_{\rm grav}$ (the thermal, rotational kinetic, and gravitational self–potential energies respectively) for them. A sink particle will not be inserted if either

$$\beta_{\rm therm} \geq \frac{1}{2}, \tag{II.137}$$

$$\beta_{\rm therm} + \beta_{\rm rot} \geq 1, \tag{II.138}$$

or

$$\beta_{\rm tot} \geq 1. \tag{II.139}$$

Here we have used the notation

$$\beta_{\rm therm} = \frac{E_{\rm therm}}{|E_{\rm grav}|}, \tag{II.140}$$

to represent the ratios of the various energy terms to the magnitude of the gravitational self–potential (so $E_{\rm tot}$ and $\beta_{\rm tot}$ represent the sum of all energies *except* the negative definite self–potential). Assuming these tests are passed, which guarantee that the region concerned is energetically bound, we then check the divergence of the particle accelerations,

and do not insert a sink if

$$\nabla^i \dot{v}^i \geq 0, \tag{II.141}$$

a situation which indicates a region undergoing a 'bounce' or that is otherwise liable to unbind. Assuming these tests are passed, the particle identified earlier is then replaced by a sink particle, and all S.P.H. gas particles within the relevant accretion radius are then added to it.

II.5.2 Accretion

Particles which pass within $r_{\rm acc}$ of a sink particle may be accreted. We invariably set a second accretion radius, usually $1/10 r_{\rm acc}$, within which *all* S.P.H. particles will be accreted unconditionally. This second threshold eliminates the risk of large accelerations being applied to a gas particle passing very close to a potentially massive ($m_{\rm sink}/\mathrm{M}_\odot \gtrsim 1/10$ is not an unrealistic situation later in a calculation) sink particle. To prevent spurious accretion of otherwise unbound material, S.P.H. gas particles are only accreted within the first accretion radius if two tests are passed. These are that the particle has been gravitationally bound by the sink particle, *i.e.* that

$$\beta_{\rm kin} \leq 1. \tag{II.142}$$

The second, subtler, condition is that the S.P.H. particle has sufficiently low angular momentum that the minimum circular orbital radius is less than $r_{\rm acc}$. A third condition applies where multiple sinks are potentially interacting with a gas particle, for example in a binary pair. Here we also verify that the sink particle concerned is the one which the gas particle is most tightly bound to. In an approximately equal mass binary this is unlikely to provide much of a variation, but where a highly unequal mass pairing is present will prevent gas particles being erroneously accreted by a less massive companion (*i.e.* the more massive protostar will be able to effectively steal mass from the less massive one).

II.5.3 Boundaries

As implemented, our sink particles have no boundaries and could be compared analogously with a black hole. Although Bate, Bonnell, and N. M. Price (1995) proposed a series of boundary corrections to S.P.H. particles near the sink accretion radius, subsequent experience has indicated that these provide very little benefit (in a hydrodynamical calculation) given the complexity of implementation. The reason for this is simply that in a protostellar collapse — or indeed any centrally condensing collapse — pressure boundaries and the like are effectively otiose. We do ensure that particles on one side of the sink particle are insensitive to pressure fields, artificial viscosity, *etc.*, from particles on the other side, although this is comparably trivial to implement.

The magnetic field within and near the sink, however, can not be so easily neglected. Although we have not implemented any form of magnetic boundary, we are careful to ensure that the divergence cleaning and related matters discussed in section II.2 *supra*

maintain a solenoidal magnetic field. Effectively deleting particles from the calculation as they are accreted onto the sink is approximately equivalent to adding a magnetic divergence equal–and–opposite to the field carried by the accreted particle. Consequently, if no attempt was made to keep the field at least approximately correct errors due to non–solenoidality of the field would rapidly build up.

For completeness, we note that the sink particles used are also 'cold' insofar as they provide no contribution to the radiative transfer scheme detailed in section II.4 *supra*. Over the timescales we consider — $t \leq 25{,}000\,\mathrm{a}$ — this is incomplete but not disastrous. Importantly, the pseudo–disc around the sink particle will still radiate and transfer energy, and this still contains the majority of the 'interesting' mass. Over larger timescales, when radiative flux from accretion flows onto the protostar becomes important, some sort of 'luminous sink' treatment would be essential. An approach incorporating a stellar evolution model, for example Baraffe and El Eid (1991), Chabrier and Baraffe (1997), and Langer, El Eid, and Baraffe (1989), may be a possible approach.

Finally, we note that unlike S.P.H. particles, the gravitational potential for sink particles acting on fluid S.P.H. particles is not solved using the tree method discussed in section II.6 *infra*. A sink particle begins with $m_{\mathrm{sink}} \gtrsim 50 m_a$ (where as usual we assume m_a is identical $\forall\, a \in N$), and this mass only increases. Consequently even a small error calculating the gravitational effect of the sink of the fluid can cause large errors. These manifest as poor momentum conservation after a sink particle is inserted, and empirically this is improved by calculating the sink particle gravity explicitly. This requires a loop over all the particles for each sink and would therefore be unfeasible if the number of sinks became even moderately large. However, we never exceed three sink particles in a calculation so we adopt this method for all the calculations performed in this thesis.

Using this approach, with a few implementation details related to individual time–stepping, we are able to follow the collapse of molecular cloud cores until significantly later than the formation of a first hydrostatic core without being limited by our time–step. The various tests ensure that sink particles are only inserted, and particles only accreted, when it is inevitable that the fluid concerned would have collapsed into a protostar in any case, reducing or eliminating any numerical issues.

II.6 Computational Method

We evolve our S.P.R.M.H.D. method, discussed above, using the hybrid `openMP`[22] and `MPI`[23] `FORTRAN` code called `sphNG`. This code originated with the three–dimensional S.P.H. code written by Benz (1990). This has then been significantly extended and expanded by various authors, including the addition of sink particles, individual particle time–steps and

22. see *openMP v. 2.5* (2005)

23. see *MPI–2* (2003)

periodic boundaries with ghost particles by Bonnell and Bate (1994). The code was then expanded to include the self–consistent variable smoothing length formalism and magnetohydrodynamics by D.J. Price. Finally, we have made a significant number of computational improvements, including a major overhaul of the code and removal of various antique or deprecated features.

II.6.1 The Runge–Kutta–Fehlberg Integrator

sphNG uses a second–order Runge–Kutta–Fehlberg (Fehlberg 1969, 1970; Kutta 1901; Runge 1895) integrator, designated RK1(2) in Fehlberg (1969). A further discussion of the implementation of this integration scheme is contained in the next chapter in sub–section III.2.1. This is an 'embedded method', in that it combines an $\mathscr{O}(h)$ Runge–Kutta method with an $\mathscr{O}(h^2)$ one to provide an error estimate. This allows a reduction in the time–step if the errors computed by the $\mathscr{O}(h^2)$ part become sufficiently large compared to the $\mathscr{O}(h)$ part. We can represent this integrator in tabular form as shown in table II.1, and the application of the co–efficents in that table in an equation is given in the next chapter in equations III.42 and III.43.

Table II.1. Butcher (1964) tableau for the RK1(2) integrator detailing the co-efficients used. The penultimate row provides the co–efficients for the $\mathscr{O}(h)$ part (the application of which to an evolution equation can be seen in equations III.42 and III.43); the final row then provides the co–efficents for the $\mathscr{O}(h^2)$ part.

0			
1/2	1/2		
1	1/256	255/256	
	1/256	255/256	0
	1/512	255/256	1/512

Each S.P.H. particle has an individual time–step, Δt. This provides a significant computational speed up, and is in effect the temporal analogy to the adaptive smoothing length scheme. This time–step is set according to the shorter of several properties, including the local Courant, Friedrichs, and Lewy (1928) condition. The first is obtained from the integrator by comparing the $\mathscr{O}(h)$ and $\mathscr{O}(h^2)$ solutions. If the magnitude of the difference between the two solution exceeds some predetermined threshold, we lower the timestep. This Runge–Kutta integration tolerance is set throughout this thesis to 1×10^{-5} for fluid–fluid interactions and 1×10^{-9} for fluid–sink and sink–sink interactions. A lower tolerance is used for sink related computations since these are purely gravitational, but as noted above the gravitational mass of a sink particle is extremely large compared to a fluid particle. Consequently enhanced accuracy is needed.

In an arbitrary mathematical system, the Courant number is given by an expression of the form

$$\Delta t = \mathscr{C}\frac{\Delta \ell}{|v|}, \tag{II.143}$$

where $\Delta\ell$ is the length interval over which the fluid motions (essentially waves in the fluid) described by the velocity magnitude $|v|$ occurs. An explicit method, which the Runge–Kutta is, invariably requires $\mathscr{C} \leq 1$, *i.e.* that the time–step be short enough to capture at least one wave per $\Delta\ell$. In S.P.H. this equation becomes

$$\Delta t|_{\mathrm{CFL}} = \mathscr{C}\frac{h}{v_{\mathrm{sig}}}. \tag{II.144}$$

We set Δt individually for each particle so that

$$\Delta t_a|_{\mathrm{CFL}} = \mathscr{C}\frac{h_a}{v_{\mathrm{sig},a}}, \tag{II.145}$$

with $v_{\mathrm{sig},a}$ set in the usual way, so as to incorporate the sound and Alfvén speeds and the velocity divergence. Empirically, we observe that setting $\mathscr{C} = 3/10$ (Lattanzio *et al.* 1986) is necessary to ensure stability in S.P.H.. A further constraint is provided by the requirement to resolve accelerations correctly, given by

$$\Delta t_a|_{\mathrm{Acceleration}} = \mathscr{C}\sqrt{\frac{h}{|\dot{v}_a|}}, \tag{II.146}$$

where $\dot{v}_a$ is the acceleration of the S.P.H. particle. We take the minimum of the Δt required by the integrator solutions, $\Delta t|_{\mathrm{CFL}}$, and $\Delta t_a|_{\mathrm{Acceleration}}$ as being the desired particle time–step. Time–steps are then binned into powers of two to provide our individual time–stepping scheme. Particles are placed in the timestep bin which is less than or equal to the minimum required time–step, and can move into longer as well as shorter time–step bins as appropriate. Sink particles are constrained to be in the lower of the bin determined by the criteria or the lowest occupied bin, again, this is necessary due to the comparably large gravitational accelerations caused by sinks.

II.6.2 The Tree and Parallelization

We use a hierarchical binary tree[24] to both calculate gravity and to find neighbours (see Benz 1988; Benz *et al.* 1990; Press 1986), exploiting the computational synergy identified in section II.4. This is a similar conceptual idea to the use of a Barnes and Hut (1986) tree, applied to S.P.H. particles rather than grid cells, by Hernquist and Katz (1989). An earlier approach to optimizing gravity calculations was the bespoke GRAPE–board (Sugimoto *et al.* 1990) — an hierarchical tree is superior to this is many ways, in particular in not requiring specialized hardware. The essential premise is that if the quotient

$$\frac{s_i}{r_i} = \theta_i, \tag{II.147}$$

24. occaisionally, these are floridly described as bifurcating arborescences (Knuth 1968)

where s_i and r_i are the size of the region represented by the tree cell and the distance between the centre of that cell and the displacement of the centre of that cell from the particle we wish to calculate a force on. If $\theta_i < \theta$, where θ is some threshold value, we treat the whole cell as one point–mass, located at the centre of the cell. This necessitates a slight loss in accuracy compared to a direct sum, but moves the complexity of the calculation from $\mathcal{O}(N^2)$ to $\mathcal{O}(N \log N)$. We can then use a search algorithm on this tree to efficently find neighbours for a particle, given that we want to find all particles within $2h$ of the particle in question and a tree naturally sub–divides the computational domain in an efficient way.

sphNG is a hybrid parallel code. Many loops are parallelised using multiple threads with openMP, for example the loop required to calculate the hydrodynamical forces and assemble the momentum equation for each particle. In addition, it is possible to decompose the computational domain using MPI. When this is done, we effectively run multiple semi–independent S.P.H. calculations communicating information at the boundaries of each computational domain. This simplifies the implementation of a significant portion of the code: once the relevent information is obtained from other processes, the evaluation of many fluid properties can proceed in a similar manner for both an MPI and non–MPI calculation. Using MPI provides two additional advantages over merely using openMP: it reduces the size of the tree thereby speeding up tree traversal and generation and it allows C.P.U.s to be used without requiring shared memory like openMP. Since we principally perform parameter sweeps, we generally eschew using MPI, and instead run multiple smaller calculations simultaneously.

For a small number of test problems in chapter III we use the unoptimized testing code ndspmhd[25] written by D. Price to utilize the extensive library of test problems available for that code.

25. see http://users.monash.edu.au/~dprice/ndspmhd/ and (D. J. Price 2011a)

CHAPTER III

Pushing the Limits of Smoothed Particle Magnetohydrodynamics

καὶ σὲ γέρον τὸ πρὶν μὲν ἀκούομεν ὄλβιον εἶναι.

Book xxiv v. 543, Ἰλιάς, Homer (*ca.* 8th. century B.C.)

In chapter II we described how S.P.H. can be extended into the magnetohydroynamical regime and we alluded to certain instabilities which can arise from a simple conservative formulation of the momentum and induction equations. Fundamentally these arise because of the discrete nature of any computational fluid dynamics system compared to a continuous infinite fluid. Whilst both equations are affected by what amounts to a non–vanishing $\nabla^i B^i$ (which in this chapter we will often denote with the notation ϱ, *i.e.* as a magnetic charge density) the proximate cause differs for the two equations.

The momentum equation is susceptible to sensing a spurious numerical monopole term when the particle lattice becomes highly disordered. Obviously maintaining perfect lattice order is impossible for any non–trivial system of shocks and other complex flows, and consequently this term rapidly becomes a limitation on any calculation. Conversely, the induction equation is affected by a non-vanishing monopole term due to truncation errors — unlike the disorder related monopole terms, this issue is not unique to S.P.H..

In section III.1 we discuss how the numerical monopole term in the momentum equation affects calculations, and ways to mitigate it. However, we limit our discussion of how to deal with the numerical issues inherent in the induction equation to a brief analysis of the approach used in the calculations in the rest of this work, as this topic is more completely and comprehensively covered in Tricco and D. J. Price (2012) and Tricco, D. J. Price, and Bate (2016). We then discuss the now abandoned 'average h' method proposed in Lewis, Bate, and D. J. Price (2015) and why it was abandoned. However, although this novel approach proved a red–herring, it did lead to a comprehensive analysis of the effects of averaging in SPH. We discuss this in section III.3 since these conclusions will still be useful for S.P.H. methods which use an averaged smoothing length, rather than the self–consistent scheme discussed in sub–section II.1.1. Such schemes are still common in non–astrophysical uses of S.P.H., for example.

III.1 Limitations of SPMHD

Fundamentally, all numerical systems for solving fluid dynamics equations have limitations which exceed those exposed by nature alone. This is simply due to the discrete nature of any computational system. Intrinsically, it is numerically infeasible to calculate the motion of every molecule of fluid, down to accuracies limited only by quantum effects. The quality of subsequent approximation made — be that via grid cells, or via particles — is the ultimate limit on how well a physical process can be captured by the numerical scheme. These limits can have different impacts for different processes. A trivial example is the assumption that all gravitational masses are point masses: close to the surface of a celestial body this is clearly nonsensical, but even at moderate distances this approximation is so close to the 'correct' value as to make attempts to do much better pointless. Magnetohydrodynamics, however, presents substantially more difficult challenges. We alluded to these earlier in the description of our numerical method in chapter II, but fun-

damentally they all stem from the (observed) lack of magnetic monopoles in nature (*e.g.*, the experimental limits from the Tevatron experiment reported by K. A. Milton 2006), or equivalently, that

$$\oiint_{S^i} B^i \mathrm{d}A^i = 0 \tag{III.1}$$

$$\nabla^i B^i = 0 \tag{III.2}$$

everywhere, at all length scales, and at all times. If this were present as a constraint in the equations of S.P.M.H.D. then the issue would be eliminated. This is not the case for ideal MHD induction equation derived from the Maxwell–Faraday and Maxwell–Ampère laws and the momentum equation derived from the M.H.D. Lagrangian (*cf.* equation II.72). Alternative approaches do exist, however, where this is true. Fundamentally, these involve temporally evolving something other than the magnetic flux density field, B^i, and then transforming this into the B^i–field. By choosing, for example, the magnetic vector potential, A^i, this inherently satisfies the equations III.1 and III.2 constraint because

$$B^i = \epsilon^{ijk} \nabla^j A^k, \tag{III.3}$$

and by definition

$$\nabla^i F^i = \nabla^i \epsilon^{ijk} \nabla^j G^k = 0 \; \forall \; \left(F^i, G^i \right). \tag{III.4}$$

If such a method were stable, we would naively assume that this has fixed S.P.M.H.D.. However, as we discuss below the cause of the non–vanishing monopole terms in the induction and momentum equations are subtly different. As a result, merely fixing the induction equation is insufficient to fix all of M.H.D. in S.P.H.— and this is in addition to the substantial difficulties that a vector potential S.P.M.H.D. has posed to date, for example as discussed by D. J. Price (2010).

III.1.1 The Induction Equation

The direct induction approach to S.P.M.H.D. evolves either B^i/ρ or B^i in time via an induction equation, *viz.*

$$\mathrm{D}_t \frac{B^i}{\rho} = \left(\frac{B^j}{\rho} \nabla^j \right) v^i, \tag{III.5}$$

$$\mathrm{D}_t B^i = \left(B^j \nabla^j \right) v^i - B^i \left(\nabla^j v^j \right). \tag{III.6}$$

Nothing important turns on which method (mass– or volume–weighted) is used[1]. By inspection, it is obvious that both of these induction equations only guarantee that

$$\nabla^i \mathrm{D}_t B^i \equiv \mathrm{D}_t \nabla^i B^i = 0 \tag{III.7}$$

1. though see the discussion in the appendix to Hopkins and Raives (2016)

to the extent to which they maintain $\nabla^i B^i = 0$ anyway. In the continuum limit, with

$$\Delta t \rightarrow 0, \tag{III.8}$$

and

$$\Delta \left\{x, y, z\right\} \rightarrow 0, \tag{III.9}$$

this is not an issue: the magnetic field is always solenoidal there, so these two equations maintain that solenoidality for all time. In S.P.H., the mass–weighted induction equation is given by

$$\mathrm{D}_t \frac{B_a^i}{\rho_a} = -\sum_b^N \frac{m_b}{\Omega_a \rho_a^2} \left(v_a^i - v_b^i\right) B_a^j \nabla_a^j W_{ab}\left(h_a\right). \tag{III.10}$$

From this we see two things: firstly that this is an anti–symmetric S.P.H. operator and therefore somewhat de–sensitised to particle disorder and that this is a sum, not an integral. We ignore the numerical error caused by the $\nabla^j v^j$ operation which is suppressed by the choice of operator in favour of simply considering the trunction error of this operation. This provides a fundamental limit on how well we can maintain a solenoidal magnetic field, which is given by

$$\mathrm{D}_t \nabla^i B^i \geq \varepsilon, \tag{III.11}$$

where ε is a measure of this necessarily non–zero error due to truncation. In other words, the limit in equation III.8 is now

$$\Delta t \rightarrow \Delta t|_{\text{minimum}} > 0. \tag{III.12}$$

The question here is why is this so much worse for the magnetic field evolution compared to all other fluid properties, given that this is not a unique (or indeed unusual) limitation. The answer lies in the necessessity for the magnetic field to be *exactly* solenoidal — rather akin to how the velocity field in an incompressible fluid must be exactly solenoidal (Shao and Lo 2003). For other fluid parameters, *e.g.* the fluid pressure, this ε error manifests as a limit on overall accuracy. Once a magnetic field has developed a spurious 'magnetic charge density' the situation only deteroriates due to the coupling between the induction and momentum equations. The momentum equation — the rate of change of v^i — contains a B^i term, and *vice versa* the induction equation — the rate of change of B^i — depends on v^i. Therefore, any error will rapidly propagate. Inaccuracies due to the inherently finite nature of floating–point calculations will also have an effect, however, these are of a significantly smaller magnitude than the truncation error.

Methods of rectifying this problem essentially fall into three categories: ignore it (and hope the resulting error doesn't become too large), deal with, or avoid it. The former is clearly unfeasible for any large calculation, though can be used in smaller test problems. We need, however, some metric of 'divergence error' to do this (and, indeed, this is useful

more generally). A useful method is (D. J. Price 2012) to measure

$$\mathrm{Err}\,\nabla^i B^i \stackrel{\mathrm{def}}{=} h\left|\frac{\nabla^i B^i}{B^i}\right|, \tag{III.13}$$

which is essentially a measure of fractional divergence error. The second approach — dealing with it — involves using a scheme like that discussed in sub–section II.2.1 to dissipate the error into the surrounding field. Because the numerical errors which lead to a non–vanishing divergence in the induction equation are primarily not due to inaccuracies in the S.P.H. operation but instead due simply to the process of numerical integration, this is remarkably effective. Tricco, D. J. Price, and Bate (2016) provides a comprehensive discussion relating to this over many test problems.

Perhaps the ideal approach would be to instead re–formulate S.P.M.H.D. to evolve a different fluid parameter and then, as mentioned above, transform this into the B^i field as required. The vector potential is the obvious choice, and has been used reasonably extensively in Eulerian schemes for this purpose. The induction equation for the vector potential A^i is given by (in general)

$$\mathrm{D}_t A^i = v^j \nabla^i A^j + \nabla^i \phi, \tag{III.14}$$

where ϕ is some continously differentiable[2] scalar field. The need for this somewhat mysterious gauge term is due to the observation that since

$$B^i = \epsilon^{ijk}\nabla^j A^k, \tag{III.15}$$

and

$$\epsilon^{ijk}\nabla^j\nabla^k\phi \equiv 0, \tag{III.16}$$

there are always infinitely many A^i–fields which can produce the same B^i–field. The trivial choice, setting

$$\phi = 0, \tag{III.17}$$

(sometimes called the Weyl gauge[3]) illustrates why this is an issue. Nowhere in the induction equation for the vector potential does this appear as a constraint, save that initially the field is set such that $\phi = 0$. Consequently, any error caused by the discretisation of the equation when it is evolved will manifest as an uncontrolled growth of the gauge term, and a consequently incorrect B^i–field. $\phi = 0$ is obviously not the only possible gauge. In Lewis, Bate, and Tricco (2016) (also Tricco (*priv. comm.*)) we considered that Gauge, the

2. At least across the computational domain, but in principle everywhere

3. In honour of Herman Weyl who first proposed gauge theory in Weyl (1918).

Gallilean invariant gauge provided by

$$\phi = v^i A^i, \tag{III.18}$$

and the modified psuedo–Lorenz gauge,

$$\partial_t \phi = -c^2 \nabla^i A^i \tag{III.19}$$

proposed by Stasyszyn and Elstner (2015). The gauge provided by equation III.18 does have the desirable effect, as noted by D. J. Price (2010), of changing the vector potential induction equation from equation III.14 to

$$\mathrm{D}_t A^i = -A^j \nabla^i v^i. \tag{III.20}$$

However, we find the same problems as identified by D. J. Price (*ibid.*): this choice of gauge is actually more susceptible to numerical instabilities caused by the particle lattice becoming disordered. In contrast to this approach, the gauge given by equation III.19 supposes that the gauge constraint can be maintained in a similar to way to maintaining the solenoidal constraint in ordinary M.H.D.. In effect, we move the problem from keeping the B^i–field solenoidal to keeping the A^i–field so. As Tricco (*priv. comm.*) identified[4], this is only successful in the Orszag and Tang (1979) vortex problem if the particles do not move off the lattice in the z–direction. Once they do so, the spurious v_z generated rapidly produces an unphysical vector potential and hence an unphysical magnetic field.

On the assumption that the gauge constraint could be maintained, a second problem means that a useful vector potential form of S.P.M.H.D. is still a challenge. The Lorentz force is a function of B^i — which is a 'physical' field, unlike the vector *potential* field. Consequently we must convert from the vector potential to the magnetic field, either by taking a pair of first derivatives or by directly calculating the second derivative. In effect, in place of

$$\mathrm{D}_t v^i|_{\text{magnetic}} = \frac{1}{8\pi} \nabla^i \delta^{ij} B^2 - \frac{1}{4\pi} \nabla^i B^i B^j, \tag{III.21}$$

we need something like

$$\mathrm{D}_t v^i|_{\text{magnetic}} = \frac{1}{8\pi} \nabla^i \delta^{ij} \left(\epsilon^{klm} \nabla^l A^m \right)^2 - \frac{1}{4\pi} \nabla^i \epsilon^{ilm} \nabla^l A^m \epsilon^{jnp} \nabla^n A^p. \tag{III.22}$$

In the continuum, computing this as a pair of first derivatives or by directly determining the second derivative and then computing that is by definition identical. However, in a discretised system this is not true. Second derivatives in S.P.H. are notoriously prob-

4. which we summarise in Lewis, Bate, and Tricco (2016)

lematic and are generally avoided whereever possible[5] (Brookshaw 1994), so the obvious approach is to perform two first derivatives. Although we earlier neglected the effect of noise from S.P.H. operators in the ordinary induction equation, the process of taking an additional first derivative magnifies this effect. This is coupled with the observation that in the induction equation, the noise is due to the S.P.H. estimate of $\nabla^j v^j$, a term which is not required to be exactly fixed but instead is a property of the fluid. The gauge function, however, *is* required to be exact, otherwise a situation emerges where there is more than one 'possible' magnetic B^i–field corresponding to the vector potential A^i–field being evaluated. The fundamental issue, therefore is that we are using a noisy estimate for changing A^i into B^i, to then combining this with a noisy estimate of the rate of change of the velocity — and this velocity is then used to calculate A^i at the next timestep.

Consequently, the current state–of–the–art is to evolve the B^i–field directly and correct for discretisation related non–solenoidality using a cleaning scheme and not to use a more exotic approach.

III.1.2 The Momentum Equation

At the end of the previous sub–section, we noted in passing the form of the S.P.H. momentum equation incorporating just the M.H.D. terms. This is produced from the usual momentum equation, given by

$$\mathrm{D}_t v^i = \nabla^i \sigma^{ij}. \tag{III.23}$$

This can be separated into an isotropic component, containing the fluid and magnetic pressures, and an anisotropic component, containing the magnetic tension terms, such that

$$\mathrm{D}_t v^i = \nabla^i \sigma^{ij}|_{\mathrm{iso}} + \nabla^i \sigma^{ij}|_{\mathrm{ani}}, \tag{III.24}$$

where

$$\mathrm{D}_t v^i|_{\mathrm{ani}} = \nabla^i \sigma^{ij}|_{\mathrm{ani}} = \frac{1}{4\pi} \nabla^i B^i B^j. \tag{III.25}$$

Using the vector identity

$$\nabla^i F^i G^j \equiv F^i \nabla^i F^j + G^j \nabla^i F^i, \tag{III.26}$$

this can be written as

$$\mathrm{D}_t v^i|_{\mathrm{ani}} = B^i \nabla^i B^j + B^j \nabla^i B^i. \tag{III.27}$$

The second term, $B^j \nabla^i B^i$, obviously should be zero in a solenoidal field. If the field *is* solenoidal, then the anisotropic stress tensor and the isotropic tensor interact so that the component of the magnetic pressure *parallel* to the field lines is exactly cancelled by the tension component in that direction, causing the characteristic preferential motion parallel

5. Notwithstanding the inherent difficulty in determining just what the divergence of the outer product of two curls of a vector even *is*.

to the field. If not, then the error conversely manifests as an unphysical force parallel to the field lines. Since there is no support from the magnetic pressure here if this error exceeds the fluid pressure then the effect on a calculation will rapidly be disastrous.

In S.P.M.H.D., we could evolve the anisotropic momentum equation in time *via*

$$\mathrm{D}_t v_a^i|_{\mathrm{ani}} = \frac{1}{4\pi} \sum_b^N m_b \left(\frac{1}{\Omega_a} \frac{B_a^i B_a^j}{\rho_a^2} \nabla_a^j W_{ab}(h_a) + \frac{1}{\Omega_b} \frac{B_b^i B_b^j}{\rho_b^2} \nabla_a^j W_{ab}(h_b) \right), \tag{III.28}$$

which is simply the symmetric S.P.H. derivative operator applied to equation III.25. This force exactly conserves energy and momentum, being derived from the M.H.D. Lagrangian (hence the symmetric derivative). It is, however, correct only insofar as it correctly maintains a field free of numerical monopoles. The symmetric S.P.H. operator is sensitive to particle disorder to a much greater extent than the anti–symmetric operator used for the induction equation (as well as not being invariant to the addition of a constant term). The result of this is that an unphysical force parallel to the magnetic field lines develops, causing particles to attract and clump together. This instability only exists when the magnetic *attraction* caused by this spurious force exceeds the support provided by the hydrodynamic fluid pressure, *i.e.* when $\beta < 1$. When this happens, however, the effects are disastrous for the calculation. This is similar to the effect seen in solid–bodies called the tensile instability, and consequently the same name was adopted for it. In section II.3 we briefly discussed an attempt to correct for this instability. Here, we will expand on that (whilst also noting in passing the existence of a few alternate methods).

Equation III.27 can be imagined as

$$\mathrm{D}_t v^i|_{\mathrm{ani}} = B^j \nabla^j B^i + B^i \varrho, \tag{III.29}$$

where ϱ represents the magnetic charge density, a term which *should* be zero. However, any error in calculating $\mathrm{D}_t v^i|_{\mathrm{ani}}$ for an S.P.H. particle effectively manifests as a non–vanishing ϱ term. The fact the machine–epsilon is *prima facia* non–zero alone will provide a spurious monopole term here, however, the effect from particle disorder is much more marked. This effect was considered by Chaussonnet *et al.* (2015), albeit in a different numerical scheme, who found that the *antisymmetric* operators (G_- in their notation) were significantly more consistent on perturbed lattices than the *symmetric* operator (G_+) used here out of necessity due to our Lagrangian derivation. Given that the particle lattice will be, by definition, highly perturbed in any interesting regions of a large magnetohydrodynamical calculation a non–vanishing ϱ term is inevitable. Unhelpfully, this effect will then be scaled by B^i, *i.e.* the field strength, since stronger fields and disordered regions often coincide (recalling that v^i and B^i are effectively coupled).

In figure III.i we compare the advection of a circularly polarized Alfvén wave[6] using our usual cubic B–spline kernel (with a $2h$ compact support radius) with the quintic B-

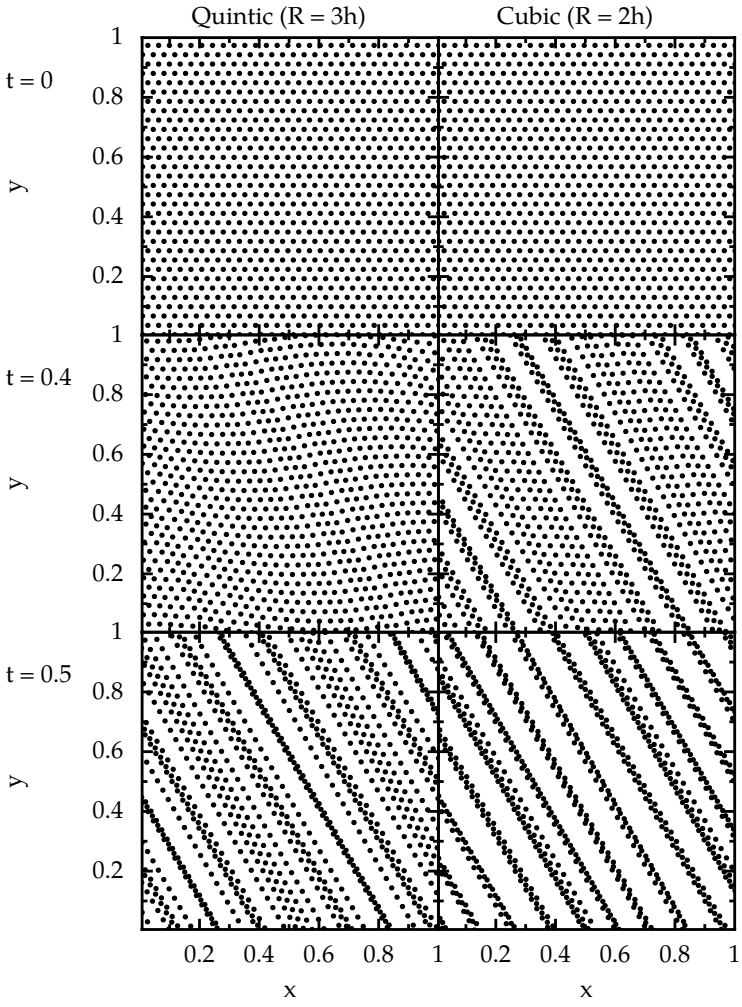

Figure III.i. Comparison of the failure of a circularly polarized Alfvén wave test between a cubic and quintic B–spline kernel. The cubic B–spline (left–hand column) fails due to the tensile instability more rapidly than the quintic B–spline (right–hand column) which has a larger compact support radius.

spline (where the radius is $3h$). In effect, the latter evaluates $\nabla^i B^i$ over a larger 'stencil' than the cubic. This larger interpolation region delays the inevitable catastrophic failure of the calculation by simply dividing the error out over a larger set of particles (or analogously, moving closer to the continuum limit, at least spatially). This provides a strong indication that the issues seen here are less a property of temporal discretisation error and more to do with the truncation of an infinite fluid of infinitesimal particles into a limited finite set of interpolation points. The wave in this test is an exact solution to the M.H.D. equations and therefore should propagate *ad infinitum*. That it fails so drastically, and so quickly, highlights a critical issue in S.P.M.H.D..

This observation, that the spurious monopole term is in effect a false 'negative pressure' term, led D. J. Price and Monaghan (2004a) to propose simply adding a short–range repulsive force to offset it. This is the first corrective term we will consider. Here, we would modify the stress–tensor to be

$$\sigma^{ij} = \sigma^{ij}|_{\text{iso}} + \sigma^{ij}|_{\text{ani}} + \sigma^{ij}|_{\text{rep}}, \tag{III.30}$$

where

$$\sigma^{ij}|_{\text{rep}} = -\mathcal{X}\frac{1}{8\pi}\left(\frac{B_a^i B_a^j}{\rho_a^2} + \frac{B_b^i B_b^j}{\rho_b^2}\right), \tag{III.31}$$

controlled by the $\mathcal{X}$ parameter, set according to something like

$$\mathcal{X} = -f\left(\frac{W_{ab}(h_a)}{W(\Delta\rho, h_a)}\right)^g. \tag{III.32}$$

The f and g are parameters to tune the the force strength, and $W(\Delta\rho, h_a)$ is the smoothing kernel with r set to the mean particle separation. Aside from being theoretically unsatisfying, this correction is also unsuitable for any situation involving varying smoothing lengths (although it does have the property that, being essentially pairwise, it does conserve energy and momentum). A problem emerges here in that it is hard to determine precisely what is 'short range' when $h_a \neq h_b$ (a problem which is amplified when $h_a \ll h_b$ and *vice versa*). Too much repulsion, obtained by taking the larger smoothing length, may well result in an unphysical distribution of the fluid; conversely too little maybe insufficient to suppress the attractive force provided by ϱ. Consequently this, and many related approaches which attempt to prevent numerical instabilities by holding the fluid up against the attractive monopole term, are unfeasible in compressible S.P.H.. At least in principle it may be possible to formulate a term of this nature for an incompressible magnetised fluid, although this is not a heavily studied field — S.P.H. is so naturally capable

6. As defined in Tóth (2000), the initial conditions are $\rho = 1$ and $p = 1/10$ throughout; with $v_\perp = B_\perp = 1/10 \sin 2\pi r_\parallel$, $v_\parallel = B_\parallel = 1$, and $v_z = B_z = 1/10$. The wave is then set to propagate in the x–y plane at $\theta = 30°$ with $r_\parallel = x\cos\theta + y\sin\theta$.

of handling highly compressible media that almost all work involving magnetised fluids in S.P.H. considers fluids which at a minimum moderately compressible.

An alternative method which has been used is to subtract a stress term from the entire S.P.M.H.D. calculation (originally proposed by Phillips and Monaghan 1985). In effect, we then evolve something that looks like (in the continuum)

$$\mathrm{D}_t v^i\big|_{\text{magnetic}} = \nabla^i \sigma^{ij} - \nabla^i B^2\big|_{\text{maximum}} . \tag{III.33}$$

The problem with this approach is the difficulty in determining a sensible $B^2|_{\text{maximum}}$. Even obtaining the actual maximal magnetic stress in the calculation requires an additional loop over all the particles (and an `MPI` reduction if necessary). It is also theoretically unsatisfying to suppress the field in this way. In some set ups, *i.e.* with strictly enforced boundary conditions, a natural value may emerge. This approach is an universal adjustment to the S.P.M.H.D. equations and is therefore *ipso facto* conservative and additionally will act to prevent the instability since it is impossible for any region of the calculation to emerge where the spurious attractive force is $> \nabla^i B^2\big|_{\text{maximum}}$ by definition.

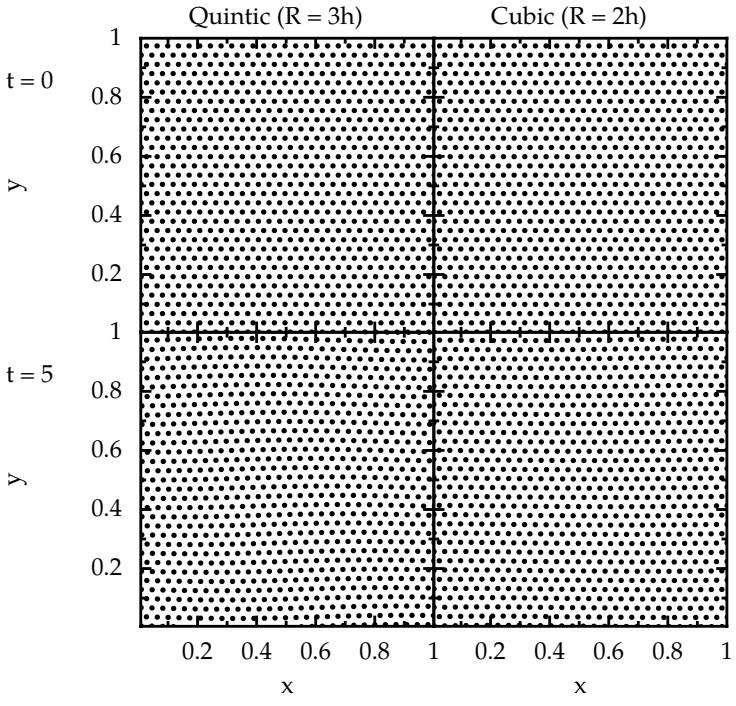

Figure III.ii. Advection of a circularly polarized Alfvén wave, with the source term correction, for both the cubic and quintic B–spline kernels. Unlike figure III.i, with the correction applied the wave propagates continually without error.

The logical progression from this is to take a different approach: instead of suppressing the effect of the force when it becomes fatal (*i.e.* at short ranges), can we eliminate the spurious force entirely. This led to two approaches, firstly the idea of computing the

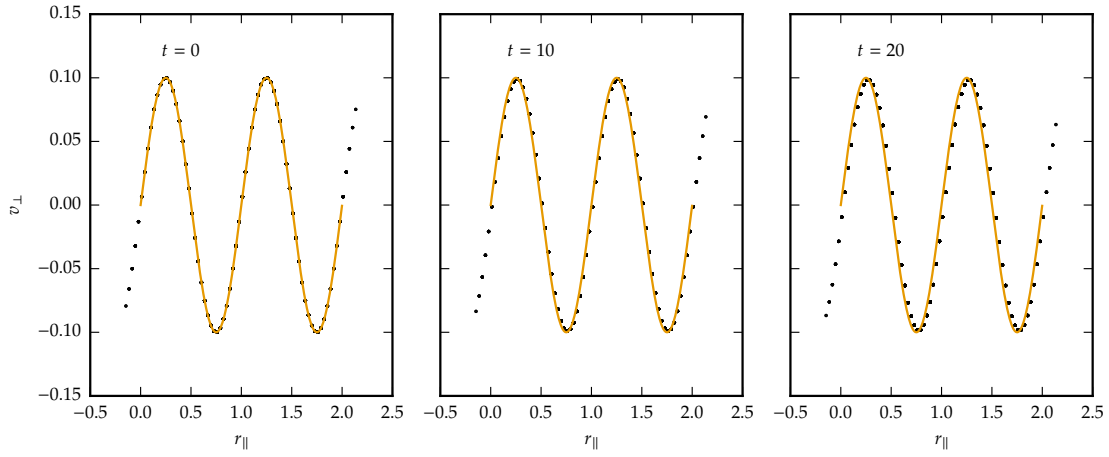

III.iii.a. $v_\perp$ as a function of $r_\parallel$

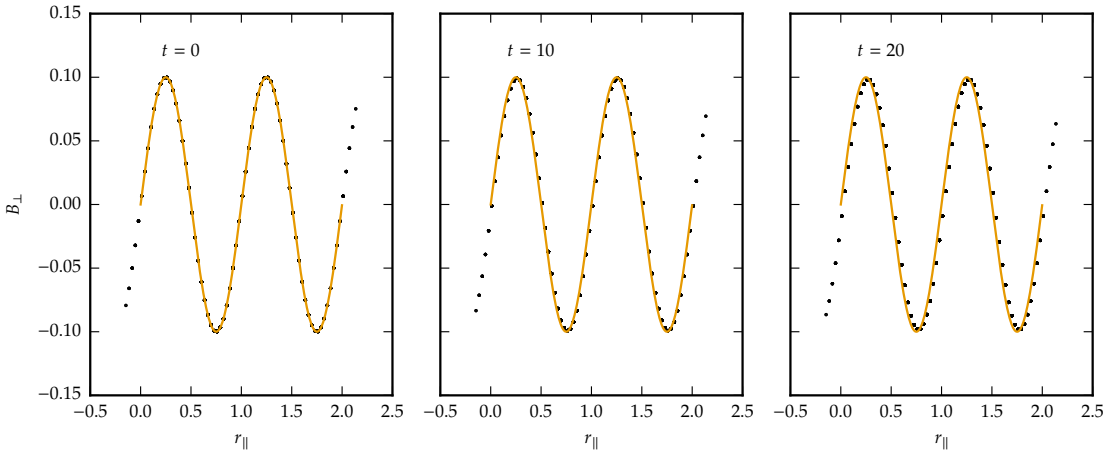

III.iii.b. $B_\perp$ as a function of $r_\parallel$

Figure III.iii. These two sub–figures compare the exact solution (orange line) of the circularly polarized Alfvén wave test shown in figure III.ii to the result obtained by our S.P.M.H.D. scheme with the source term correction applied (black dots). The appropriate co–ordinate transform has been applied so that $r_\parallel = x\cos\theta + y\sin\theta$ is the direction the Alfvén wave propagates, where $\theta = 30°$.

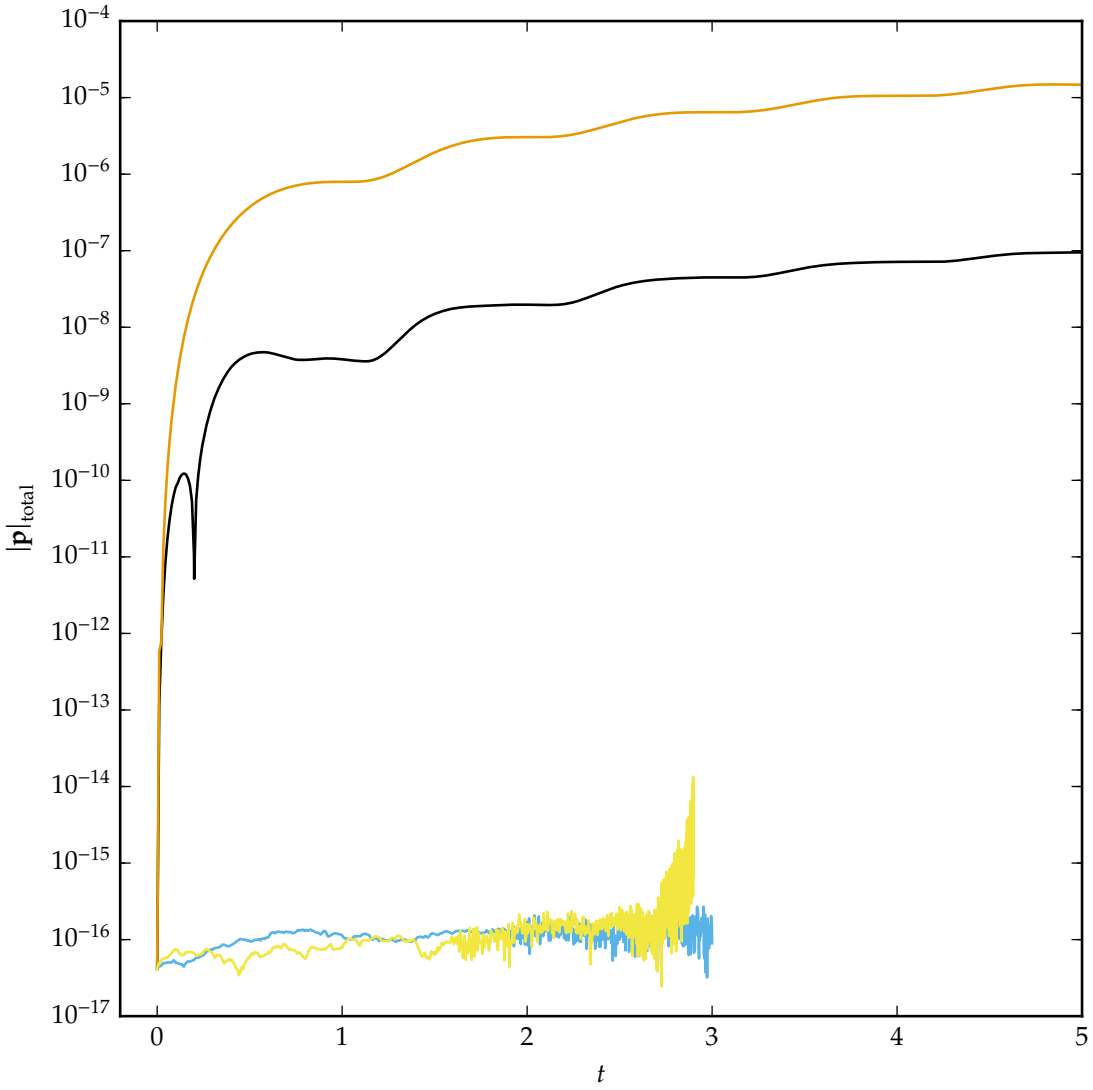

Figure III.iv. Temporal evolution of the total linear momentum for four circularly polarized Alfvén waves. The black and orange lines show the evolution for a quintic and cubic B–spline kernel with the source term correction applied, whilst the blue and yellow lines show the same kernels without the correction term. Although the particle lattice has collapsed (*vide* figure III.i *supra*) when the correction term is not applied, the calculation maintains momentum conservation to approximately machine precision. Conversely, although with the correction applied the lattice remains stable (figure III.ii *supra*) this comes at the cost of rapidly deteriorating momentum. We note that the cubic kernel, with the small support radius, exhibits a greater increase in momentum compared to the quintic.

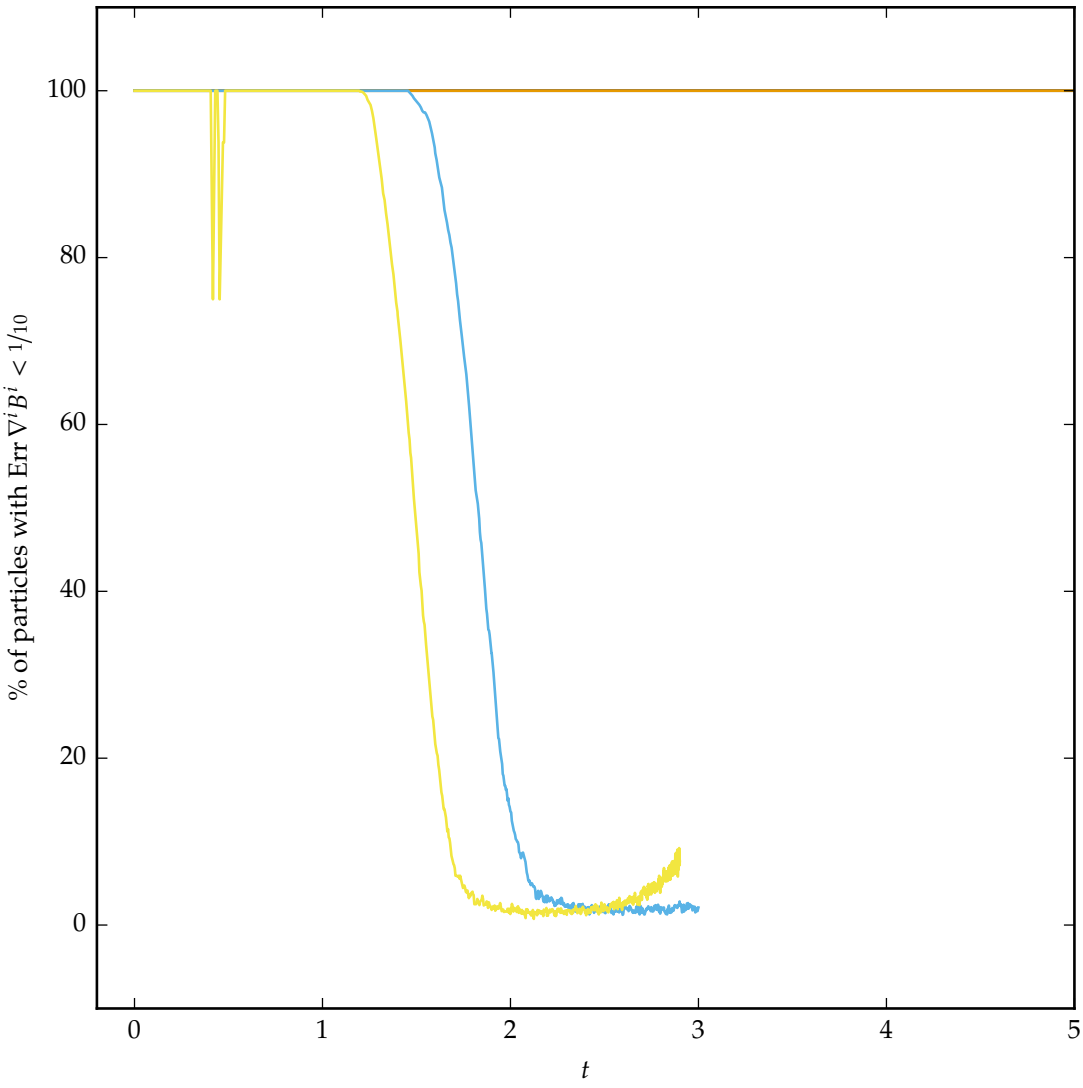

Figure III.v. Temporal evolution of the number of particles for which Err $\nabla^i B^i < 1/10$ for four circularly polarized Alfvén waves. The black and orange lines show the evolution for a quintic and cubic B–spline kernel with the source term correction applied, whilst the blue and yellow lines show the same kernels without the correction term. The two calculations with the source term correction applied maintain the solenoidal constraint, whilst the two unmodified calculations collapse and produce an unphysical field with a large monopole term.

troublesome anisotropic term (equation III.25) with an ostensibly more accurate operator Morris (1996), D. J. Price (2010), and D. J. Price and Monaghan (2005). In this, instead of taking the S.P.H. operator from the Langrangian to discretise equation III.25, one instead writes

$$\mathrm{D}_t v^i\big|_{\mathrm{ani}} = \frac{1}{4\pi}\sum_b^N m_b \frac{1}{\rho_a\rho_b}\left(B_b^i B_b^j - B_a^i B_a^j\right)\overline{\nabla^j W_{ab}}. \tag{III.34}$$

The principal issue with this approach is obvious: we now use what is effectively an anti–symmetric derivative operator to compute one part of the M.H.D. force, and a symmetric operator to compute another. Empirically (see, *inter alia*, D. J. Price 2010, 2012; D. J. Price and Monaghan 2005) this non–conservation of momentum rapidly builds up and renders this approach unusable for any non–trivial problem (*cf.* the application to shock tubes in D. J. Price 2004). That this approach is, momentum issues notwithstanding, resilient to the tensile instability, does highlight how the anti–symmetric derivative operators are insensitive to errors due to disorder in the particle lattice.

The issues discussed above led Børve, Omang, and Trulsen (2001) to propose a 'source term' correction to the momentum equation. In summary, the principle here to actually evolve

$$\mathrm{D}_t v^i|_{\mathrm{ani}} = B^j\nabla^j B^i + B^i\varrho - B^i\widetilde{\varrho}, \tag{III.35}$$

where the first two terms are obtained from evaluating $\nabla^i B^i B^j$ but the third term, $\widetilde{\varrho}$, is obtained from $\nabla^j B^j$ directly. Obviously in the continuum limit this will be correct, since there $\varrho \equiv \widetilde{\varrho} \equiv 0$. In a numerical scheme the effectiveness will be principally limited by how well $\widetilde{\varrho}$ approximated ϱ. However, an additional complexity arises: the $\nabla^j B^j$ operation is not pairwise on the S.P.H. particles — $\nabla_a^j B_a^j \neq \nabla_b^j B_b^j$. In terms of S.P.H. operations, this is written as

$$\begin{aligned}\mathrm{D}_t v_a^i|_{\mathrm{ani}} = &\sum_b^N m_b\left(\frac{B_a^i B_a^j}{\Omega_a\rho_a^2}\nabla_a^j W_{ab}(h_a) + \frac{B_b^i B_b^j}{\Omega_b\rho_b^2}\nabla_b^j W_{ab}(h_b)\right)\\ &- \chi B_a^i\sum_b^N m_b\left(\frac{B_a^j}{\Omega_a\rho_a^2}\nabla_a^j W_{ab}(h_a) + \frac{B_b^j}{\Omega_b\rho_b^2}\nabla_b^j W_{ab}(h_b)\right),\end{aligned} \tag{III.36}$$

or some equivalent construction, where χ is a scalar representing the degree of correction applied. Although the original proposal from Børve, Omang, and Trulsen (*ibid.*) was to set $\chi = 1/2$ to provide a 'minimum' of correction, subsequent experience has indicated that $\chi = 1$ is almost invariably needed for stability. As we discuss below there are good theoretical justifications for this observation.

If the particle disorder remains low, *i.e.* the particles remain roughly on their initial lattice, this correction is effective and the nominal loss of conservation properties is unimportant. For example, the calculation in figure III.i can be now run *ad infinitum*. Although we present the lattice at $t = 5$ in figure III.ii to demonstrate the stability compared

to figure III.i, in which the particle structure had completely broken down by $t = 1/2$, we have run the calculation to beyond $t = 50$ without issue. In figure III.iii we compare the evolution of this wave compared to the exact solution and obtain good agreement. However, in figure III.iv we show the change in total linear momentum for all four calculations, which demonstrates that the ostensibly correct approach (applying the source term correction) leads to a complete failure to conserve momentum. Here the linear momentum when the correction term is applied has increased by up to ten orders–of–magnitude (from 1×10^{-17}, effectively the machine ϵ, to $> 1 \times 10^{-7}$) and this deterioration is worse when the cubic B–spline kernel is used. Conversely, although the calculations without the source term correction fail to propagate the wave for any substantial period of time, the total momentum remains approximately equivalent to the machine ϵ. Figure III.v then shows the percentage of particles for which Err $\nabla^i B^i$ exceeds $1/10$. This is a measure of the monopole error, and show that none is present when the source term correction is applied. This is not a surprising result as the correction applied here keeps the particle lattice ordered and the numerical monopole term is sensitive to particle disorder.

These results demonstrate an interesting property concerning test problems in fluid dynamics (and particularly S.P.M.H.D.): being able to successfully evaluate a test problem is *necessary* but not *sufficient* for a stable and correct method. We will now demonstrate that in a real calculation, which necessarily has a highly disordered particle distribution, this the complete failure to conserve momentum identified above ultimately results in an unstable calculation.

Figure III.vi shows four protostellar collapse calculations just before (at $t = 1.00\, t_{\rm ff}$) and just after (at $t = 1.02\, t_{\rm ff}$) a hydrostatic core is formed (and a sink particle inserted) and also a further $1/50\, t_{\rm ff}$ later. The most obvious conclusion is the striking effect changing χ has on the calculation results: setting $\chi = 0$ or $\chi = 1/10$, *i.e.* disabling the correction, eliminates the jets but also produces clear artefacts in the density distribution — these appear on the projection plot as 'wave–like' structures, and analysis of the particle lattice indicates they are actually caused by clumping of S.P.H. particles. Conversely setting $\chi = 1/2$ or $\chi = 1$ maintains the jets, but then causes the sink particle to 'wander' out of the pseudo–disc as the momentum conservation errors build up. Additionally we note the troubling conclusion that jet velocity and χ appear to correlate. Figure III.vii shows an intriguing effect of tensile pairing as opposed to the pairing instability caused by a stretched kernel. Errors in the density distribution caused by a failure of the M.H.D. method do not affect the underlying operation of the S.P.H. kernel. This is not necessarily surprising: although the tensile instability will cause particle lattice to clump, it does not fundamentally interfere with the operation of the self–consistent smoothing length scheme. Consequently, although regions of spurious high density are formed, these are then given correct h values. This prevents an analysis of the q parameter being used to detect the tensile instability, and also provides a further reason why S.P.M.H.D. remains fully conservative even as the particle lattice is being obliterated.

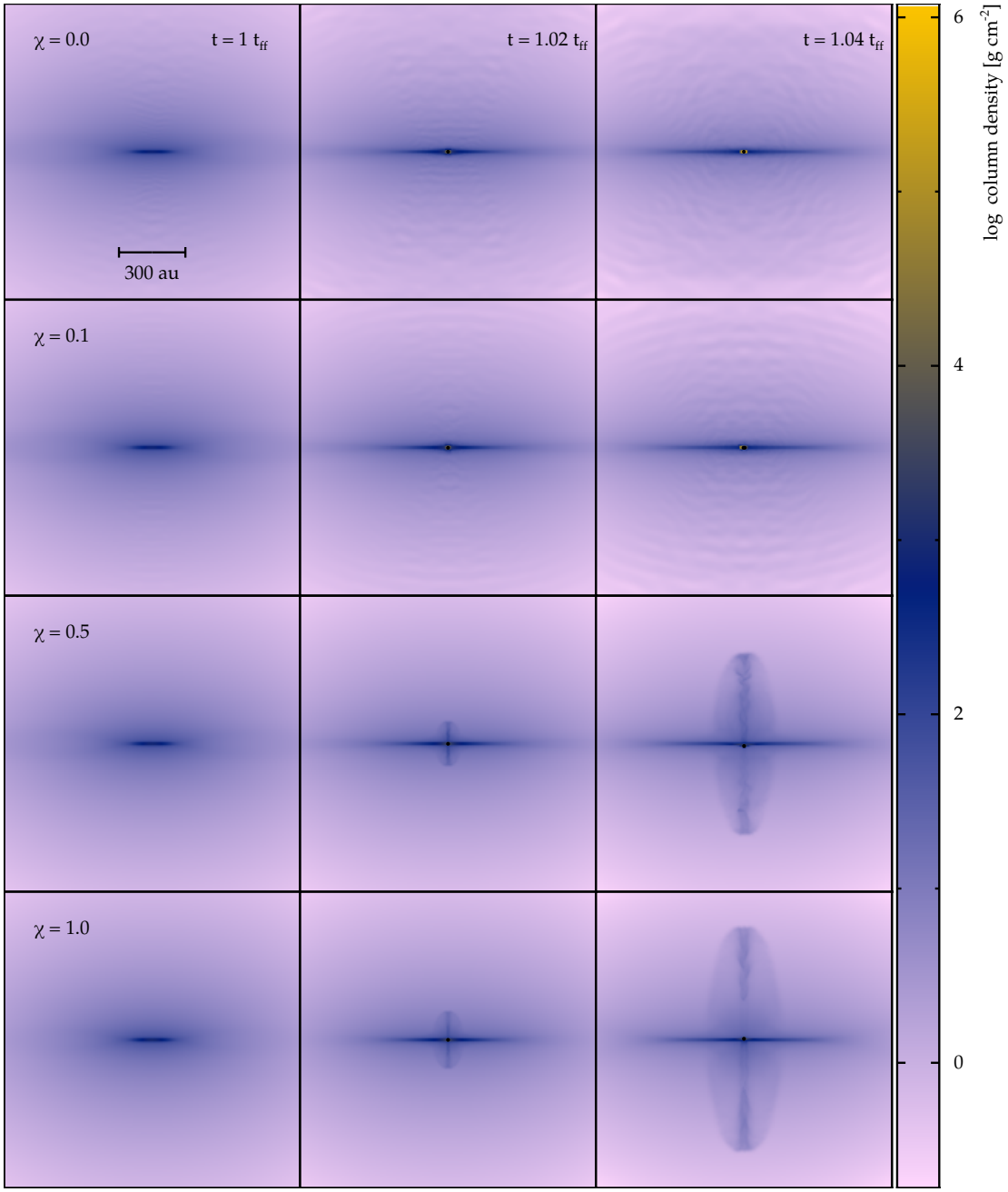

Figure III.vi. Column density rojections in the y–direction for $\chi = 0$, $1/10$, $1/2$, and 1 (down the page) at $t = 1.00\,t_{\rm ff}$, $1.02\,t_{\rm ff}$, and $1.04\,t_{\rm ff}$. The lowest values of χ, which are effectively an unmodified scheme, exhibit errors in the density distribution (which appear as 'waves' on the projection) but no sink particle wandering. Higher values ($\chi \geq 1/2$) no longer display density errors but do cause the sink particle to wander.

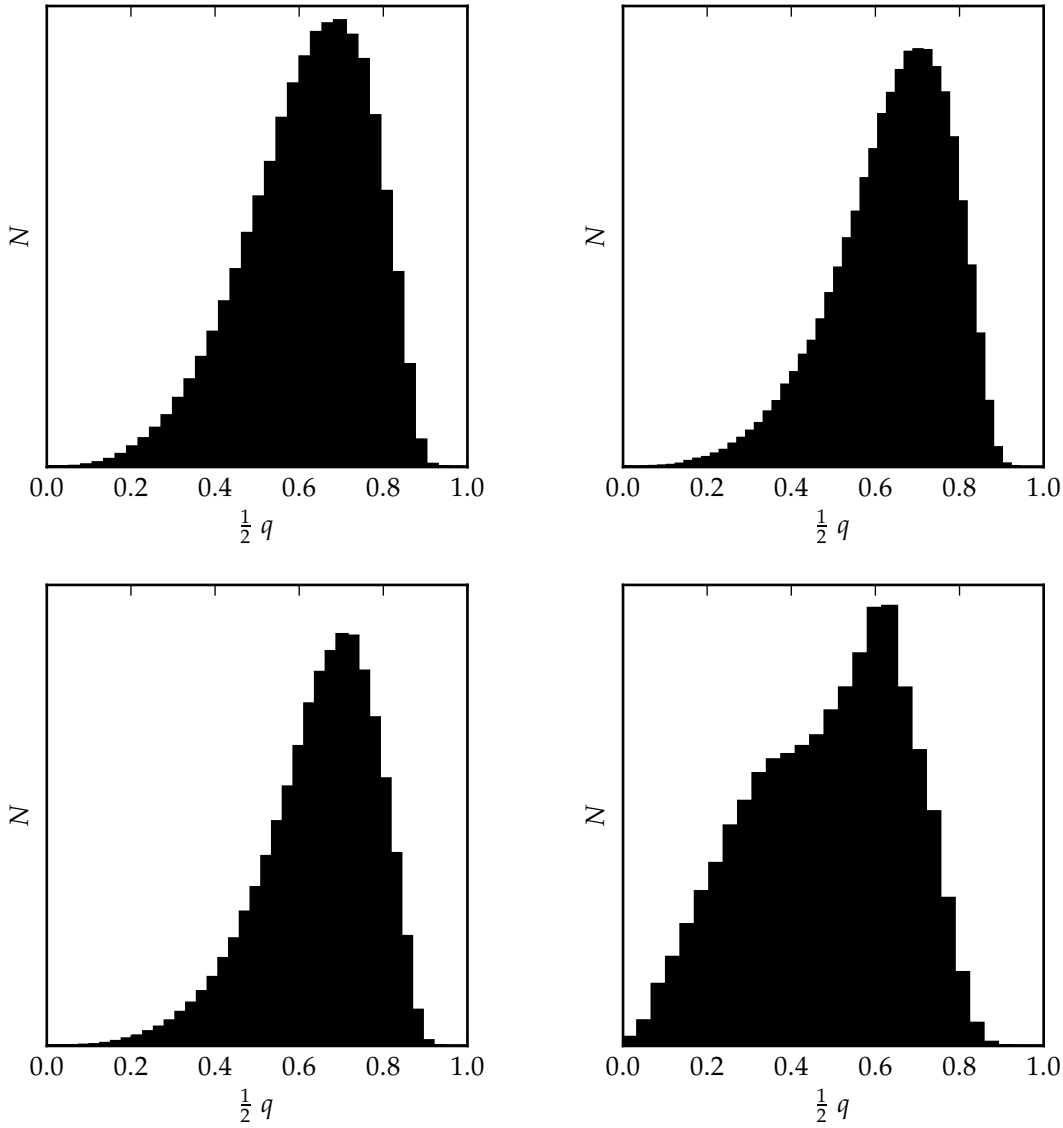

Figure III.vii. Histograms of q (see equation II.15) for $\chi = 0$ and $\chi = 1/2$ (upper row) and $\chi = 1$ (left hand side of the lower row) contrasted with a comparable calculation with a deliberately stretched kernel (with $\eta = 2 \gg 1.2$). We note that although figure III.vi shows clear density errors when $\chi < 1/2$, this does not cause a change in the underlying operation of the S.P.H. interpolations in the way stretching the kernel does.

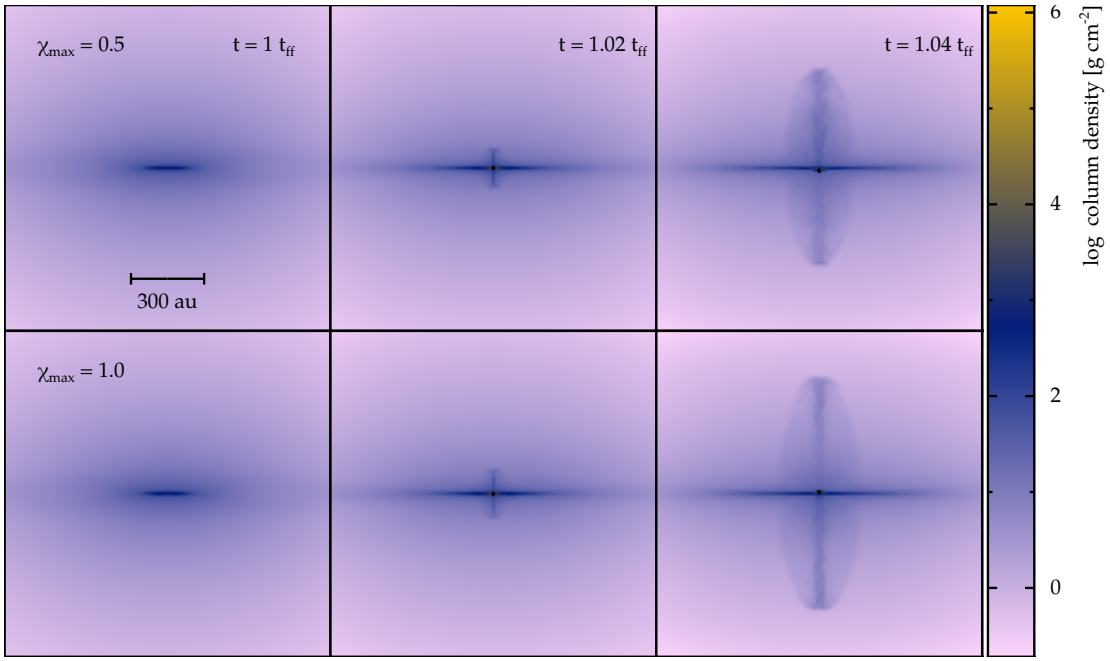

Figure III.viii. Column density rojections in the y–direction for $\chi_{\max} = 1/2$,and 1 (down the page) at $t = 1.00\, t_{\rm ff}$, $1.02\, t_{\rm ff}$, and $1.04\, t_{\rm ff}$. Both these calculations use the variable χ scheme detailed in equation III.37. No substantial differences are seen with these schemes compared to a constant fixed χ, *cf.* figure III.vi.

Figure III.viii shows the effect of adopting a variable χ 'switch'. Here we have used a naïve switch, where simply

$$\chi_a = \text{MIN}\left(\chi_{\max}\left[1 - \beta\right], 0\right), \tag{III.37}$$

with $\chi_{\max} = 1$. The idea behind this was to reduce the effect of non–conservation of momentum on the calculation by only applying a correction when needed. Demonstrably this doesn't actually improve the situation much, though we note that D. J. Price *et al.* (2017) and Wurster, D. J. Price, and Bate (2016) report some limited success with a slightly more nuanced switch. In some sense, this is not entirely surprising: the very region with the highest degree of particle disorder, coupled with a strong B^i–field is the same region with $\beta \ll 1$. Consequently this switch does very little to actually improve the conservation properties of the method in the region of interest. This point is echoed by figure III.ix, where we see that the deteroration in linear momentum conservation with variable χ approach is comparable to the fixed $\chi = 1$ calculation (the order–of–magnitude lesser deterioration in the linear momentum for $\chi \leq 1/10$ is a product of the sink particle's large mass causing small issues with the tree–gravity code and is directly comparable to that seen in purely hydrodynamic calculations). We have a quandary: we either have an ostensibly correct (until $t \approx 1.01 - 1.02\, t_{\rm ff}$) M.H.D. method, or a demonstrably incorrect yet conservative one. A related question, however, is why this is such an issue in this

calculation but not in the Alfvén wave test problem discussed earlier.

To analyse this, we consider the S.P.H. error terms mentioned in chapter II. Taking a Taylor expansion of the symmetric S.P.H. derivative operator we obtain a term of the form

$$\text{Err } \nabla_a^i F_a^j = \rho_a F_a^j \sum_b^N \left(\frac{1}{\rho_a^2} + \frac{1}{\rho_a^2} \right) \nabla_a^i W_{ab}(h_a) + \mathscr{O}(h^2), \tag{III.38}$$

assuming, for simplicity, fixed smoothing lengths so that $h_a = h \; \forall a \in N$ (and consequently $\Omega_a = 1 \; \forall a$). Comparing this to the S.P.H. operator for the magnetic divergence (the magnetic charge density),

$$\widetilde{\varrho_a} = \sum_b^N m_b \left(\frac{B_a^i}{\rho_a^2} + \frac{B_b^i}{\rho_b^2} \right) \nabla_a^i W_{ab}(h_a), \tag{III.39}$$

allows us to make an interesting observation. Ignoring for a moment that the B^i–field is not spatially constant, *i.e.* if $B_a^i = B^i \; \forall a \in N$, this term becomes

$$\widetilde{\varrho_a} = B_a^i \sum_b^N m_b \left(\frac{1}{\rho_a^2} + \frac{1}{\rho_b^2} \right) \nabla_a^i W_{ab}(h_a). \tag{III.40}$$

On its own, this is the correct symmetric S.P.H. operator for a spatially constant smoothing length and magnetic field. However, we instead *subtract* this term off of the S.P.H. momentum equation, an action which is clearly (factors of ρ aside) equivalent to trying to eliminate the first–order error from the S.P.H. symmetric derivative. This is an action which is ordinarily excluded for three important reasons: that the symmetric and anti–symmetric derivatives must remain exactly conjugate, that this first order error allows the particle lattice to reorder into a low energy state (D. J. Price 2012), and most importantly that the symmetric operator derived from the Lagrangian must not be modified (otherwise we no longer have S.P.H. from a Lagrangian).

This highlights an inevitable problem — even if we can obtain $\widetilde{\varrho}$ to accurately represent ϱ, subtracting this term from the momentum equation will lead to a loss of conservation proportional to $\nabla_a^i W_{ab}(h_a)$ (which is what we observed in figure III.iv). As it happens, it is probable that in any case we would incorrectly estimate the numerical monopole term due to the inherent noise in this S.P.H. operation. It is also this conclusion which illustrates why setting $\chi = 1$ appears to produce empirically superior results — until the momentum conservation failures take over, and we leave the regime where the monopole term is kept in check by the lattice order, *i.e.* when $\text{Err } \nabla^i B^i < 0$ as we saw for the Alfvén wave test *supra*. $\chi = 1/2$ is effectively equivalent to setting $\widetilde{\varrho} = 1/2\varrho$ which would be imperfect even if the momentum related issues could be overcome. Indeed, this point is echoed by comparing figure III.ix with figure III.iv: the former begins at about 1×10^{-7}, comparable to the values obtained at $t > 1$ in the latter. Then, when a sink particle is inserted and

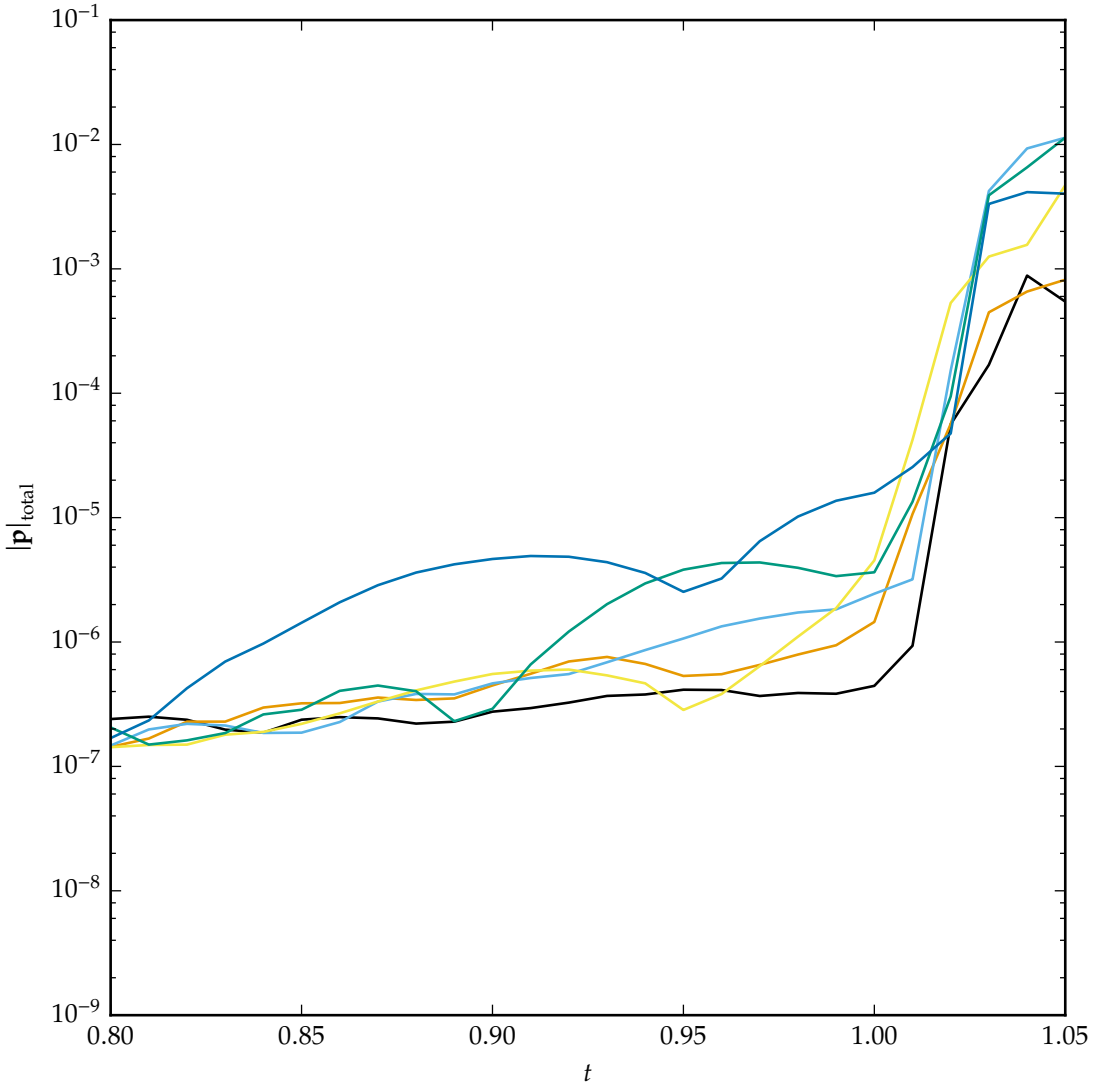

Figure III.ix. Total linear momentum plotted against free–fall time for all six fixed and variable χ schemes, *viz.* fixed $\chi = 0$ (black), $1/10$ (orange), $1/2$ (sky–blue), 1 (yellow), and variable χ with $\chi_{\max} = 1/2$ (turquoise) and 1 (blue). The schemes with $\chi < 1/2$ exhibit approximately an order–of–magnitude better momentum conservation than other schemes, in addition no significant improvement is observed switching from a fixed χ to a variable χ scheme. We also note that there is a general preference, even before $t = 1.00\, t_{\text{ff}}$, for the $\chi = 0$ scheme to exhibit superior momentum conservation.

the central region becomes even more complicated and disordered (notwithstanding the inveitable growth in the magnetic field at the same time) the linear momentum increases *again* by four or five orders of magnitude. Essentially the calculations remains stable as long as the particle distribution is approximately regular, once this is no longer true the momentum conservation errors cause the sink particle to be ejected.

No obvious solution to this conundrum exists. One approach we have considered, with reasonable success, is to try and 'rig' the particle lattice to be more ordered. The problem with beginning with a uniform density sphere is that the arrangement of S.P.H. particles necessarily becomes extremely disordered as the sphere collapses, notwithstanding the effects of rotation, magnetised outflows, or anything else. If we instead begin with a Bonnor–Ebert sphere, which is in effect a partially collapsed uniform sphere, we may be able to reduce the deterioration in the lattice and therefore extract a longer evolution from the calculation[7]. Inevitably the momentum conservation issues will catch up with us but we will have followed a collapse to a later evolutionary epoch before they do.

We now consider this is some more detail. One way to do this is to take one of our calculations of a collapsing molecular cloud core and compare the evolution of a calculation with an ordered particle lattice to a disordered one. We omit the discussion of the initial conditions here, except to note that modifications to the lattice aside we do not adjust any other parameters. This is a similar approach to that taken above when discussing the χ parameter (and the non–perturbed calculation is identical to the $\chi = 1$ calculation above).

Figure III.x shows a column density projection of a calculation with an initially ordered cubic lattice compared to calculations where the initial lattice has been perturbed. This perturbation is achieved by displacing each S.P.H. particle in a direction and magnitude obtained from a pseudo–random number generator, with the maximum displacement limited to $1/10$, $1/5$ and $1/2$ of the initial value of $\Delta\rho$, $\left(\Delta\rho\right)_0$ (the particle separation). In this way, the average density, *etc.*, on scales larger than an individual particle smoothing length remains approximately unchanged. The initial particle spacing is $\Delta\rho = 5.61 \times 10^{14}$ cm, so this corresponds to perturbing the particles by up to 5.61×10^{13} cm, 1.12×10^{14} cm, and 2.81×10^{14} cm respectively. In all the calculations the sink particle has drifted or 'wandered' out of the pseudo–disc. This is the characteristic failure mode discussed earlier. A slight increase in the distance the sink particle moves in $1/100\, t_{\rm ff}$ can just about be determined. More quantitatively, in figure III.xii we plot the 'normalised z–axis sink particle displacement'[8] against the 'normalised time'[9]. Here we see that the perturbed

7. Additionally, approaches like setting a stiffer equation of state, or using radiative transfer to transport heat energy through the lattice providing additional fluid pressure, seem to provide a small degree of additional lattice order.

8. *i.e.* the magnitude of the displacement of the sink particle compared to the initial formation location

9. more obviously, the time since sink particle insertion

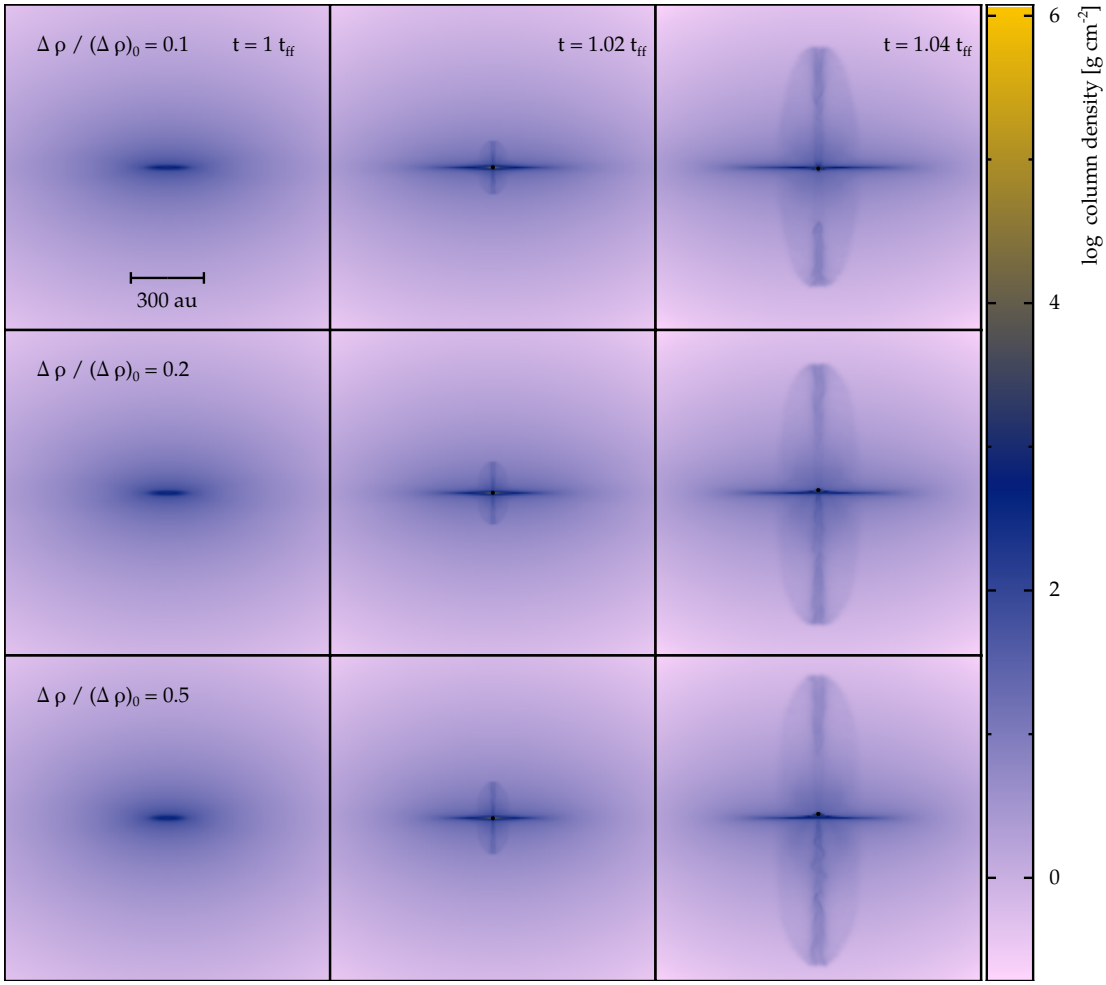

Figure III.x. Column density projections in the y–direction lattices perturbed by $^{\Delta\rho}/_{(\Delta\rho)_o} = {}^1/_{10}$, $^1/_5$, and $^1/_2$ with an initial magnetic field of $\mu = 5$. These can be compared to the unperturbed lattice in figure III.vi, and we note that the lower row shows a slight increase in the distance the sink particle has wandered compared to lesser degrees of perturbation.

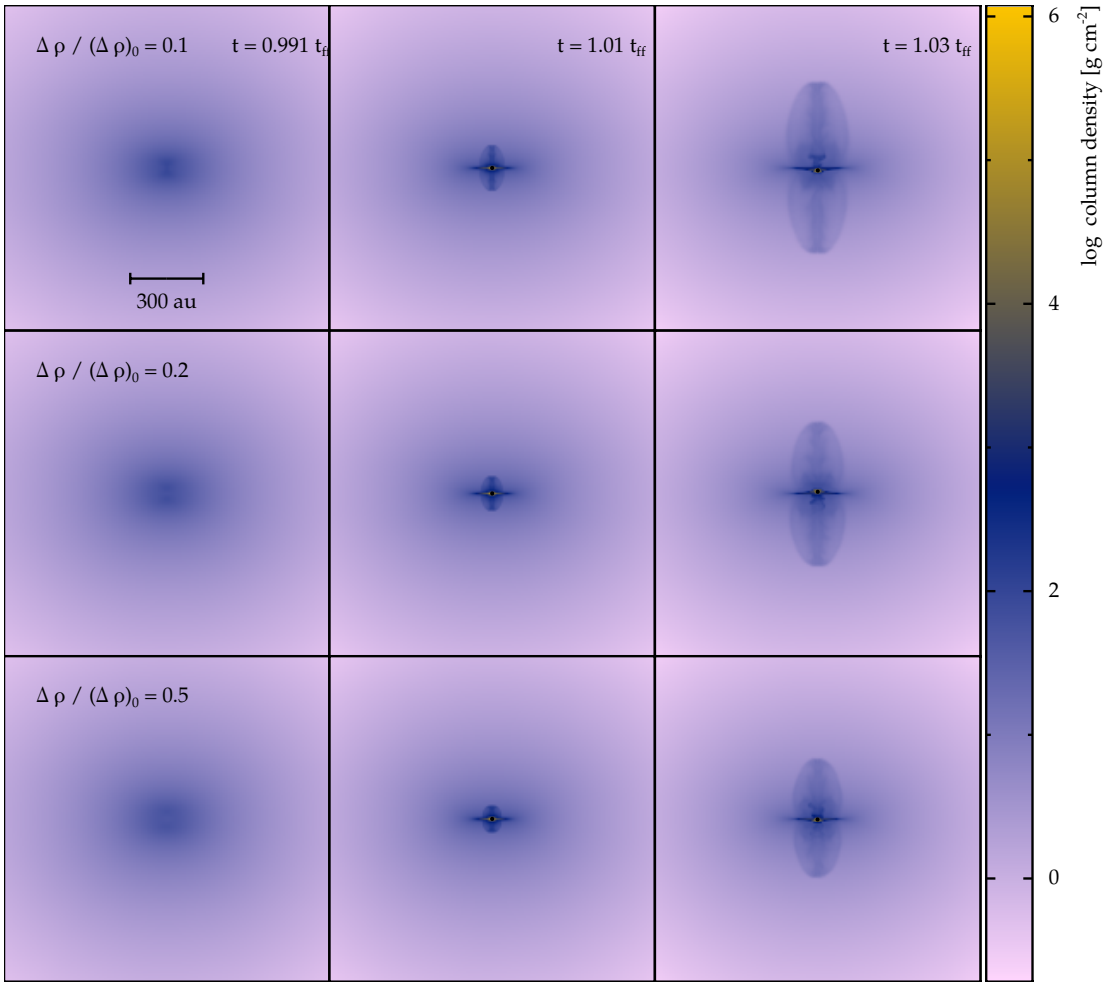

Figure III.xi. Column density projections in the y–direction lattices perturbed by $\Delta\rho/(\Delta\rho)_o = 1/10$, $1/5$, and $1/2$ with an initial magnetic field of $\mu = 10$, $1/2$ the magnitude of the field used in figure III.x. Due to the consequent reduction in magnetic pressure these calculations are shown $1/100\, t_{ff}$ earlier. These can again be compared to the unperturbed lattice in figure III.vi, and we again note that the lower row shows a slight increase in the distance the sink particle has wandered compared to lesser degrees of perturbation.

lattices — except for the first perturbed configuration – do indeed result in an increase in sink drift, indicating a link between particle disorder and momentum error. That this is apparently a small effect is unsurprising: most of the perturbation applies to particles well removed from the central region which is unstable. This point is echoed by a consideration of the total linear momentum in the system, where we see in sub–figure III.xiii.a that before $t = 1.00t_{\rm ff}$, when the mean density of the calculation is still close to the initial density, the perturbed lattices all have clearly elevated linear momenta; albeit orders–of–magnitude lower than that which occurs after a sink particle is inserted. Even so, the total momentum when the calculation begins to fail is still elevated. In addition, sub–figure III.xiii.b we show the total energy for all the calculations. We again find that the perturbed calculations are less conservative, and that this effect is (broadly speaking) proportional to the degree of disorder. This corroborates the analytical analysis above and demonstrates how particle disorder inexorably leads to poor momentum conservation and ultimately to an unstable M.H.D. calculation.

III.2 The 'average h' method

> That quite definitely is the answer. I think the problem, to be quite honest with you, is that you've never actually known what the question is.
>
> Chapter 28, The Hitchhiker's Guide to the Galaxy, Douglas Adams (1979)

The limitations of the state–of–the–art S.P.M.H.D. method discussion in section II.2 coupled with a bug in the integrator in sphNG led to disastrous results — and ultimately unnecessary efforts to prevent these. This bug was introduced in the mid–2000s when the direct induction S.P.M.H.D. method was first added to sphNG, where the RK1(2) integrator used was not correctly applied to the induction equation. The bug did not affect the D. J. Price and Bate (2007, 2008, 2009) calculations all of which used an Euler (1769) potential method (see, *inter alia*, Rosswog and D. J. Price 2007), but it did affect D. J. Price, Tricco, and Bate (2012). The bug remained unresolved until late mid–2015, for example Bate, Tricco, and D. J. Price (2014) and Lewis, Bate, and D. J. Price (2015) are both affected by the bug. Work subsequent to Lewis, Bate, and D. J. Price (*ibid.*), as detailed in Lewis, Bate, and D. J. Price (2017), including Lewis and Bate (2017) is not affected. Before being identified as a defect in the code itself, it was incorrectly assumed that the erroneous results caused by this bug were actually a defect in the S.P.M.H.D. method[10]. Consequently many approaches were proposed to adjust the S.P.M.H.D. method to mitigate the issues.

Early work focussed on accentuating the divergence cleaning method by two means: 'overcleaning' and sub–cycling the cleaning wave. The latter — and the difficulty in using it with individual time steps — is discussed more fully in Tricco (2015). Overcleaning

10. given how many other difficulties S.P.M.H.D. has thrown up, this was not an unreasonable assumption.

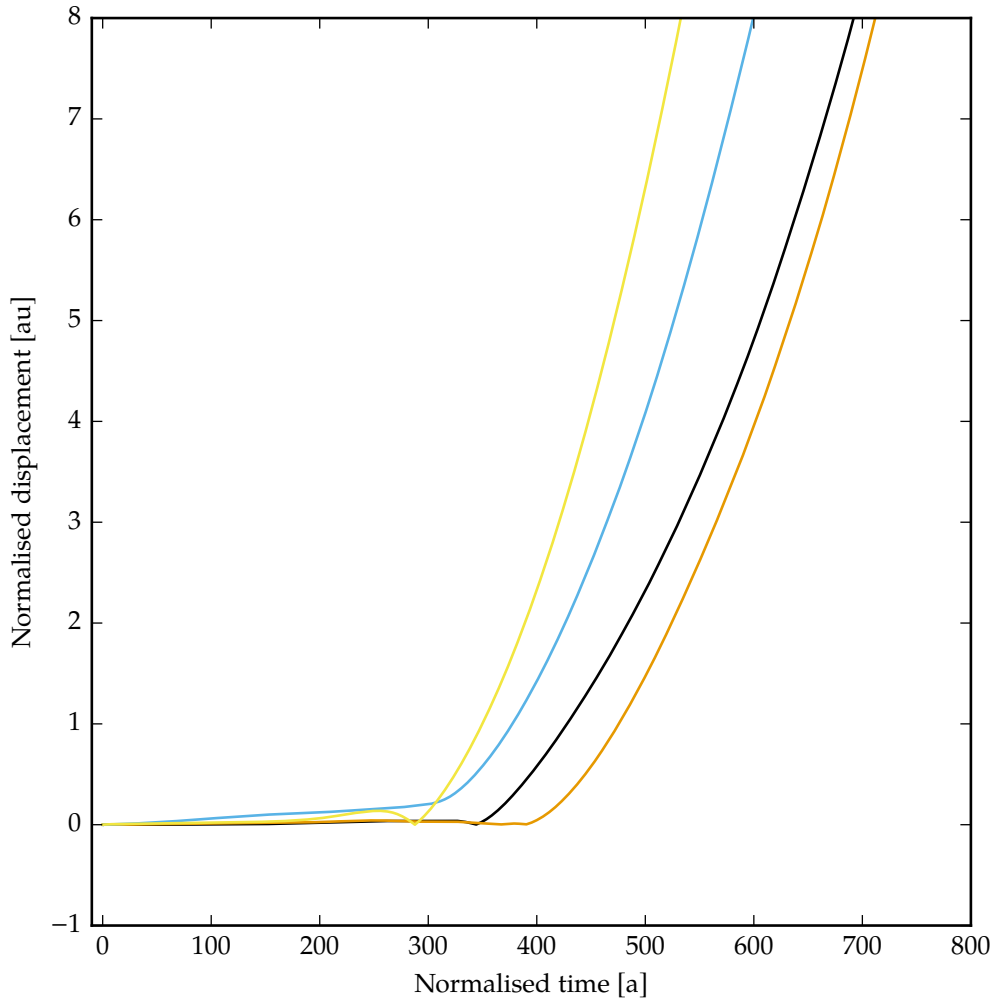

Figure III.xii. Plot of normalised sink particle displacement for one unperturbed (black) and three perturbed uniform lattices with $^{\Delta\rho}/_{(\Delta\rho)_0} = {}^{1}/_{10}$ (orange), $^{1}/_{5}$ (sky–blue), and $^{1}/_{2}$ (yellow). Aside from the first perturbed lattice, which wanders slightly later but with a comparable gradient to the unperturbed configuration, the amount of sink particle drift and lattice perturbation are correlated.

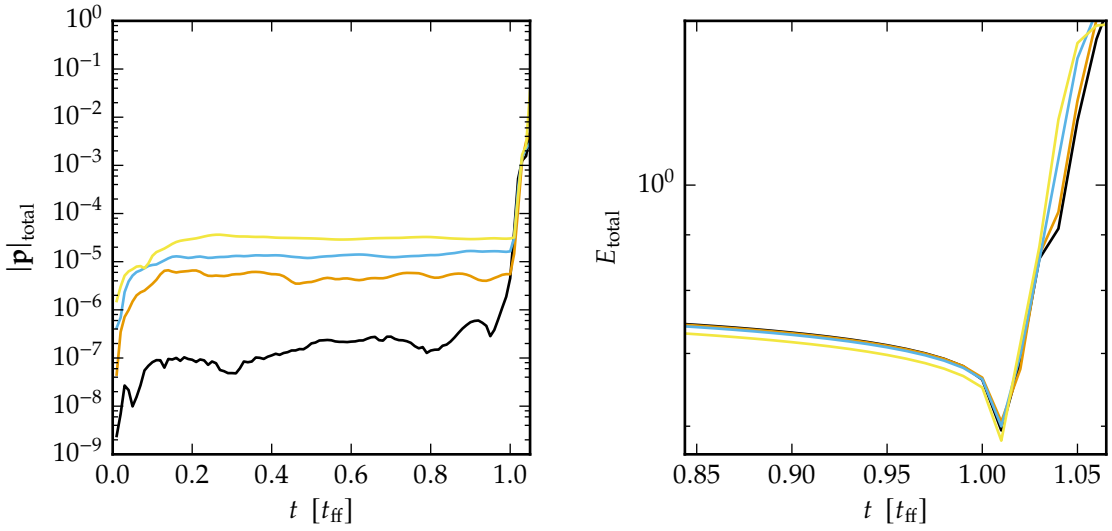

III.xiii.a. Total linear momentum

III.xiii.b. Total energy

Figure III.xiii. Evolution of linear momentum (sub–figure III.xiii.a) and total energy (sub–figure III.xiii.b) for an unperturbed (black) and three perturbed uniform lattices with ${}^{\Delta\rho}/_{(\Delta\rho)_{\text{o}}} = {}^{1}/_{10}$ (orange), ${}^{1}/_{5}$ (sky–blue), and ${}^{1}/_{2}$ (yellow). The perturbed lattices exhibit a generally elevated linear momentum before $t = 1.00\, t_{\text{ff}}$ and a slight trend towards elevated total momentum after. A similar relationship is seen for total energy.

is a simpler process whereby the cleaning wave speed, c_c in equations II.80 and II.81, is multiplied by some positive scalar, *i.e.*

$$c_{\text{c}} = f_{\text{oc}} c_{\text{c,o}}. \tag{III.41}$$

At the time the instabilities seen were attributed to the use of a sink particle and the way this caused a numerically incorrect 'hole' in the magnetic field distribution, and hence increasing the rate or effectiveness of the divergence cleaning method to suppress this.

The inability of this technique to completely stabilise calculations then led to idea that the instability was instead caused by the combined effect of the variable smoothing length regime, the way particle neighbour counts varied in steep density gradients, and an asymmetry in the S.P.M.H.D. equations caused by the source–term correction. A common misconception about the self-consistent variable smoothing length formalism of D. J. Price and Monaghan (2004b) is that it guarantees a fixed neighbour count — in effect that $N_{\text{ngh}} = 53$ at all times for the cubic B–spline. In reality, the η parameter in equation II.34 actually ensures that the average number of neighbours will be this value: in practice the neighbour count for an individual particle can vary between four and over a hundred provided that the average is maintained. In the presence of a *very* steep gradient in the fluid density, for example at the centre of one of our protostellar collapse calculations, we observed that it was possible for a particle a at the top of the gradient to have a smoothing length h_a

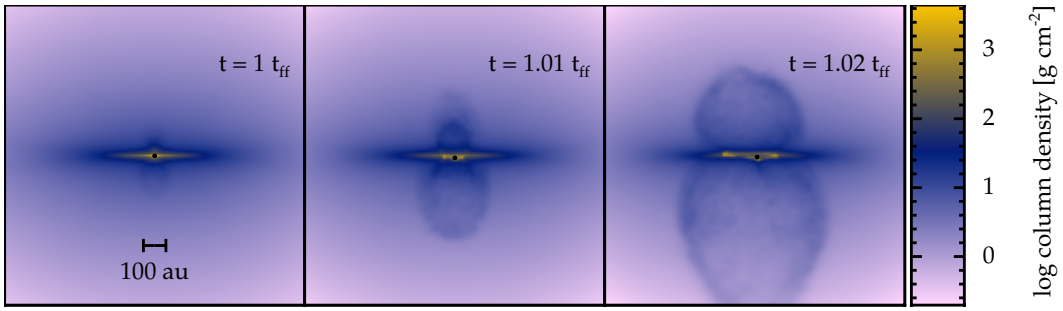

Figure III.xiv. Column density projections from $t = 1.00\,t_{\rm ff}$–$1.02\,t_{\rm ff}$ of a collapsing molecular cloud core as the integrator bug causes a catastrophic explosion. Fluid velocities within the explosion can easily exceed $40\,{\rm km}\cdot{\rm s}^{-1}$ compared to the typical velocities seen in a protostellar collapse calculations of $10\,{\rm km}\cdot{\rm s}^{-1}$.

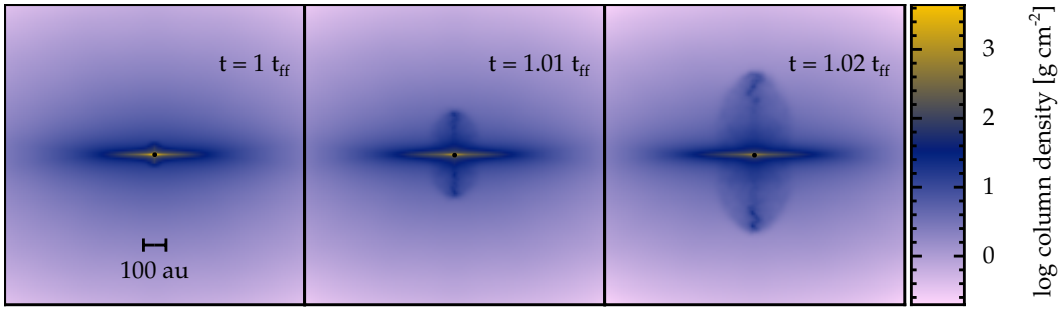

Figure III.xv. Column density projections from $t = 1.00\,t_{\rm ff}$–$1.02\,t_{\rm ff}$ of a collapsing molecular cloud core, with identical initial conditions to figure III.xiv using the 'average h' scheme but still with a defective integrator. The fluid velocity within the outflow is now consistently $< 10\,{\rm km}\cdot{\rm s}^{-1}$.

so small that it could not 'see' the bottom of the gradient; and that conversely a particle b at the base of the gradient could have an h_b sufficiently large to encompass the whole high–density region. Although it is correct to observe that this regime is the cause of many S.P.M.H.D. related issues, we incorrectly diagnosed the over–/under–sampling of the gradient by particles b and a as a problem in and of itself. Before we consider the now redundant 'average h' method, we will first demonstrate the 'explosion' instability and then discuss briefly the integrator bug which caused it.

III.2.1 The Integrator Bug

In figure III.xiv we show the evolution of a collapsing molecular cloud core (the initial conditions for which are immaterial here, and are discussed in chapter IV) between $t = 0.98\,t_{\rm ff}$ and $1.02\,t_{\rm ff}$. The complete destruction of the calculation by the 'instability' can be readily seen, and in figure III.xvii we show the velocity in the z–direction at the moment the

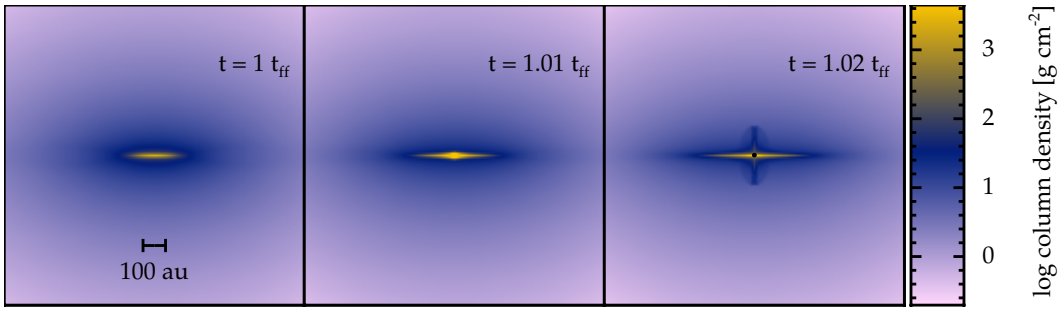

Figure III.xvi. Column density projections from $t = 1.00\,t_{\rm ff}$–$1.02\,t_{\rm ff}$ of a collapsing molecular cloud core, with identical initial conditions to figure III.xiv *not* using the 'average h' scheme but *with* a fixed integrator. The fluid velocity within the outflow is again consistently $< 10\,{\rm km\cdot s^{-1}}$, however, the outflow is now also more uniform and no longer contains anisotropies (the 'kinks' and 'wobbles'). The reduced spatial extent of the outflow is due to the outflow being launched slightly later than for a calculation using the redundant formalism.

calculation fails, where particle velocities significantly greater than the outflow velocity expected from a 1 au protostellar core are present (*i.e.* $v_z > 10\,{\rm km\cdot s^{-1}}$). In addition, the outflow is clearly asymmetrical and does not exhibit the characteristic shape — an outer bulk outflow surrounding a collimated central region — of a protostellar jet. We initially belived this to be a real instability — particularly as it was not present if the sink particle accretion radius was sufficently large to prevent a very steep density gradient ($r_{\rm acc} = 5$ au was found to be 'stable', whilst $r_{\rm acc} = 1$ au was not; the practical limit on the radius was never determined precisely). In addition, as we show in figure III.xv, changing the way the kernel was averaged appeared to correct this. Dobbs (*priv. comm.*), however, found the cause was much more prosaic. The sphNG code uses a second–order Runge–Kutta–Fehlberg (RK1(2) in Fehlberg 1969) integrator (see sub–section II.6.1 and table II.1), which can be represented algebraically for an arbitrary quantity φ as

$$\varphi_{t+1/2} = \varphi_t + \frac{\Delta t}{2}\dot{\varphi}_t \tag{III.42}$$

for the first half of the time-step, Δt, and

$$\varphi_{t+1} = \varphi_t + \frac{1}{256}\dot{\varphi}_t\Delta t + \frac{255}{256}\dot{\varphi}_{t+1/2}\Delta t \tag{III.43}$$

for the complete time–step. For every evolved fluid quantity in sphNG this was evaluated correctly, except for the magnetic field vector. Here, instead of the $1/256$ component of equation III.43 being

$$\frac{1}{256}\left.\frac{\Delta B^i}{\Delta t}\right|_t \Delta t \tag{III.44}$$

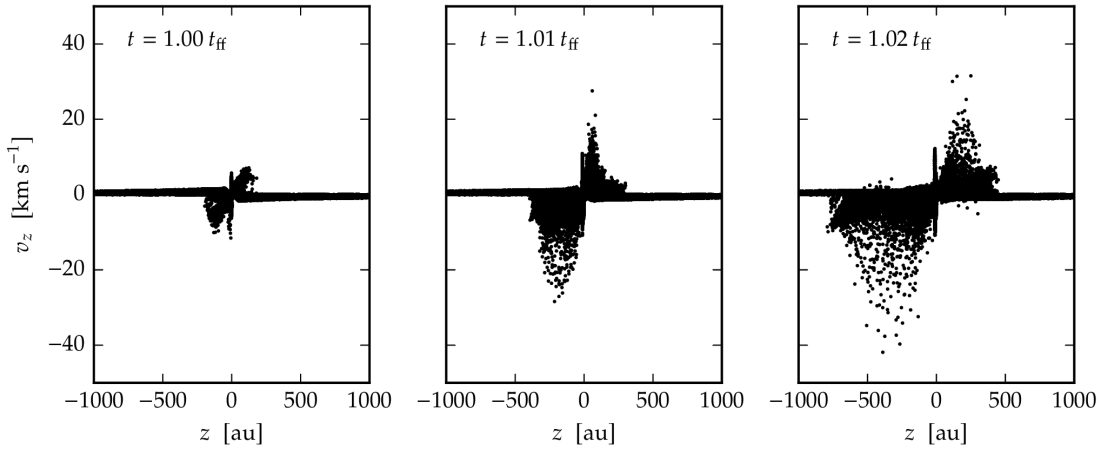

Figure III.xvii. Plots of S.P.H. particle velocity in the z–direction against z–position at $t = 1.00\,t_{\rm ff}$, $1.01\,t_{\rm ff}$, and $1.02\,t_{\rm ff}$ for a code with the integrator bug. The velocity signature of the explosion 'bubble' seen in figure III.xiv is clearly evident as a pair of asymmetrical ≈ 30–$40\,\mathrm{km}\cdot\mathrm{s}^{-1}$ regions above and below the origin.

the value from when $t = 0$ was erroneously retained[11], in effect

$$\frac{1}{256}\left.\frac{\Delta B^i}{\Delta t}\right|_0 \Delta t \ . \tag{III.45}$$

Superficially, this appears to be *very* serious, however, a crucial property of our setup make it less so. At $t = 0$, the rate of change of the magnetic field is very small.

Therefore, this error is somewhat equivalent to adding a small constant stress into the field, and even then this only contributes a factor of $1/256$ to the field evolution. Nonetheless, this does cause errors – particularly on smaller length-scales, because these correlate with Δt being very small due to individual timestepping: values of $\Delta t/(\Delta t)_0 < 1/2^8$ are common in the central area of the calculation. These regions are also where more complicated fields are present, however, and this erroneous stress acted to produce a spuriously large magnetic field and hence the 'explosion'.

Correcting this bug eliminates the explosive instability, *cf.* figure III.xvi, without the need for any further modifications to the S.P.M.H.D. equations, although the underlying issues related to solenoidality remain. Importantly, correcting the underlying bug has eliminated the difficult to explain anisotropies and inhomogeneities within the outflow, and results in a much more uniform and symmetric outflow profile.

11. the higher–order error measuring term (in particular, the first $1/512$ term) suffered from a comparable issue.

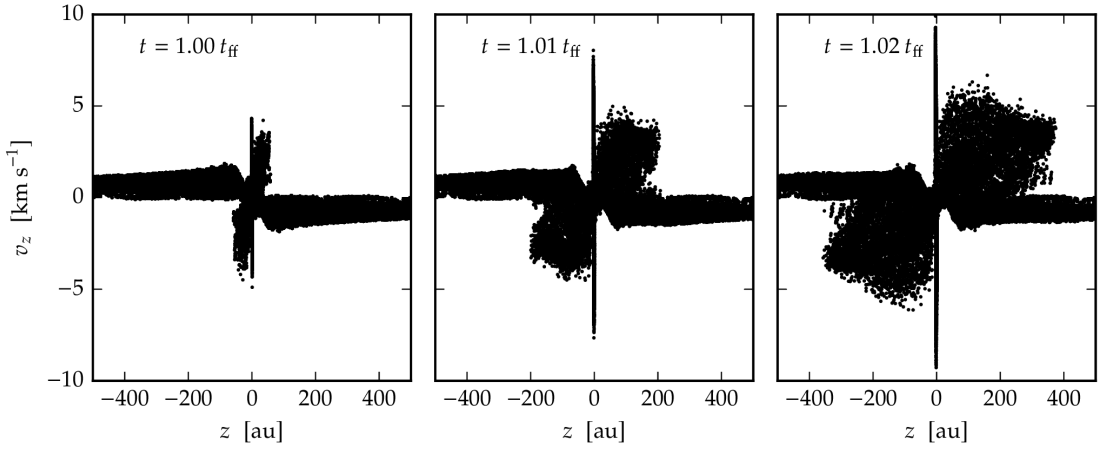

Figure III.xviii. Plots of S.P.H. particle velocity in the z–direction against z–position at $t = 1.00\,t_{\rm ff}$, $1.01\,t_{\rm ff}$, and $1.02\,t_{\rm ff}$ for a code with the integrator bug but using the 'average h' scheme. The classic outflow signature can now be seen in place of the unphysical bubble produced without the modified S.P.M.H.D. scheme (*cf.* figure III.xvii, *n.b.* the change of scale on this figure.)

III.2.2 h–averaging

Although redundant, we now discuss the the 'average h' method mentioned above. If we consider only the anisotropic part of the stress tensor,

$$\sigma^{ij}|_{\rm ani} = \frac{1}{4\pi} B^i B^j, \tag{III.46}$$

and hence the anisotropic component of the momentum equation,

$$\mathrm{D}_t v^i|_{\rm ani} = -\frac{1}{\rho}\nabla^j \sigma^{ij}|_{\rm ani} = -\frac{1}{\rho}\frac{1}{4\pi}\nabla^j B^i B^j. \tag{III.47}$$

In S.P.M.H.D. this becomes (applying the full $\chi = 1$ source term correction)

$$\mathrm{D}_t v_a^i|_{\rm ani} = \frac{1}{4\pi}\sum_b^N \frac{m_b}{\Omega_b \rho_b^2}\left(B_b^i - B_a^i\right) B_b^j \nabla_a^j W_{ab}\left(h_b\right). \tag{III.48}$$

In contrast, the induction equation is given by

$$\mathrm{D}_t \frac{B_a^i}{\rho_a} = -\frac{1}{\Omega_a \rho_a^2}\sum_b^N m_b \left(v_a^i - v_b^i\right) B_a^j \nabla_a^j W_{ab}\left(h_a\right), \tag{III.49}$$

and we observe that equation III.48 depends only on $W_{ab}\left(h_b\right)$ but that equation III.49 depends only on $W_{ab}\left(h_a\right)$. When the gradient in ρ is small this was believed to present

no issues, but conversely the observation that as $\rho_a \gg \rho_b$, $h_b \gg h_a$ was thought to be problematic. In effect, the concern was that a particle having the temporal evolution of its magnetic field interpolated over a very small neighbour set whilst having the corresponding force term interpolated over a significantly larger set would allow small errors to rapidly multiply. This situation is obviously undesirable – though not it transpired unstable, but may well act to amplify the momentum conservation issues (and probably exacerbated the intergrator bug). The solution proposed was to replace the $h_{\{a,b\}}$ terms in equations III.48 and III.49 with the mean value

$$\bar{h}_{ab} = \frac{h_a + h_b}{2}, \tag{III.50}$$

so that

$$\mathrm{D}_t v_a^i|_{\mathrm{ani}} = \frac{1}{4\pi} \sum_b^N \frac{m_b}{\rho_b^2} \left(B_b^i - B_a^i \right) B_b^j \nabla_a^j W_{ab} \left(\bar{h}_{ab} \right), \tag{III.51}$$

$$\mathrm{D}_t \frac{B_a^i}{\rho_a} = -\frac{1}{\rho_a^2} \sum_b^N m_b \left(v_a^i - v_b^i \right) B_a^j \nabla_a^j W_{ab} \left(\bar{h}_{ab} \right). \tag{III.52}$$

This has the effect that the whole gradient is sampled, which follows from the observation that $\bar{h}_{ab} \to h_a$ when $h_a \gg h_b$. Although this scheme is now redundant, it provided some interesting insights into how S.P.H. behaves when the self–consistent smoothing length scheme produces very unequal neighbour sets. In particular, it provided the impetus for considering why steep density gradients, coupled with strong magnetic fields, are so deleterious for momentum conservation.

An interesting observation about this now redundant scheme is that it is still perfectly conservative — both with regards to momentum and total energy. It is also an entirely theoretically valid modification to the S.P.H. operators: there is no *in general* requirement to use the same smoothing kernel across the code. We note however, that maintaining conjugate operators is still essential. However, it is not sufficiently more resistant to the tensile instability to justify the marked loss of resolution caused by taking an average smoothing length. We would expect a slight improvement in how the source term correction works simply from using a *generally* larger 'stencil'[12] to evaluate $B^i \nabla^j B^j$, in effect a term of the form

$$B_a^i \nabla_a^j B_a^j = \frac{B_a^i}{4\pi} \sum_b^N m_b \left(\frac{B_a^j}{\rho_a^2} + \frac{B_b^j}{\rho_b^2} \right) W_{ab} \left(\bar{h}_{ab} \right). \tag{III.53}$$

If a larger stencil for evaluating fluid properties in S.P.H. is desired a more robust approach

12. With the observation that in some circumstances an average will actually produce a *smaller* effective smoothing sphere.

is to switch to a higher order kernel. This has the advantage of not sacrificing effective resolution (by virtue of being a properly normalised weighted mean).

III.3 Concerning Averages in Smoothed Particle Hydrodynamics

Extreme gradients in density are not uncommon in astrophysical simulations, and these can result in correspondingly very small and very large smoothing lengths being needed in a physically small region of the simulation. In some cases, for example in the pseudo–disc surrounding a protostar the smoothing length at the top of one of these gradients can be so short that the gradient is not properly sampled, *i.e.* a situation can arise where the particle spacing, $\Delta\rho \sim \rho/h$. In ordinary hydrodynamic S.P.H. (and also when radiative transfer schemes are employed) no deleterious effects are observed since all the equations of S.P.H. either employ both the smoothing length of a particle itself and its neighbours (*e.g.* as in equation II.47) or, in the case of the density, can be solved self-consistently (see equation II.34). However, in the most common formalism of magnetohydrodynamics (*cf.* equations II.70 and II.72) in S.P.H. this is no longer true, causing what was believed to be a violent instability, although the actual cause turned out to be more prosaic, as detailed in section III.2 above.

In Lewis, Bate, and D. J. Price (2015), as discussed above, we replaced the individual smoothing length terms, $h_{\{a,b\}}$, in these equations with an average term,

$$\bar{h}_{ab} = \frac{1}{2}\left(h_a + h_b\right) \tag{III.54}$$

which had what we believed to be the desirable property that at an extreme gradient $\bar{h}_{ab}$ tends towards $1/2$ of the larger value, ensuring the full gradient is sampled and that the equations are evaluated over an identical neighbour set. This modified scheme allowed for arbitrarily small sink particles to be employed, and consequently a much larger range of physical processes to be studied than was hitherto possible. We rejected simply imposing a minimum smoothing length for two reasons, firstly that it is essentially impossible to determine *a priori* a correct value to use; and secondly that in practice the minima needed were so large that particle pairing caused by stretching the smoothing kernel became an serious issue.

In principle, this pairing could be mitigated by the use of a Wendland kernel (Dehnen and Aly 2012), but is still wasteful of resolution in regions where the equations were already stable. The use of an average could be more nuanced since when $h_a \sim h_b$, $\bar{h}_{ab} \approx h_{\{a,b\}}$ and therefore resolution is not wasted. Additionally, the average can be applied to only the equations which are apparently unstable, preserving full resolution elsewhere.

However, the arithmetic mean is not the only plausible choice of average — for example the other two Pythagorean means both tend to zero if either of $h_{\{a,b\}}$ is zero whilst the arithmetic mean will approach one-half of the non–zero quantity. In sub–section III.3.1

we consider the potential advantages of other choices of average. In practice, as seen when applied to our test 'cylinder–in–a–box' model in sub–section III.3.2, no substantial differences are observed.

The inclusion of this discussion is not otiose, notwithstanding the conclusions in section III.2. Many S.P.H. schemes still use average smoothing lengths rather than a self–consistent scheme, but almost invariably use the arithmetic mean without further discussion or comment. That the results obtained here are so insensitive to the choice of *any* of the Pythagorean averages strongly indicates that this is a robust choice. Indeed, by virtue of having a slightly smaller neighbour set in general, an argument could be made to switch in these codes to the harmonic mean if an extra few percent of computational efficiency is desired. We expect a similar conclusion to hold for averaged kernels.

III.3.1 Comparison of Averages

As discussed *supra*, the arithmetic mean used in sub–section III.2.2 is not the only plausible average. Consequently, we now consider the effect of choosing different averages. Whilst there are limitless potentially viable averages, we consider only the three Pythagorean means, *viz.* the arithmetic mean in equation III.54 (hereafter A), the geometric mean (G) defined as

$$\bar{h}_{ab} = \sqrt{h_a h_b}\,, \tag{III.55}$$

and the harmonic mean (H) defined as

$$\bar{h}_{ab} = \frac{2h_a h_b}{h_a + h_b}\,, \tag{III.56}$$

in addition to a quadratic mean (Q) defined as

$$\bar{h}_{ab} = \sqrt{\frac{1}{2}\left(h_a^2 + h_b^2\right)}\,. \tag{III.57}$$

All these options take the same value when $h_a = h_b$ but exhibit significant differences, as seen in table III.1, in the limiting case where $h_a \gg h_b$ or *vice versa*. In particular, whilst A and Q are non-zero in the limit $h_{\{a,b\}} \to 0$, G and H are not. It can also be shown that for all values of h_a and h_b, $A \geq G \geq H$. At the other extreme, the differing growth rates of the various means can be seen when $h_a = 10h_b$, where Q is nearly 4 times larger than H. In essence, this affects how much of the gradient each average samples, not only in the limit when the difference between h_a and h_b can be greater a factor of ten, but also when the gradient is shallower.

III.3.2 Numerical Tests — Cylinder in Box

We use the simple isothermal cylinder–in–a–box test originally presented in Lewis, Bate, and D. J. Price (2015) to compare each of these averages and an unmodified S.P.M.H.D.

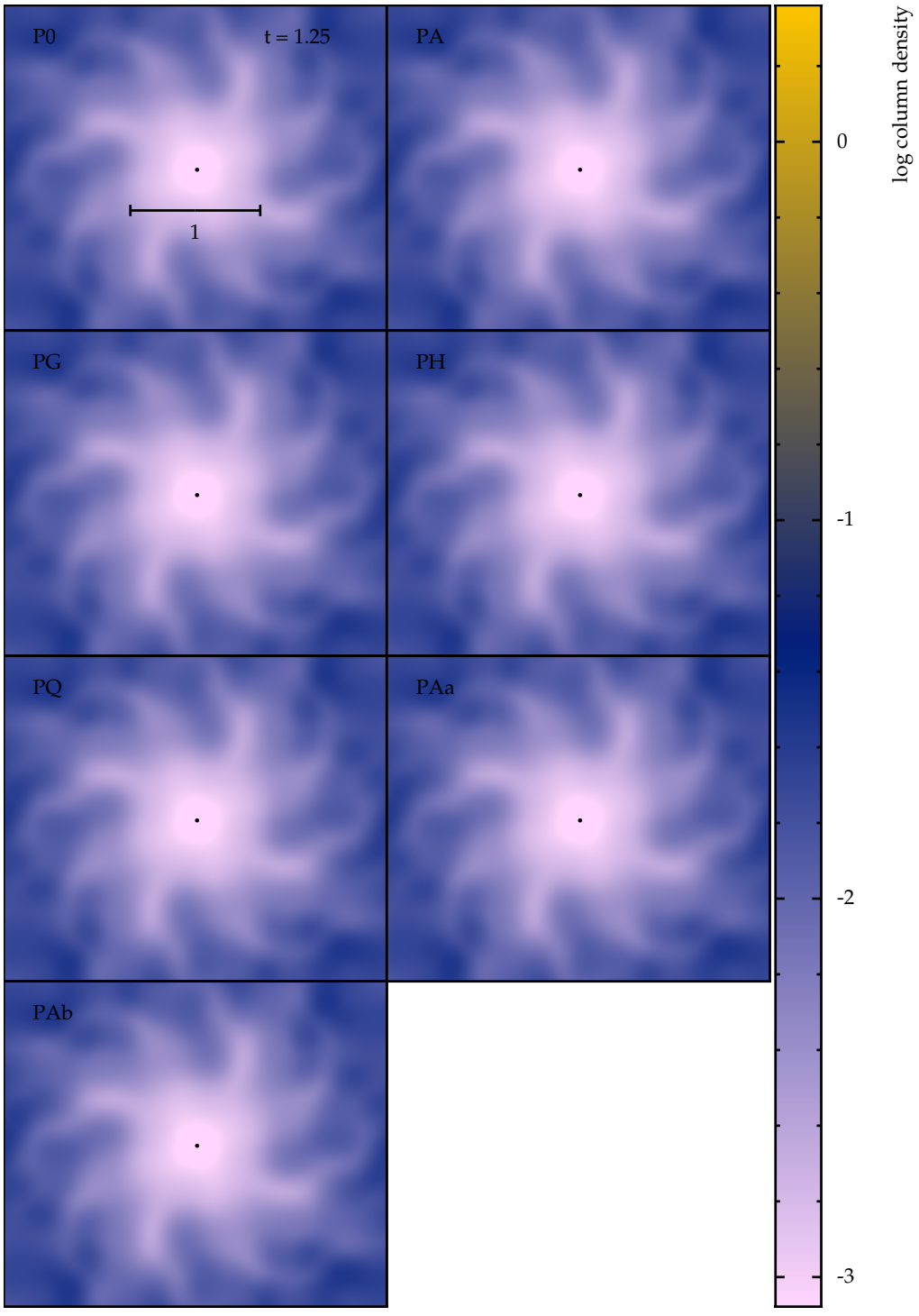

III.xix.a. $t = 1.25$

Figure III.xix. continued below

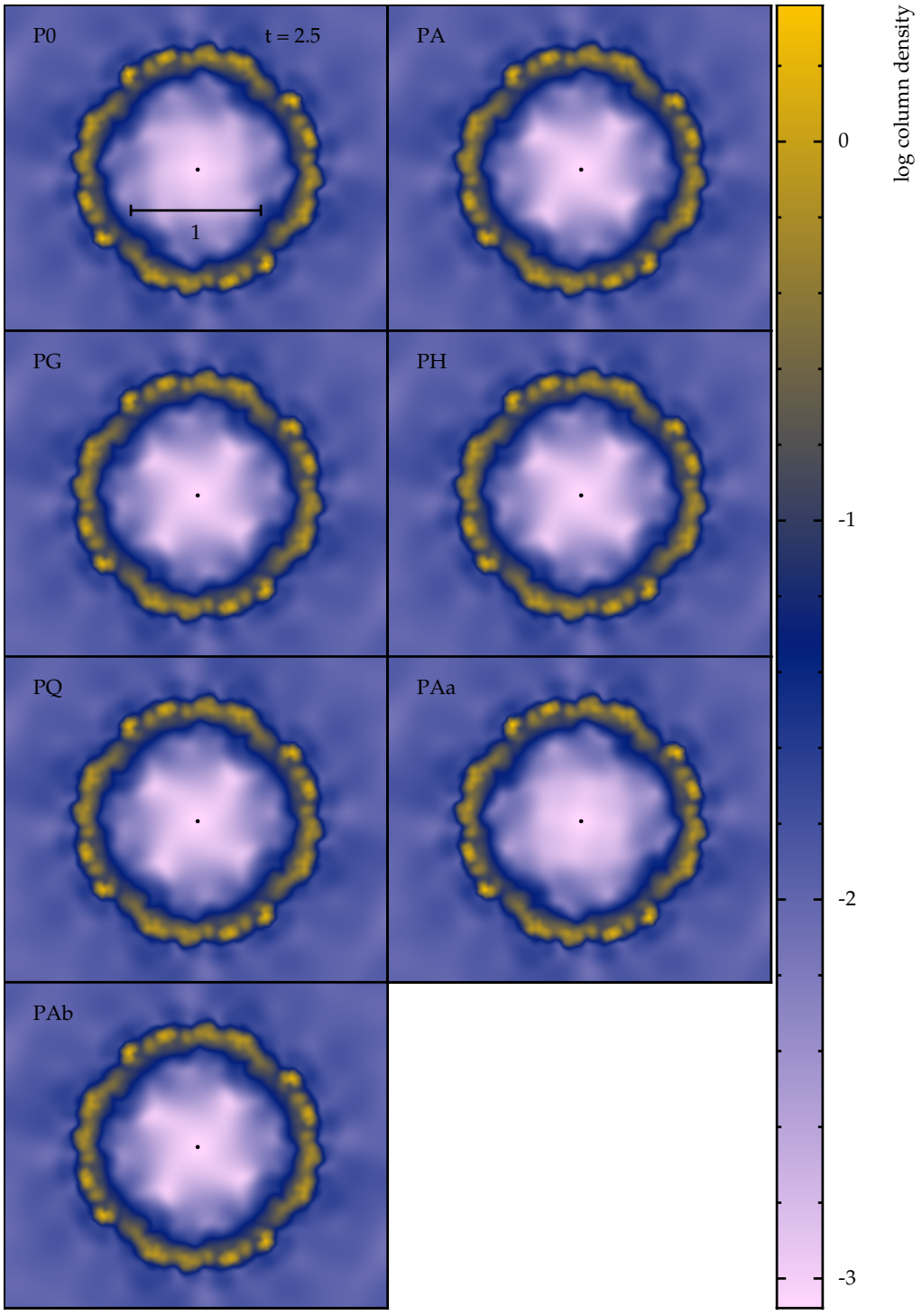

III.xix.b. $t = 2.5$

Figure III.xix. Density projections at $t = 1.25$ (sub–figure III.xix.a) and $t = 2.5$ (sub–figure III.xix.b) in the z–direction for the isothermal cylinder test. No qualitative differences at any epoch can be observed across all four averaging schemes, nor can these be clearly differentiated from the self–consistent scheme used normally and schemes where the average is applied to only one of the two M.H.D. equations.

Table III.1. Behaviour of the four means detailed in sub–section III.3.1 in limiting cases

Mean	$h_a \to 0$	$h_a = 2h_b$	$h_a = 10h_b$	$h_a \to \infty$
A	$\frac{1}{2}h_b$	$\frac{3}{2}h_b$	$\frac{11}{2}h_b$	∞
G	0	$\sqrt{2}h_b$	$\sqrt{10}h_b$	∞
H	0	$\frac{4}{3}h_b$	$\frac{20}{11}h_b$	∞
Q	$\frac{1}{\sqrt{2}}h_b$	$\sqrt{5}h_b$	$\sqrt{\frac{101}{2}}h_b$	∞

method. A cylinder of radius $r_{\text{cyl}} = 5$ code units (units defined such that $G = 1$ and $\mu_0 = 1$) with a height-to-radius of $1/2$ ($2 1/2$ code units thick) and a central hole of radius $1/10 r_{\text{cyl}} = 0.5$ code units was placed in a periodic box with a central sink particle to provide a potential equivalent to 10 times the mass of the material in the cylinder. Sink particles (as detailed more comprehensively in Bate, Bonnell, and N. M. Price 1995 and section II.5) are particles that exert no force on the system other than gravity and with an 'accretion radius', r_{acc}, whereby any S.P.H. (*i.e.* gas) particle which passes within r_{acc} of the sink particle is eliminated from the simulation and its mass and momentum added to the sink particle. We use a sink rather than a simpler potential well since this will eliminate any particles which fall out of the cylinder and into the centre preventing the time–step from becoming needlessly small in this region. Since we are using an isothermal equation of state, the Courant-limited time–step of particles collecting in a central well is very short compared to those in the fluid pressure and magnetically supported cylinder. The equation of state is given by $P(\rho) = 2/3 \epsilon \rho$ with ϵ fixed so that the sound speed was $1/10$ code units. An initial magnetic field aligned with the z–axis was applied to give a plasma β, *i.e.* the ratio of hydrodynamic and magnetic pressure, of $\beta \approx 8.4$. (This is equivalent to that derived by assuming the cylinder is a sphere of material and using the mass–to–flux equations discussed in chapter IV *infra* with $\mu = 5$). The cylinder was then given a $1/r^2$ differential velocity profile with the initial velocity set to obtain a rotation period of $T = 2$ code units at unit radius.

We would expect the cylinder material to pile up, forming a high density ring with a steep density gradient, so that material within a unit radius moves outwards (since it is moving faster than the Keplerian velocity) and more distant material spiraling inwards. Additionally, some material will fall out of the cylinder and towards the sink particle due to magnetic and viscous braking effects. The cylinder itself will then flatten and become more disc like due to rotational and self–gravitational forces, for example gravitational attraction in the z–direction will flatten the initially 'thick' cylinder. The objective here is to create a condition with a large density gradient, a highly disordered particle lattice, and a complicated magnetic field. Originally this was to demonstrate that averaging the smoothing length improved the calculation, we now use it to demonstrate that even in large gradients any sensible average choice of average (or a self–consistent scheme) is robust.

Calculations were then performed using the four means presented above (models D*A*–D*Q*) and additionally with the arithmetic mean but applied to either the induction equation only (D*A*a) or the anisotropic momentum equation only (D*A*b). We also performed the same simulation with an unmodified code for comparison (D0).

In sub–figure III.xix.a we plot the density profile for all seven calculations at $t = 1.25$ code–units. Clearly there is no qualitative difference in the evolution of the fluid for each average at this early moment. We then let the calculation evolve for a further $t = 1.25$ code–units and plot comparable column density profiles at $t = 2.5$ in sub–figure III.xix.b. The column density where the cylinder material has piled up has increased by approximately two orders–of–magnitude. This high density region presents a sharp density gradient, with the column density falling by two to three orders–of–magnitude within 0.1 code length units of the centre of the high density ring. This presents a challenge for any scheme which is vulnerable to instabilities from sharp density increases, and the rapidly and differentially rotating nature of the cylinder will cause a significant degree of lattice disorder. However, no qualitative differences can be seen across all the calculation. This clearly shows that the choice of average (or using an unmodified S.P.M.H.D. scheme) has little impact even in this extreme test. Quantitative results are presented in figure III.xx, which shows the temporal evolution of several fluid parameters. We see that aside from the small variations in the current density for D*A*a, the qualitative equivalence shown in figure III.xix is confirmed by this quantitative analysis. Consequently, we conclude that an S.P.H. scheme which uses an average smoothing length is robust to the choice of average.

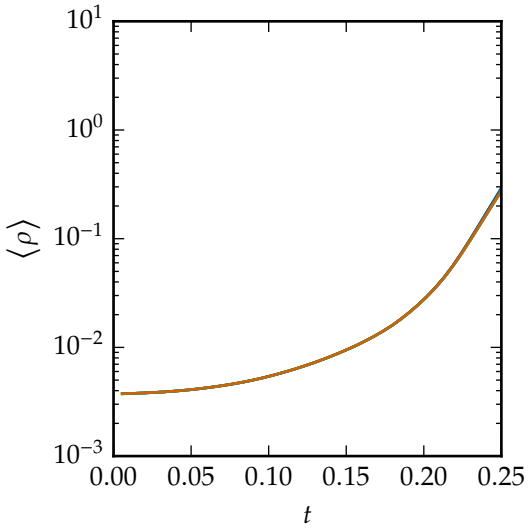

III.xx.a. Mean fluid density

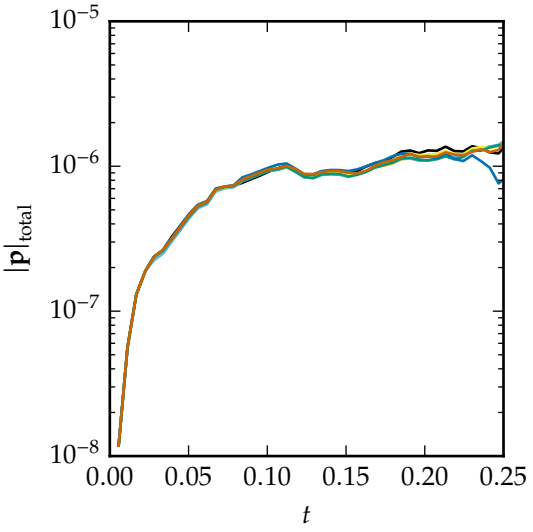

III.xx.b. Total linear momentum

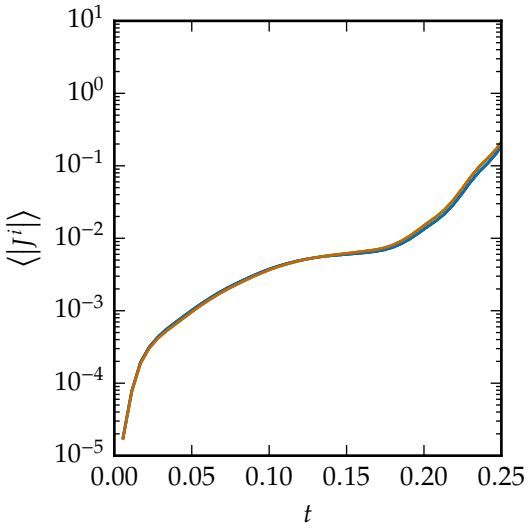

III.xx.c. Mean current density

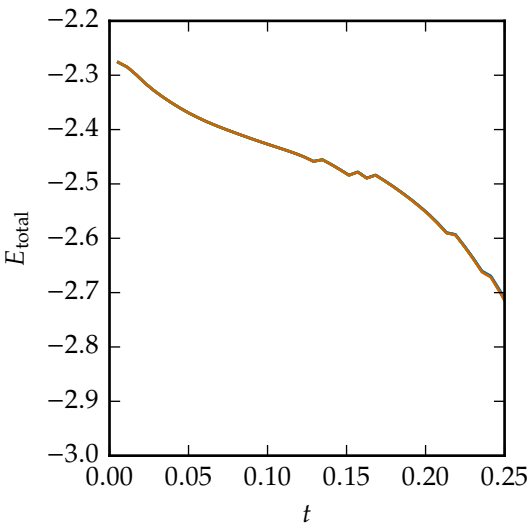

III.xx.d. Total energy

Figure III.xx. Plots of mean fluid density (sub–figure III.xx.a), total linear momentum (sub–figure III.xx.b), mean current density (sub–figure III.xx.c), and total energy (sub–figure III.xx.d) against time for all seven disc calculations. Do, D*A*, D*G*, D*H*, D*Q*, D*A*a and D*A*b are shown by black, orange, sky–blue, yellow, turquoise, blue, and vermillion lines respectively. Essentially no variantion is observed between all seven calculations, save for an almost *de minimis* change in the evolution of the current density when the averaging is not applied to the induction equation (*i.e.* calculations Do and D*A*a).

CHAPTER IV

The Evolution of Protostellar Cores with Misaligned Magnetic Fields and Rotation axes

Qu'est-ce que la tolérance ? C'est l'apanage de l'humanité. Nous sommes tous pétris de faiblesses et d'erreurs ; pardonnons-nous réciproquement nos sottises, c'est la première loi de la nature.

« Tolerance », Dictionnaire philosophique, Voltaire (1764)

The calculations in this chapter owe their genesis to Lewis, Bate, and D. J. Price (2015). However, that work was affected by the integrator bug discussed in section III.2 and used the redundant 'average h' method. Consequently, we have re–run the calculations with a correct code and with the 'normal' S.P.M.H.D. equations. This chapter nonetheless follows a similar structure to the progenitor paper, and could be considered an 'updated' version. In section IV.2 we present the initial conditions used, which we then evolve using our S.P.M.H.D. method discussed in chapter II. We then present the results and a discussion in sections IV.3 and IV.5 following a similar approach to the original paper.

IV.1 Motivation

Magnetic fields exert one of the most important forces influencing the formation of protostars and may resolve several questions about the formation of stars that are left unanswered by purely hydrodynamic theories. That the molecular clouds that ultimately produce protostars are magnetised is well known (Crutcher 2012; Crutcher *et al.* 1993), and this can be confirmed with observations of Herbig–Haro objects with distinctive bipolar outflows, which must have a magnetic origin and which we discussed in chapter I. Additionally, these outflows may help explain the difference between the angular momentum observed in molecular cloud cores and that of the resultant stars. This is, however, dependent on the ability of the protostar to produce a strong outflow — if at certain angles this is impossible this will place constraints on the initial field geometry. Recent advances in observational technology have shown that this magnetic field structure can be quite complex (Stephens *et al.* 2014) and that the hitherto common assumption that field, outflow, and rotation axis are all aligned may be incorrect (*cf.* Hull *et al.* 2013a, and others). On very small scales Donati *et al.* (2010) have observed a 20° misalignment between the rotation and field axes of AA Tau. Previous work, *e.g.* Ciardi and Hennebelle (2010), using adaptive mesh refinement (A.M.R.) codes has shown that the nature and extent of the protostellar outflow is strongly dependent on the angle (which we denote with ϑ) between the field and rotation axis.

More recently, D. J. Price, Tricco, and Bate (2012) examined the collapse of a magnetised molecular cloud core all the way to the formation of the first hydrostatic core (Larson 1969) and Bate, Tricco, and D. J. Price (2014) have continued beyond that to the stellar core. To model the evolution significantly beyond protostar formation, sink particles (*vide supra* the discussion in section II.5) are a necessary evil since modelling both the magnetohydrodynamics of the protostar and also the surrounding cloud is computationally unfeasible due to the widely different length and time scales involved. Previous S.P.M.H.D. modelling of collapsing cores used somewhat large (5 au) sink particles and thus, whilst stable[1], failed to capture the full range of physical processes. In particular,

1. Given that the code used contained the integrator bug (*vide* sub–section III.2.1 *supra*).

they would exclude any process which occurs between a radius of 5 au and our significantly reduced inner boundary of 1 au. This is an important limitation to consider, not least because the maximum outflow velocity is closely linked to the rotational velocity of the progenitor disc (a point we will return to in significant detail in chapter V, see also D. J. Price, Pringle, and King 2003). The Keplerian velocity at 1 au is $\sqrt{5}$ faster[2] than at 5 au and this clearly will have an impact on the numerical results.

To examine the way that changing the initial magnetic field geometry affects the consequent protostellar object, we perform a parameter sweep across six field geometries. These range from a fully aligned magnetic field, similar to that used in D. J. Price, Tricco, and Bate (2012) through to a fully misaligned field. This latter arrangement was studied in D. J. Price and Bate (2007). However, both of these calculation used comparably larger sink particles nor did they consider the intermediary regimes where the displacement between the rotation field and magnetic field is neither zero nor 90°. In addition, D. J. Price, Tricco, and Bate (2012) was affecred by the integrator bug (sub–section III.2.1) and D. J. Price and Bate (2007) used an 'Euler potential' method (Euler 1769; Rosswog and D. J. Price 2007) as opposed to the direct induction method detailed in section II.3. The results presented here, therefore, complete this analysis by combining a range of field geometries with a method that should be capable of producing outflows — a major limitation of the Euler potentials is the inability to capture complex field windings.

After performing the parameter sweep, we then compare the results obtained to the broadly comparable work of Ciardi and Hennebelle (2010) as mentioned above. We also consider how the field geometry affects the way material is accreted onto the protostellar core itself to provide an insight into how the primordial magnetic field can influence the accretion rate and profile of a first hydrostatic core.

IV.2 Initial Conditions

The initial conditions for our calculations of protostellar collapse are broadly the same as those in D. J. Price, Tricco, and Bate (2012). However, we use more S.P.H. particles and smaller accretion radii for our sink particles. We begin with an approximately 1 1/2 million S.P.H. particle uniform density sphere of cold gas, more than sufficient to resolve a Jeans length according to the criteria in Bate and Burkert (1997), placed in a periodic box and surrounded by an external medium of *ca.* 500,000 warm gas particles. There is a density ratio of 30:1 between the warm outer medium and the cool sphere with a pressure equilibrium between the sphere and the medium. Particles are initially laid out on a cubic lattice, the initial radius of the sphere is $r_{\rm cloud} = 4 \times 10^{16}\,{\rm cm}$ with a mass of $M = 1\,{\rm M}_\odot$ giving an initial density in the sphere $\rho_0 = 7.4 \times 10^{-18}\,{\rm g \cdot cm^{-3}}$ The sphere has an initial isothermal sound speed $c_s = 2.2 \times 10^4\,{\rm cm \cdot s^{-1}}$ and we use the barotropic equation of state

2. since $v_{\rm kepl} \propto 1/\sqrt{r}$

$$P\left(\rho\right) = c_s^2 \begin{cases} \rho & \rho \leq \rho_{c,1} \\ \rho_{c,1}\left(\dfrac{\rho}{\rho_{c,1}}\right)^{\frac{7}{5}} & \rho_{c,1} < \rho \leq \rho_{c,2} \\ \rho_{c,1}\left(\dfrac{\rho_{c,2}}{\rho_{c,1}}\right)^{\frac{7}{5}}\left(\dfrac{\rho}{\rho_{c,2}}\right)^{\frac{11}{10}} & \rho > \rho_{c,2} \end{cases} \tag{IV.1}$$

where the two critical densities are given by $\rho_{c,1} = 1 \times 10^{-14}\,\mathrm{g\cdot cm^{-3}}$ and $\rho_{c,2} = 1 \times 10^{-10}\,\mathrm{g\cdot cm^{-3}}$. This is similar to that used, for example, in Machida, Inutsuka, and Matsumoto (2008) with the removal of the final $\gamma = 5/3$ step at the highest densities. The sphere has an initial temperature of approximately 10 K; since the outer medium also begins with the same initial pressure it has a correspondingly higher initial temperature of approximately 300 K. The sphere is set in solid body rotation at $\Omega = 1.77 \times 10^{-13}\,\mathrm{rad\cdot s^{-1}}$, such that the magnitude of the ratio of rotational to gravitational energy is ≈ 0.005, within the range observed by Goodman *et al.* (1993).

We then define a new parameter, ϑ, which is the angle between the rotation axis of the sphere (which is always aligned with the z-axis) and the initial magnetic field. The magnetic field is then initially

$$B_x = B_0 \sin\vartheta, \tag{IV.2}$$

$$B_z = B_0 \cos\vartheta, \tag{IV.3}$$

i.e. when $\vartheta = 0°$ the field is aligned with the z–axis. The initial magnetic field B_0 is determined using the parameter μ, which is (Mac Low and Klessen 2004; Nakano and Nakamura 1978) the ratio between the sphere's mass–to–flux ratio and the critical mass–to–flux ratio for a spherical cloud, *i.e.*

$$\mu = \frac{\varpi_{\mathrm{cloud}}}{\varpi_{\mathrm{crit}}}, \tag{IV.4}$$

where,

$$\varpi_{\mathrm{cloud}} = \frac{M}{\pi r_{\mathrm{cloud}}^2 B_0} \tag{IV.5}$$

$$\varpi_{\mathrm{crit}} = \frac{2c_1}{3}\sqrt{\frac{5}{\pi G \mu_0}}, \tag{IV.6}$$

with the ratio between the minimum self–collapsing gravitational mass obtained from the virial theorem and that required for a magnetised astrophysical cloud, $c_1 = 0.53$ as obtained numerically by Mouschovias and Spitzer (1976). Throughout this chapter we will set $\mu = 5$.

Sink particles are added to the simulation once a critical density of $10^{-10}\,\mathrm{g\cdot cm^{-3}}$ is achieved, and the usual tests are passed (Bate, Bonnell, and N. M. Price 1995). We use an accretion radius of 1 au as a compromise between capturing physics and numerical efficiency, which is a smaller size sink particle than the 5 au sinks used in D. J. Price, Tricco,

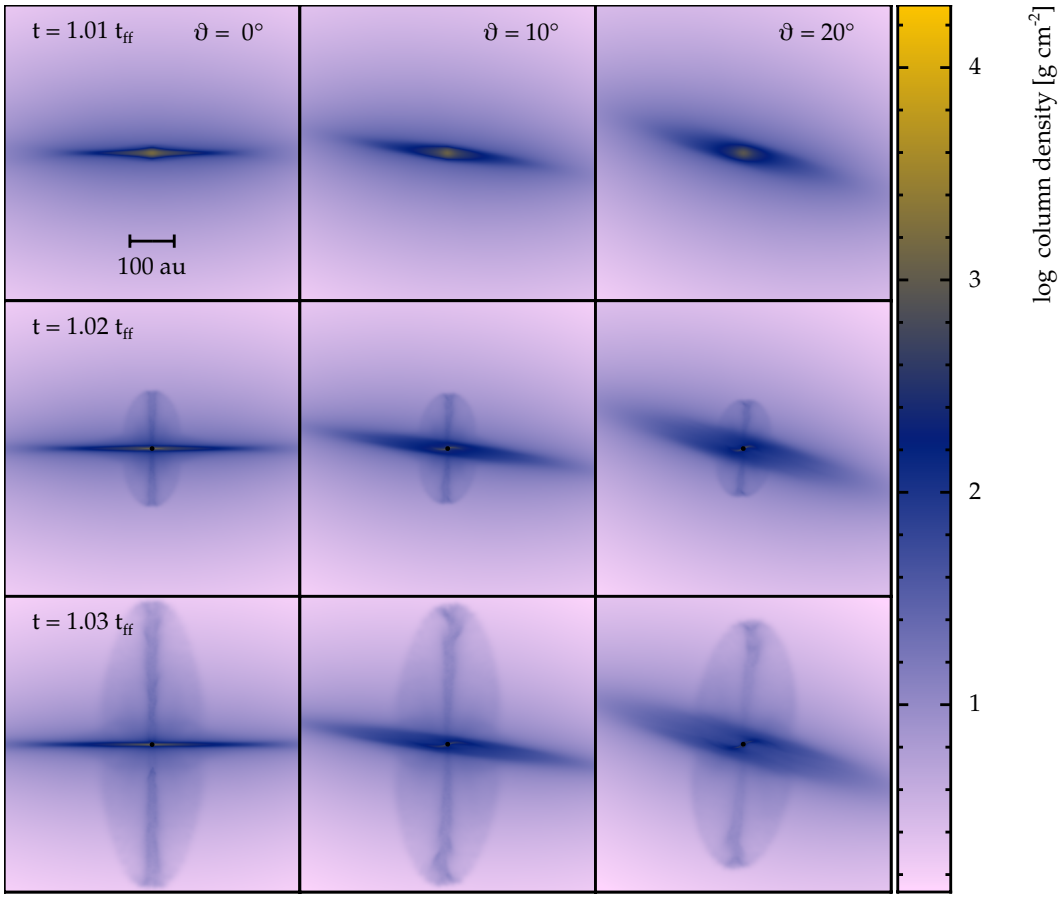

IV.i.a. Column density projection plots for $\vartheta = 0°$, 10° and , 20° (across the page) at $t = 1.01\ t_{\rm ff}$, $1.02\ t_{\rm ff}$, $1.03\ t_{\rm ff}$ (down the page). All three calculations produce a collimated jet after a sink particle is formed. When $\vartheta > 0°$, this jet is produced at an angle between the magnetic field axis (ϑ) and the rotation axis (which is aligned to the z–axis).

Figure IV.i. continued below

and Bate (2012). Our sink particle will accrete unconditionally once a particle crosses its accretion radius; since all our simulations are of a collapsing core this should not result in any deleterious effects[3]. As in all previous work, the sink particle does not carry a magnetic field — when a particle is eliminated from the simulation, the mass is added to the sink (which does not exert a hydrodynamic pressure). In effect, as usual the sink particle provides a cold inner boundary to the calculation.

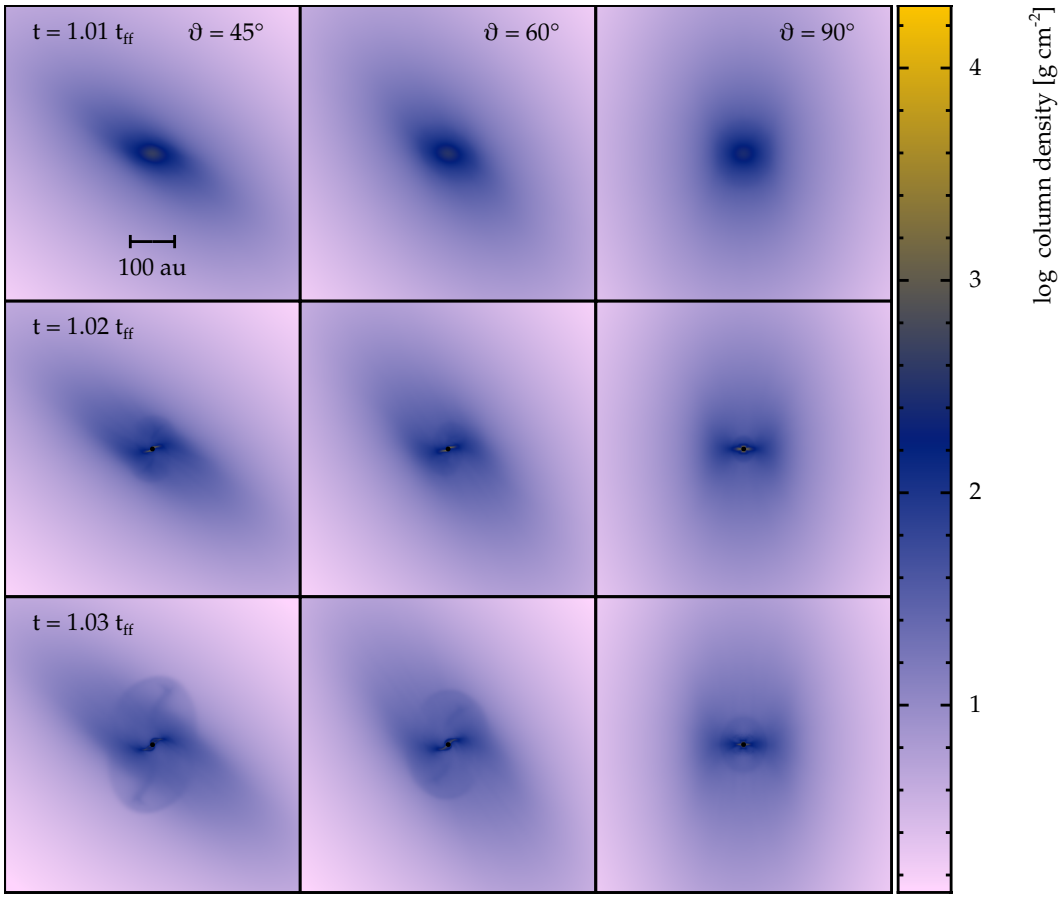

IV.i.b. Column density projection plots for $\vartheta = 0°$, $10°$ and , $20°$ (across the page) at $t = 1.01\ t_{\rm ff}$, $1.02\ t_{\rm ff}$, $1.03\ t_{\rm ff}$ (down the page). Here, a collimated jet is only produced for $\vartheta = 45°$ and no jet–like outflow at all is produced for $\vartheta = 90°$. As before, when a bipolar jet is formed it is aligned between the z–axis and the field axis — an effect which can be clearly seen in the $45°$ calculation.

Figure IV.i. These two figures show column density projections for all six calculations ($0° \leq \vartheta \leq 90°$). We begin at $t = 1.01\ t_{\rm ff}$ just before a sink particle is inserted into the calculation, where the alignment of the pseudo–disc structure perpendicular to the field axis is clearly seen. We then see how for $\vartheta \leq 45°$ a collimated bipolar jet outflow is produced but for $\vartheta \geq 60°$ this outflow is a larger and slower bulk outflow. As all the jets and outflows form at the same dynamical time, the differing extent of the outflow structures at $t = 1.03\ t_{\rm ff}$ is indicative of the way outflow velocity reduces as ϑ increases.

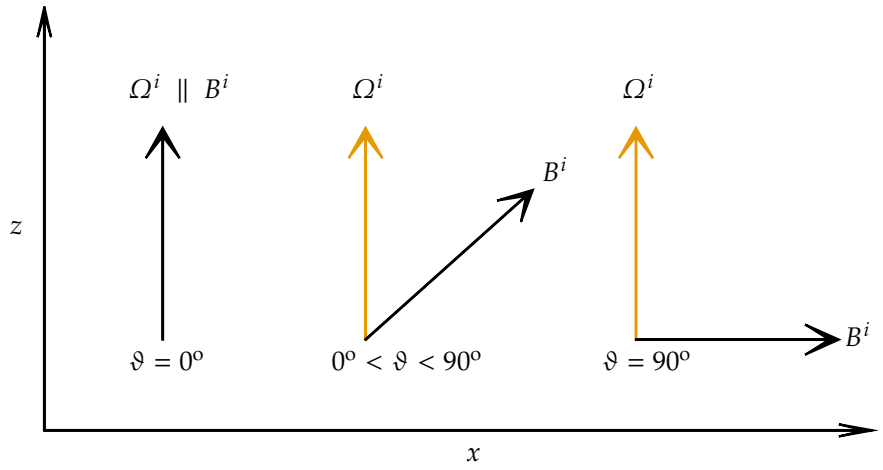

IV.ii.a. x–z plane

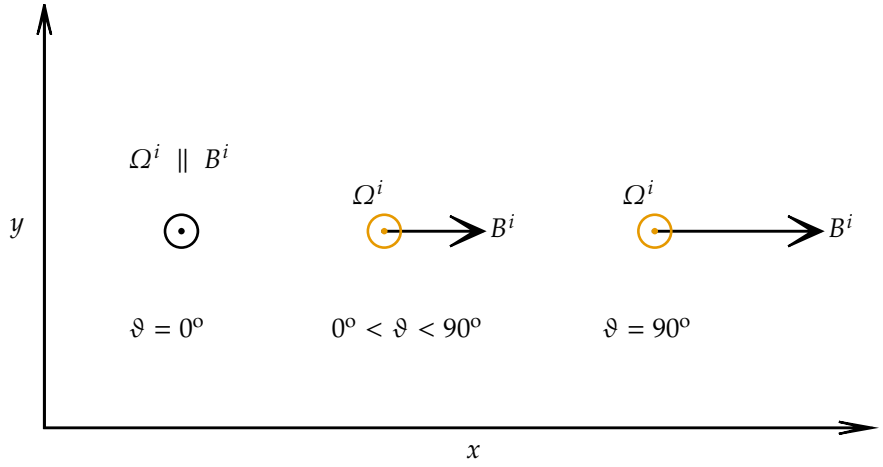

IV.ii.b. x–y plane

Figure IV.ii. Schematic diagrams of the relative orientation of the rotation field vector, Ω^i, and the magnetic field vector, B^i, as a function of the inclination angle, ϑ. Sub–figure IV.ii.a shows the orientation in the x–z plane as seen, *e.g.*, in figure IV.i, and sub–figure IV.ii.b is the corresponding diagram for the x–y plane, *e.g.* as in figure IV.vii. Except when $\vartheta = 0^\circ$, where black represents both vectors, the colour black represents the B^i vector and orange the Ω^i vector. The symbol $\odot$ represents a vector 'out of the page'.

IV.3 The Nature of Outflows and Jets

We performed calculations with six values of ϑ, *viz.* 0°, 10°, 20°, 45°, 60°, 90°. Figure IV.i shows the time evolution for these six angles. The relative orientation of the rotation field and magnetic field vectors in shown in the schematic diagram in figure IV.ii . These orientations apply throughout this thesis. We note that the the results for the $\vartheta = 0°$ case are broadly the same as in D. J. Price, Tricco, and Bate (2012), albeit with a slightly faster jet velocity — in this case ~ 8 km $\cdot$ s^{-1}. This is expected (as we discussed earlier) since the smaller accretion radii used here will allow a faster velocity near the sink particle, and since the axial velocity of a collimated jet is proportional to the velocity of the matter spiraling in to create it this naturally leads to a faster jet (D. J. Price, Pringle, and King 2003). This is the only significant difference between this result and the earlier calcuation that used a 5 au sink, showing that reducing the size of the sink particle accretion radius does not have any effect other than allowing smaller scale disc physics to be captured.

The most striking result is the lack of any real outflow at all from the $\vartheta = [60°, 90°]$ models. Whilst all shallower angles produce an outflow of some significance, this only takes the form of a collimated jet for $\vartheta \leq 20°$. Similarly, the pseudo–disc which is clearly defined for $\vartheta = 0°$ is either disrupted or, in the most misaligned cases, does not form at all. Since the formation of a stable bipolar outflow requires a stable and defined disc structure, this naturally prevents a substantial outflow being formed. In the intermediate $\vartheta = 45°$ case, the pseudo–disc formed is highly disrupted but still manages to drive a broad, albeit slower, outflow.

IV.3.1 Current Density

Figure IV.iii shows the connection between the magnetic field, here represented by the current density, *i.e.*

$$J^i = \epsilon^{ijk} \nabla^j B^k \,, \tag{IV.7}$$

and the generation of an outflow. When the field and rotation axes are closely aligned, an inner region with a large J^i field is produced which then drives a strong jet and outflow. Conversely, we see how the $\vartheta = 45°$ calculation still contains an inner region with $\left|J^i\right| > 1 \times 10^4$ statA $\cdot$ cm^{-2},[4] however, this no longer comprises a vertical region and an approximately perpendicular disc aligned region. The vertical region when $\vartheta \leq 20°$ is closely correlated with the rotation axis — which is the direction of the angular momentum vector, although this correlation weakens as the angle increases. The corresponding jet velocity also reduces — and becomes essentially uncollimated when $\vartheta = 45°$. This im-

3. This was chosen for the original version of these calculations to simplify analysis of the way the h–averaging worked. We have maintained it here for consistency.

4. where a statA $\equiv$ statampère $\stackrel{\text{def}}{=}$ statcoulomb $\cdot$ s^{-1} $\stackrel{\text{def}}{=}$ $1/10c$ ampère.

plies that a misalignment $\geq 45°$ is not conducive to the formation of a strongly collimated outflow.

IV.3.2 Velocities

The conclusions drawn from the $\left|J^i\right|$ tracer are echoed by the velocity field, which we show in figure IV.iv (although we omit $\vartheta = 10°$ for clarity). Outflow strength and field geometry are clearly highly correlated. As ϑ increases, the velocity of the outflow reduces, ultimately almost ceasing when $\vartheta = 90°$. The latter case does still have an outflow of sorts, however, this is now a small bubble surrounding the protostar rather than a driven jet or similar process. This is not necessarily an unexpected result: in this calculation the pseudo–disc is rotating through the magnetic field rather than winding up a perpendicular field. In figure IV.iv we compare the z–axis velocities for all six calculations at $t = 1.03\, t_{\rm ff}$ and again see this correlation. Obviously this analysis neglects the deviation of the jet axis from the vertical. This is less of a concern than one would initially imagine, however. Figure IV.v shows the internal density profile for a representative sample of the calculations with misaligned jets. Here we see that the inner–most region of the jet is affected by both the rotation axis *and* the magnetic field axis. The effect of this is to warp the inner disc, and drive the region of the outflow nearest to the sink particle closer to the rotation axis — the direction of principal angular momentum flow — than the magnetic field axis. Provide that this warp is sufficently small, *cf.* $\vartheta = 45°$ *contra* $\vartheta = 20°$, that it does not prevent this partial internal re–alignment a jet can be produced. When $\vartheta \geq 45°$ the warp is too large and consequently the inner collimation of the jet ceases producing a slower less jet–like outflow.

IV.3.3 The plasma β

This result is also echoed by a consideration of the plasma β in the calculation. Figure IV.vi shows a cross–section of β, defined as usual as

$$\beta = \frac{p_{\rm hyd}}{p_{\rm mag}} = \frac{2\mu_{\rm o} p}{B^2}, \tag{IV.8}$$

where $\mu_{\rm o}$ is the permeability of free space, for a representative sample of calculations at $t = 1.03\, t_{\rm ff}$. We see that the pseudo–disc is clearly supported by the fluid pressure and has a $\beta > 1$ throughout. Conversely we see that the outflow regions are consistently dominated by magnetic pressure even when these do not contain a jet region. The jet itself actually manifests as a region of slightly reduced magnetic pressure within the broader outflow region. The cause of this the change from a field structure where the field lines broadly follow the overall magnetic field axis to one which is more tightly wound. This causes an increased J^i field, as we showed in figure IV.iii, — due to the greater deformation and transformation of the field structure — at the expense of the isotropy of the magnetic

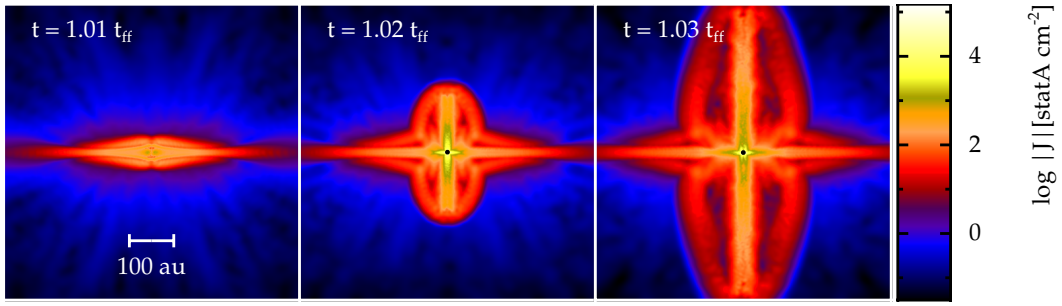

IV.iii.a. $\vartheta = 0°$

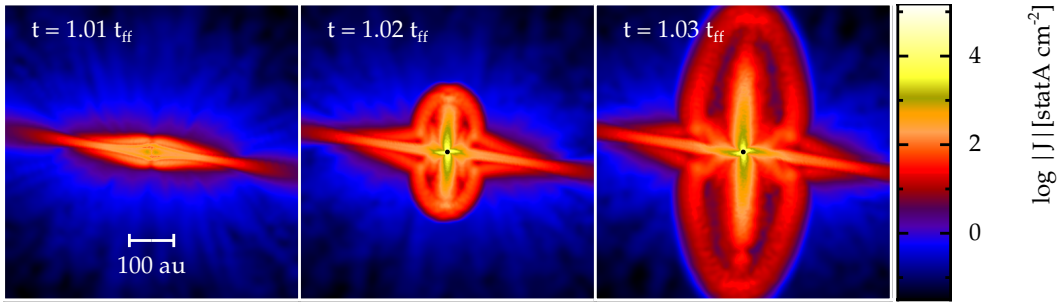

IV.iii.b. $\vartheta = 10°$

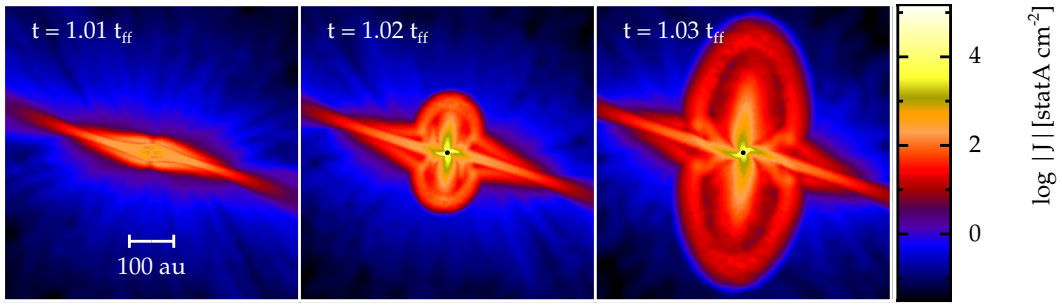

IV.iii.c. $\vartheta = 20°$

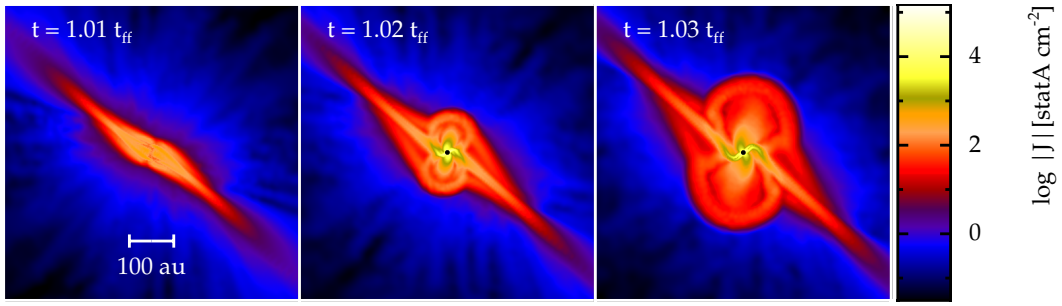

IV.iii.d. $\vartheta = 45°$

Figure IV.iii. Cross–sections of $|J|$ at $t = 25,420$ a for four different values of ϑ, *viz.* 0°, 10°, 20°, and 45°, shown on sub–figures IV.iii.a to IV.iii.d. The magnetic field geometry is more complicated in the latter two cases, and this corresponds with a substantially changed outflow. However, the inner collimated region can still be seen for $\vartheta \leq 20°$, which correlates with a strongly collimated outflow. Conversely the $\vartheta = 45°$ calculation has a less defined inner region and a corresponding lack of a strong jet–like outflow.

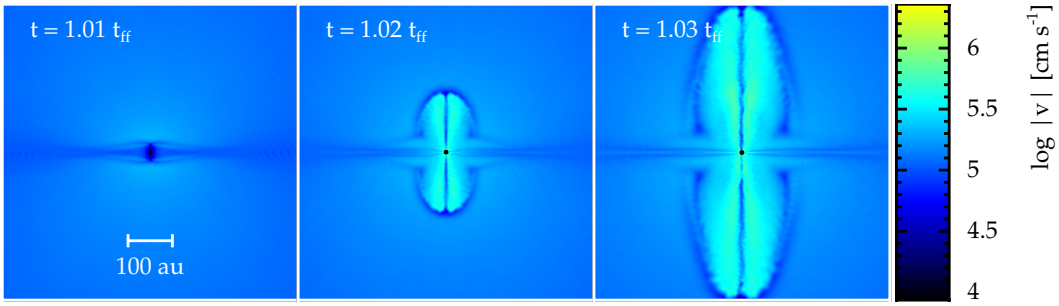

IV.iv.a. $\vartheta = 0°$

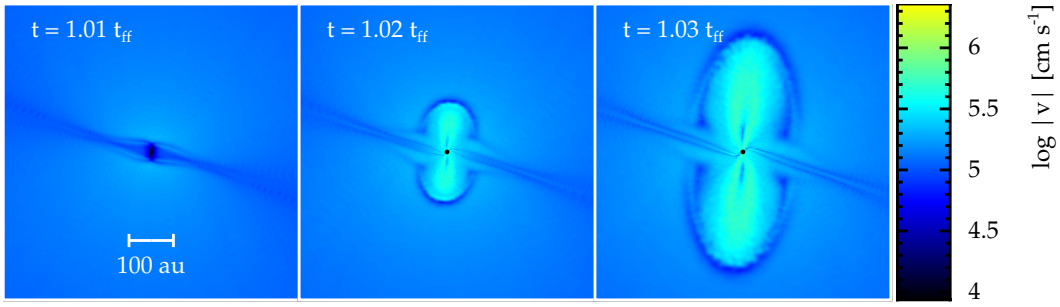

IV.iv.b. $\vartheta = 20°$

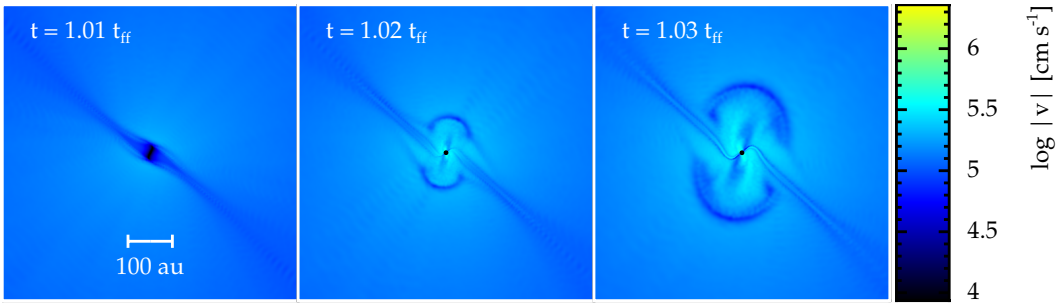

IV.iv.c. $\vartheta = 45°$

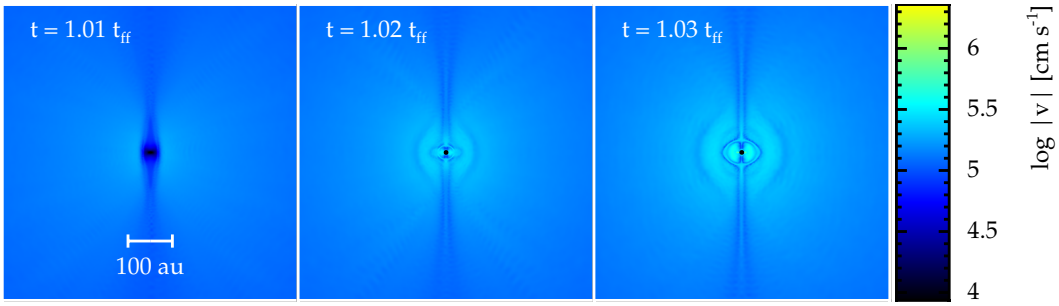

IV.iv.d. $\vartheta = 90°$

Figure IV.iv. Cross–sections of $|v^i|$ for four angles, $\vartheta = 0°, 20°, 45°$, and $90°$, at $t = 1.01$–$1.03\ t_{\rm ff}$. The change in outflow structure as the field geometry is varied is clearly demonstrated: $\vartheta \leq 20°$ has a define fast region of the outflow, and in particular on the $\vartheta = 0°$ calculation the inner collimation can be seen. Conversely the weaker $\vartheta = 45°$ outflow is demonstrated by the clearly reduced outflow velocity, and a comparable observation can be made for $\vartheta = 90°$.

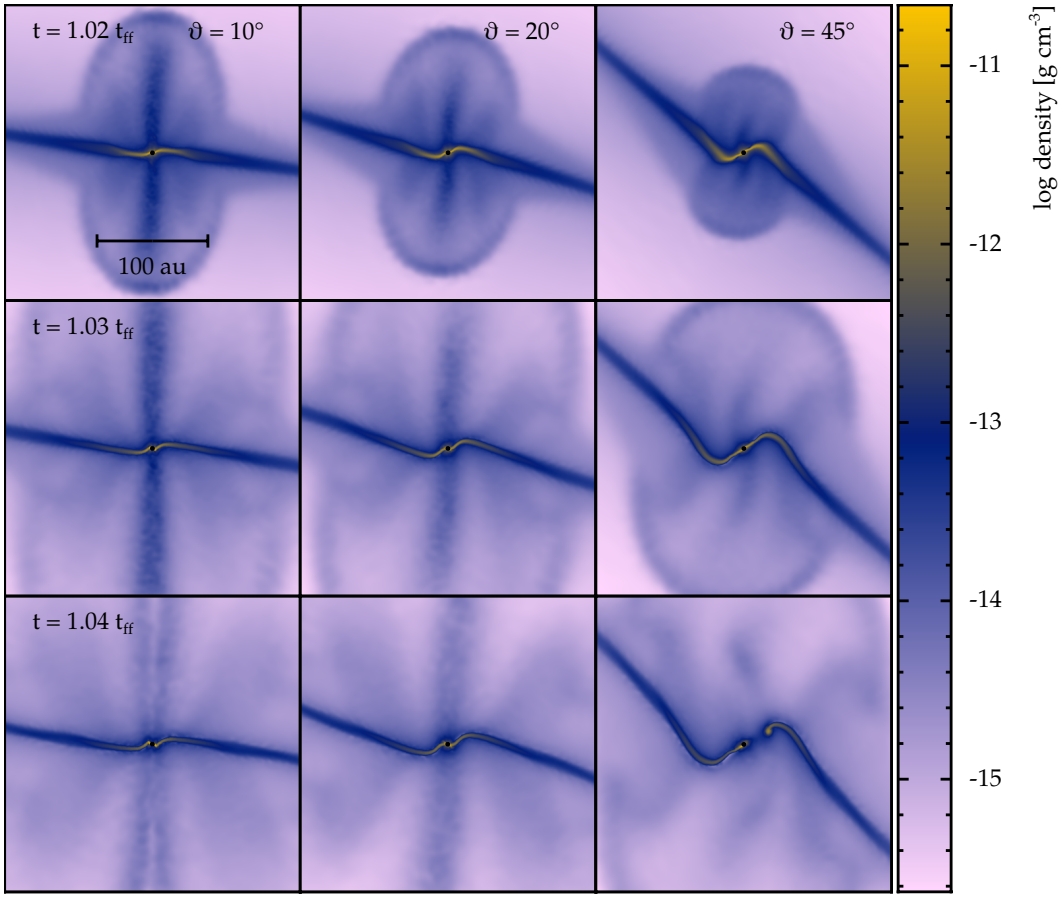

Figure IV.v. Cross–sections of density in the z–x plane for $\vartheta = 10°$ (left–hand column), 20° (centre column), and 45° (right–hand column). Whilst the outer regions of the pseudo–disc align perpendicular to the magnetic field, the innermost region exhibits a more complicated structure. As it deforms, the collimated jet changes from being parallel to the rotation axis to being parallel to the field axis.

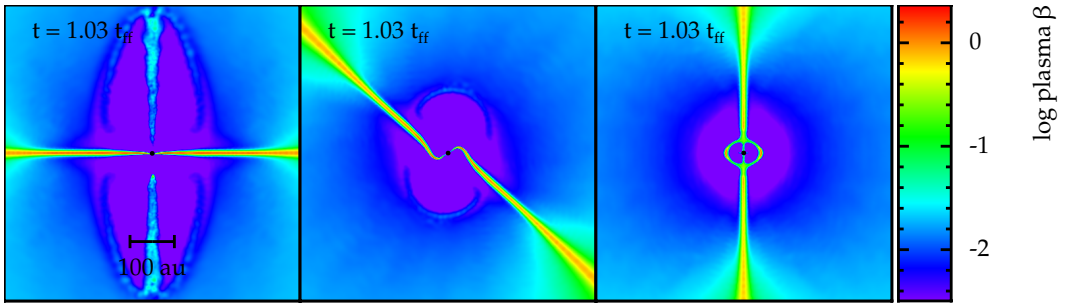

Figure IV.vi. Plasma β cross–sections for $\vartheta = 0°$, 45°, and 90°. In the aligned case, a pressure supported pseudo–disc (aligned perpendicularly to the field) is present with the signature of a collimated jet — a region where the plasma β is approximately an order of magnitude lower than the bulk outflow. In the intermediate case, with $\vartheta = 45°$, the warped shape of the pseudo–disc can be seen whilst the bulk outflow no longer contains a collimated region. Markedly different, the fully misaligned $\vartheta = 90°$ calculation instead has a small magnetically supported bubble around the protostar as opposed to an outflow or jet.

field. Magnetic pressure is a measure of the force provided by the isotropic field so this effect manifests as a suppressed β. This winding, however, then produces the faster jets seen. The $\vartheta = 45°$ calculation still has a low β outflow without this inner winding zone and hence a jet. In addition, the warp in the pseudo–disc can still be seen, showing that the sigmoidal disc is still supported by the fluid pressure even as it is deformed by the interaction of the magnetic field and rotational velocity field.

IV.4 Discs

Reference has been made in the preceding section to the structure of the discs produced around the sink particle. These clearly vary considerably across the range of field geometries, and this variation is a major cause of the variation in outflow morphologies seen. Figure IV.vii shows the temporal evolution of these discs from just before a sink particle is inserted until $1/50\ t_{ff}$ after. Earlier we observed that once the misalignment of the magnetic field was sufficient to interfere with the propensity of the inner region of the pseudo–disc to re–orient towards the rotation axis this prevented collimation and hence reduced the jet speed. Here we see that this also affects the structure of the disc itself. In a sufficiently misaligned calculation, rather than former an approximately flat pseudo–disc, a more complicated sigmoidal or spiral structure is formed. This lack of a flat disc will clearly disrupt any vertical outflow or similar structure. We also observe that the $\vartheta = 90°$ calculation has not formed a disc with a central denser region in the manner of the other calculations but instead a more extensive structure.

Figure IV.viii echoes this analysis: in the same way that outflows can be divided into two morphological classes, *viz.* $0° \leq \vartheta \leq 20°$ and $20° < \vartheta \leq 90°$, the same division

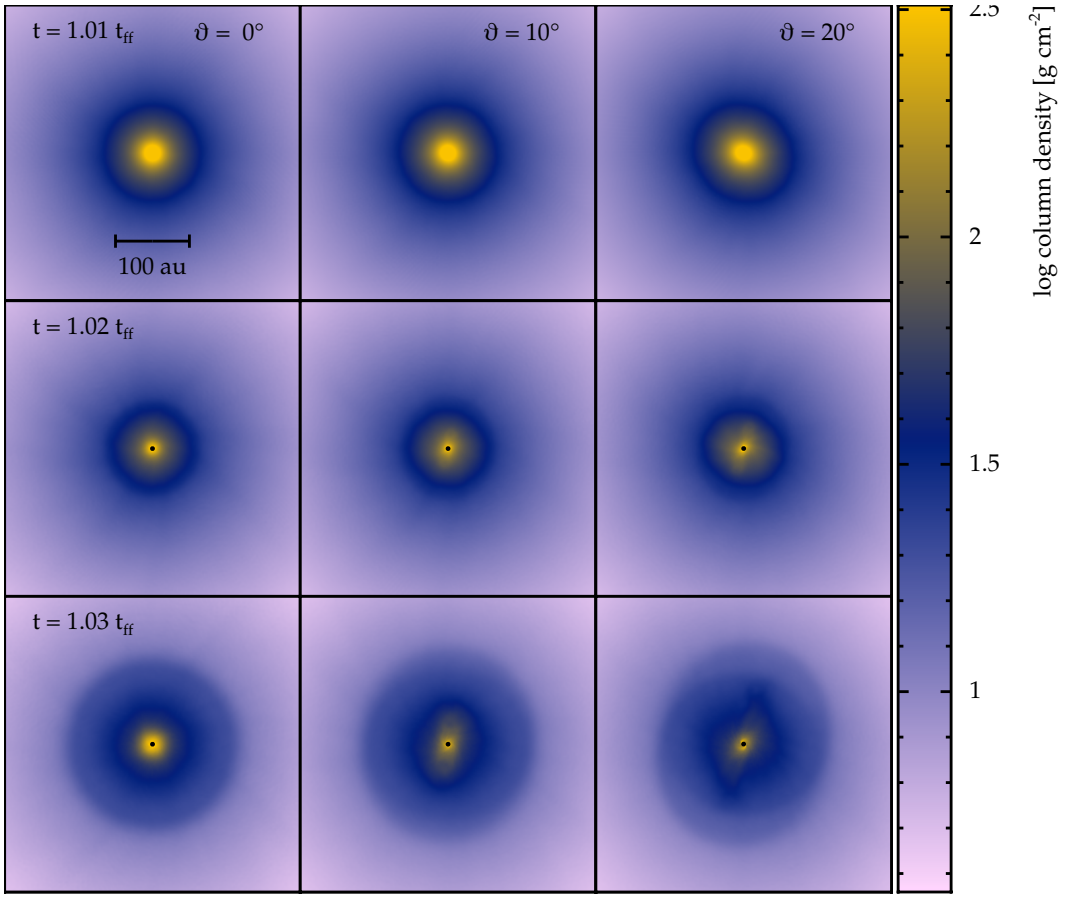

IV.vii.a. Column density projection plots in the z–direction for $\vartheta = 0°$, $10°$ and , $20°$ (across the page) at $t = 1.01\ t_{\rm ff}$, $1.02\ t_{\rm ff}$, $1.03\ t_{\rm ff}$ (down the page).

Figure IV.vii. continued below

can be seen for the pseudo–discs. The first phase, which produces a strong outflow and collimated jet has a comparably large — > 100 au — rotating disc structure. Conversely in the second morphological phase we see that the disc structure has a generally slower velocity and occupies a much reduced spatial extent.

The formation of a flat disc structure is controlled by angular momentum. The displacement of the angular momentum vector from the overall magnetic field vector means that instead of rotating perpendicular to the magnetic field axis the fluid is instead rotating parallel to the field lines. This interferes with the process of winding up the field and producing a larger disc. When the two axes are aligned, the field is twisted by the rotation and collapse of the core and remerges on the other side of the central region, in the fully misaligned case a much more complex structures is formed. This complex structure suppresses the formation of an outflow or jets.

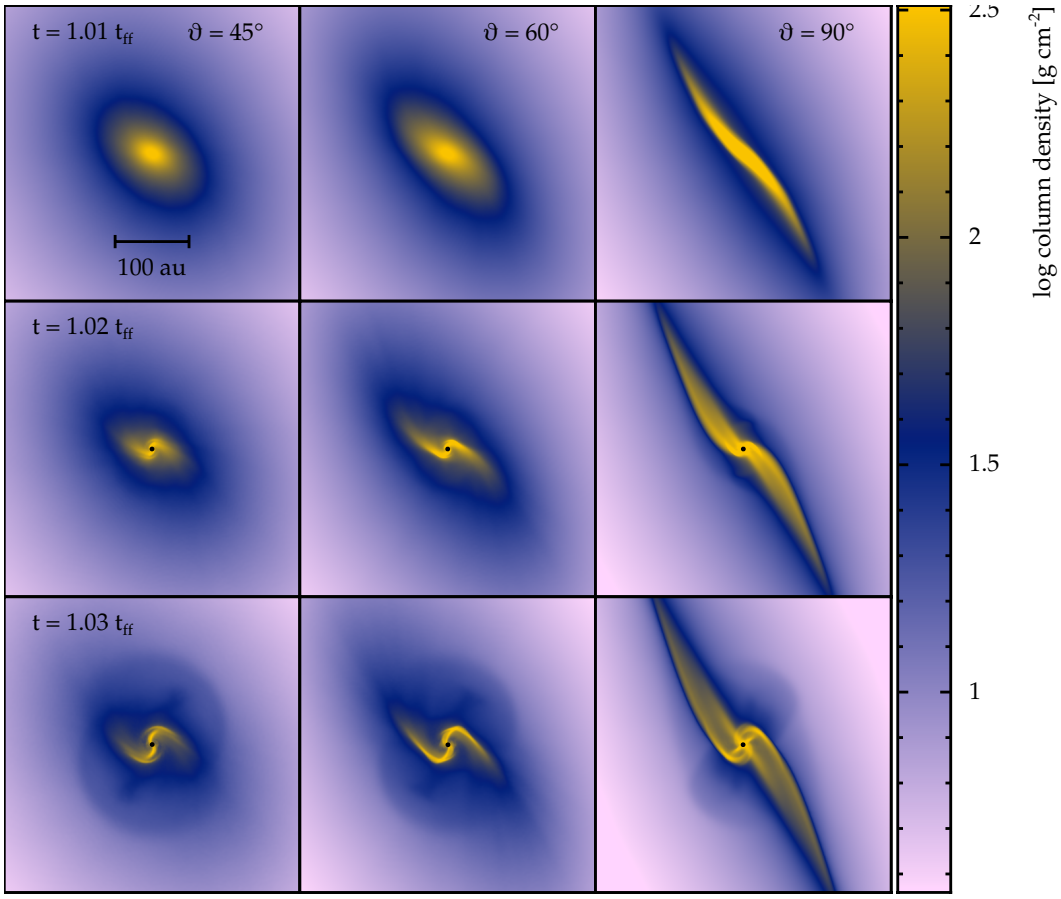

IV.vii.b. Column density projection plots for $\vartheta = 45°$, 60°, and 90° (across the page) at $t = 1.01\ t_{\rm ff}$, $1.02\ t_{\rm ff}$, $1.03\ t_{\rm ff}$ (down the page).

Figure IV.vii. These two sub–figures show column density projections for all six calculations ($0° \leq \vartheta \leq 90°$), this time in the z–direction. Sub–figure IV.vii.a shows the pseudo–disc structure for the three calculations — $0 \leq \vartheta \leq 20°$ — with a clear collimated jet, whilst sub–figure IV.vii.b shows the three calculations where this jet is suppressed and ultimately, at $\vartheta = 90°$, where the outflow itself all–but ceases. There is a clear correlation between the pseudo–disc having a 'flatter' structure, *cf.* the first sub–figure *contra* the more complex sigmoidal or spiral structures in the second sub–figure, and the production of a jet and fast outflow. The more complicated disc structures seen when $\vartheta \geq 45°$ prevent the collimation of the inner region of the jet and consequently disrupt the outflow.

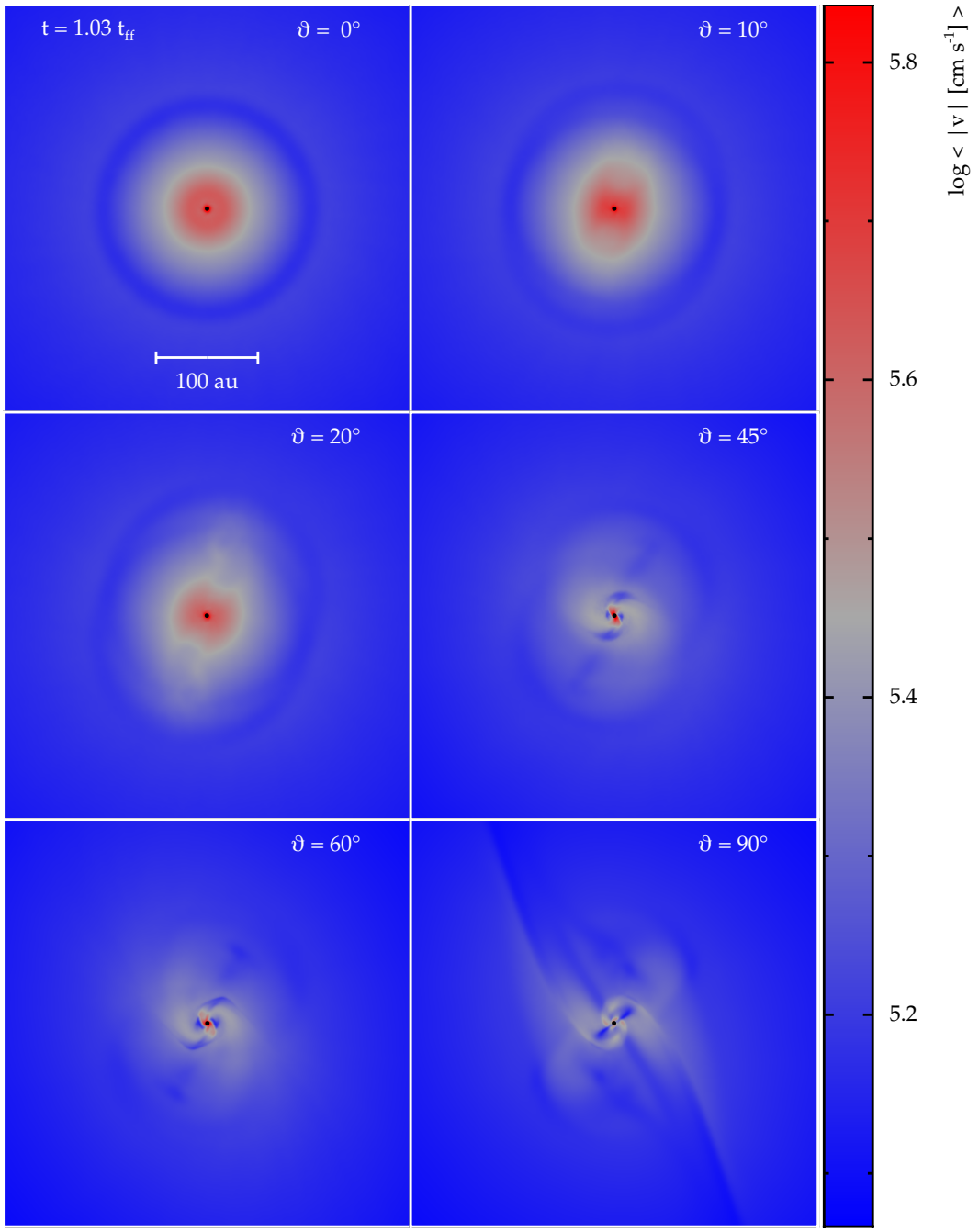

Figure IV.viii. Projections in the z–direction of the density–weighted average of the magnitude of the velocity field for all six calculations at $t = 1.03\, t_{\rm ff}$. We use a density–weighted average not a cross–section to correctly consider the warped discs at large values of ϑ.

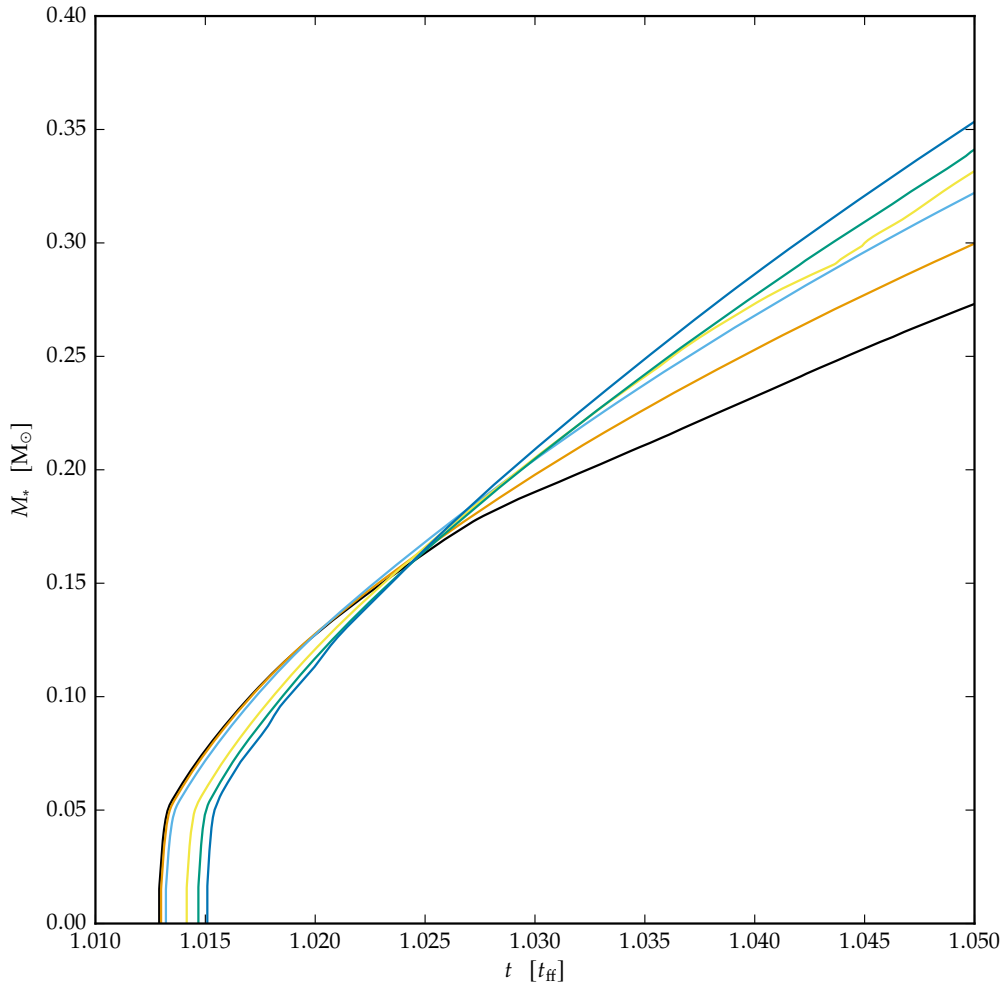

Figure IV.ix. Accretion of mass by the sink particle for $\vartheta = 0°$ (black), 10° (orange), 20° (sky–blue), 45° (yellow), 60° (turquoise), and 90° (blue). After $t \simeq 1.025\, t_{\rm ff}$ higher values of ϑ correlate with increased total masses accreted. The variation before this point is a result of differences in the exact moment a sink particle is inserted not a physical difference in accretion rates.

IV.5 Accretion

In the early part of the simulation, after the sink is inserted, we observe very rapid accretion. This rate then decreases, both due to matter being expelled from the core by outflows and also due to the dynamics of the collapse (Foster and Chevalier 1993), however, the eventual accretion rate does depend on the value of ϑ used.

Figure IV.ix shows the mass accreted by the sink particle for each model as a function of time. The suppression of an outflow as ϑ increases naturally indicates that more material may be falling into the sink and this is born out by figure IV.ix.

This is the expected result given the structure of the cloud core and the very low plasma β in this regime. This is also in concordance with Ciardi and Hennebelle (2010) who found that there was no regime in which the accretion rate fell. Ciardi and Hennebelle (*ibid.*) developed an analytical model (from the C. Hunter (1977) model for an isothermal collapsing sphere) whereby

$$M_{\text{core}}(t) = \tau_{\text{ae}} \dot{M}_{\text{inf}} \left(1 - \frac{1}{\exp t/\tau_{\text{ae}}}\right), \tag{IV.9}$$

where $\dot{M}_{\text{inf}}$ is a constant determined from the sound speed of the medium and

$$\tau_{\text{ae}} \propto \frac{1}{\cos \vartheta}. \tag{IV.10}$$

Equations IV.9 and IV.10 will produce ever faster accretion rates as ϑ increases and we obtain the same result using an S.P.H. method as opposed to an A.M.R. approach. This provides some support to the assumptions made: the sphere collapses held up by thermal and magnetic pressure and by material being removed by the outflow. The pseudo–discs we produce at increasing values of ϑ (and particularly as ϑ exceeds 45°) become increasingly less like discs which are supported by both magnetic and fluid pressure (*vide infra* figure IV.vii)and therefore more conducive to accretion onto the central sink particle. In addition, the velocity and scale of the outflow reduces as ϑ increases, meaning increasingly more material is left to be accreted. We note that this effect was *not* found in Lewis, Bate, and D. J. Price (2015).

We also note that the effects of magnetic braking should be broadly comparable across all the field geometries considered here: the only direction with no braking effects is exactly parallel to the field lines. Naïvely this would seem to indicate a reduction in braking effects when $\vartheta = 90°$ since the overall field axis is now in the plane of the disc. However, the rapidly rotating disc will actually produce a much more complicated field on smaller scales than the initial uniform field, negating this effect.

We see in figure IV.x one of the causes of this increase in accretion rate as ϑ increases. For strongly aligned fields and rotation axes, the accretion process can only happen along the edge of the disc. This would remain true even if the disc itself was disrupted by

physical effects — in essence, rather than being a constant equatorial line, material would accreted at the edges of any bubble or disturbances in the pseudo–disc. For much larger angles, the solid angle over which accretion can occur is much larger — whilst the rotational forces are trying to hold the material into a disc-like structure, the magnetic field acts to counteract this. There is a still a general preference to accrete material along the equator of the sink, rather than the poles because the material is still spinning.

A comparison can be made between sub–figures IV.x.c and IV.x.d, which are for $\vartheta = 20°$ and $45°$ respectively. Both show accretion principally in the plane of a disc, exemplified by a sinusoidal accretion signature on the sink particle. However, as the misalignment increases from $20°$ to $45°$ the solid angle subtended by the accretion from the 'disc' widens. Further, the two spiral arm structures seen in figure IV.vii for $45°$ correspond to the two circular regions with elevated mass flux within the sinusoid. This demonstrates how the warped and complex disc structures produced by misaligned initial magnetic fields can increase the accretion rate onto the protostar. The process then continues, with sub–figure IV.x.e showing how at $\vartheta = 60°$ the imprint of the disc is difficult to discern due to a spherically–symmetrical 'background' mass–flux combined with the two circular signatures of mass flow from spiral structures. Finally, in sub–figure IV.x.f we that at $\vartheta = 90°$ the mass flows are essentially uniform except for the slight remnant of a pseudo–disc and the mass–flux from the two extended arm structures noted in figure IV.vii. The fundamental assumption mentioned above was that accretion in the limit as $\vartheta \to 90°$ was spherically–symmetrical and these results support this.

In essence, we generally confirm the analytical conclusions of Ciardi and Hennebelle (2010) and also provide a further justification to the conclusion that increasing the degree of misalignment between the initial magnetic field axis and the rotation axis increases the accretion rate of the protostar.

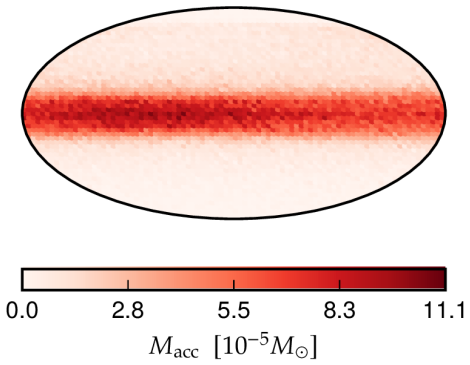

IV.x.a. $\vartheta = 0°$

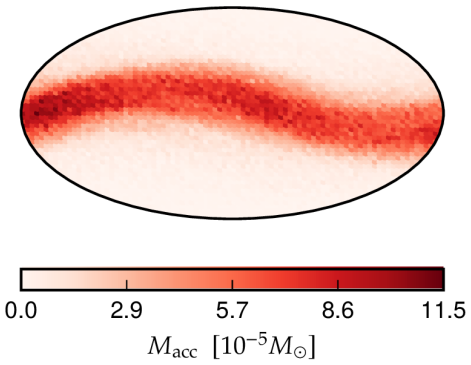

IV.x.b. $\vartheta = 10°$

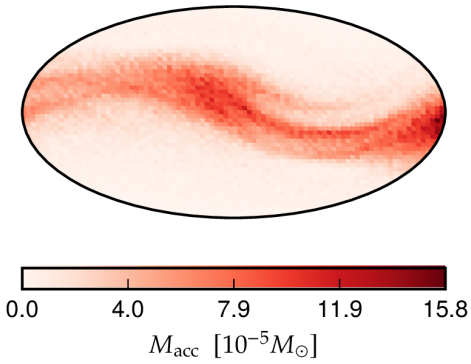

IV.x.c. $\vartheta = 20°$

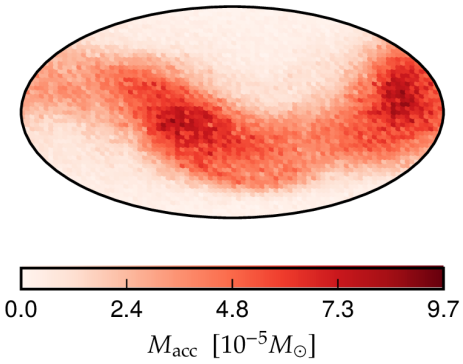

IV.x.d. $\vartheta = 45°$

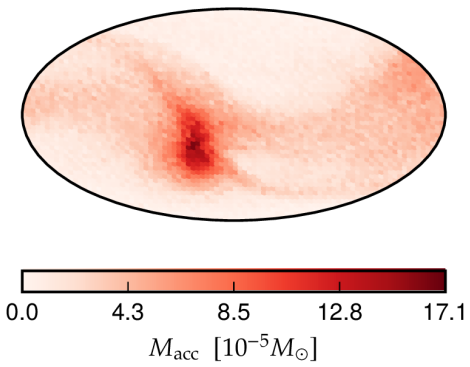

IV.x.e. $\vartheta = 60°$

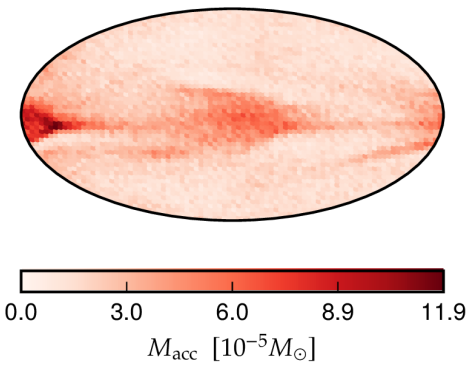

IV.x.f. $\vartheta = 90°$

Figure IV.x. Latitude–longitude maps of fluid accretion for the first 500 a after a sink is inserted for all six calculations, ranging from $\vartheta = 0°$ on IV.x.a to $\vartheta = 90°$ on sub–figure IV.x.f. For the more aligned calculations material is principally accreted only in the plane of the disc, *e.g.* equatorially in sub–figure IV.x.a and sinusoidally in sub–figures IV.x.b and IV.x.c. More misaligned calculations accrete more material and over a greater solid angle, becoming approximately isotropic but with a slight equatorial bias (due to rotational forces still favouring the formation of disc structures) in sub–figure IV.x.f.

CHAPTER V

The Dependence of Protostar Evolution on the Magnitude and Geometry of the Initial Magnetic Field

Du mußt steigen oder sinken
Du mußt herrschen und gewinnen,
Oder dienen und verlieren,
Leiden oder triumphieren,
Amboß oder Hammer sein.

Ein andres, Gesellige Lieder, Johann Wolfgang von Goethe (1787)

Another example is the Hammer and the Anvil, now always used with the implication that the anvil gets the worst of it. In real life it is always the anvil that breaks the hammer, never the other way about.

Politics and the English Language, George Orwell (1946)

We now continue the analysis presented in chapter IV and expand it to consider the interaction between the field geometry and also the magnetic field strength on the evolution of the resulting protostar. This was originally published in Lewis and Bate (2017), and we repeat and expand on that analysis here.

V.1 Motivation

We have already noted that molecular clouds, and hence the molecular cloud cores which collapse to form protostars, are magnetised (Crutcher 2012; Crutcher *et al.* 1993) (and see the discussion in chapter I *supra*), as are protostars and the structures surrounding them. In particular, magnetic outflows are proposed as a mechanism to remove angular momentum from protostars. Some mechanism to transport angular momentum away is necessary since simulations without magnetic fields (Bonnell and Bate 1994; Norman and Wilson 1978) and (semi–)analytic calculations (*e.g.* Terebey, Shu, and Cassen 1984) show that the total angular momentum of cores are too high to form stars without some angular momentum transport mechanism. In addition, Hartmann *et al.* (1986) find that the rotation rates of `T Tauri` stars are substantially lower than the energy required to break up the stellar core. If, for certain field strength or geometries, these outflows can be altered or suppressed, this will constrain how star formation proceeds. In the preceding chapter we showed how the initial geometry of the magnetic field relative to the rotation axis affects the production of these outflows.

Misalignment between magnetic fields and outflows have been observed on scales of molecular clouds (*e.g.* Hull et al., 2013a,b; Stephens *et al.* 2014) down to stellar length–scales, (*e.g.* Donati *et al.* 2010), which drove the consideration *supra*. However, in addition to this a range of mass–to–flux ratios are observed in molecular clouds, ranging from the observation by Crutcher (2005) that the mean mass–to–flux ratio, expressed in terms of the critical value, for *massive* star–forming regions is approximately unity, to Beuther *et al.* (2010) and Giannetti *et al.* (2013). The latter found a much larger range of mass–to–flux ratios in star forming regions, including both sub– and super–critical clouds, a result reinforced by the Bayesian analysis of Crutcher *et al.* (2010). This motivates our consideration of *both* the field strength and the field geometry in this chapter.

Clearly an outflow or comparable angular momentum transport mechanisms exist and can prevent fragmentation due to rotational effects. However, some cores must fragment to produce binaries, while still removing sufficient angular momentum to form stellar cores which do not break up — in effect an intermediary phase between the unary core with an outflow extracting angular momentum from the core and the prolific fragmentation seen in purely hydrodynamical calculations. By varying the field strength a regime whereby some magnetic braking, plus a weak magnetic outflow (but *not* a jet), removes enough angular momentum to allow stellar core formation while still forming a binary may be obtained.

In chapter IV (*cf.* Lewis, Bate, and D. J. Price 2015) we adopted an initial magnetic field strength corresponding to a mass–flux ratio of $\mu = 5$. While mass–to–flux ratios close to the critical value are observed, it is instructive to test the effects of weaker fields. Previous work has indicated that the nature of the outflow in an aligned model ($\vartheta = 0°$) changes with magnetic field strength. This is to be expected — purely hydrodynamic simulations do not produce outflows, so the nature and strength of these outflows must be related to the strength of the magnetic field (see, *e.g.*, D. J. Price, Pringle, and King 2003). Bate, Tricco, and D. J. Price (2014) found that whilst the velocity of the first–core outflow is essentially unchanged, the width of the outflow (*i.e.* the opening angle) increases when the initial field is weaker. In addition, stronger and weaker fields will affect the initial collapse of the molecular cloud core (and may prevent it collapsing at all if a sufficient magnetic pressure can be realised).

Therefore, in this chapter we perform a similar series of calculations to chapter IV, but with weaker fields — corresponding to mass-flux ratios of $\mu = 10$ and 20. We present S.P.M.H.D. simulations of three mass–to–flux ratios and four field geometries. This allows us to probe a range of field strengths. Additionally we can observe how the changing field geometries changes the nature and extent of the outflows observed. We do not include non–ideal M.H.D. effects (see Tsukamoto *et al.* 2015a,b; Wardle 2007; Wurster, D. J. Price, and Ayliffe 2014; Wurster, D. J. Price, and Bate 2016) and therefore can not probe the regime where μ is less than or equal to unity and therefore do not continue our work to field strengths stronger than $\mu = 5$. However, the results presented here cover the majority of initial conditions present in laminar, sub–critical, cores.

We first discuss our initial conditions in section V.2. We will then discuss the first isothermal phase of the collapse of the cloud core, which is essentially common to all initial fields, in section V.3; followed by a consideration of each field strength in turn in sections V.4 to V.6. We first return to our consideration of the $\mu = 5$ initial conditions to introduce a new analysis of jet and outflow formation based on a poloidal–toroidal decomposition of the magnetic field vector in section V.4, before considering $\mu = 10$ and 20 respectively in the following two sections.

V.2 Initial Conditions

We adopt initial conditions broadly identical to section IV.2: we use $1\,1/2$ million S.P.H. calculations in the core and a further $1/2$ million in the container medium, arrayed on a cubic lattice. We then set these particles so that the core has an initial mass of $M_{\rm core} = 1\,{\rm M}_\odot$ with a 30:1 density contrast between the uniform density core and the outer medium. We use the barotropic equation of state given in equation IV.1 (Machida, Inutsuka, and Matsumoto 2008) with the usual critical densities of $\rho_{c,1} = 10^{-14}\ {\rm g\cdot cm^{-3}}$ and $\rho_{c,2} = 10^{-10}\ {\rm g\cdot cm^{-3}}$. The core and the medium are in pressure equilibrium, so setting the initial temperature in the core to 13.8 K sets the container medium to ≈ 400 K. We then thread

an initially uniform magnetic field through the core and medium, set as before according to the dimensionless mass–to–flux ratio, μ, and the angle between the magnetic field and rotation axes, ϑ. As before, the initial velocity field in the core is set so that the core is in solid–body rotation with $\Omega_0 = 1.77 \times 10^{-13}\,\mathrm{rad}\cdot\mathrm{s}^{-1}$, which is equivalent to $\beta_{\mathrm{rot}} = 0.005$.

In this chapter we use field strengths corresponding to $\mu \in [5, 10, 20]$, or $\left|B^i\right|_0 = [163, 81, 41]$ $\mu\cdot\mathrm{G}$, respectively. For each of these values of μ we then perform calculations with $\vartheta \in [0°, 20°, 45°, 90°]$.

V.3 Isothermal Collapse

The sphere of cold gas described in section V.2 is allowed to collapse. For this discussion, we divide the collapse of the cloud core into two phases: firstly an initial isothermal collapse, where the maximum densities are below $\rho = \rho_{c,1} = 10^{-14}\,\mathrm{g}\cdot\mathrm{cm}^{-3}$ and then a second phase where a disc structure and pre–stellar core is formed. We first describe the initial isothermal phase which, aside from slight variations in timings, is comparable for all three field strengths. We then, in sections V.4 to V.6, consider the three field strengths in more detail, focusing in sections V.4 and V.5 on the formation of bipolar outflows and how these vary with the field geometry, and in section V.6 on how the weakest field strength can form binary and multiple protostellar systems.

The first phase of the collapse extends from $t = 0$ to $0.98\,t_{\mathrm{ff}}$ (where the free–fall time, $t_{\mathrm{ff}} = 24{,}430$ a). The latter portion of this is shown on the left of the plots in figure V.i where the maximum density increases more slowly with time. The main effect from the initial conditions observed here is that the lower mass–to–flux ratios provide higher magnetic pressures — $p_{\mathrm{mag}} \propto B^2$ so the doubling of the field strength between $\mu = 10$ and 5 provides a corresponding quadrupling of the pressure support. This results in the duration first phase of the collapse being slightly extended for the stronger fields. For example, the $\mu = 10$ calculations reach a density of $10^{-10}\,\mathrm{g}\cdot\mathrm{cm}^{-3}$ $1/100\,t_{\mathrm{ff}}$ quicker than the stronger field calculations, delaying the subsequent phase of evolution accordingly. Figure V.ii shows the formation of the bipolar outflows for an aligned calculation (*i.e.* where $\vartheta = 0°$), which are launched when a pseudo–disc forms and the density exceeds $\approx 10^{-10}\,\mathrm{g}\cdot\mathrm{cm}^{-3}$ (and consequently the $1/100\,t_{\mathrm{ff}}$ delay when $\mu = 5$). A comparable effect is shown in figure V.iii for $\vartheta = 45°$, demonstrating that this is independent of the field geometry. We discuss this in more detail in sections V.4 and V.5.

The field geometry, *i.e.* ϑ, does not affect the overall rate of the collapse since the magnetic pressure terms, which act to support the cloud against gravity, are isotropic and therefore independent of ϑ. However, the tension component *is* anisotropic and, in general, acts to stop the fluid moving perpendicular to the magnetic field lines. Consequently this causes the collapsing core to become ellipsoidal. Thus, the $\vartheta = 0°$ calculations produce an oblate spheroid while conversely the $\vartheta = 90°$ calculations produce prolate spheroids and 20° and 45° produces a tri–axial ellipsoid. Figure V.iv shows how

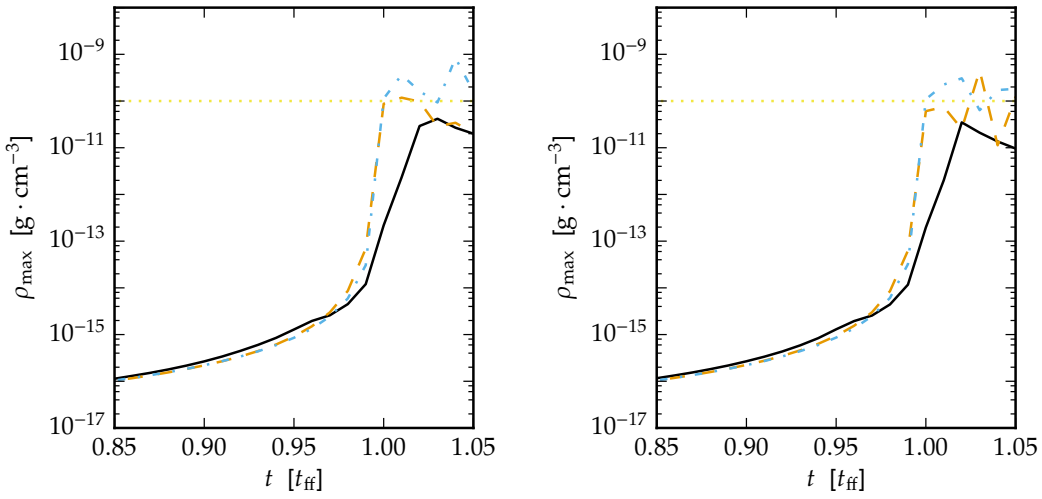

V.i.a. $\vartheta = 0°$ *V.i.b.* $\vartheta = 20°$

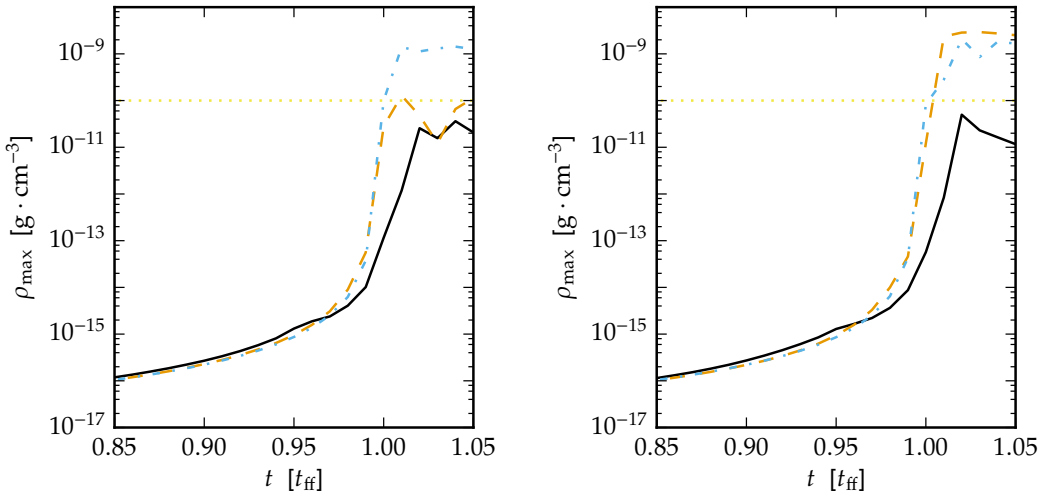

V.i.c. $\vartheta = 45°$ *V.i.d.* $\vartheta = 90°$

Figure V.i. Maximum density as a function of time (where one free–fall time, $t_{\rm ff} = 24{,}430$ a) for each of the $\mu = 5$ (solid black line), 10 (dashed orange line), and 20 (dot–dashed blue line) calculations with $\vartheta = 0°$ (sub–figure V.i.a), $\vartheta = 20°$ (sub–figure V.i.b), 45° (sub–figure V.i.c), and 90° (sub–figure V.i.d) respectively. In all cases, the $\mu = 10$ and 20 calculations reach $\rho_{\max} > 10^{-11}$g · cm^{-3} $1/100$ $t_{\rm ff}$ earlier than the $\mu = 5$ calculations. However, until $t \approx 0.97$ $t_{\rm ff}$ the maximum densities are similar. The yellow dotted line at $\rho_{\rm crit} = 10^{-10}$ g · cm^{-3} indicates the critical density above which sink particles may be inserted if the appropriate formation tests are passed, and is therefore an approximate maximum density for the calculation. In the $\mu = 5$ calculations, the sink insertion quickly removes the entire region where $\rho > \rho_{\rm crit}$ and consequently the maximum density appears to not exceed the sink formation threshold; for both $\mu = 10$ and 20 a region where $\rho > \rho_{\rm crit}$ persists and is not removed by the insertion of further sink particles since one or more of the creation tests in Bate, Bonnell, and N. M. Price (1995) has failed. This high density gas exists in a disc around the sink particle.

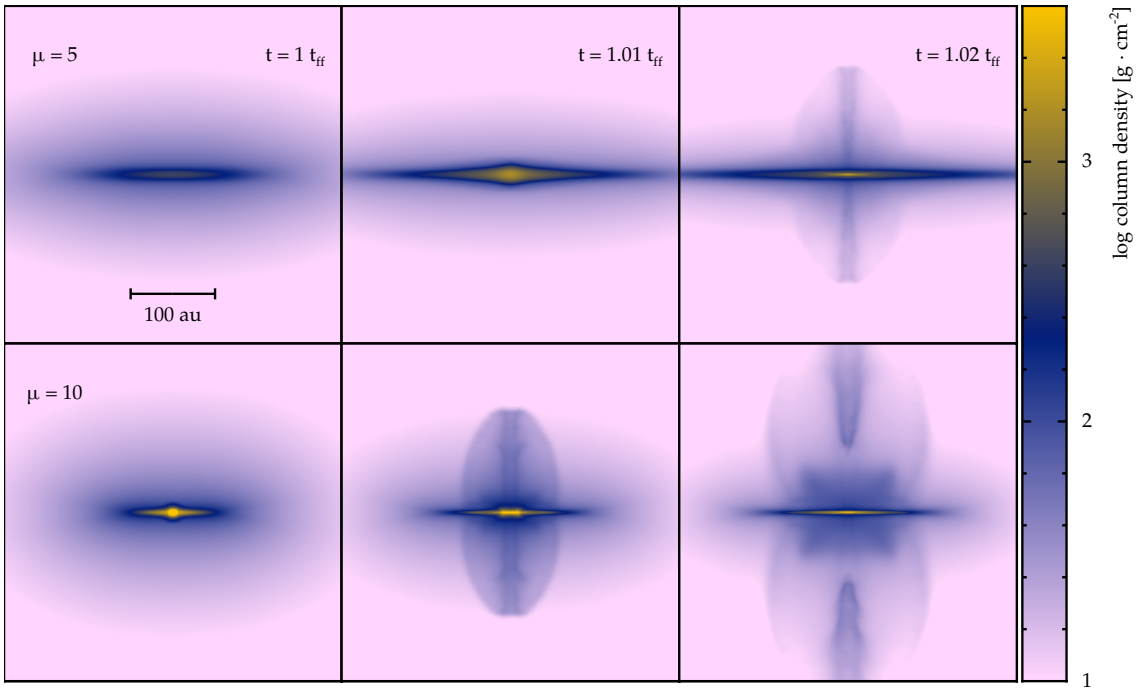

Figure V.ii. Column density projections in the z–x plane for the $\vartheta = 0°$ $\mu = 5$ and 10 models as the sink particle is inserted and jets are formed. The $\mu = 10$ calculation collapses to a dense disc, and hence forms an outflow, at a dynamical time $\approx 1/100\ t_{\rm ff}$ earlier than $\mu = 5$.

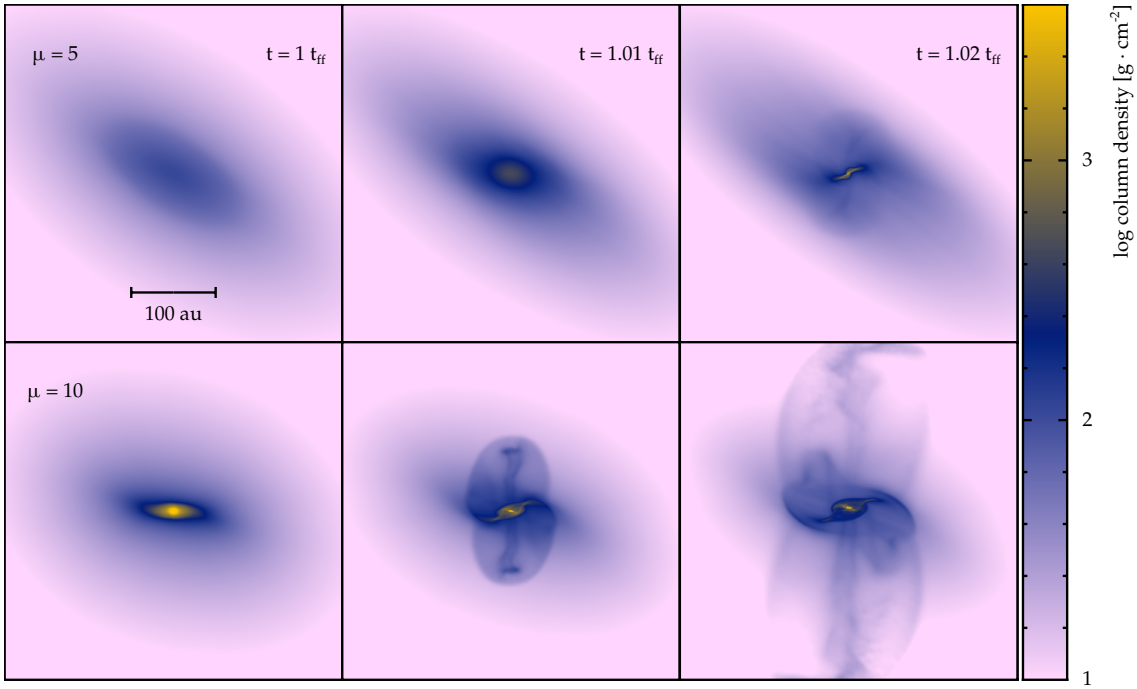

Figure V.iii. Column density projections in the z–x plane for the $\vartheta = 45°$ $\mu = 5$ and 10 models as the sink particle is inserted and jets are formed, similar to figure V.ii above. As before the $\mu = 10$ calculation forms a jet $\approx 1/100\ t_{\rm ff}$ earlier than $\mu = 5$, notwithstanding the change in field geometry.

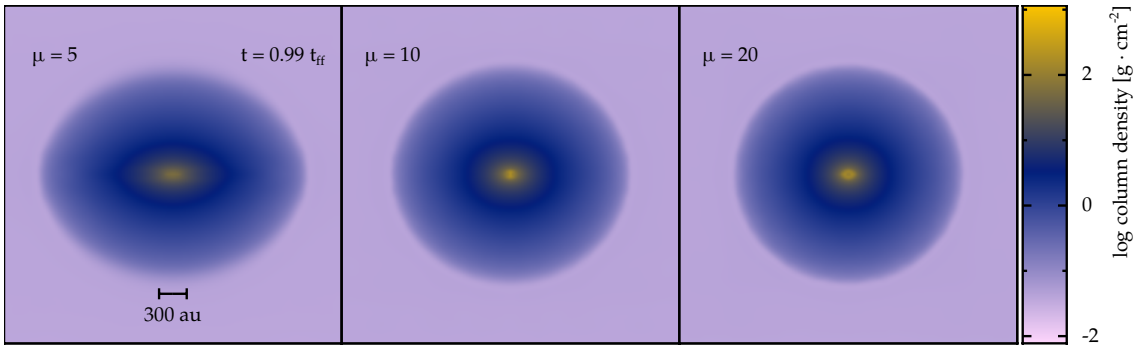

V.iv.a. $\vartheta = 0°$

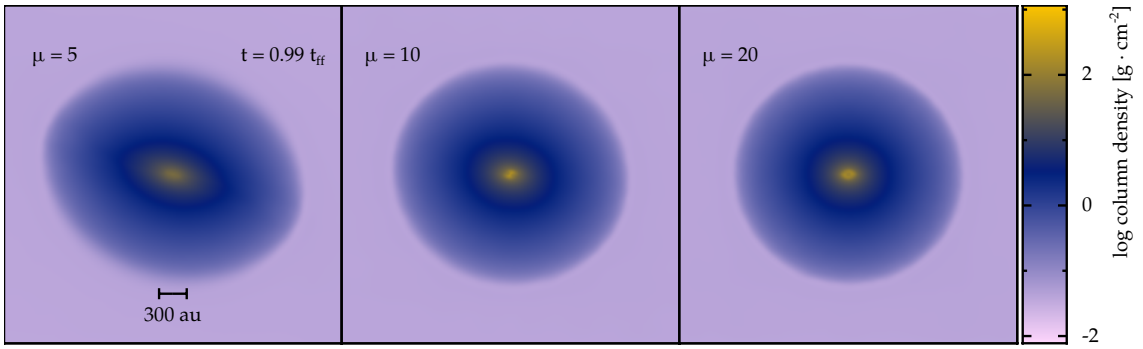

V.iv.b. $\vartheta = 20°$

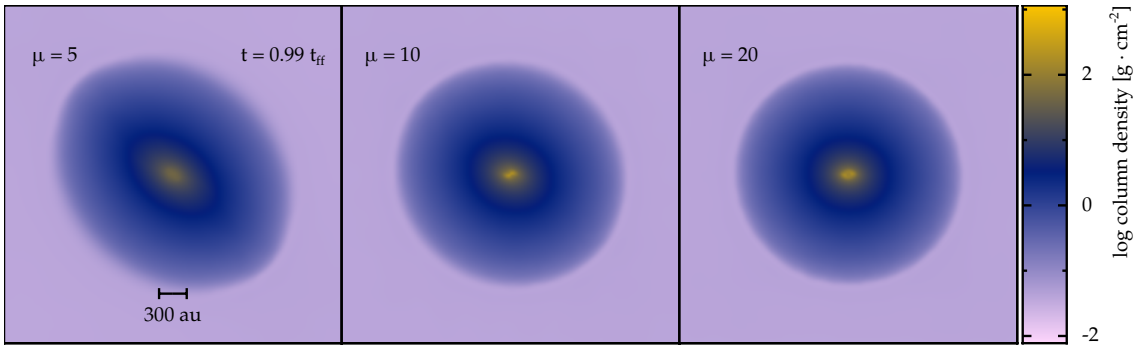

V.iv.c. $\vartheta = 45°$

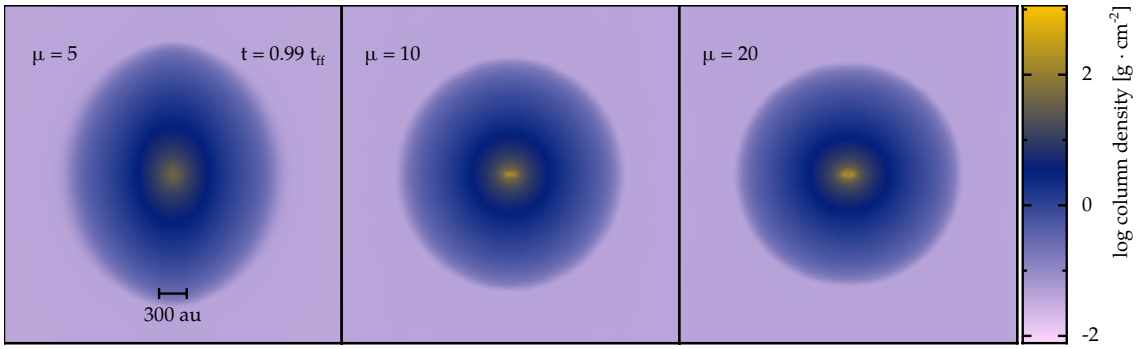

V.iv.d. $\vartheta = 90°$

Figure V.iv. Column density projections in the z–x plane for $\mu = 5$, 10, and 20 at $t = 0.99\ t_{\rm ff}$ showing the change in ellipsoidality of the collapsing core. The case with the stronger field, with $\mu = 5$, is much more oblate than those with either $\mu = 10$ or 20. We obtain approximate eccentricities of 0.66, 0.34, and 0.24 for each calculation, respectively.

the oblateness of the spheroids changes with field strength, with the axis ratios of 0.66, 0.34, and 0.24 for $\mu = 5$, 10, and 20 at $\vartheta = 0°$ respectively observed in sub–figure V.iv.a. We also see that as the core changes from an oblate spheroid to being triaxial and ultimatly prolate (sub–figures V.iv.b to V.iv.d) these axis ratios are maintained.

Figure V.i shows how the maximum fluid density evolves as a function of time for all twelve calculations. At 0.98–0.99$t_{\rm ff}$ (depending on the calculation) the density begins to rapidly increase. This marks the change from the isothermal and weakly oblate collapsing core to the second phase. The magnetic forces described above which acted to make the core oblate now cause the formation of a flattened disc-like structure. We use the term pseudo–disc to describe this object, which is not a 'classical' accretion disc in Keplerian rotation around a protostellar core. Nevertheless it is rotating albeit with a sub–Keplerian rotation profile, is supported by the gas pressure perpendicular to the pseudo–disc plane against further gravitational collapse parallel to the magnetic field axis, and is accreting onto the protostar (*i.e.* the radial velocity of the disc relative to the protostar is negative). We discuss this further in sections V.4 and V.5.

V.4 $\mu = 5$

The strongest initial field strength used in this chapter is $\mu = 5$. After the initial isothermal collapse phase discussed above, all four field geometries form small pseudo–discs and bipolar outflows, which we show at $t = 1.02\ t_{\rm ff}$ in figure V.v.

Once a significant pseudo–disc forms, magnetic and rotational forces become comparable in magnitude to gravitational forces — driving the formation of effects like the bipolar outflows. Previous simulations of magnetised collapse and outflows used strong fields, aligned with the rotation axis (*e.g.* Machida, Inutsuka, and Matsumoto 2008; Matsumoto and Tomisaka 2004; Tomisaka 2002); here we also vary ϑ similar to the approach in Ciardi and Hennebelle (2010) and Lewis, Bate, and D. J. Price (2015).

Inclination angles $\vartheta \leq 45°$ produce a bipolar outflow. It is convenient to divide these outflows into two regions: an overall bulk outflow and an inner collimated jet. We decompose the magnetic field into cylindrical co-ordinates, where

$$\begin{cases} r = \sqrt{x^2 + y^2} \\ \phi = \arctan \dfrac{y}{x} \\ z = z, \end{cases} \tag{V.1}$$

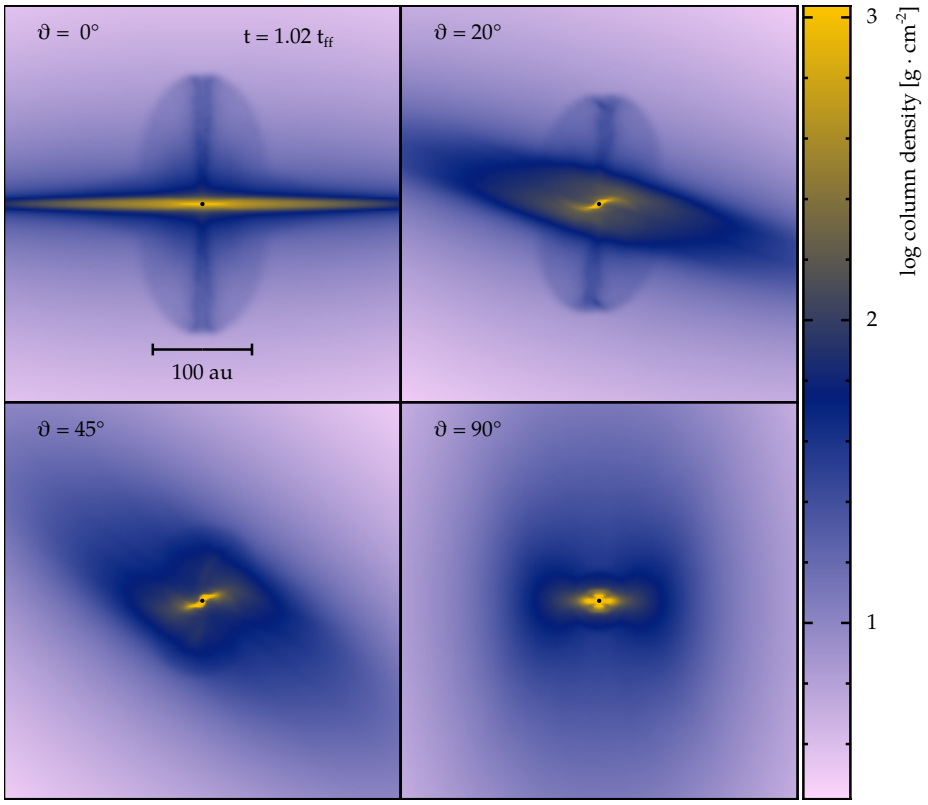

V.v.a. Column density projection in the direction of the y–axis

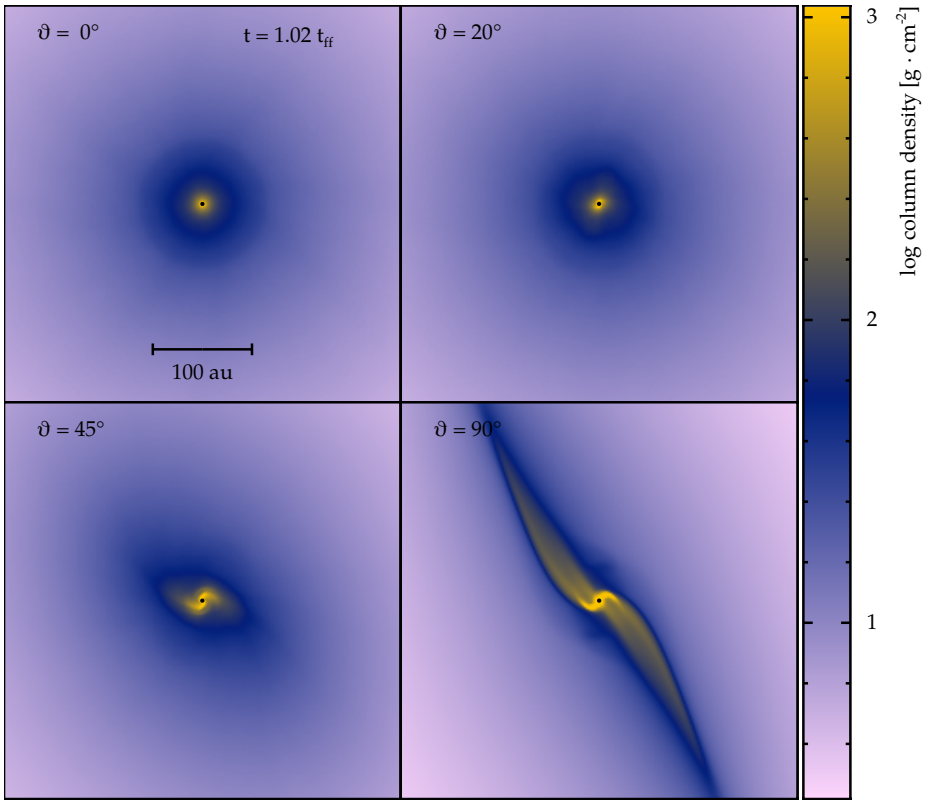

V.v.b. Column density projection in the direction of the z–axis

Figure V.v. continued below

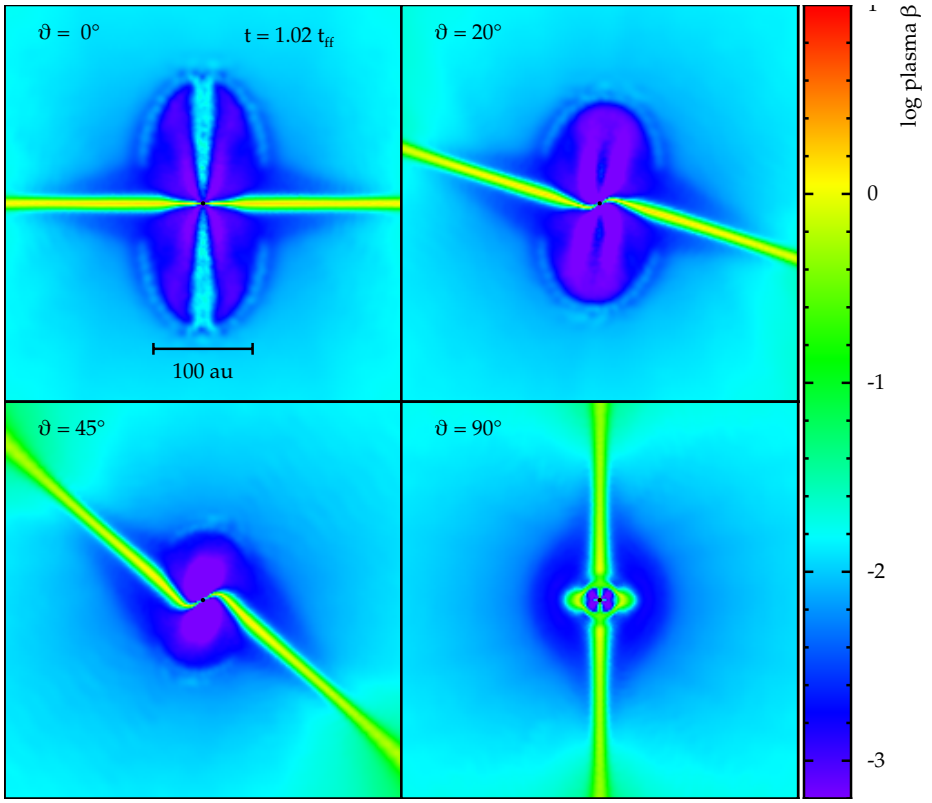

V.v.c. β cross–section in the x–y plane

Figure V.v. Column density projections in the direction of the y–axis (sub–figure V.v.a) and z–axis (sub–figure V.v.b), and cross–sections of the plasma β in the z–x plane (sub–figure V.v.c) for the four $\mu = 5$ calculations at $t = 1.02\ t_{\rm ff}$. The initial inclination between the rotation and magnetic field on each sub–figure is identical, with the upper row being $\vartheta = 0°$ and $20°$ and the lower row being $\vartheta = 45°$ and $90°$. Sink particles are represented by a black dot, approximately four times larger than the accretion radius. The alignment of the large scale pseudo–disc perpendicular to the magnetic field axis can be clearly seen, as can the reduction in the outflow velocity and eventual suppression as $\vartheta \rightarrow 90°$, as can the co–location of an outflow, *i.e.* material moving away from the pseudo–disc, and the region where $\beta < 1$.

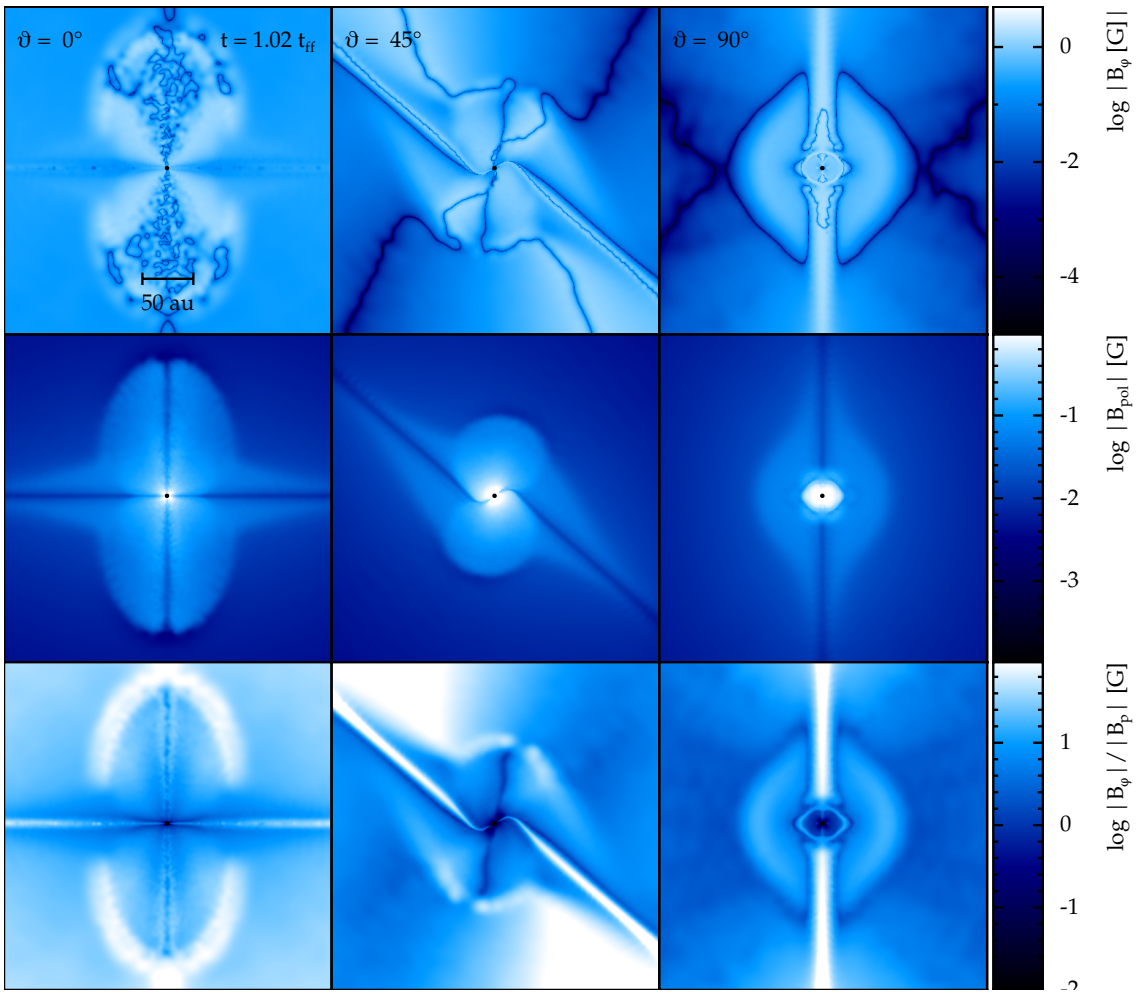

Figure V.vi. Cross–sections of the toroidal magnetic field (upper row, *cf.* equation V.4), poloidal magnetic field (middle row, *cf.* equation V.3), and the ratio of the toroidal to poloidal field components (lower row), for $\vartheta = 0°, 45°, 90°$, $\mu = 5$ calculations at $t = 1.02\ t_{\rm ff}$. Values < 1, *i.e.* black and dark blue, on the lower row indicate regions where the poloidal field is dominant; conversely values > 1 which are indicated with lighter blues and whites are regions where the toroidal field dominates. A clear poloidal region around the sink particle (approximately a radius of 12 au) in the $\vartheta = 90°$ calculation can be seen on both the lower and middle rows, as can the strongly toroidal region centered on the rotation axis on the lower and upper rows. This can be contrasted with the other two calculations where the toroidal field (which acts to collimate an outflow) stretches into the pseudo–disc and the region around the sink particle, producing the characteristic bipolar jet.

so that the magnetic field in this co–ordinate system is given by

$$\begin{cases} B_r = B_x \dfrac{x}{r} + B_y \dfrac{y}{r} \\ B_\phi = B_y \dfrac{x}{r} - B_x \dfrac{y}{r} \\ B_z = B_z. \end{cases} \tag{V.2}$$

Then (*e.g.*, as in Parker 1955) the azimuthal field, B_ϕ , and the toroidal field component are identical,

$$B_{\rm tor} = B_\phi, \tag{V.3}$$

and the magitude of the poloidal component is given by

$$\left|B_{\rm p}\right| = \sqrt{B_r^2 + B_z^2}. \tag{V.4}$$

Figure V.vi shows the ratio of the poloidal to toroidal field in a cross–section slice for the $\vartheta = 0°$, $45°$, and $90°$ calculations. A thin (*ca.* 5 au wide) region dominated by the poloidal field may be observed, centred on the rotation axis and hence the jet. This poloidal field acts to move material away from the pseudo–disc which is dominated by the toroidal field. The disc and its toroidal field act to 'wind–up' the magnetic field and then material and angular momentum are ejected in the outflow; the central region of which is collimated by the toroidal component. A comparable effect, albeit with a somewhat lesser toroidal field contribution, is seen for $\vartheta = 45°$ (central panel of figure V.vi).

In sharp contrast, the $\vartheta = 90°$ calculation has no jet — but does have a small (with a maximum height above the disc of 10 au) bulk outflow. This is produced by the small region around the pseudo–disc which is dominated by the poloidal magnetic field (shown in the right–hand panel of figure V.vi). We observe that above this, again centered on the rotation axis, a thin highly toroidal region exists centered on the rotation axis. However, this is not connected to the pseudo–disc and consequently can not act to collimate a jet — in essence, because the pseudo–disc is rotating in the same plane as the magnetic field lines it is unable to perform the same 'winding' effect seen when $\vartheta = 0°$. The presence of a collimated bipolar outflow therefore clearly implies a combination of sufficent magnetic pressure (exemplified by the poloidal field magnitude) to lift material out of the pseudo–disc *combined with* a toroidal field which can collimate and drive the jet (*cf.* Lynden–Bell 1996, 2001).

Earlier, we observed that changing the values of ϑ changed the collapsing cloud core from oblate to tri–axial. This effect continues into the later phase of the collapse where the consequent pseudo–disc aligns perpendicular to the magnetic field axis (and hence parallel to the major axis of the antecedent ellipsoid) (Galli and Shu 1993). However, we find that the innermost region of the disc, with a radius of < 20 au, attempts to re–align

with the rotation axis, caused by the angular momentum at this scale being sufficient to overcome the magnetic tension force which is aligning the larger scale disc. This produces warped pseudo–discs for $\vartheta > 0°$. This effect is most marked when $\vartheta = 90°$ where the inner disc has a radius of 25 au, but can also be seen for 20° and 45° albeit with a radii of 5–10 au, and with a clearer connection to the rest of the pseudo–disc.

This change in disc morphology then affects the rotation speed of the pseudo–disc, and consequently the nature of the outflow produced. Figure V.vii shows the radially averaged tangential velocity of the pseudo–disc for each value of ϑ compared to the Keplerian velocity at that radius. We find that although the $\vartheta = 90°$ calculation (which produced no bipolar outflow) has a faster rotation profile overall, it lacks the rapid inner region seen when $\vartheta = 0°$. The two intermediate geometries exhibit a rapid increase in rotation speed within $r < 5$ au but generally slower rotation profiles overall, consistent with the other observations about the structure of the discs in these calculations.

This inner region drives the central collimated region of the outflow. Although the opening angle of the bulk outflow is very large — the diameter of the whole outflow is on the order of 100 au — the collimated inner region is much smaller and is correlated with the inner disc. As a result the outflow initially aligns much closer to the rotation axis than the magnetic field axis, for example when $\vartheta = 20°$, the inclination of the jet to the rotation axis is less than 10°. The outflow (and in particular the jet) is removing angular momentum from the pseudo–disc so a close alignment between this and the direction of the angular momentum vector is to be expected.

V.5 $\mu = 10$

The subsequent evolution of the $\mu = 10$ calculations follows a similar overall pattern to $\mu = 5$ calculations. Those with $\vartheta \leq 45°$ produce collimated outflows, which are faster and more closely aligned to the rotation axis for lower ϑ. As we discussed earlier, however, the reduction in the magnetic field strength and the consequently reduced magnetic pressure support causes the core to collapse to higher densities more quickly. A more rapid collapse results in a correspondingly earlier formation of the outflow and jet; whilst the reduced magnetic braking produces different pseudo–discs and outflow velocities compare to $\mu = 5$.

In the $\mu = 5$ calculations we obtained a pseudo–disc with a radii of ≈ 50 au for $\vartheta < 45°$ and < 15 au for $\vartheta \geq 45°$. Figure V.viii (central columns) shows how for $\mu = 10$ the same initial values of ϑ produce much larger pseudo–discs: we obtain radii of ≈ 100 au for $\vartheta \leq 45°$ and 25 au for 90°. We see the same correlation between pseudo–disc radius and ϑ, whereby the disc radii reduce as the initial inclination of the field axis to the rotation axis is increased, but for $\mu = 10$ these are in general larger than the corresponding $\mu = 5$ calculation. The apparently larger discs seen in the left column of figure V.v, particularly for $\vartheta = 0°$ compared to figure V.viii is due to a projection effect caused by looking along

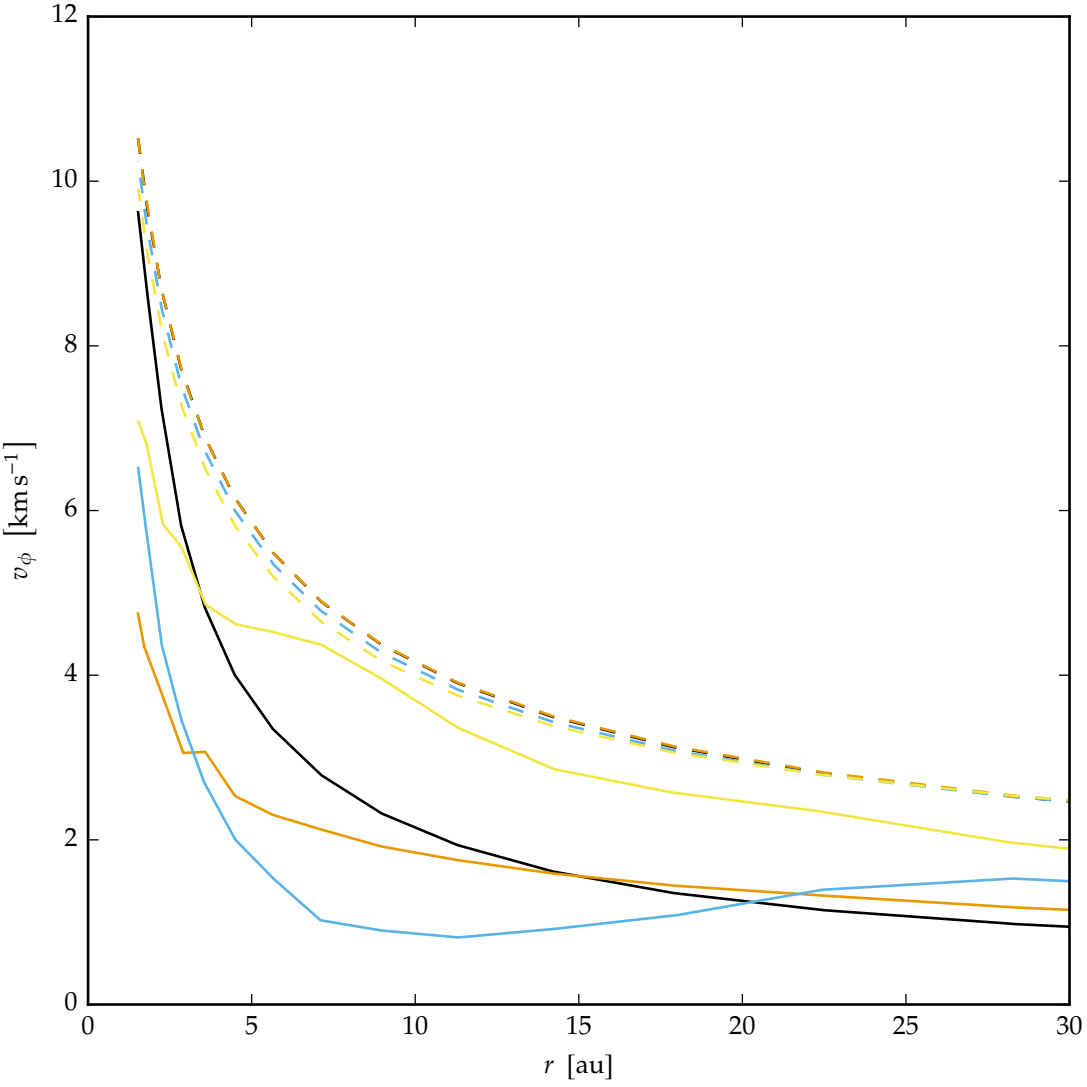

Figure V.vii. Radially averaged tangential velocity, v_ϕ, as a function of radius, r, for $\mu = 5$, $\vartheta = 0°$ (solid black line), $\vartheta = 20°$ (orange line), $\vartheta = 45°$ (blue line), and $\vartheta = 90°$ (yellow line), compared to the corresponding Keplerian velocities for each geometry (dashed lines).

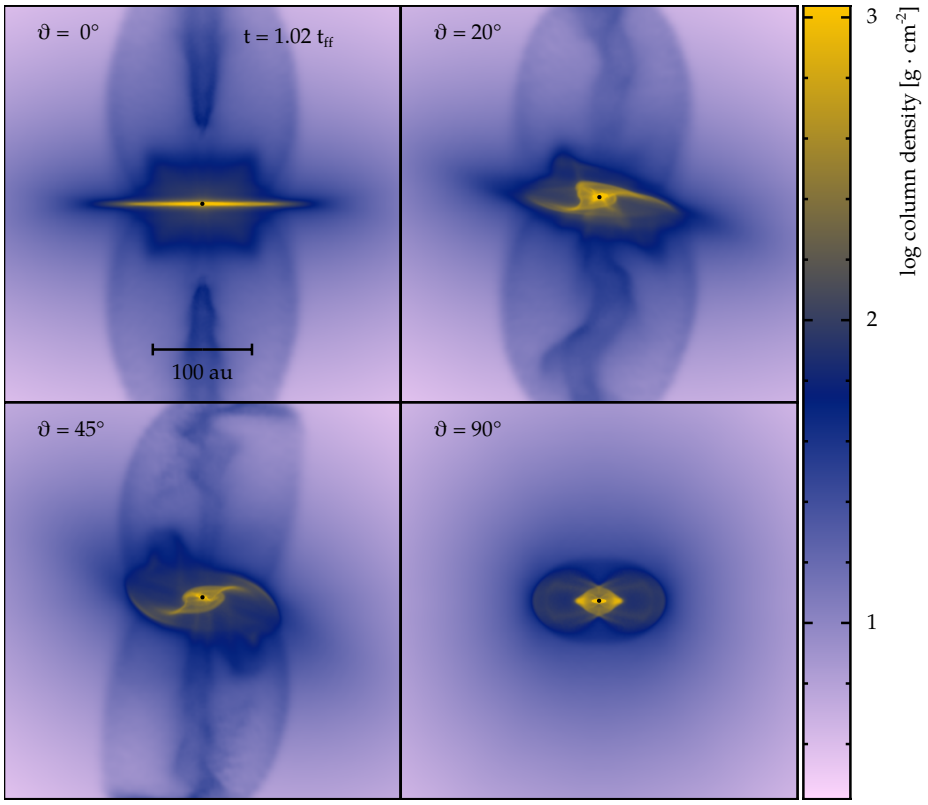

V.viii.a. Column density projection in the direction of the y–axis

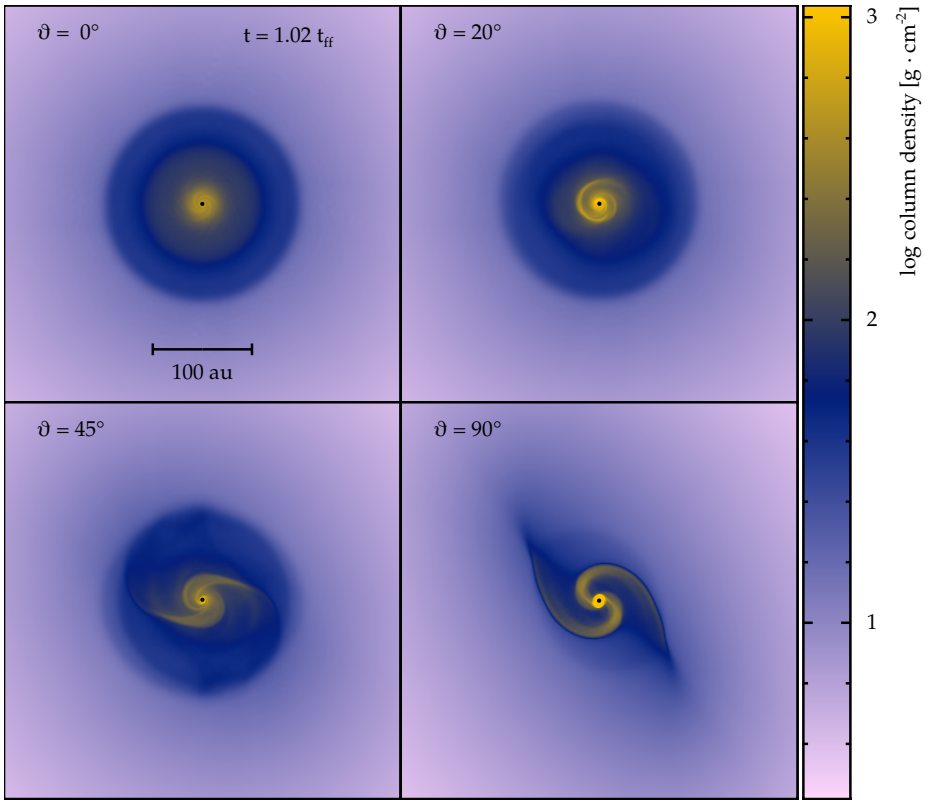

V.viii.b. Column density projection in the direction of the z–axis

Figure V.viii. continued below

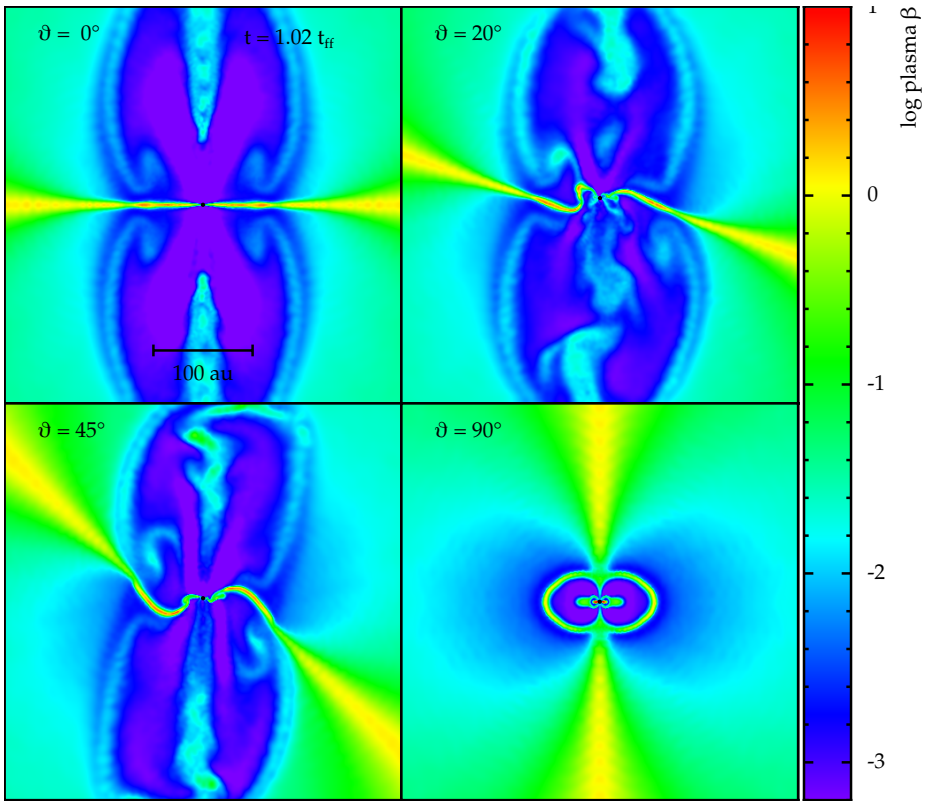

V.viii.c. β cross–section in the x–y plane

Figure V.viii. Column density projections in the direction of the y–axis (sub–figure V.viii.a) and z–axis (sub–figure V.viii.b), and cross–sections of the plasma β in the z–x plane (sub–figure V.viii.c) for the four $\mu = 10$ calculations at $t = 1.02\ t_{\rm ff}$. The initial inclination between the rotation and magnetic field on each sub–figure is identical, with the upper row being $\vartheta = 0°$ and 20° and the lower row being $\vartheta = 45°$ and 90°. Sink particles are represented by a black dot, approximately four times larger than the accretion radius. The initial inclination between the rotation and magnetic field axes decreases down the page, with the first row being $\vartheta = 0°$, then 20°, 45°, and the bottom row having $\vartheta = 90°$. A similar distribution of structures can be seen to those in figure V.v; however, the pseudo–discs with this weaker initial magnetic field are in general larger due to the reduced angular momentum transport from magnetic braking. The consequently faster rotation rate of the disc produces faster outflow jets, for example the 'disconnection' region when $\vartheta = 0°$ has an outflow speed of $|v_z| = 8\ \mathrm{km \cdot s^{-1}}$.

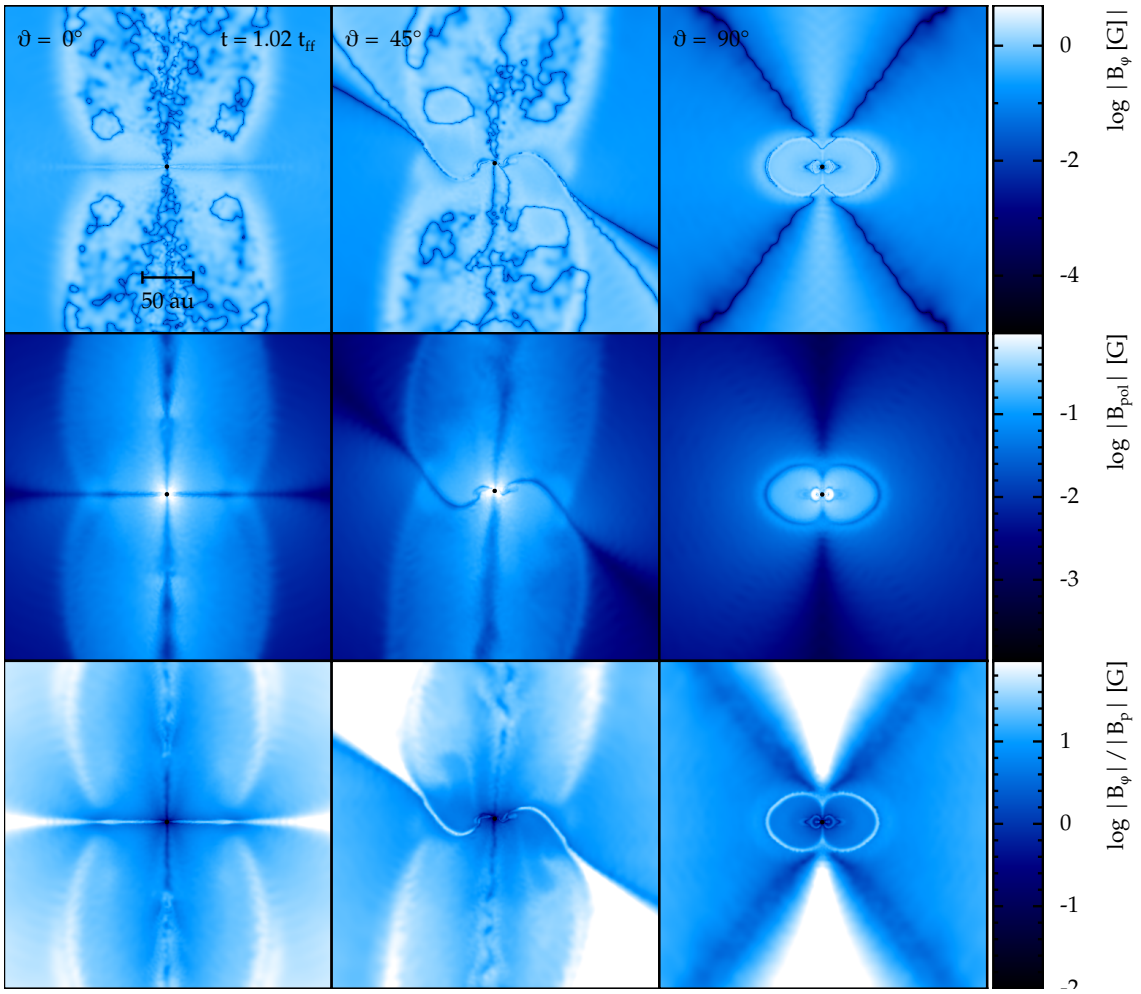

Figure V.ix. Cross–sections of the toroidal magnetic field (upper row, *cf.* equation V.4), poloidal magnetic field (middle row, *cf.* equation V.3), and the ratio of the toroidal to poloidal field components (lower row), for $\vartheta = 0°, 45°, 90°$, $\mu = 10$ calculations at $t = 1.02\ t_{\rm ff}$. Values < 1, *i.e.* black and dark blue, on the lower row indicate regions where the poloidal field is dominant; conversely values > 1 which are indicated with lighter blues and whites are regions where the toroidal field dominates. The 'disconnection' effect in the aligned calculation for $\mu = 10$ (see the upper left panels of figure V.viii.a and figure V.viii.c) can be attributed to the much larger poloidal region, compared to that seen in figure V.vi; $\vartheta = 45°$ and $90°$ also exhibit larger poloidal regions but these do not cause any marked effect on the jet structure (or in the case of $90°$, the lack of it.)

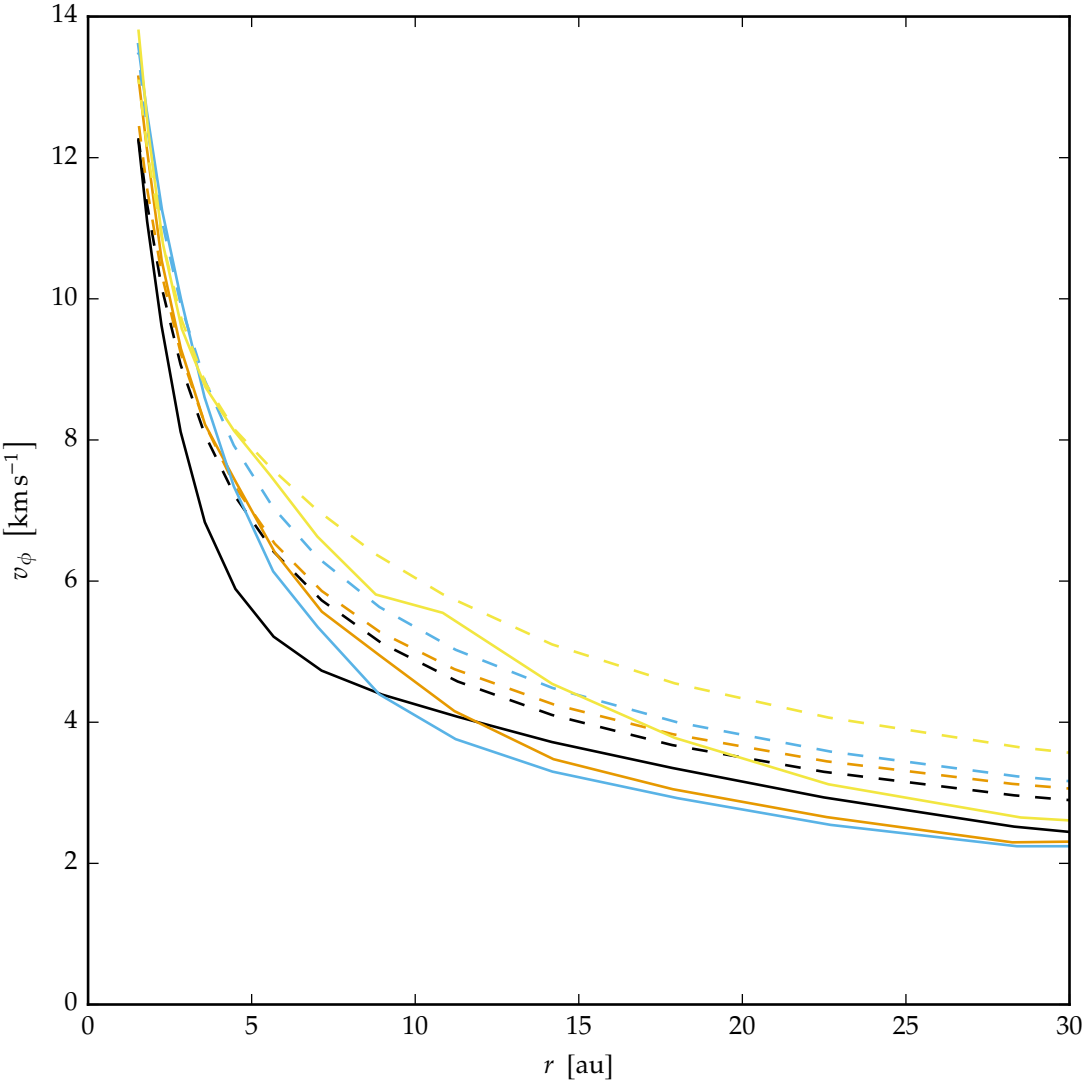

Figure V.x. Radially averaged tangential velocity, v_ϕ, as a function of radius, r, for $\mu = 10$, $\vartheta = 0°$ (solid black line), $\vartheta = 20°$ (solid orange line), $\vartheta = 45°$ (solid blue line), and $\vartheta = 90°$ (solid yellow line), compared to the Keplerian velocities for each field geometry (corresponding dashed lines).

the plane of the disc, which due to preferential collapse of the the fluid parallel to the field lines has a higher density than the rest of the collapsed core. Our calculation does not include a physical viscosity treatment, therefore the main process for transporting angular momentum — and hence allowing material to move towards the centre of the pseudo–disc — is magnetic braking. The calculations do include artificial viscosity, but this is limited using the Morris and Monaghan (1997) switch and should produce negligible angular momentum transport compared to that produced by the magnetic field. The degree of magnetic braking increases with the magnetic field strength, $|B^i|$, and $\mu = 10$ implies an initial field which is half the magnitude of the $\mu = 5$ calculations, causing the formation of the large discs. As we noted for $\mu = 5$, the innermost region of the pseudo–disc (which drives the toroidal field and hence the collimated jet component of the outflow) realigns perpendicular to the rotation axis, although it is correspondingly larger for these calculations.

The most important difference between the two field strengths is that the outflows produced with $\mu = 10$ are 60 % faster. This effect is most pronounced for the $\vartheta = 0°$ calculation. Like the corresponding calculation in section V.4, this system initially had $|v_z| = 5$ km $\cdot$ s^{-1} with the characteristic collimated jet. However, the inner jet region detaches and a region of faster flowing material with $|v_z| = 8$ km $\cdot$ s^{-1} forms with the plasma β above and below the pseudo–disc reducing from 10^{-2} to 10^{-3}.

Figure V.ix shows the ratio of the poloidal to toroidal field for this calculation. Whilst the $\mu = 5$ calculation had a weak poloidal component which was then tightly would by the toroidal field from the disc; as the cross–section in figure V.ix shows this calculation has a much stronger poloidal component, covering a larger region, above and below the disc. The disc is still dominated by the torodial 'winding' field, but the extra pressure contributed by the poloidal region acts to detach the collimated component of the jet and increase the overall speed. This effect, which manifests as an extra (magnetic) pressure contribution, causes the reduced plasma β seen. A similar, although weaker, effect causes the partial disconnections seen when $20° \leq \vartheta \leq 45°$.

We defined $B_{\rm pol}$ in section V.4 as essentially the magnetic pressure. The cause of this extra field is then simply the more rapidly rotating pseudo–disc, as shown in the radially average v_ϕ plot in figure V.x compared to the plot for $\mu = 5$ in figure V.vii, due to the initially reduced magnetic braking. This effect is present at all geometries. In addition, unlike the $\mu = 5$ calculations, the distribution of mass and hence the Keplerian velocity exhibits a much greater degree of variance for these weaker field calculations. In essence a larger disc and a faster outflow velocity are linked because the maximum jet velocity is itself linked to the maximum pseudo–disc rotational velocity, and this effect is continued across a range of misalignments. Additionally, because the initial field is weaker in these calculations, the $\vartheta = 45°$ calculation — which for $\mu = 5$ produced a notably weaker jet than for $\vartheta = 20°$ — has a more comparable velocity and structure, and a similarly larger inner disc region.

V.6 $\mu = 20$

Figure V.xi shows the results from the $\mu = 20$ calculations. These do not form bipolar outflows instead fragmenting into binary (or multiple) systems, as seen in the central column of figure V.xi. The precursor to this is the formation of a small (ca. 10 au radius) dense rotating disc: without the magnetic braking (and angular momentum loss from the outflow). These smaller discs, which are closer in nature to true accretion discs (*cf.* figure V.xii) than the pseudo–discs discussed earlier, are gravitationally unstable. This can be seen from the distinct spiral arm–like structures.

The $\vartheta = 0°$ and 20° calculations form tight binaries with separations of < 5 au. We add a cautionary note that in a calculation including additional physical processes, for example a radiative transfer scheme like that in Whitehouse and Bate (2004, 2006), these may not be formed due to the excess thermal support acting to stabilise the disc; alternatively they may merge together. In contrast, the separation between the two protostars for $\vartheta = 90°$ is ≈ 13 au at $1.03 t_{\rm ff}$. In all cases, the binary pairs are surrounded by a massive circumbinary disc, with a radius of 50 au, while the wider binaries have two distinct dense circumstellar discs (with radii of < 5 au) embedded within this.

All four values of ϑ produce an initial protostar by $t = 1.01\ t_{\rm ff}$, which is comparable to the time frame for a $\mu = 10$ calculation. However, these calculations then go on to produce a second protostar by $1.02\ t_{\rm ff}$, forming the binary pairs seen in figure V.xi. In addition, the $\vartheta = 0°$ model eventually produces a further sink particle from the circumbinary material, shown in figure V.xiv. The ultimate fate of this third potential protostar is unclear — whilst a stable triple star system is possible, by three-body interaction it could be ejected from the system or the two closer sinks could merge leaving a system similar to the 90° model albeit without the two discs). We note that this is a similar formation process to that proposed for the ternary system observed by Tobin *et al.* (2016), albeit with a much smaller separation between the binary pair and the younger third protostar. However, an important difference between all the $\mu = 20$ models and the stronger fields is the absence of an outflow — without which angular momentum can not be rapidly removed from the disc. This reduction in angular momentum transport means that fragmentation into a binary (which can store more angular momentum) is the result.

Although we noted earlier that these four calculations do not produce a bipolar outflow, there are still regions with substantial magnetic fields. Consequently a significant magnetic pressure is still realised and this produces a region around the circumstellar (or circumbinary) disc with $\beta < 1$. This causes some material to be moved away from the plane of the disc, although not in the rapid and directed manner of a jet. We see, for example, in figure V.xiii that although a small poloidal region exists near the protostar, there is no collimating toroidal component present. This is more similar to the field structure seen for $\vartheta = 90°$ in figures V.vi and V.ix, which similarly have no bipolar outflow and no significant toroidal component near the protostar.

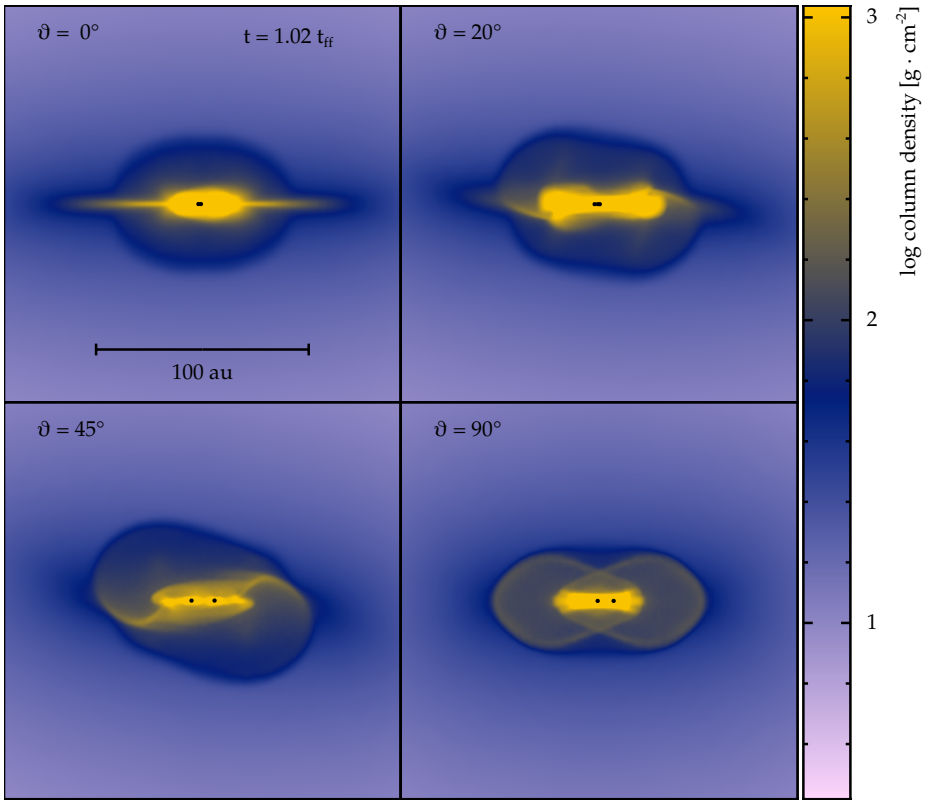

V.xi.a. Column density projection in the direction of the y–axis

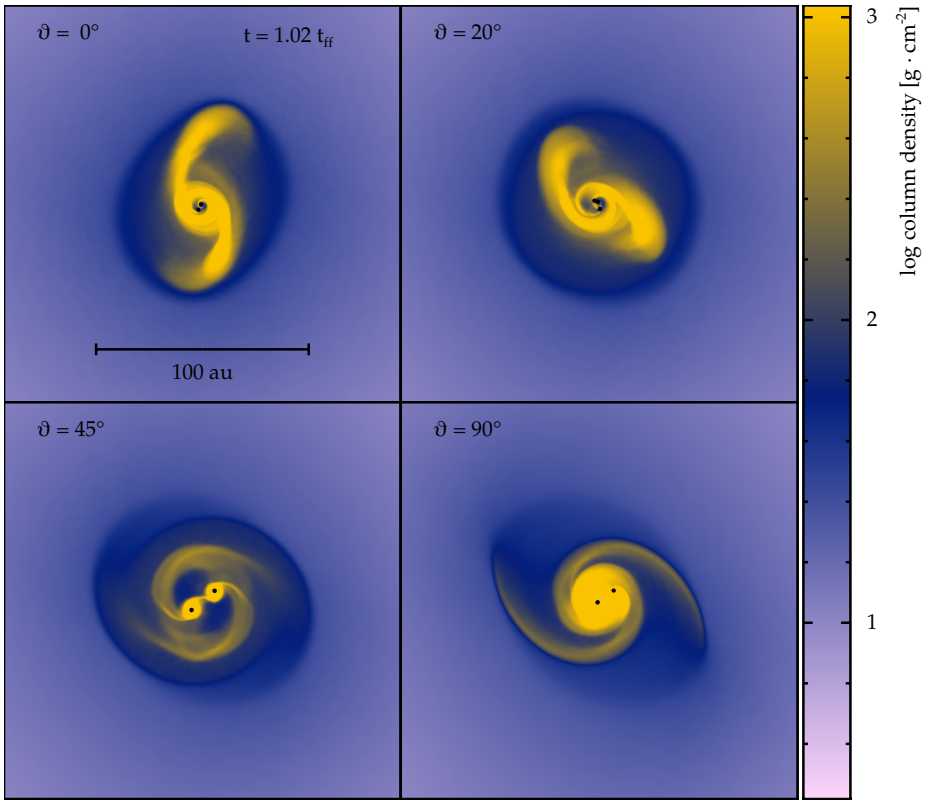

V.xi.b. Column density projection in the direction of the z–axis

Figure V.xi. continued below

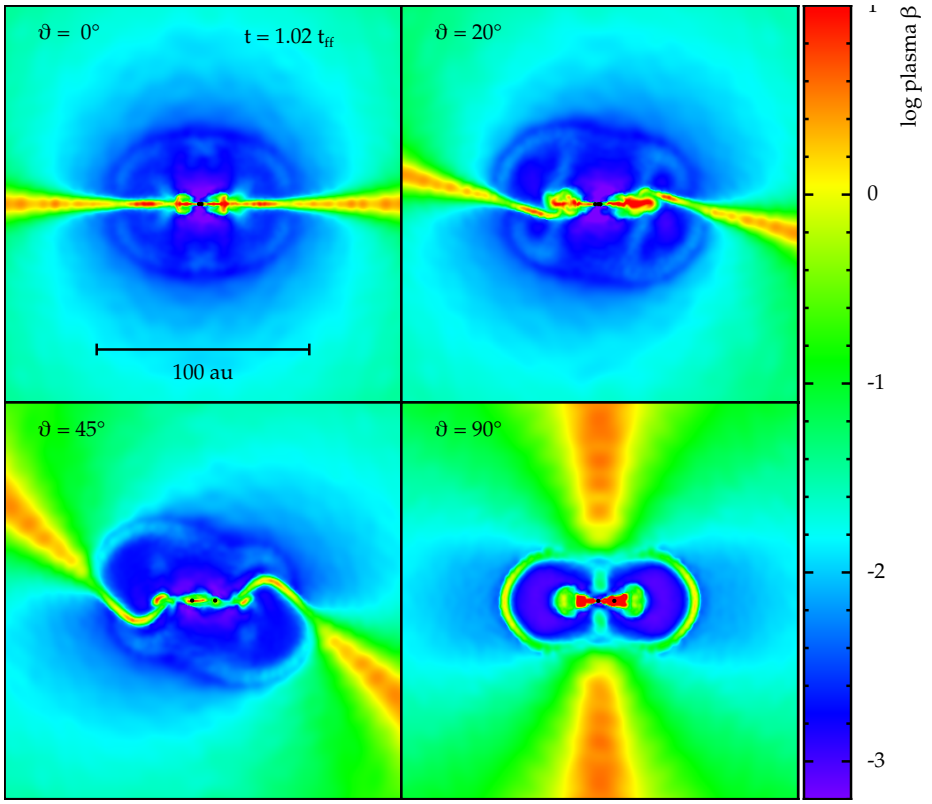

V.xi.c. β cross–section in the x–y plane

Figure V.xi. Column density projections in the direction of the y–axis (sub–figure V.xi.a) and z–axis (sub–figure V.xi.b), and cross–sections of the plasma β in the z–x plane (sub–figure V.xi.c) for the four $\mu = 20$ calculations at $t = 1.02\ t_{\rm ff}$. The initial inclination between the rotation and magnetic field on each sub–figure is identical, with the upper row being $\vartheta = 0°$ and $20°$ and the lower row being $\vartheta = 45°$ and $90°$. Sink particles are represented by a black dot, slightly larger than the accretion radius. The markedly different evolution for the weakest magnetic field calculations, compared to those shown in figures V.v and V.viii, including the formation of binary or multiple systems can be seen. We note that increasing ϑ increases the binary separation, and that at lower values both protostars are co–located within one disc, whilst at higher values a pair of discs are embedded in a circumbinary disc.

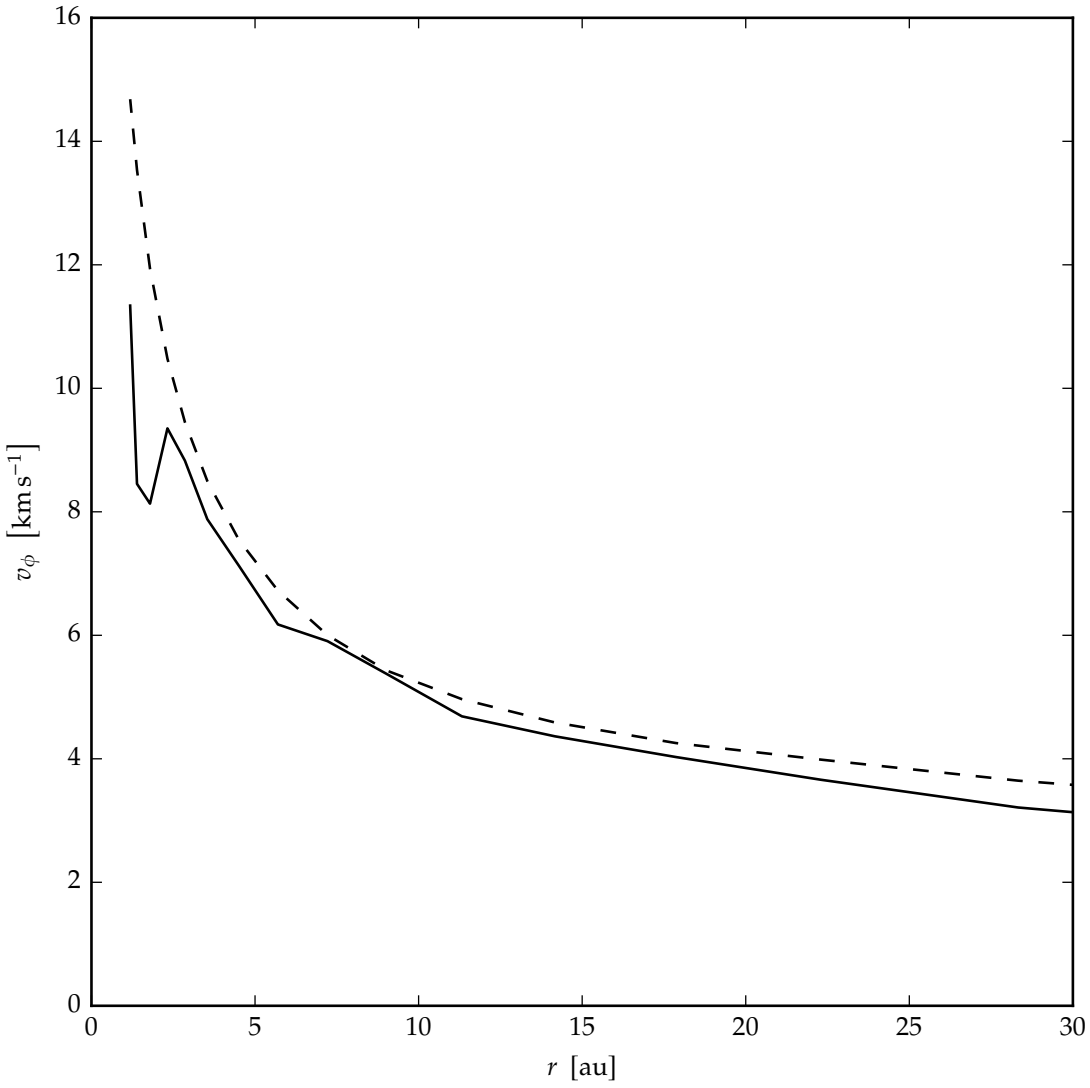

Figure V.xii. Average tangential velocity (v_φ) as a function of radius in the pseudo–disc, calculated in the same way as figures V.vii and V.x but centered on the barycentre of the system rather than one of the protostars, at $t = 1.02\ t_{\rm ff}$ for the $\vartheta = 0°$ $\mu = 20$ calculation (black solid line) with the corresponding black dashed line showing the Keplerian velocity profile. Compared to figures V.vii and V.x the significantly reduced magnetic braking in this calculation allows the disc to become Keplerian within $r < 12$ au of the system barycentre. The formation of wider binary systems means a useful comparison with other field geometries is not possible in this case (an early signature of this is seen at $r = 1\,1/2$ au where a sink particle appears to artificially reduce the velocity average)

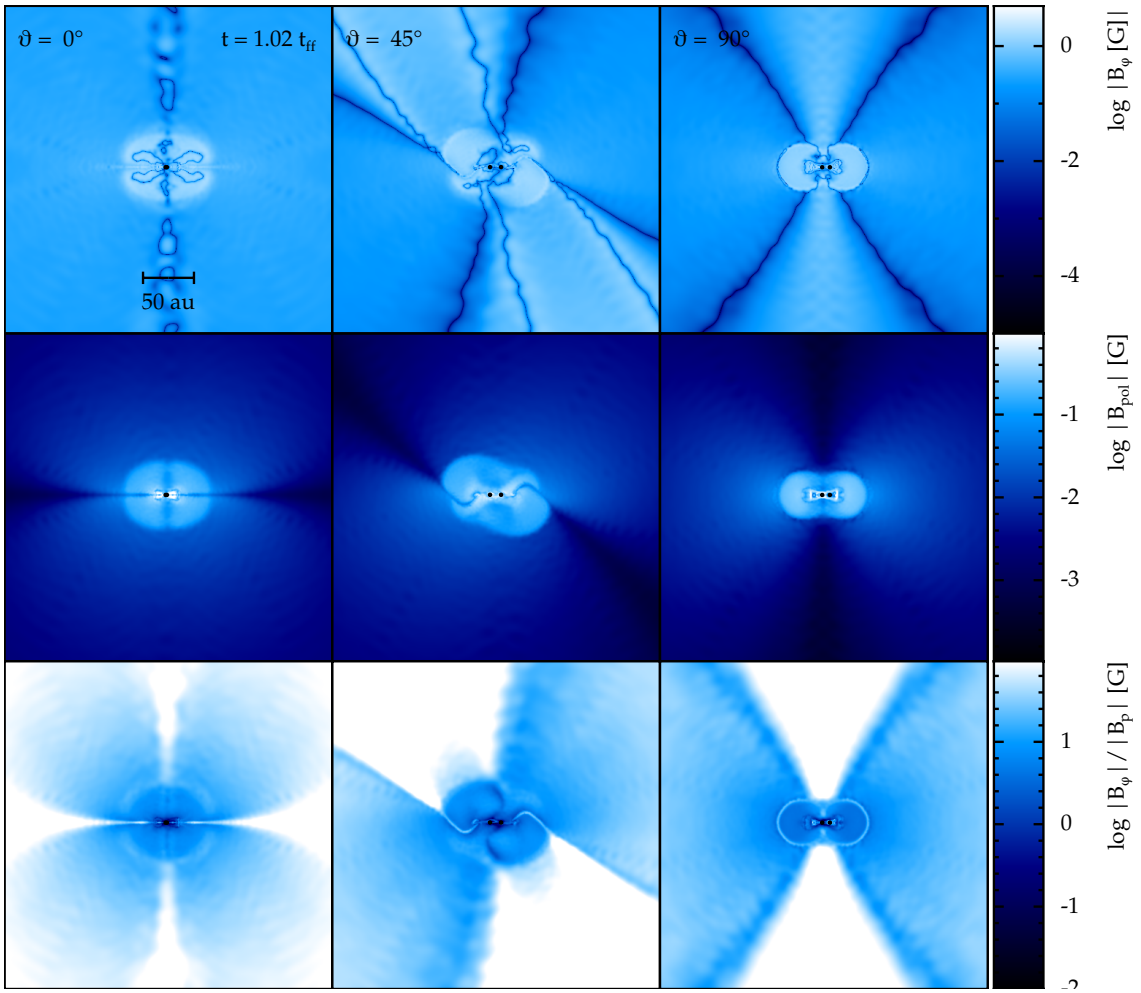

Figure V.xiii. Cross–sections of the toroidal magnetic field (upper row, *cf.* equation V.4), poloidal magnetic field (middle row, *cf.* equation V.3), and the ratio of the toroidal to poloidal field components (lower row), for $\vartheta = 0°, 45°, 90°$, $\mu = 20$ calculations at $t = 1.02\ t_{\rm ff}$. Values < 1, *i.e.* black and dark blue, on the lower row indicate regions where the poloidal field is dominant; conversely values > 1 which are indicated with lighter blues and whites are regions where the toroidal field dominates.

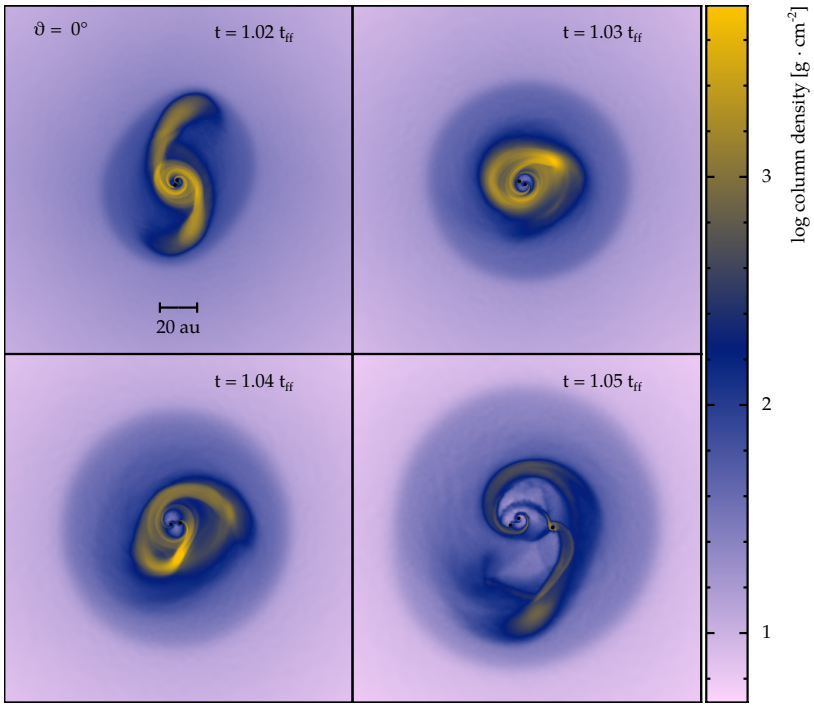

V.xiv.a. $\vartheta = 0°$

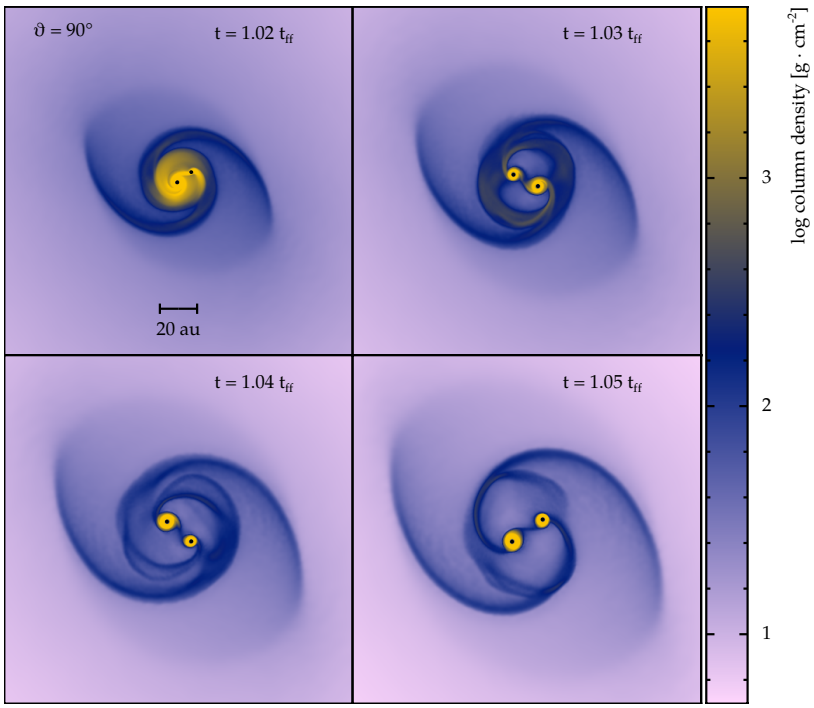

V.xiv.b. $\vartheta = 90°$

Figure V.xiv. Column density projections for $\mu = 20$, $\vartheta = 0°$ (sub–figure V.xiv.a), and 90° (sub–figure V.xiv.b) between $t = 1.02$ and $1.05\ t_{\rm ff}$. Sink particles are represented by a black dot, slightly larger than the accretion radius. Both models have formed two sink by $1.02 t_{\rm ff}$ but in a very different configuration: surrounded by one large disc for 0° compared to two smaller, separate, discs when 90°. The 0° model eventually forms a third sink ≈ 10 au away from the original pair.

In principle, this may indicate that binary stars may be formed by fragmentation even in non–turbulent clouds, or clouds which have not been perturbed (*e.g.* by an external impulse as in Pringle 1989) and are no longer axisymmetric; provided, of course, that the field is sufficiently weak so as to not drive a strong outflow. In practice, this may not be as strong a constraint as it seems — in our quasi–ideal M.H.D. the only method of dissipating magnetic energy is by artificial resistivity, which is intentionally limited to the minimum required for stability. In reality, non–ideal effects (resistivity, ambipolar diffusion, and the Hall effect) will act to reduce or transform the field and may therefore allow an effect similar to that seen here to occur for stronger initial fields. Wurster, D. J. Price, and Bate (2016) propose a consistent SPMHD method that extends the ideal M.H.D. presented here to include all three non–ideal effects, and find that the Hall effect and the relative orientation of the rotation and magnetic field axes can have a significant effect on the consequent evolution of the core. Alternatively, as suggested in Machida *et al.* (2005) it may be sufficient to just increase the initial angular momentum of the cloud to promote fragmentation at higher field strengths (or some combination of both mechanisms).

Conversely, there should exist a range of sufficiently strong initial fields so that no matter what other physical processes are at play, binary or multiple star systems are difficult to form, and hence solitary stars may be produced. Stronger fields naturally drive stronger jets and outflows or increased magnetic braking which transport angular momentum obviating the need for companion stars to store angular momentum.

V.7 Accretion onto protostars

As well as producing outflows and discs with varying morphologies, each model also results in a different profile of accretion onto the sink particle (which represents a forming protostar). As before, a general trend is observed whereby the $\mu = 20$ models and $\vartheta = 90°$ models differ substantially from stronger fields and shallower angles. In figure V.xv we plot maps of the material accreted during the 500 yr after a sink particle is inserted.

Figure V.xvi shows that the amount of material accreted onto the sink is broadly similar (at $t = 1.04\ t_{\rm ff}$) across all of the $\mu = 5$ and 10 models, which is born out by the similar outflow morphology seen earlier in section V.3. All calculations principally accrete material in the plane of their pseudo–disc, as seen in figure V.xv. When $\vartheta = 0°$ this clearly aligns with the equator. Similarly, for weak magnetic fields, where $\mu = 20$ (*cf.* figure V.xi), the accretion disc forms perpendicular to the rotation axis for all field geometries. The bottom row of figure V.xv shows how this results in a strongly equatorial accretion profile. For $\vartheta = 45°$ in the stronger field calculations a sinusoidal structure is seen in figure V.xv, which is the expected shape for a warped pseudo–disc like those seen in figures V.v and V.viii. The $\mu = 5$, $\vartheta = 90°$ has not produced a clear disc and has instead taken on a sigmoidal structure. This causes a hemispherically symmetrical and rotationally symmetrical accretion pattern corresponding to each 'arm' of the sigmoid.

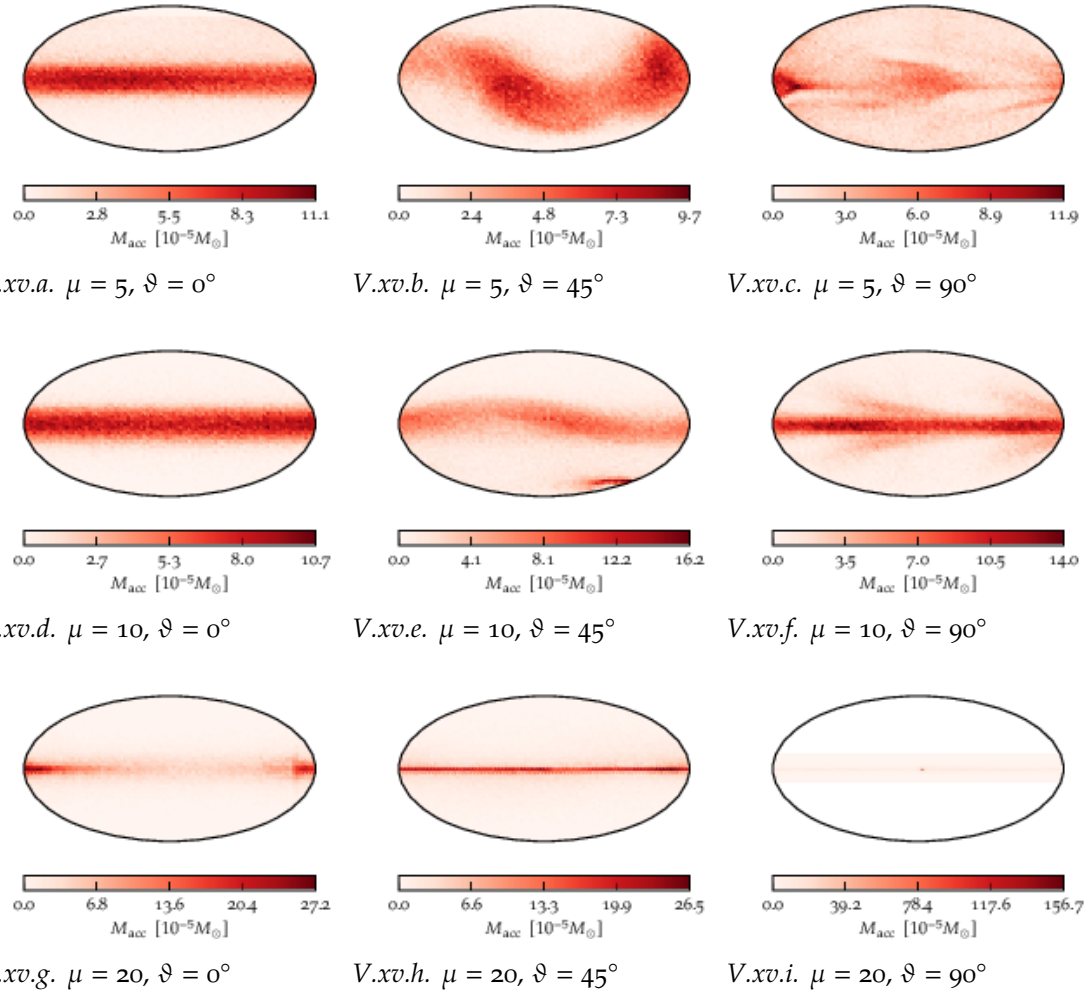

V.xv.a. $\mu = 5$, $\vartheta = 0°$ *V.xv.b.* $\mu = 5$, $\vartheta = 45°$ *V.xv.c.* $\mu = 5$, $\vartheta = 90°$

V.xv.d. $\mu = 10$, $\vartheta = 0°$ *V.xv.e.* $\mu = 10$, $\vartheta = 45°$ *V.xv.f.* $\mu = 10$, $\vartheta = 90°$

V.xv.g. $\mu = 20$, $\vartheta = 0°$ *V.xv.h.* $\mu = 20$, $\vartheta = 45°$ *V.xv.i.* $\mu = 20$, $\vartheta = 90°$

Figure V.xv. Mollweide projections of the mass accreted onto a sink particle as functions of latitude and longitude during the first 500 a after formation. The top, middle and bottom rows are $\mu = 5$, 10, and 20 respectively, and the first, second and third columns are $\vartheta = 0°$, 45°, and 90° (for $\mu = 20$ only the first sink particle is shown, a similar plot would be produced for the second particle). Accreted particles are placed in hexagonal bins and then projected into two dimensions using the Mollweide projection, the logarithm of the accreted mass is then used to set the colours. All models preferentially accreted in the plane of their pseudo–disc, *e.g.* the sinusoidal structure seen in two of the 45° models corresponds to a warped pseudo–disc.

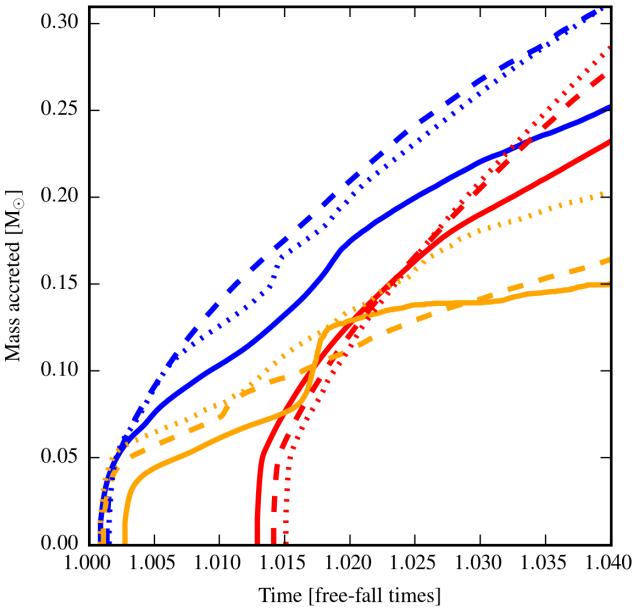

Figure V.xvi. Mass accreted by each sink particle plotted against time. The three magnetic field strengths are represented by red, blue and orange respectively for $\mu = [5,\ 10,\ 20]$ and solid, dashed and dotted lines represented $\vartheta = [0°,\ 45°,\ 90°]$. The later formation of the sink particle for $\mu = 5$ (see figure V.ii) at $t \approx 1.015 t_{\rm ff}$ is clearly shown. Additionally, we observe that whilst the $\mu = 10$ models form earlier, the total mass accreted for each field geometry is similar for $\mu = 5$ and 10 at $t = 1.04 t_{\rm ff}$. Whilst the $\mu = 20$ models appear to be accreting less, all these models produce a second sink by $t = 1.02 t_{\rm ff}$ and which rapidly accretes an approximately similar mass; in addition a sink-sink interaction for $\vartheta = 0°$ causes the sharp knee in that model.

An imprint of a similar structure is seen for $\mu = 10$ from the two spiral arms of the disc. However, unlike in Lewis, Bate, and D. J. Price (2015), we find that the change to the small scale structure results in a roughly equivalent accretion rate for both $\vartheta = 45°$ and $90°$.

V.8 Comparison to observations

Observations of young stellar objects (Y.S.O.s) substantially more evolved than a first core (Larson 1969) are plentiful compared to detections of objects which, although they have formed some sort of core, are much less evolved. Detections of an earlier phase — a dense starless core which is approaching the point of forming a star — are better represented, *e.g.* those found by Crapsi *et al.* (2005). Therefore, constraints on the dynamics a first hydrostatic core and its environs would be useful. The insertion of sink particles means we do not follow the collapse to exactly first hydrostatic core proposed by Larson (1969). However, our sink particle has comparable dimensions so the overall structure of the pseudo–disc and any outflow should be similar.

In models where we obtain a collimated (or jet–like) outflow we find that the bulk velocity ranges between ≈ 2 and ≈ 8 km $\cdot$ s^{-1} depending on the exact configuration of parameters, with higher values of ϑ corresponding to generally reduced outflow velocities. This substantially increases the range of potential outflow velocities which may be first cores as opposed to 'very low luminosity objects' (Ve.L.L.Os., see Kauffmann *et al.* 2005; Myers *et al.* 2005). One example is given in Pineda *et al.* (2011), who find that `L1451-mm` has a slow outflow with a velocity of about 3 km $\cdot$ s^{-1}. Similarly, Dunham *et al.* (2011) observe an bipolar outflow of comparable velocity in `Per-Bolo 58`. These velocities are apparently slightly too slow if we only consider lower values of ϑ, however, an outflow of this velocity would be approximately consistent with our results for $\vartheta = 45°$.

At the other extreme, Chen *et al.* (2010) find that `L1448 IRS2E` (another first core candidate) has a clearly collimated outflow with a velocity of around 25 km $\cdot$ s^{-1}. This is much faster than any of the models presented here, which have an artificial limit of 1 au placed on the collapse. Outflow velocity and the maximum rotation speed (which is controlled by the larger of the size of the protostar or sink particle) are closely linked (D. J. Price, Pringle, and King 2003) and consequently this indicates that whatever object is present in `L1448 IRS2E`, it has a substantially smaller radius than 1 au, and may therefore be more evolved than a first core.

In effect we find that slow bipolar outflows are characteristic of first cores at all but the weakest field strengths or inclination angles $\vartheta > 45°$. This implies that there is a strong constraint on first core candidates: any outflow, if present, should be between ≈ 2 and 8 km $\cdot$ s^{-1} and that faster outflows may be indicative of a more evolved object.

CHAPTER VI

The Role of Turbulence in the Evolution of Molecular Cloud Cores

> And I would like a medium Vodka dry Martini — with a slice of lemon peel. Shaken and not stirred, please. I would prefer Russian or Polish vodka.
>
> Chapter 14, Dr. No, Ian Fleming (1958)

VI.1 Background and Motivation

Chaotic, turbulent, molecular clouds are the birthplaces of stars (McKee and E. C. Ostriker 2007; Padoan and Nordlund 2002). These large clouds evolve and ultimately structures therein (André *et al.* 2010; Men'shchikov *et al.* 2010; Myers 2009; Ward-Thompson *et al.* 2010) succumb to the Jeans (1902) instability and collapse — creating the the molecular cloud cores that ultimately form protostars (Motte and André 2001; Shu 1977). Many open questions in astronomy are related to how these cores evolve, for example, how are multiple star systems formed and the related question of how is the very large initial angular momentum of the core reduced to the stellar angular momenta observed for young stars (Li, Krasnopolsky, and Shang 2013). Molecular clouds are comprised of a magnetised astrophysical plasma (Crutcher 2012; Heyer and Dame 2015) which results in magnetic effects playing an important role in the collapse of the cloud cores. Ultimately, once these core collapse to protostellar densities, jets and other outflows are produced. These outflows, and particularly collimated jets, may help to remove angular momentum from the collapsing gas and, thus, explain the observed low angular momentum in young stars. Consequently an understanding of how the initial conditions — and particularly the role of the initial velocity field — in the molecular core affect the generation of outflows is an important area of study.

The gas within a galaxy is invariably turbulent (Roberts 1969). As discussed in sub–section I.1.1, the molecular gas within a cloud also is. Examples of this are seen, *inter alia*, in the Horsehead nebula (Pound, Reipurth, and Bally 2003, Hily-Blant *et al.* 2005), and also more generally, (Heyer and Brunt 2004). These turbulent conditions must then cascade down to the scales of molecular cloud cores. In the process, the magnitude of the turbulence will decay from being supersonic (in a molecular cloud) to transonic or subsonic in the core. Many numerical calculations, including Larson (1981), Klessen, Heitsch, and Mac Low (2000), Mac Low and Klessen (2004), Bate (2009), and Bate (2012), Federrath (2015) have demonstrated that the turbulent motions within the cloud are an essential part of its evolution. These motions produce a filamentary structure and then localised overdensities which can collapse and form stars (Elmegreen 1993a).

In the preceding two chapters (chapters IV and V) we explored how the gravitational collapse of magnetised molecular cloud cores is affected by changing the geometry and strength of the initial magnetic field. However, all of the calculations presented in those two chapters used cloud cores which, although rotating, had completely laminar velocity fields. These chapters continued a long series of work in this field including Tomisaka (2002), Matsumoto and Tomisaka (2004), D. J. Price and Bate (2007), Machida, Inutsuka, and Matsumoto (2008), Ciardi and Hennebelle (2010), and Bate, Tricco, and D. J. Price (2014). More recently, although not discussed in this thesis, attention has turned to including non–ideal M.H.D. effects (Pandey and Wardle 2008, Wurster, D. J. Price, and Ayliffe 2014, Wurster, D. J. Price, and Bate 2016, Tsukamoto *et al.* 2015a).

Burkert and Bodenheimer (2000) proposed that the observed line–widths of molecular cloud cores could be caused by turbulent motion following a power law (*i.e.* where the wavenumber of the turbulence, k, follows $P(k) \propto k^n$) with $n \in [-3, -4]$). This turbulence could originate on the larger scales of the molecular cloud itself, following the same power law. In this chapter, we present the results of a series of calculations involving turbulent cores with this same turbulent power spectrum. We show that the initial velocity field of a molecular cloud core has as important an impact as the initial magnetic field strength — both of which are seeded by the overall molecular cloud. In addition we show that the initial angular momentum of the cloud is closely linked to the nature of any protostellar outflows (along with the magnetic field strength and geometry, as we observed in chapters IV and V).

We present the results of an ensemble of seventeen smoothed particle radiation magnetohydrodynamical (S.P.R.M.H.D.) calculations and three smoothed particle magnetohydrodynamics (S.P.M.H.D.) calculation of the collapse of a one solar mass molecular cloud core. Each core studied has a different set of initial conditions, ranging from being almost laminar to transonic cores, and covering different initial angular momenta. We also take the opportunity to compare the use of an approximate barotropic equation of state with a flux–limited diffusion (F.L.D.) radiative transfer (R.T.) scheme.

As in the preceding chapters we use the numerical scheme set out in chapter II. However, in most of the calculations in this chapter we also incorporate the R.T. scheme in section II.3 to provide an S.P.R.M.H.D. with self–gravity scheme. In section VI.2 we discuss the initial conditions used for the ensemble of calculations, including how the turbulence velocity field is generated. In section VI.3 we compare the results from calculations using the barotropic equation of state with the F.L.D. R.T. scheme. Following this, in sections VI.4 to VI.6 we discuss the common early phase of the collapse, the effect of increasing turbulence and the effect of increasing angular momentum on the subsequent evolution of the core, respectively. We then compare these results both to observations and existing theoretical work in section VI.7.

VI.2 Initial Conditions

We again adopt similar initial conditions to chapters IV and V. However, we now set the initial velocity field so it contains *both* a turbulent and rotational component, and also use the flux–limited diffusion (F.L.D.) radiative transfer (R.T.) scheme detailed in section II.4 along with a radiative equation of state.

In the previous chapters we started each calculation with a velocity field so that the core was in solid body rotation with an initial rotation rate of $\Omega_0 = 1.77 \times 10^{-13}$ rad $\cdot$ s^{-1}. In this chapter we combine a turbulent velocity field with this solid body rotation. Although turbulence will necessarily add *some* angular momentum, by super–imposing the two fields we are able to more directly consider the influence of linear and angular on

the formation of the subsequent protostar.

As before, the surrounding medium has an initial velocity of zero throughout. The initial velocity profile of the core is produced by combining a turbulent component, $v^i_{\rm turb}$, and a solid–body rotation component, $v^i_{\rm rot}$, *i.e.*

$$v^i = v^i_{\rm turb} + v^i_{\rm rot}. \tag{VI.1}$$

To make comparisons with other calculations simpler, we use two dimensionless parameters, $\beta_{\rm turb}$ and $\beta_{\rm rot}$ representing the ratio of turbulent and rotational energy to gravitational potential energy respectively, to set the velocity field. These parameters are defined as

$$\beta_{\rm rot} = \frac{1}{3}\frac{r^3_{\rm core,o}\Omega^2_{\rm o}}{GM_{\rm core,o}}, \tag{VI.2}$$

where Ω^2_0 is the initial angular velocity of the core (as noted above this was set to $\Omega_{\rm o} = 1.77 \times 10^{-13}\,{\rm rad}\cdot{\rm s}^{-1}$ in previous chapter), and

$$\beta_{\rm turb} = \frac{1}{2}\frac{r_{\rm core,o}\overline{v^2_{\rm turb}}}{GM_{\rm core,o}}. \tag{VI.3}$$

$\overline{v_{\rm turb}}$ is the root–mean–square average velocity of the turbulence, since the velocity of any individual particle will vary according the Gaussian normal distribution discussed below, and is related to the Mach number, $\mathscr{M}$, of the turbulence via

$$\overline{v_{\rm turb}} = \mathscr{M} c_{\rm s}, \tag{VI.4}$$

where $c_{\rm s}$ is the sound speed of the fluid (which is initially spatially constant). For completeness, we also define the ratio of magnetic energy to gravitational potential energy as

$$\beta_{\rm mag} = \frac{1}{2}\frac{r_{\rm core,o}B^2_{\rm o}}{GM^2_{\rm core,o}}. \tag{VI.5}$$

From this, we can define the ratio of all non–thermal support to the gravitational self–potential as

$$\beta_{\rm tot} = \beta_{\rm mag} + \beta_{\rm turb} + \beta_{\rm rot}. \tag{VI.6}$$

We neglect the support provided by the fluid pressure since this is essentially negligible until the final moments of the collapse when the density increases significantly.

The turbulent component, $\overline{v_{\rm turb}}$, is provided by giving every particle in the core an initial velocity at $t = 0$ — the turbulence is not driven and therefore decays over time. We impose turbulence in a similar manner to E. C. Ostriker, Stone, and Gammie (2001) and Bate, Bonnell, and Bromm (2003). A uniform 128^3 grid of velocities was generated and the initial particle velocities were interpolated from this, multiplied by a co–efficient to produce the correct overall turbulent Mach number. The generated grid represents a

divergence–free (*i.e.* our turbulence is not compressive, *cf.* Federrath *et al.* 2010) random Gaussian field with a power spectrum which follows $P\left(k\right) \propto k^{-4}$, where k is the wavenumber, consistent with Burkert and Bodenheimer (2000). The velocity dispersion, σ, of such a distribution follows scaling law of Larson (1981), with $\sigma\left(r\right) \propto \sqrt{r}$, where r is the distance. From this we obtain values of β_{turb} of 0.0013, 0.012, and 0.13 for $\mathscr{M} = 1/10$, $3/10$, and 1 turbulence respectively.

We note that our initial conditions differ from Matsumoto, Machida, and Inutsuka (2017), who use a Bonnor–Ebert sphere and apply *only* an initially turbulent velocity field, rather than a superposition of a turbulent and a rotational field.

We set the initial rotational component, v^{i}_{rot}, so that $\beta_{\mathrm{rot}} = 0.005$ as before, or 0.01 or 0.02. These correspond to increasing the initial rotation rate by a factor of two and four respectively, *i.e.* to $\Omega = 3.54 \times 10^{-13}$ and 7.08×10^{-13}. Notably, compared to the value of β_{turb}, even the largest value of β_{rot} is only $1/50^{\mathrm{th}}$ of the 'critical value'. All three values are still consistent with Goodman *et al.* (1993) (see, in particular, the distribution in figure 11 therein) albeit with slightly less angular momentum than proposed by Burkert and Bodenheimer (2000).

Finally, we set the initial magnetic field using the dimensionless mass–to–flux ratio as before (in this chapter we use $\vartheta = 0°$ throughout). We use $\mu = 5$, 10, and 20, which correspond to $\beta_{\mathrm{mag}} = 0.71$, 0.18, 0.044. This provides a wide range of initial conditions, ranging from $\mathscr{M} = 1$, $\beta_{\mathrm{rot}} = 0.02$, $\mu = 5$ (a transonic, fast rotating and highly magnetised core) where $\beta_{\mathrm{tot}} = 0.86$ to $\mathscr{M} = 0$, $\beta_{\mathrm{rot}} = 0.005$, $\mu = 20$ (a laminar, slower rotating weakly magnetised core) where $\beta_{\mathrm{tot}} = 0.0445$. In this way we can probe the influence of the velocity and magnetic fields — and strongly and weakly bound cores — on the subsequent formation of a protostar.

In addition to these initial conditions, we also use two differing equations of state. The first is the approximate barotropic equation of state, as used in chapters IV and V, given by (*cf.* Machida, Inutsuka, and Matsumoto 2008)

$$P\left(\rho\right) = c_{s}^{2} \begin{cases} \rho & \rho \leq \rho_{\mathrm{c},1} \\ \rho_{\mathrm{c},1} \left(\dfrac{\rho}{\rho_{\mathrm{c},1}}\right)^{\frac{7}{5}} & \rho_{\mathrm{c},1} < \rho \leq \rho_{\mathrm{c},2} \\ \rho_{\mathrm{c},1} \left(\dfrac{\rho_{\mathrm{c},2}}{\rho_{\mathrm{c},1}}\right)^{\frac{7}{5}} \left(\dfrac{\rho}{\rho_{\mathrm{c},2}}\right)^{\frac{11}{10}} & \rho > \rho_{\mathrm{c},2}. \end{cases} \tag{VI.7}$$

As before, the critical densities are set to $\rho_{\mathrm{c},1} = 10^{-14}$ g $\cdot$ cm^{-3} and $\rho_{\mathrm{c},2} = 10^{-10}$ g $\cdot$ cm^{-3}. The physical consequences of these choices are discussed in chapter V. When using this equation of state we do not use a R.T. scheme (and accordingly use an S.P.M.H.D. with self–gravity method as before).

Alternately, we use the equation of state given by

$$P\left(\rho, T_{\rm fl}\right) = \frac{\mathscr{R}_g}{\mu_{\rm mol}} \rho T_{\rm fl}, \tag{VI.8}$$

where the gas constant is given by $\mathscr{R}_g = 8.3145 \times 10^7$ erg $\cdot$ K^{-1} $\cdot$ mol^{-1}, we use a mean molecular weight of $\mu_{\rm mol} = 2.38$ and the fluid temperature $T_{\rm fl} = \epsilon / C_{\rm v}$, where $C_{\rm v}$ represents the *isochoric* specific heat capacity. The mean molecular weight and heat capacity used represent a mixture of hydrogen and helium and incorporate the effects of hydrogen dissociation and the ionization of hydrogen and helium, but do not incorporate any contribution from metals (see Black and Bodenheimer 1975). The fluid opacities, κ, (see section II.3) are interpolated from the opacity tables of Alexander (1975) and Pollack, McKay, and Christofferson (1985) as detailed in Whitehouse and Bate (2006)

Sink particles (*vide supra* section II.5) are inserted once the critical density is exceeded and (subject to the following the caveat) the boundness checks are passed. In an R.T. calculation these boundness checks are computational infeasible, consequently in some calculations we increase the critical density from the usual value of $\rho_{\rm crit} = 1 \times 10^{-10}$ g$\cdot$ cm^{-3} to 1×10^{-5} g$\cdot$cm^{-3} to prevent spurious fragmentation if the particle density is too low, particularly in rapidly rotating cores. This is principally an issue where $\beta_{\rm rot} \geq 1/100$, where a larger high density region forms, as opposed to a very centrally condensed structure and we use the higher critical density in any such calculation. Consequently, delaying the insertion of the sink particle should be approximately equivalent to simply testing for boundness, as is done in purely M.H.D. calculations. The accretion radius of the sink particles is unchanged from that discussed in section II.5, where $r_{\rm acc} = 1$ au.

We use these initial conditions to run a representative sample of seventeen calculations, as detailed in table VI.1. These calculations span mass–to–flux ratios from $\mu = 5$ to 20, turbulent velocities from $\mathscr{M} = 0$ (a laminar core) to $\mathscr{M} = 1$ (a transonic core), rotational velocities from $\beta_{\rm rot} = 0.005$ to 0.02, and include both barotropic and F.L.D. R.T. formalisms. In this way, we sample a wide area of the parameter space, from a tightly bound, weakly magnetized, laminar core to an almost unbound, transonic, strongly magnetized, and rapidly rotating core. Due to the increased resolution requirements introduced by the turbulent initial conditions, we increase the number of S.P.H. particles used by a factor of two: we use 3 million S.P.H. particles in the core, and consequently 1 1/2 million in the container medium.

VI.3 Dependence of the Results on the Equation of State

All the molecular cloud cores considered in this chapter are sub–critical, and therefore the self–gravity of the gas will cause the core to centrally collapse. As a characteristic time, we use the free–fall time of a initially motionless (*i.e.* non–rotating and laminar, $\beta_{\rm rot} = \beta_{\rm turb} = 0$), non-magnetised ($\mu = \infty$, $\beta_{\rm mag} = 0$), sphere, so that for a core with mass

Table VI.1. Initial conditions for the calculations presented in this chapter. μ is the mass-to-flux ratio (see), $\left|B^i\right|_0$ is the corresponding initial magnetic field strength, $\mathscr{M}$ is the initial turbulent Mach number, Ω_0 is the initial angular speed of the core; $\beta_{\rm mag}$, $\beta_{\rm turb}$ and $\beta_{\rm rot}$ are the ratios of magnetic, turbulent kinetic and rotational kinetic energy to gravitational energy (equations VI.2, VI.3 and VI.5), and $\beta_{\rm tot}$ is the ratio of all non–thermal supporting energy to the gravitational energy (equation VI.6). Note that calculations μ05-M10-r001(R) and μ05-M10-r002(R) use $\rho_{\rm crit} = 10^{-5}{\rm g\cdot cm^{-3}}$, and all other calculations use $\rho_{\rm crit} = 10^{-10}{\rm g\cdot cm^{-3}}$ as the critical density for sink particle creation.

Calc. Name	Eq. of State	μ	$\left\|B^i\right\|_0$ [μ·G]	$\beta_{\rm mag}$	$\mathscr{M}$	$\beta_{\rm turb}$	Ω_0 [$\times 10^{-13}$rad·s^{-1}]	$\beta_{\rm rot}$	$\beta_{\rm tot}$
μ05–M00	F.L.D. R.T.	5	163	0.71	0	70	1.77	0.005	0.715
μ05–M01(M)	Barotropic	5	163	0.71	0.1	0.0013	1.77	0.005	0.716
μ05–M01(R)	F.L.D. R.T.	5	163	0.71	0.1	0.0013	1.77	0.005	0.716
μ05–M03(M)	Barotropic	5	163	0.71	0.3	0.012	1.77	0.005	0.727
μ05–M03(R)	F.L.D. R.T.	5	163	0.71	0.3	0.012	1.77	0.005	0.727
μ05–M10(M)	Barotropic	5	163	0.71	1.0	0.13	1.77	0.005	0.845
μ05–M10(R)	F.L.D. R.T.	5	163	0.71	1.0	0.13	1.77	0.005	0.845
μ05–M10–r001(R)	F.L.D. R.T.	5	163	0.71	1.0	0.13	3.54	0.01	0.850
μ05–M10–r002(R)	F.L.D. R.T.	5	163	0.71	1.0	0.13	7.08	0.02	0.860
μ10–M00	F.L.D. R.T.	10	81	0.18	0	0	1.77	0.005	0.185
μ10–M01	F.L.D. R.T.	10	81	0.18	0.1	0.0013	1.77	0.005	0.186
μ10–M03	F.L.D. R.T.	10	81	0.18	0.3	0.012	1.77	0.005	0.197
μ10–M10	F.L.D. R.T.	10	81	0.18	1.0	0.13	1.77	0.005	0.315
μ20–M00	F.L.D. R.T.	10	41	0.044	0	0	1.77	0.005	0.0445
μ20–M01	F.L.D. R.T.	20	41	0.044	0.1	0.0013	1.77	0.005	0.0503
μ20–M03	F.L.D. R.T.	20	41	0.044	0.3	0.012	1.77	0.005	0.0610
μ20–M10	F.L.D. R.T.	20	41	0.044	1.0	0.13	1.77	0.005	0.179

$M_{\rm core} = 1\,{\rm M}_\odot$, $t_{\rm ff} = 24{,}400\,{\rm a}$. This is in effect a lower bound on how long the core will take to collapse to 'interesting' densities, and any other initial conditions, for example a large $\beta_{\rm turb}$ will act to delay this. Conversely, we would expect a core with $\beta_{\rm tot} \geq 1$ to unbind, and the centre of one with a large, but less than unity, value to collapse but potentially lose some of the outer regions.

Before considering the results using the radiative transfer scheme, we first consider how this differs from the earlier barotropic equation of state. Here we show six calculations where three sets of initial conditions have been solved using both the barotropic 'M.H.D. ' equation of state and the 'R.M.H.D. ' algorithm. The addition of R.T. naturally causes heating of the fluid to occur unlike the fixed equation of state, as shown by the relationship between the fluid density and temperature for the radiative equation of state shown in figure VI.ii and the temporal evolution of the maximum fluid temperature compared to the maximum density shown in figure VI.i. This in turn promotes the formation of a larger pseudo–disc supported by the fluid pressure. As expected, the calculations proceeds essentially identically with the core centrally collapsing due to self–gravity, until the fluid density has risen significantly from its initial value. Figure VI.iii demonstrates how M.H.D. and R.M.H.D. calculations are virtually indistinguishable at this evolutionary epoch. The $\mathscr{M} = 1/10$ and $3/10$ calculations approach a maximum density of $\approx 1 \times 10^{-10}\,{\rm g \cdot cm^{-3}}$ at $t \approx 1.02\,t_{\rm ff}$ whilst the $\mathscr{M} = 1.0$ calculation reaches a similar evolutionary point at $t \approx 1.14\,t_{\rm ff}$. After this, some divergence between the M.H.D. and R.M.H.D. calculations can be seen. We also note that adding R.T. very slightly slows the collapse rate down, for instance the sink particle is inserted in the $\mathscr{M} = 1/10$ calculations $0.01\,t_{\rm ff}$ later. The additional thermal support provided by radiative feedback operates in a comparable way to how additional magnetic pressure opposes the gravitational collapse. This effect is echoed by the projections in figure VI.v, where the barotropic equation of state causes the fluid to form more compact and denser structures compared to the R.T. scheme.

These results show that, even with very complicated initial conditions, the addition of radiation terms into calculations of collapsing cloud cores is important only at the shortest length scales. Figure VI.iv shows density projections of two pseudo–discs, one with R.T. and one with a barotropic equation of state. The addition of radiation promotes stability by allowing a larger pseudo-disc, with greater pressure support to form. For the remainder of this chapter we will consider the R.M.H.D. calculations only.

VI.4 The Initial Phase of the Collapse

Figure VI.vii shows the evolution of the maximum density for three turbulent Mach numbers ($\mathscr{M} = 1/10$, $3/10$, and 1) across three mass–to–flux ratios ($\mu = 5$, 10, 20), which correspond to models μ05–M01(R), μ05–M03(R), μ05–M10(R), μ10–M01, μ10–M03, μ10–M10, μ20–M01, μ20–M03, and μ20–M10 in table VI.1. We note that the density appears to reach an approximate maximum because of the insertion of a sink particle at (in this case)

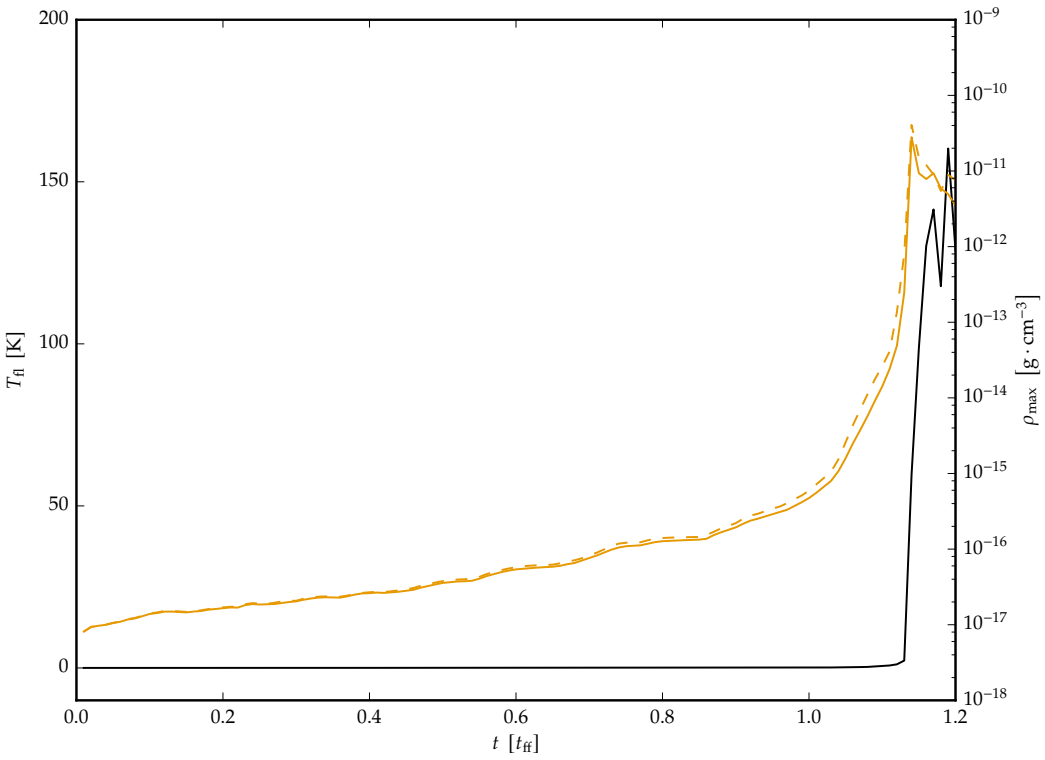

Figure VI.i. Evolution of the maximum fluid density (orange lines) and maximum fluid temperature (black line) for $\mu = 5$ with a $\mathscr{M} = 1$ initial turbulence field. The maximum temperature is shown for the R.M.H.D. calculation only; the solid and dashed orange lines correspond to the maximal densities for the R.M.H.D. and M.H.D. calculations respectively. In the early phase of the calculation, when the maximum density in the cloud core is $\rho \ll 10^{-12}\mathrm{g{\cdot}cm^{-3}}$ the temperature of the core is effectively isothermal with $T = 13.8\,\mathrm{K}$. At higher densities the fluid is heated and this energy is then transported by the radiative transfer scheme through the fluid. That this results in a broader distribution of fluid material around the sink particle is indicated by the slightly elevated maximum density for the M.H.D. calculation.

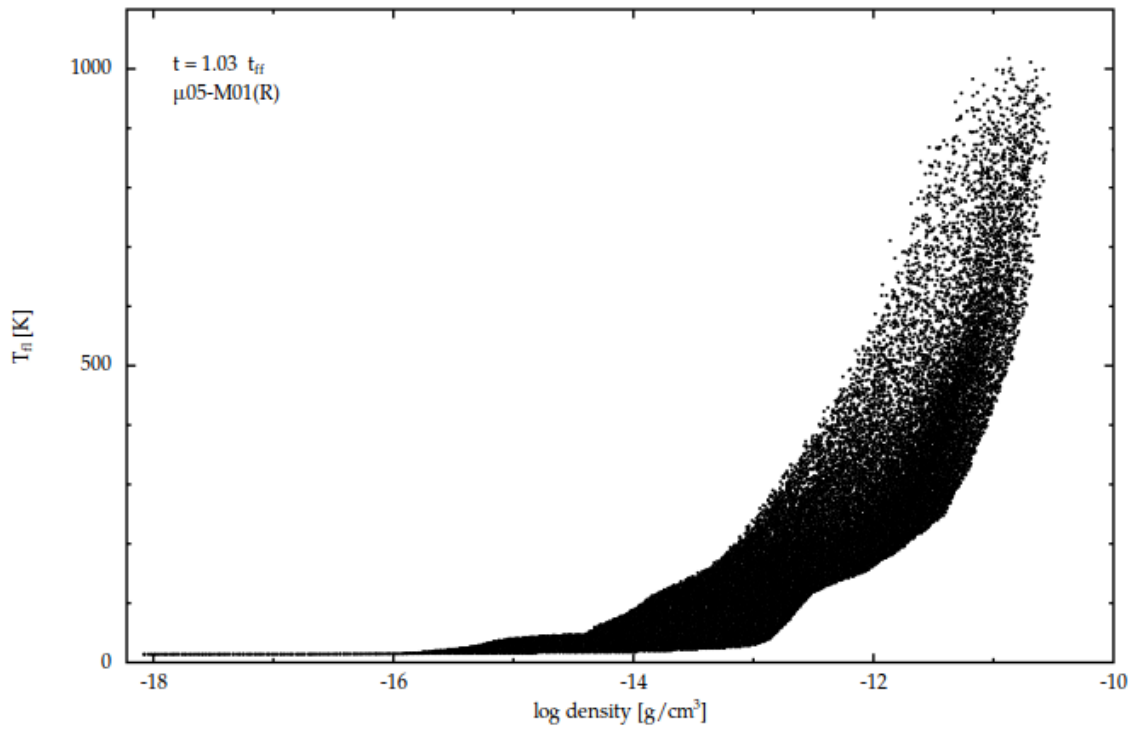

Figure VI.ii. Fluid temperature, $T_{\rm fl}$, as a function of fluid density, ρ, for all S.P.H. particles within the core for the μ05–M01(R) calculation. At higher densities the R.T. scheme causes an increase in the temperature of the fluid. Similarly, changes in the opacity κ, and the influence of this on the heat capcity of the fluid mean that this change is not a simple function of the density (*e.g.* the 'knee' in the temperature distribution between $\rho \approx 1 \times 10^{-13}\,{\rm g\cdot cm^{-3}}$ and $\rho \approx 1 \times 10^{-12}\,{\rm g\cdot cm^{-3}}$).

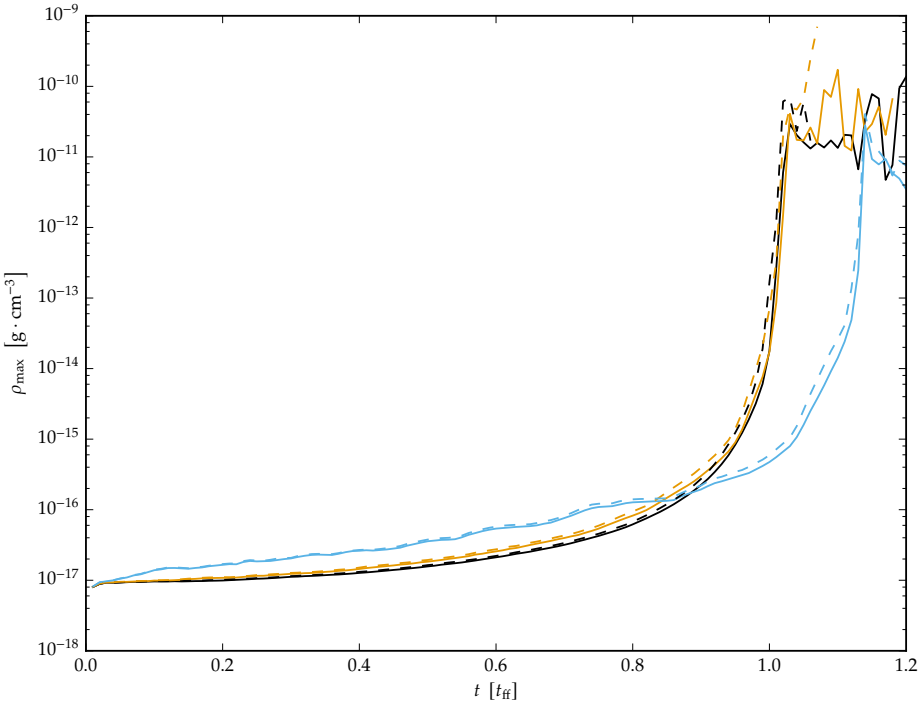

VI.iii.a. Maximum fluid density, $\rho_{\max}$.

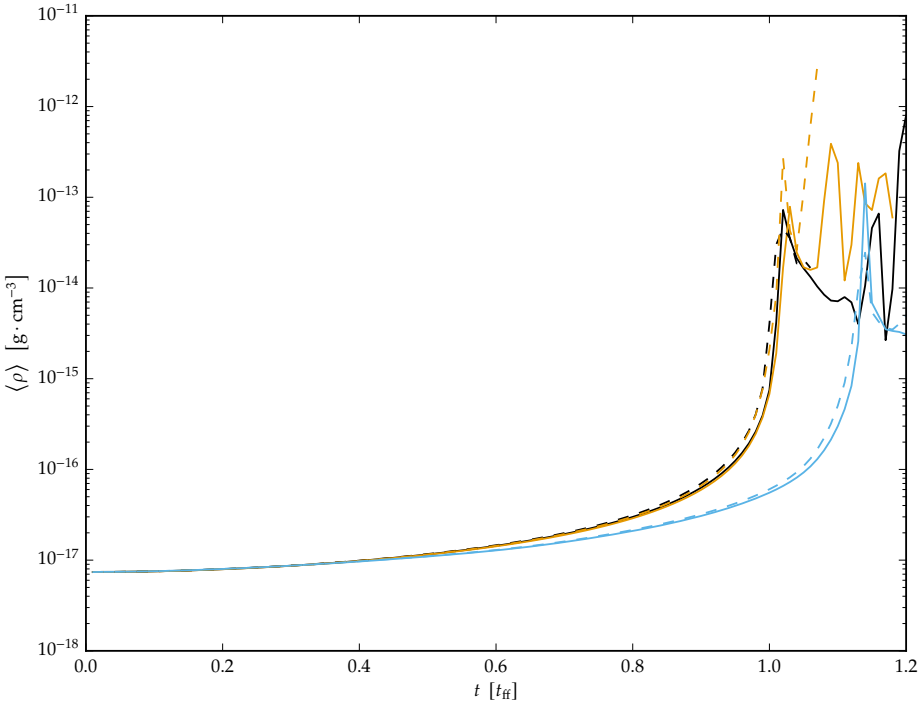

VI.iii.b. Mean fluid density, $\langle\rho\rangle$.

Figure VI.iii. continued below

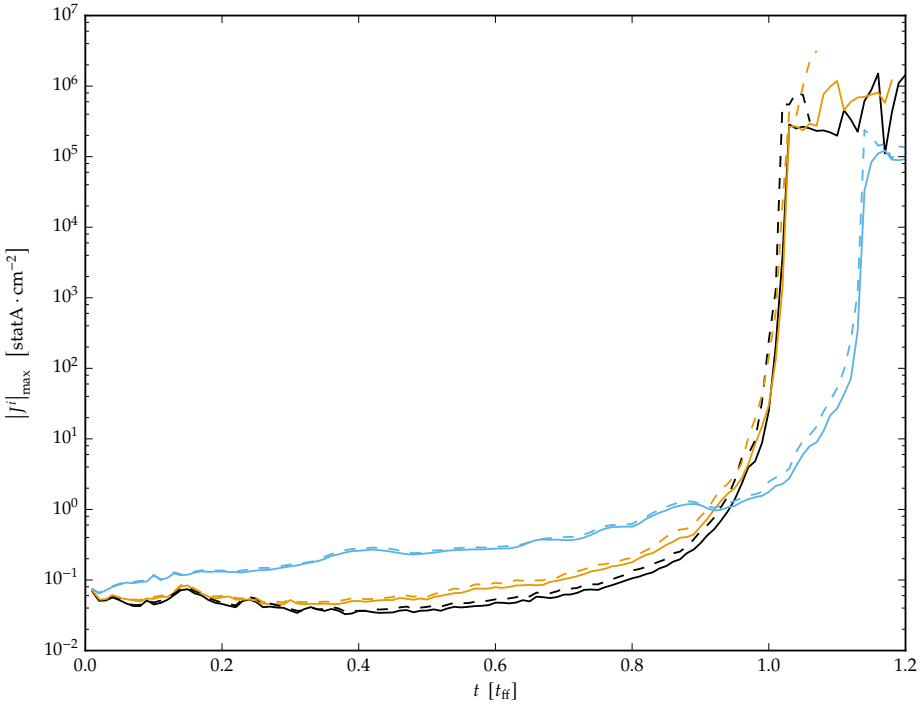

VI.iii.c. Maximum current density, $\left|J^i\right|_{\max}$.

Figure VI.iii. Evolution of maximum fluid density, $\rho_{\max}$, (sub–figure VI.iii.a) mean fluid density, $\langle\rho\rangle$, (sub–figure VI.iii.b) and the maximum current density, $\left|J^i_{\max}\right|$, (sub–figure VI.iii.c) for $\mathscr{M} = 1/10$, $3/10$ and 1 turbulence calculations at $\mu = 5$ with both the barotropic and radiative–transfer equations of state. The black, orange and blue lines correspond to the $\mathscr{M} = 1/10$, $3/10$ and 1 calculations, with the solid lines corresponding to the radiative equation of state and the dashed lines to the barotropic equation of state. The evolution until $\approx 1.00\, t_{ff}$ is comparable for all four sub–sonic calculations, although the addition of radiation and the increase in the Mach number to $3/10$ each delay the final collapse by $\approx 0.01\, t_{ff}$. The two transonic calculations are also comparable until the final stage of the collapse, although there is an increased fluid density (and hence current density) in the early part of the calculation compared to the subsonic calculations due to the formation of turbulent structures.

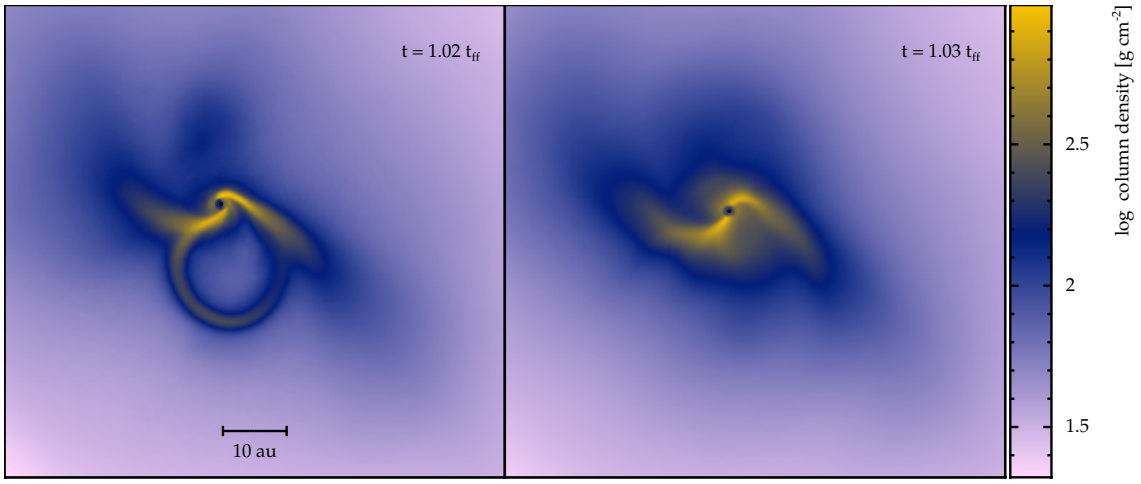

Figure VI.iv. Column density projections in the z–direction for the $\mu = 5$, $\mathscr{M} = 1/10$ calculations. The left panel shows the barotropic equation of state and the right panel the radiative-transfer scheme. A more extensive pseudo–disc with a radius of approximately 10 au has been produced by the R.T. calculation compared to the much smaller and more unstable disc on the left panel. The barotropic equation of state produces a higher density and smaller pseudo–disc which is therefore more susceptible to gravitational instabilities.

$\rho = 10^{-10}\mathrm{g}\cdot\mathrm{cm}^{-3}$. Here we see that the degree of turbulent support has a vastly greater influence on the collapse time of the core. Magnetic pressure support is extremely weak until the core reaches the highest densities and consequently decreasing the mass–to–flux ratio from, for example, 10 to 5 has a much smaller impact. We observed in chapter V and Lewis and Bate (2017) and earlier in chapter IV and Lewis, Bate, and D. J. Price (2015) that the initial field strength and geometry has an effect on the collapsing core, and we again see this effect here. There is (effectively) no magnetic pressure support along the field lines, and this is consequently the preferential direction for fluid to graviationally collapse. Figure VI.vi shows the evolution of three $\mu = 5$ cores and three $\mu = 20$ cores with $\rho_{\mathrm{max}} \approx 10^{-11}\mathrm{g}\cdot\mathrm{cm}^{-3}$ where the characteristic 'oblate spheroid' shape proportional to the initial field strength can be clearly seen when $\mathscr{M} \leq 0.3$. We obtain a comparable range of ellipticities (*i.e.* axis ratios) to the laminar cores presented in the previous chapter with values of 0.6, 0.64, for $\mu = 5$, $\mathscr{M} = 0.1$ and 0.3 and 0.29, and 0.33 for $\mu = 20$ respectively, compared to 0.66 and 0.24 for a laminar core. Although the transonic $\mathscr{M} = 1$ cores are clearly somewhat oblate, it is not possible to demonstrate (due to the complex structure) that the $\mu = 20$ core has a lower oblateness than for $\mu = 5$. In any event, in this transonic regime the turbulent kinetic energy — and hence the filament-like structures produced — has a much greater effect on the initial collapse the magnetic field (*cf.* figure VI.vii).

Once the core reaches densities of $\approx 1 \times 10^{-10}\,\mathrm{g}\cdot\mathrm{cm}^{-3}$, the magnetic field becomes a significant contributor to the subsequent evolution of the system. In addition, because of the radiative transfer scheme, radiation effects become important, as discussed earlier

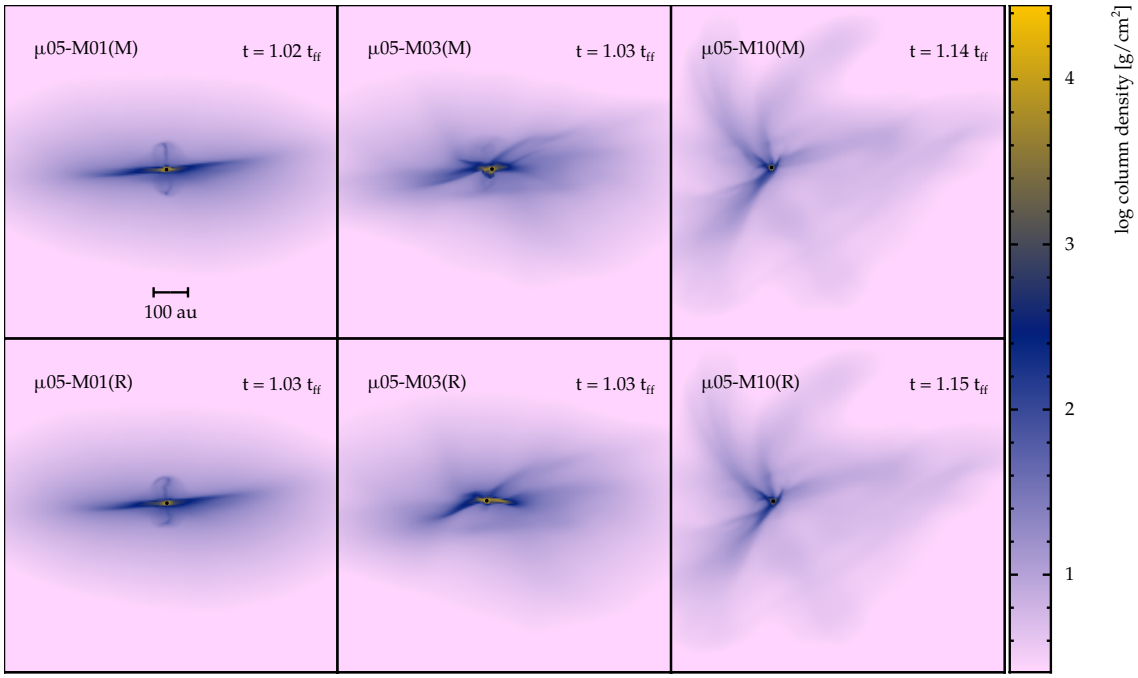

Figure VI.v. Column density projections in the y–direction for the $\mu = 5$ calculations with $\mathscr{M} \in [1/10, 3/10, 1]$ (left–hand, central, and right–hand columns) and the radiative and barotropic equations of state (upper and lower rows, respectively). The barotropic equation of state causes the fluid to form qualitatively higher density and more compact structures, compared to the wider distribution when an R.T. scheme is used. This effect is most obvious when $\mathscr{M} = 3/10$, but is present for all velocity fields (*cf.* the differences in the maximal and average densities in figure VI.iii).

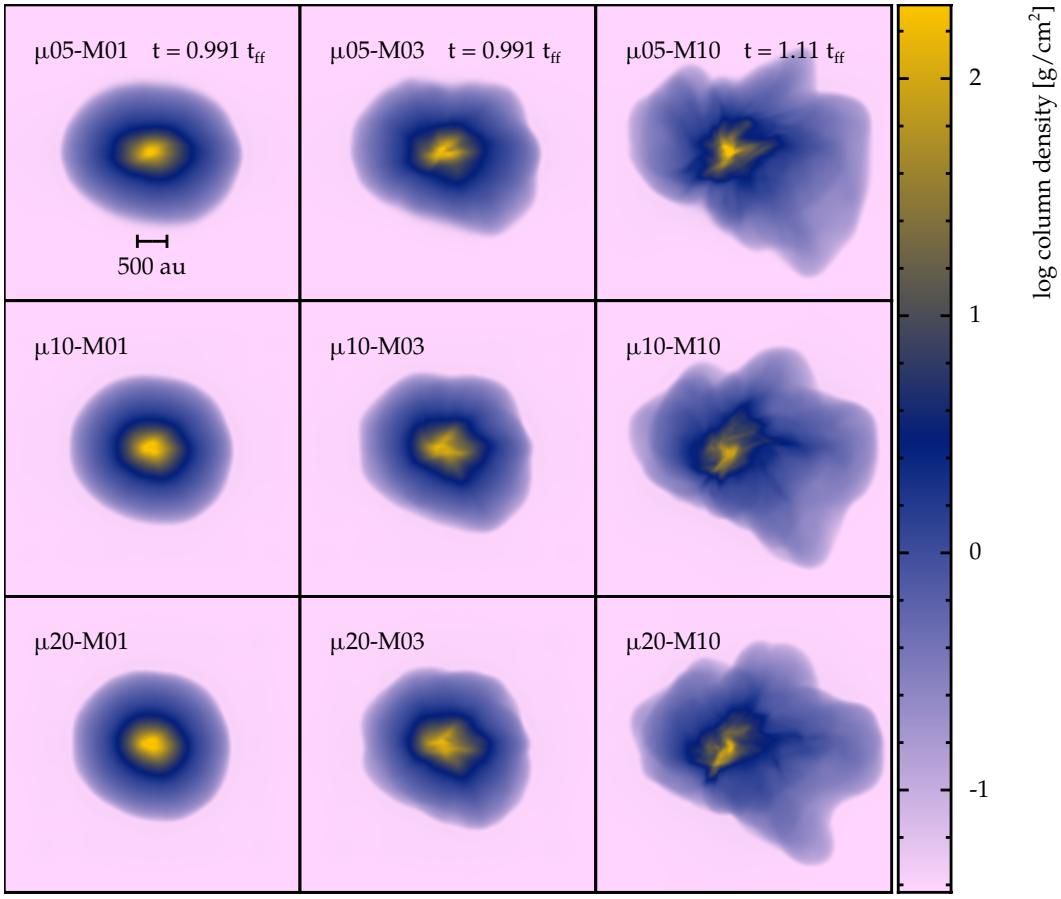

Figure VI.vi. Column density projections for all three turbulent calculations (left–to–right, $\mathscr{M} \in [1/10, 3/10, 1]$) with $\mu = 5$ (upper–row), $\mu = 10$ (centre–row), and $\mu = 20$ (lower–row) showing how increasing the mass–to–flux ratio (and consequently decreasing the initial magnetic field) results in a less oblate core. This effect is less pronounced at higher turbulent Mach numbers where the structure of the core becomes dominated by the turbulent velocity field.

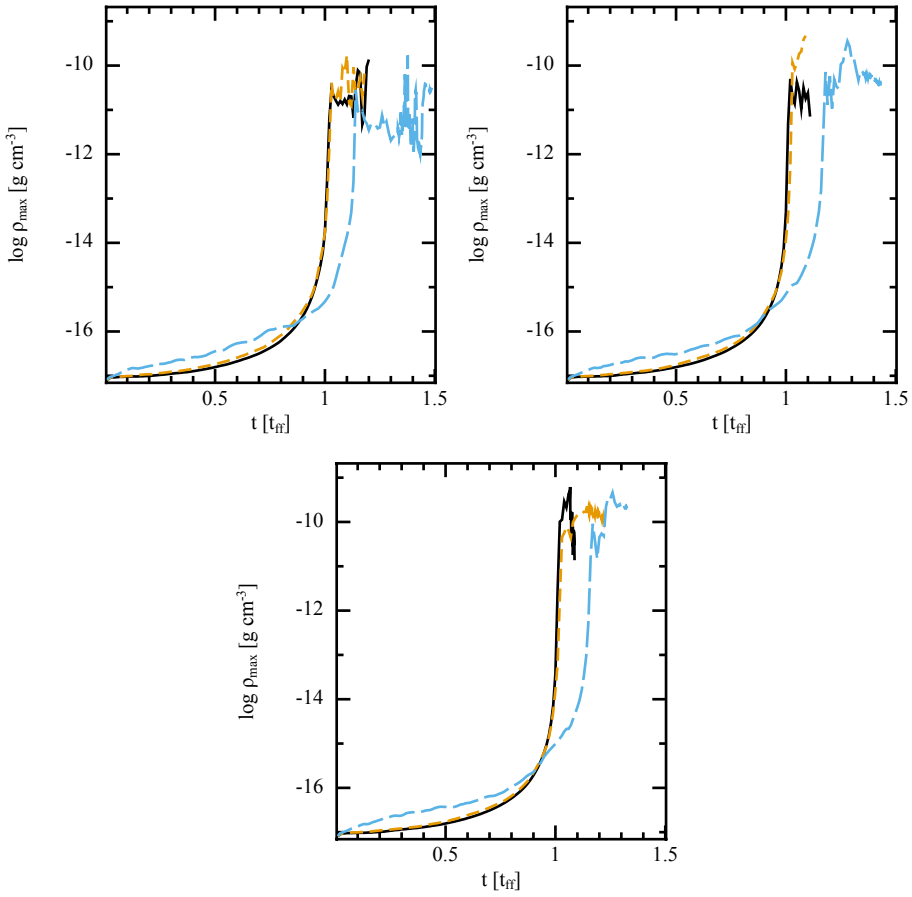

Figure VI.vii. Evolution of the maximum fluid density for $\mathscr{M} = 1/10$ (solid black line), $\mathscr{M} = 3/10$ (short–dashed orange line), and $\mathscr{M} = 1$ (long–dashed purple line) initial turbulent velocity fields for an initial mass-to-flux ratio of $\mu = 5$ (upper–left panel), 10 (upper–right panel), and 20 (lower panel). For all three values of μ, increasing the initial turbulence velocity delays the collapse of the molecular cloud core by providing additional energy to support the core against gravity. An effective 'maximum' density is provided by the insertion of a sink particle at $\rho = 1 \times 10^{-10}\,\mathrm{g \cdot cm^{-3}}$.

(see, *e.g.*, figure VI.i).

In summary, at high Mach numbers the turbulent velocity field dominates the initial phase of the evolution. R.T. becomes important when the density exceeds $\approx 10^{-13}$ g $\cdot$ cm^{-3}. M.H.D. effects in the initial phase are limited to changing the oblateness of the core, more complicated magnetic effects only occuring when the density is higher than about 10^{-11} g$\cdot$cm^{-3}. At lower Mach numbers, the turbulent velocity field instead acts to perturb and disrupt the uniformity of the collapse. This highlights a small difficulty in using the ideal free–fall time as a dimensionless temporal unit: the number of free–fall times at which the core will reach an 'interesting' density will vary depending on the sources of support against gravitational collapse present, for example a $\mathscr{M} = 1$ core will reach these densities $\sim {}^1/_5 t_{\rm ff}$ later than a laminar core. However, this unit is still useful for providing a dimensionless comparison between differing mass and volume cores. Consequently, in the following sections we will in general synchronize the calculations so that a comparable evolutionary epoch is discussed, rather than a fixed $t_{\rm ff}$.

VI.5 Shaken: varying the initial Mach number

Figure VI.viii shows the effect of increasing the initial turbulent velocity field for all three mass–to–flux ratios. A clear pattern emerges: firstly as in our previous laminar work, $\mu = 20$ calculations are unable to produce a bipolar outflow — which we see in sub–figure VI.viii.c. Secondly, that increasing the Mach number disrupts the system and inhibits the formation of a jet, as seen in the lower rows of sub–figures VI.viii.a to VI.viii.c. A rotating pseudo–disc is a necessary precursor to the formation of a bipolar jet (see *e.g.* Ciardi and Hennebelle 2010; Joos, Hennebelle, and Ciardi 2012; Lewis, Bate, and D. J. Price 2015; D. J. Price, Pringle, and King 2003) and an initially turbulent core acts to prevent the formation of this disc. Figure VI.viii demonstrates this effect: at $\mathscr{M} = {}^1/_{10}$ the $\mu = 5$ and 10 calculations clearly exhibit disc structures similar to, though less uniform, those produced by laminar calculations, which are increasingly disrupted as the initial turbulent Mach number is increased. This effect is also present (albeit without the bipolar jets) for $\mu = 20$ (see also Joos, Hennebelle, and Ciardi 2012). Figure VI.ix compares the radially averaged azimuthal velocity of the three $\mathscr{M} = {}^1/_{10}$ discs. We do not include more turbulent cores on this figure because the highly disrupted nature of the discs results in an impossibly confused graph. Additionally, the concept of a Keplerian velocity is difficult to define when the disc–structure is neither flat nor uniformly distributed around a protostar. These results are broadly comparable with the conclusions of Matsumoto, Machida, and Inutsuka (2017).

We also observe that adding radiative transfer to our laminar calculations does not markedly affect the shape or velocity of the outflow produced compared to the barotropic results obtained in Lewis and Bate (2017). This concurs with our observations in section VI.3 (and also with Bate, Tricco, and D. J. Price 2014) that adding a radiative transfer

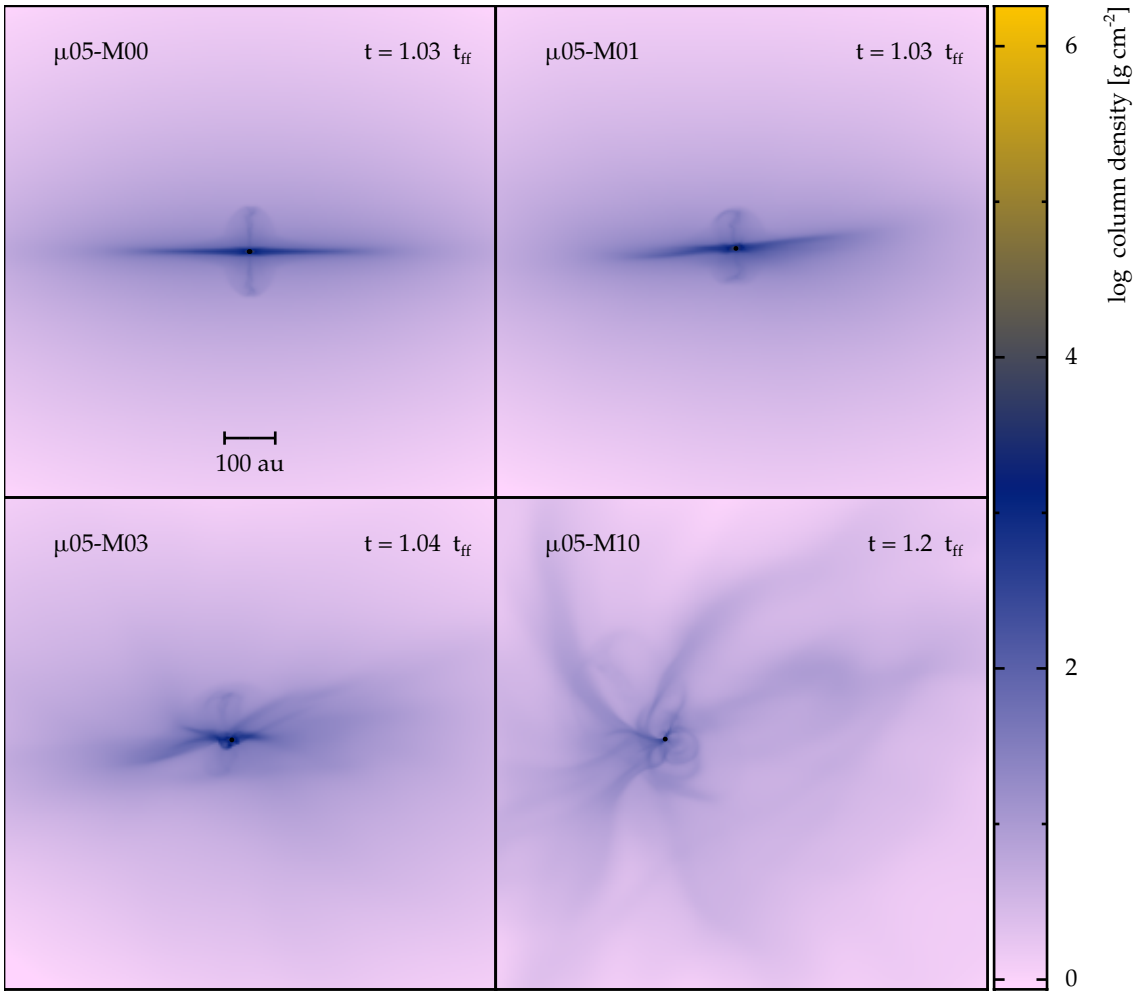

VI.viii.a. $\mu = 5$

Figure VI.viii. continued below

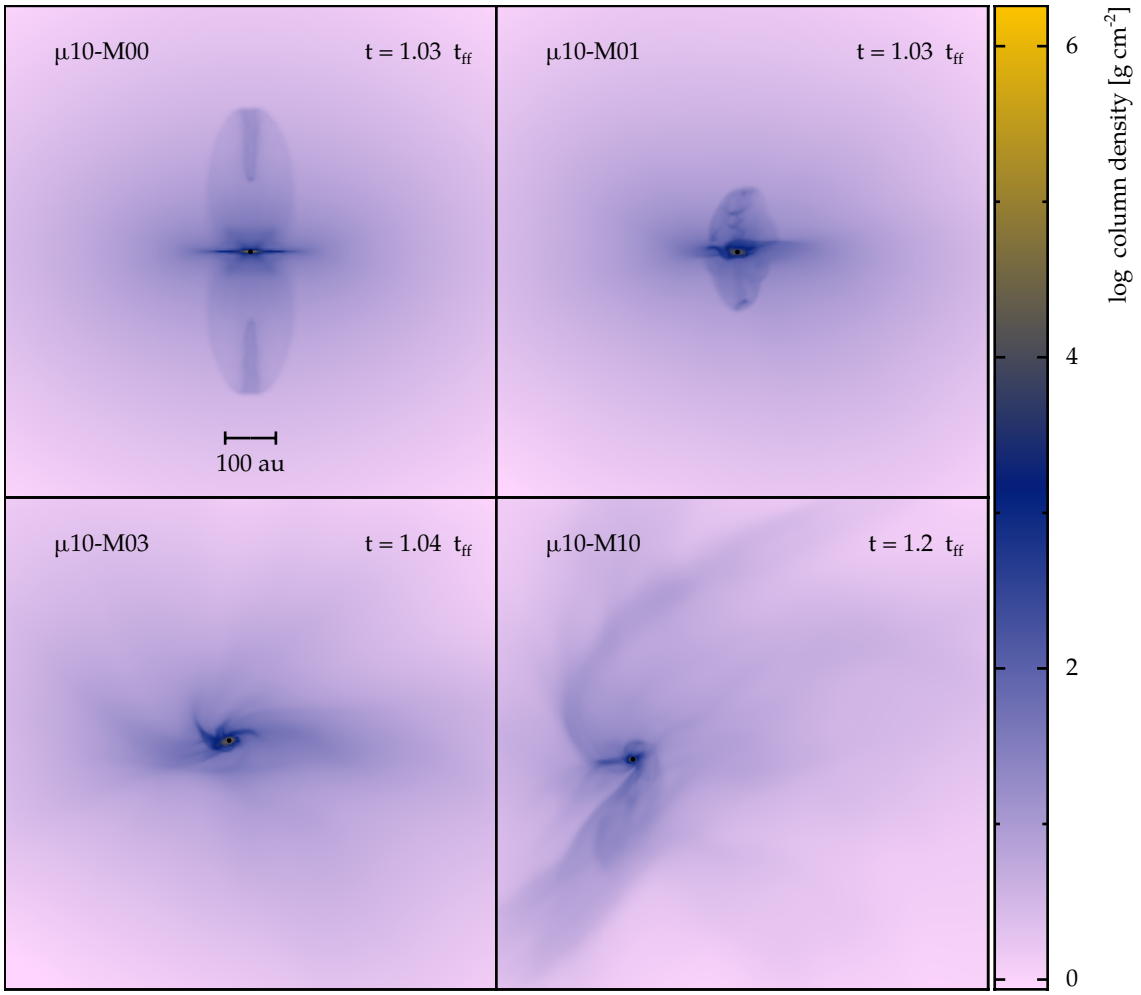

VI.viii.b. $\mu = 10$

Figure VI.viii. continued below

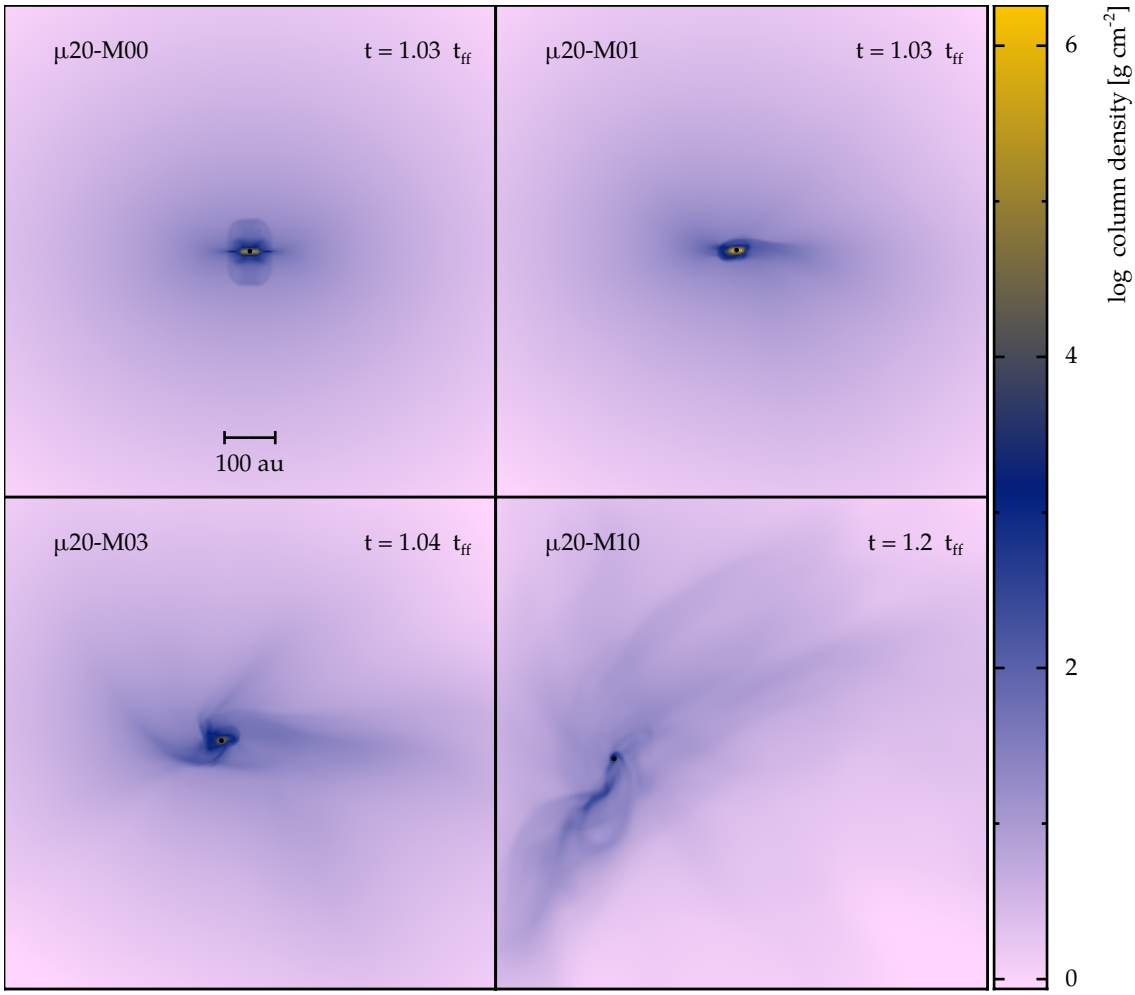

VI.viii.c. $\mu = 20$

Figure VI.viii. Column density projections in the y–direction for twelve R.M.H.D. calculations of a collapsing molecular cloud core, the time synchronization has been chosen so that the $\mu = 5$ calculations are an equivalent time after the insertion of a sink particle (which is coterminous with a maximum density being achieved). Sub–figure VI.viii.a has an initial magnetic field strength given by $\mu = 5$, sub–figure VI.viii.b has $\mu = 10$, and sub–figure VI.viii.c has $\mu = 20$. The initial turbulent Mach number is $\mathscr{M} = 0$, and $\mathscr{M} = 1/10$ on the upper–row of each sub–figure, then $3/10$ (sub–sonic cores), and 1 (transonic) on the lower–row. Bipolar outflows are only obvious for $\mu \leq 10$ coupled with $\mathscr{M} \leq 0.1$ although the $\mu = 5$, $\mathscr{M} = 0.3$ calculation has a weak outflow. In addition, higher values of $\mathscr{M}$ are correlated with a more complex structure.

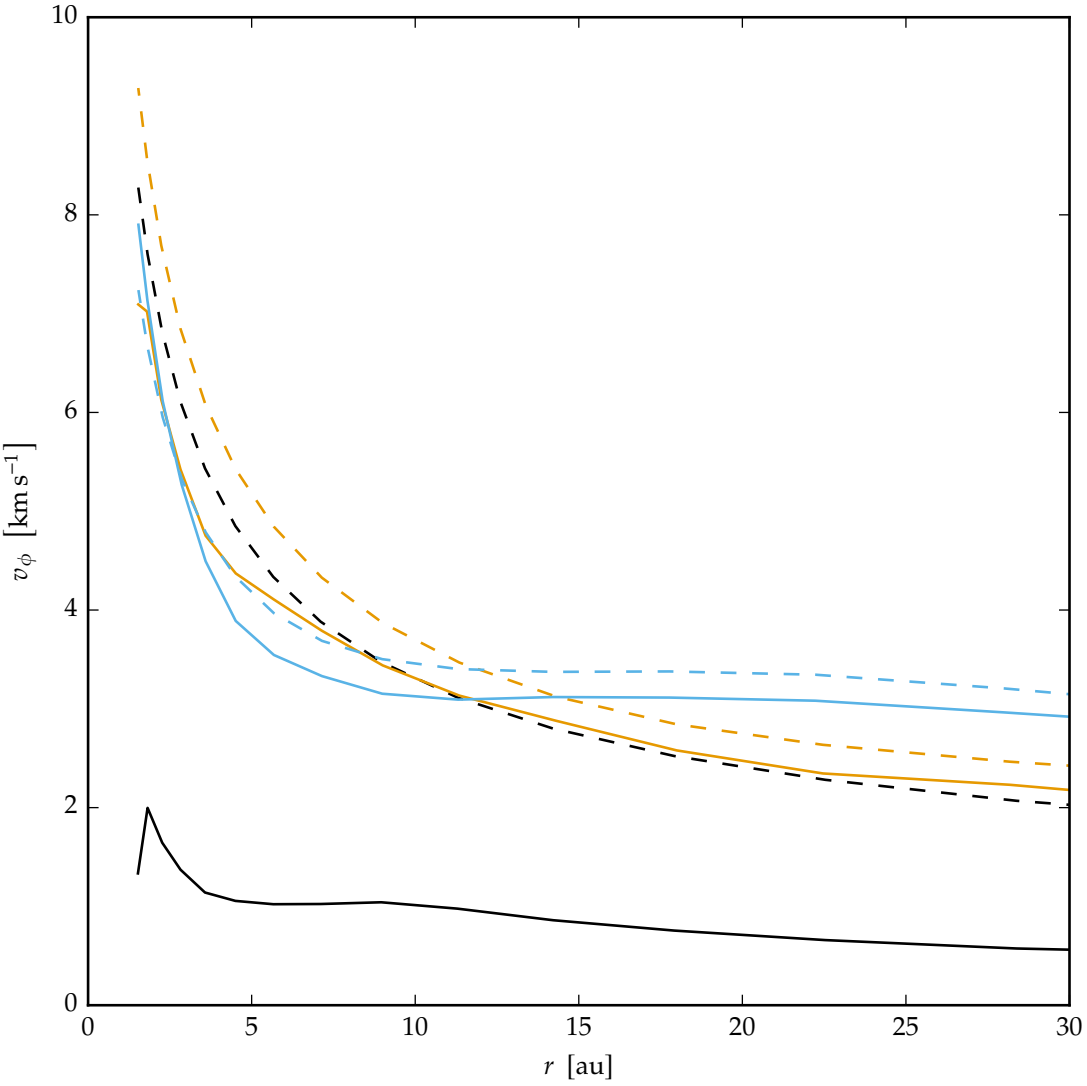

VI.ix.a. $\mathscr{M} = 1/10$

Figure VI.ix. continued below

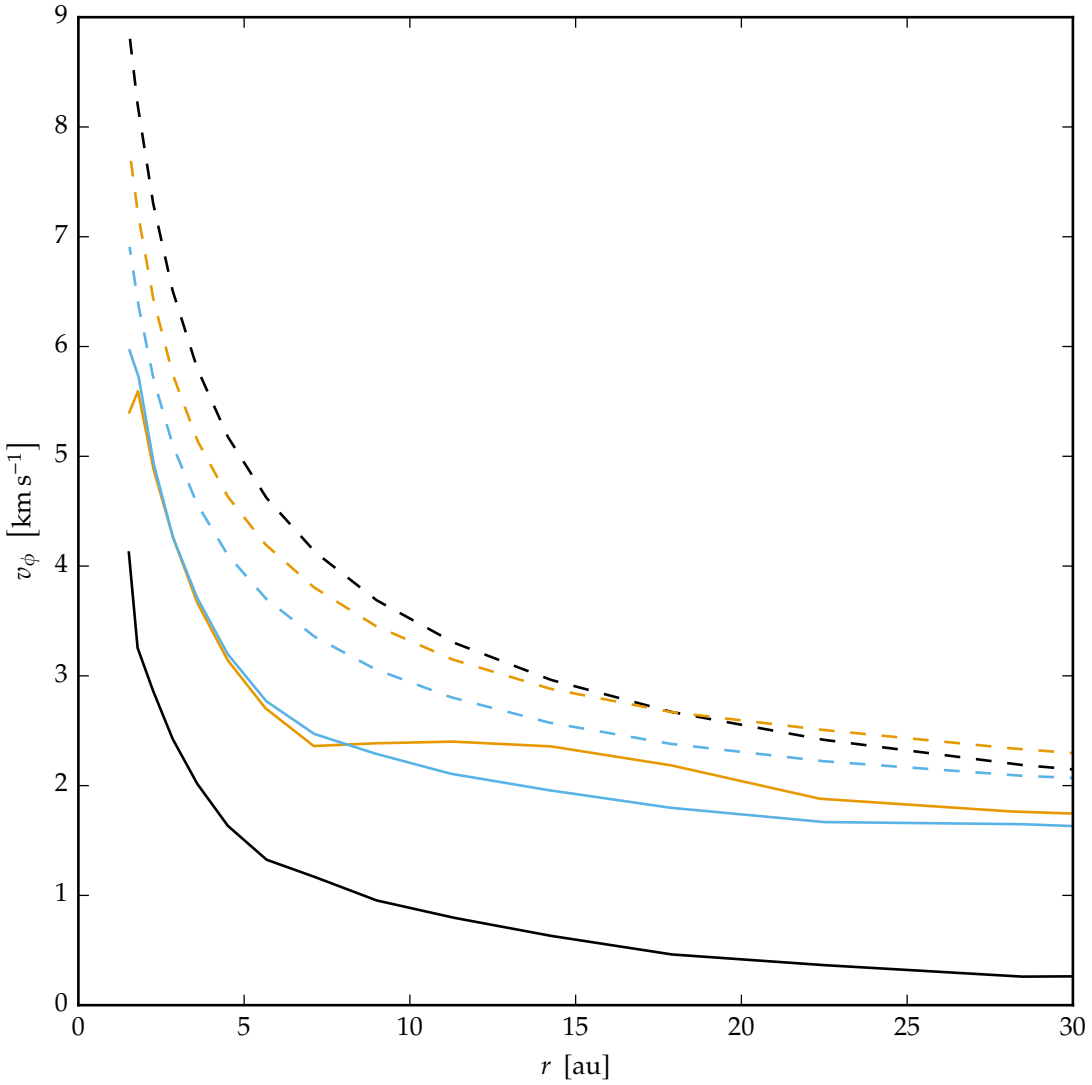

VI.ix.b. $\mathscr{M} = 3/10$

Figure VI.ix. Radially averaged azimuthal velocity as a function of radius from the sink–particle for the three $\mu = 5$, 10, and 20 calculations (black, orange and blue solid lines respectively) compared to the Keplerian velocity at that radius (dashed lines). Sub–figure VI.ix.a is for $\mathscr{M} = 1/10$ and sub–figure VI.ix.b is for $\mathscr{M} = 3/10$. The pseudo–discs become progressively further from Keplerian as μ decreases (*i.e.* as the field strength increases); in addition, for weaker fields increasing $\mathscr{M}$ also results in a more sub–Keplerian rotation profile.

treatment is a small overall effect, operating principally to produce a larger and warmer disc.

This qualitatively explains the differing evolution of the core as the initial turbulence is increased. We now use the co–ordinate transformation given in equations V.1 and V.2 to transform the magnetic field into cylindrical co–ordinates. We can then obtain the toroidal magnetic field component directly from the azimuthal component as

$$B_{\rm tor} = B_{\phi} \tag{VI.9}$$

and the magnitue of the poloidal component using

$$\left|B_{\rm p}\right| = \sqrt{B_r^2 + B_z^2}, \tag{VI.10}$$

as done, *e.g.*, by Parker (1955).

In chapter V and Lewis and Bate (2017) we concluded that the essential ingredients for collimated outflows were a strong poloidal field to lift material out of the disc–plane *coupled with* a strongly toroidal component to collimate the outflow. A solely torodial field trapped fluid in the disc and a solely poloidal field would produce a bulk outflow (*cf.* the 'detachment' seen for a $\mu = 10$ calculation in section V.5 when the poloidal component overhauls the torodial one). In figure VI.x we show how this effect is mirrored for these calculations. Firstly, the sub–sonic $\mu = 20$ calculations have a strongly toroidal disc, with no significant region where the poloidal field dominates. This can be seen in sub–figure VI.x.c: here in the first panel the differing morphology compared to the first panels of sub–figures VI.x.a and VI.x.b is evident. Rather than a thin poloidal region centred on the bipolar jet, a weakly toroidal region can be seen above and below the disc (between the 'lobes' of the polodial region). When $\mathscr{M} = 1/10$ this poloidal region is further reduced in size.

Conversely, the $\mu = 5$ and 10 calculations *with* an outflow have a poloidally dominated region (exemplified by the thin poloidal structure extending approximately vertically above and below the disc) which is then wound-up by the strongly toroidal disc (exemplified by the toroidal inner region of the jet). Clearly, then, by disrupted the formation of a pseudo–disc, turbulence is able to prevent angular momentum transport via a bipolar outflow. Instead, in a qualitatively similar way to the $\mu = 20$ calculations, a bulk poloidal region is formed around the pseudo–disc. However, unlike for a laminar core, this does not lead to fragmentation. Whilst fragmentation can be suppressed in stronger fields ($\mu \geq 10$) by magnetic braking, hitherto we found that all $\mu = 20$ discs were gravitationally unstable and liable to fragment into binary or ternary systems. We note, however, that the increased turbulent velocity field has the effect of both making the (pseudo–)discs less massive and also placing less angular momentum in the disc. Both of these effects make the disc less vulnerable to fragmentation from gravitational–rotational torques. This

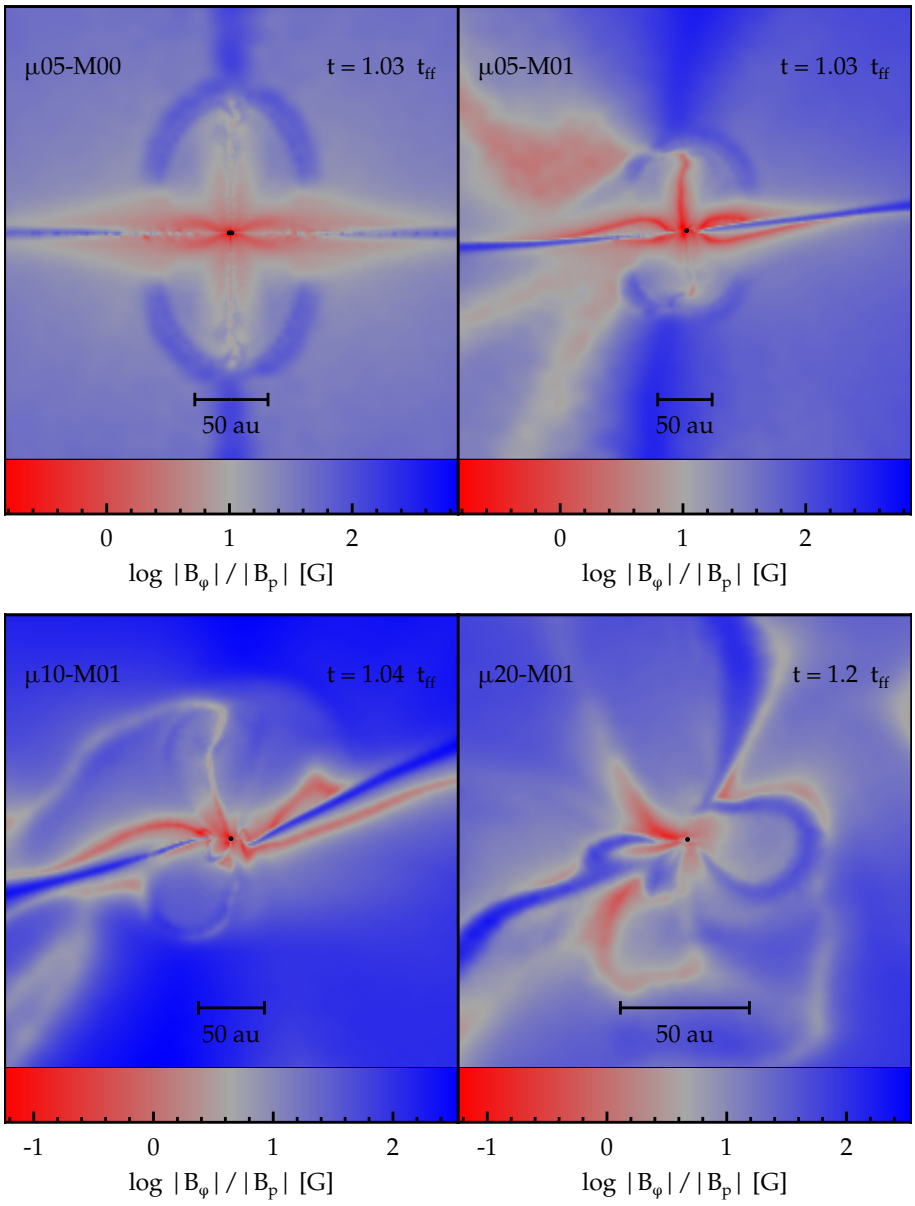

VI.x.a. $\mu = 5$

Figure VI.x. continued below

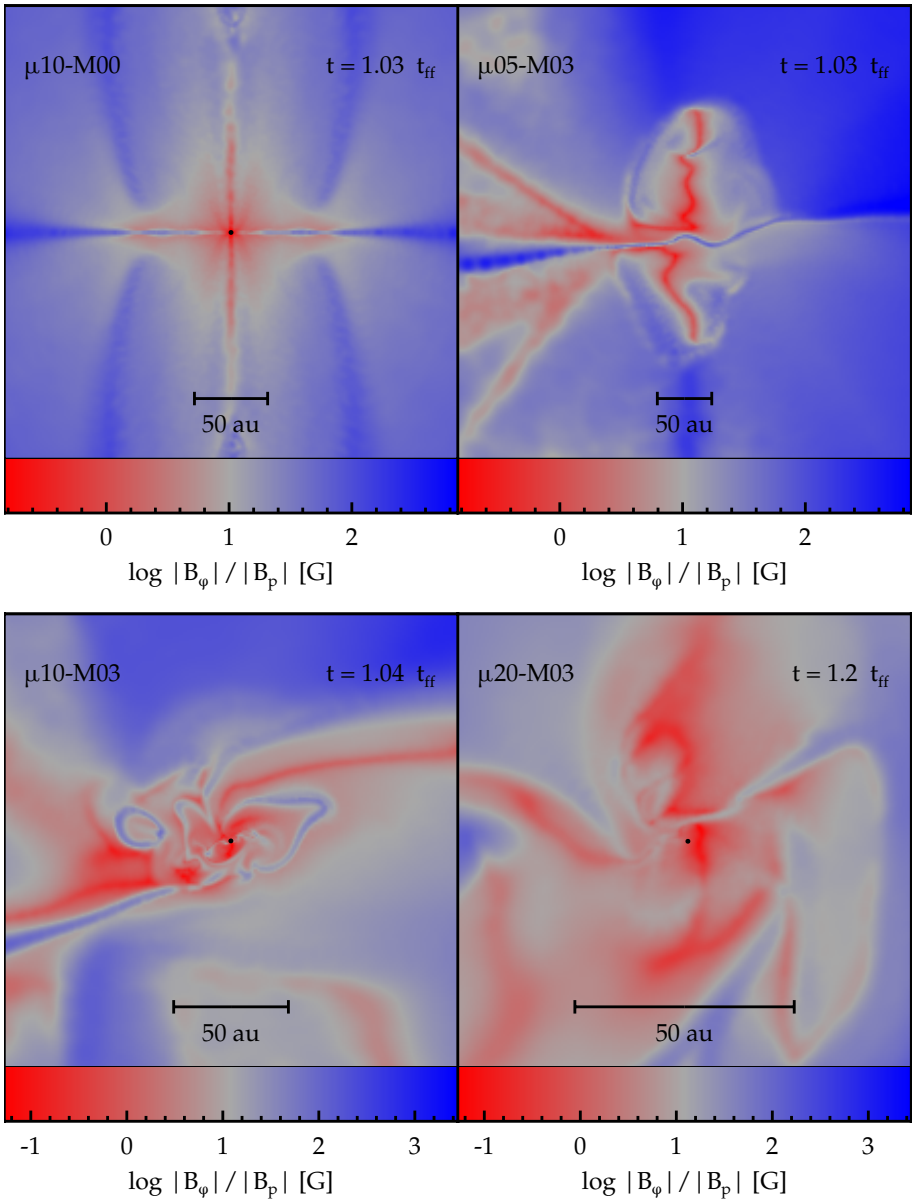

VI.x.b. $\mu = 10$

Figure VI.x. continued below

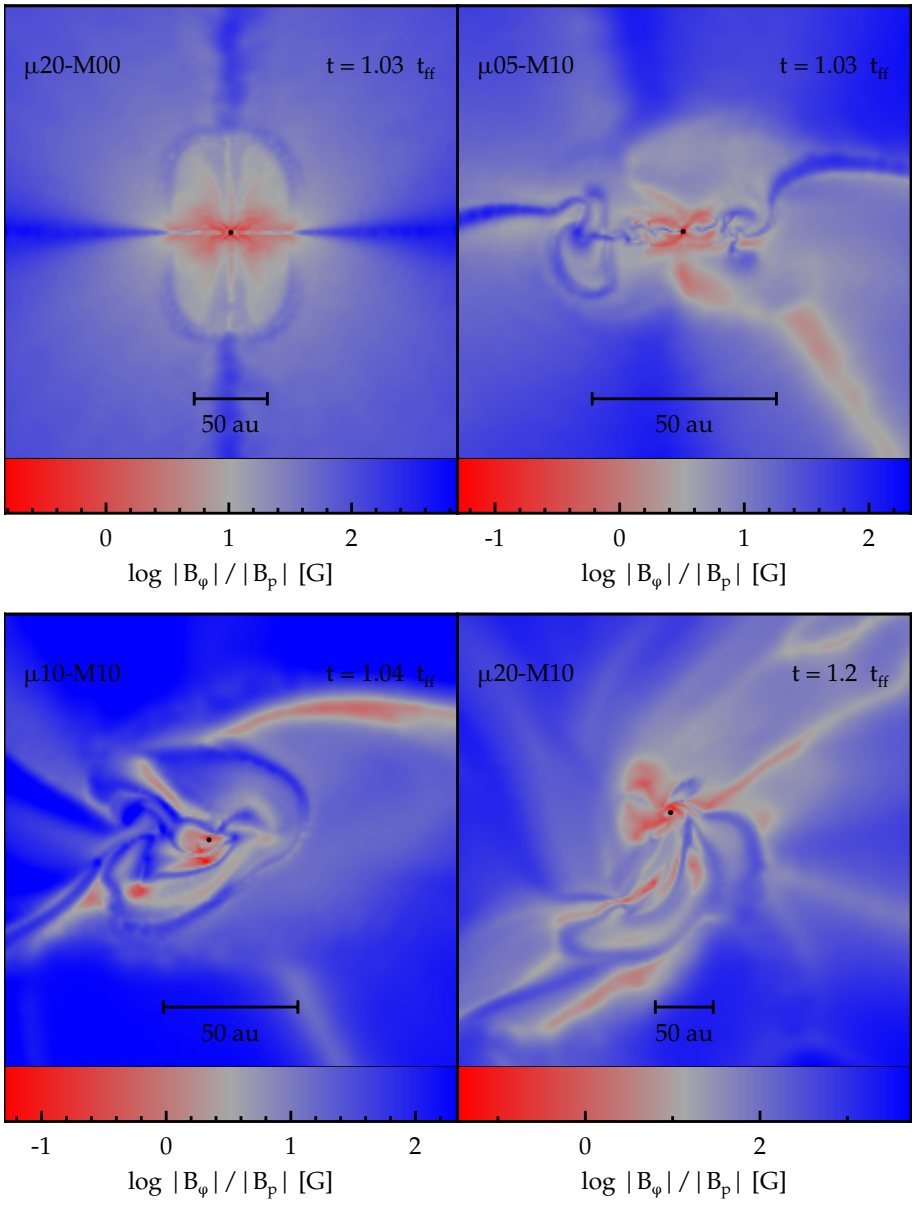

VI.x.c. $\mu = 20$

Figure VI.x. Tranverse sections, in an approximate z–x plane through the sink particle of the ratio of the poloidal magnetic field component to the toroidal component for all twelve calculations presented in figure VI.viii. The sections are presented in the same order as in that figure, so that sub–figure VI.x.a, sub–figure VI.x.b, and sub–figure VI.x.c are $\mu = 5$, 10, and 20 respectively and then the upper–row of each sub–figure is $\mathscr{M} = 0$ and $1/10$ and the lower–row $\mathscr{M} = 3/10$, and 1 respectively. Red indicates regions where the poloidal field component (*cf.* equation VI.10) is dominant and conversely blue indicates regions where the toroidal field (*cf.* equation VI.9) is dominant. Material is removed from the region around the sink–particle by the poloidal field. This process, however, is more efficient and results in a collimated jet — in particular as seen in the top–left panel — when the toroidal field is able to wind up the material as it is being lifted away from a pseudo-disc.

latter point is echoed by comparing the total rotational energy of the whole core, which is reduced in the transonic cores compared to the sub–sonic ones as the turbulent motion acts to prevent simple rotation around the z–axis. We note also that the 'toroidal' region is a good tracer for the location of a pseudo–disc, albeit not the extent since this region will extend out the the edge of the core. For example, the transonic, $\mathscr{M} = 1$, cores all develop discs which are neither flat nor close to perpendicular to the rotation axis (or equivalently perpendicular to the initial magnetic field axis).

From this, we conclude that highly turbulent initial conditions are — all other things being equal — inimical to the formation of bipolar jets and well defined pseudo–discs. This has consequences for observations: an observation that a very young protostellar object has a jet–like outflow (where $\beta_{\rm rot} = 0.005$) implies that the core was initially sub–sonic.

VI.6 Stirred: varying the initial angular momentum

In section VI.5 *supra*, we showed that increasing the initial turbulent velocity field of the core into a transonic regime inhibits the formation of a (pseudo–)disc and therefore suppresses the formation of a bipolar outflow. Since disc structures are inherently connected with the angular momentum in a collapsing core, we now take the $\mu = 5$ calculations with a $\mathscr{M} = 1$ velocity field and increase the initial rotation rate. These are calculations μ05–M10–r001 and μ05–M10–r002 in table VI.1. μ05–M10 has $\beta_{\rm rot} = 0.005$, so these two calculations have double and quadruple the initial rotational energy (and hence the angular momenta are $\sqrt{2}$ and double the initial values) respectively. figure VI.xi compares these three calculations at a comparable evolutionary epoch. We find that μ05–M10–r001 (the calculation with double the initial angular momentum) has a very weak outflow, corresponding to a confused disc–like structure; however, μ05–M10–r002 produces a clear disc and a corresponding bipolar outflow. Figure VI.xii clearly shows this, with a region of fluid moving the outward from the sink particle, *i.e.* where $v_z > 0$ for $z > 0$ (above the plane of the disc) and *vice versa*.. We note that material undergoing a gravitational self collapse invariably has $v_z \leq 0$ above the disc and *vice versa*. Unlike the sub–sonic cores presented above and the laminar cores presented in chapter V, this outflow is much slower (*ca.* $|v_z| \approx 1\,{\rm km}\cdot{\rm s}^{-1}$) and much less substantial. The latter effect is shown by the reduced column density contrast between the outflow material and the surrounding cloud core.

The nature of any disc structure is related to the initial rotation rate. At the lowest initial rotation rate, *i.e.* calculation μ05–M10(R), no disc forms. Conversely at the highest rotation rate — calculation μ05–M10–r0.02 — a clear pseudo–disc has formed. However, this disc has a rotation speed slower than that seen in figure VI.ix for a sub–sonic core (and which is therefore even slower than a laminar core, e.g. μ05–M00). This is the cause of the weaker outflow seen here. Nonetheless, this illustrates that whilst turbulent kinetic energy can disrupt a core so much that it does not form a pseudo–disc, adding additional *rotational* energy can act to re–form that disc structure. To quantify this effect, we define a

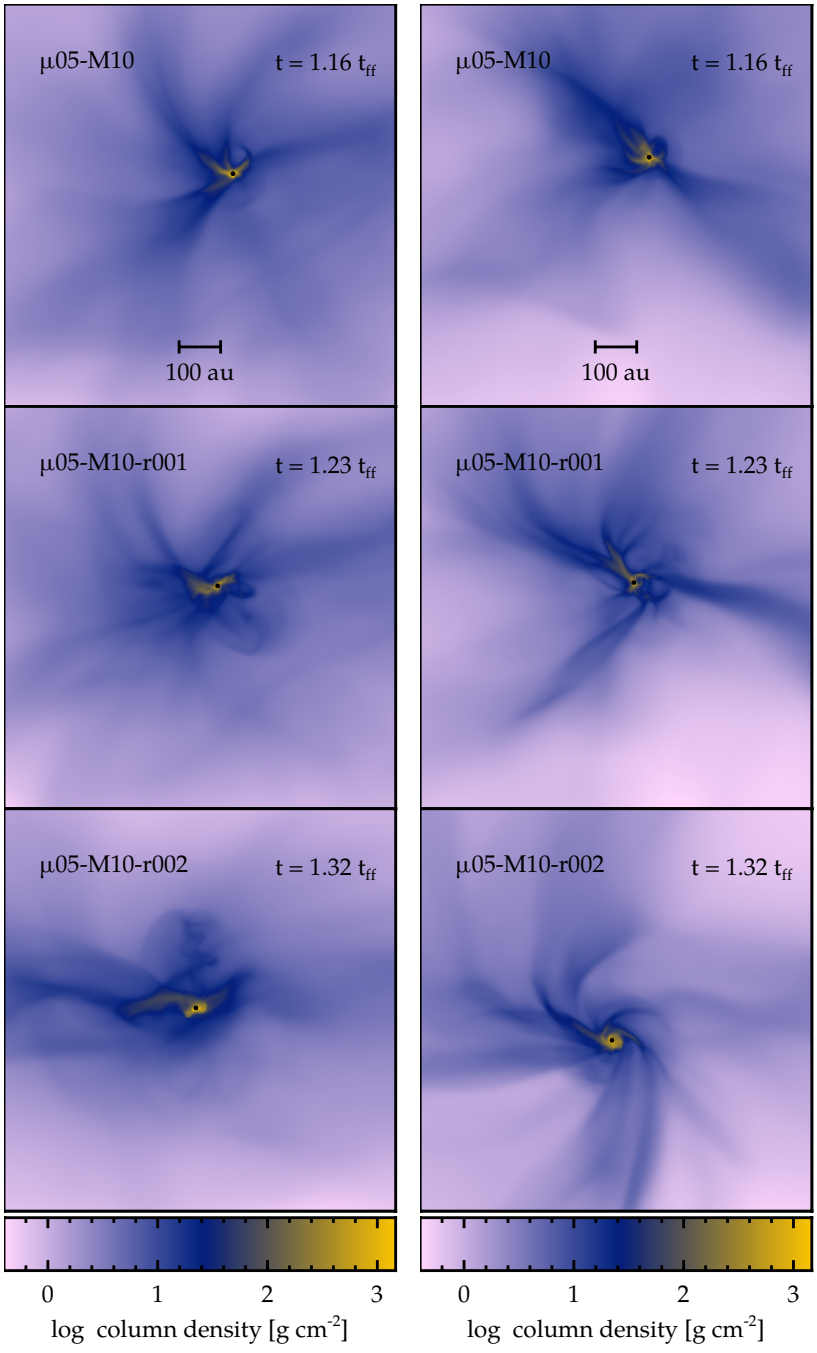

VI.xi.a. y–direction *VI.xi.b.* z–direction

Figure VI.xi. Column density projections in the y–direction (sub–figure VI.xi.a) and z–direction (sub–figure VI.xi.b) for three R.M.H.D. calculations of a collapsing molecular cloud core, all with $\mu = 5$ and an initial Mach number of $\mathscr{M} = 1$. The upper row is the same calculation presented in section VI.5, shown here again as a comparison, which has $\beta_{\rm rot} = 0.005$. The centre and lower rows then have $\beta_{\rm rot} = 0.01$ and 0.02, *i.e.* double and quadruple, respectively. This increase in angular momentum results in the formation of a pseudo–disc structure and, ultimately, an outflow.

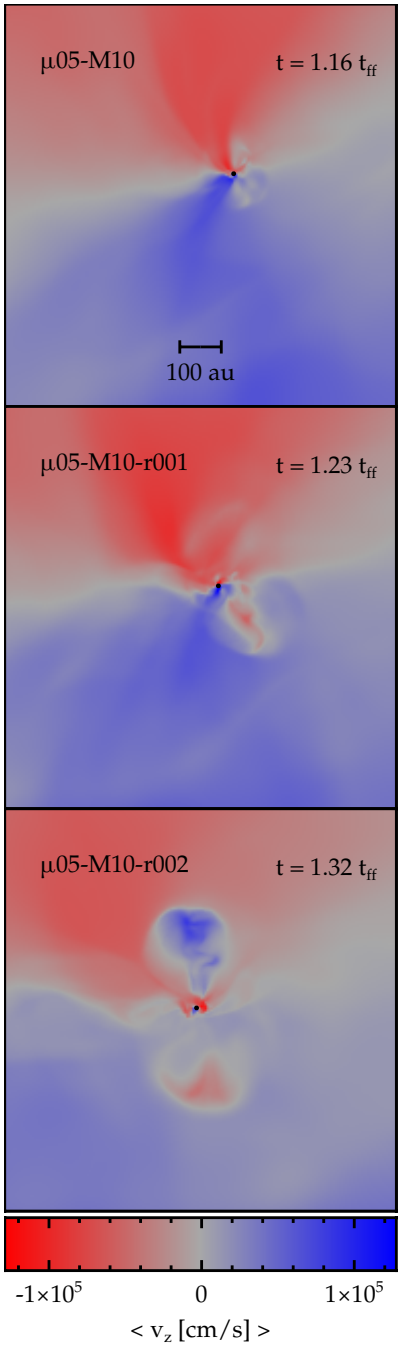

Figure VI.xii. Density–weighted average of the z–component of the velocity field for the three calculations presented in figure VI.xi, *i.e.* where the upper panel, centre panel and lower panel have $\beta_{\rm rot}$ = 0.005, 0.01, and 0.02 respectively. The signature of an outflow, a region with material moving the 'wrong way' is clearly visible in the right–hand panel, as opposed to the highly disrupted calculations presented in the other two panels.

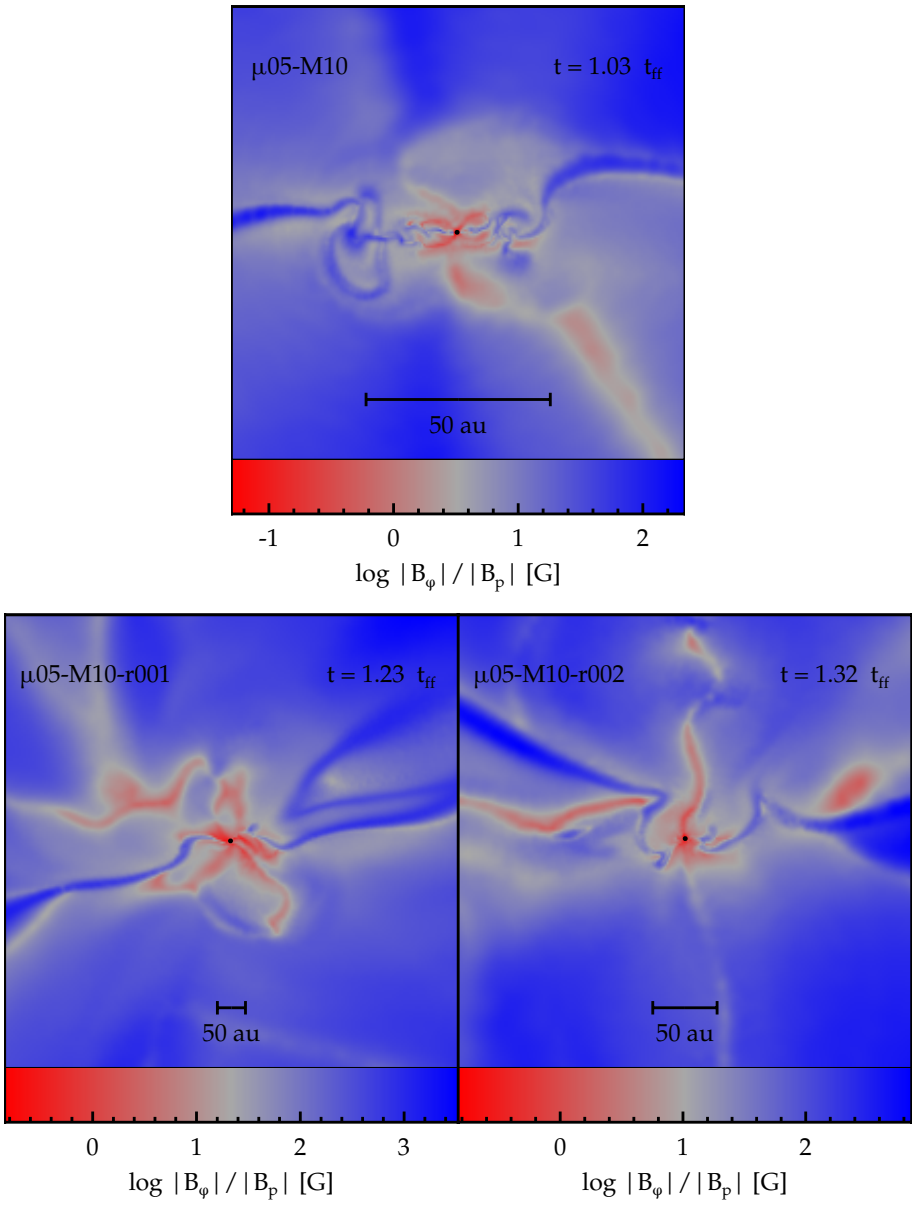

Figure VI.xiii. Tranverse sections, in a z–x plane through the sink particle of the ratio of the poloidal magnetic field component to the toroidal component for the three calculations presented in figure VI.xi. As in figure VI.x, red indicates regions where the poloidal field component dominates compared to blue regions where the toroidal field is dominant.

new parameter,

$$\varepsilon = \frac{\beta_{\text{turb}}}{\beta_{\text{rot}}} \equiv \frac{E_{\text{turb}}}{E_{\text{rot}}}, \tag{VI.11}$$

such that $\varepsilon > 1$ implies turbulence is the dominant source of kinetic energy, conversely $\varepsilon < 1$ implies rotation is, and $\varepsilon \approx 1$ implies an approximate equality between the two fields. A value of $\varepsilon \lesssim 1$ is a necessary pre–requisite for the formation of a pseudo–disc and outflow. The μ05–M10(R) calculation has $\varepsilon = 26 \gg 1$ and correspondingly the pseudo–disc was highly disrupted; conversely μ05–M10–r002 had $\varepsilon = 1.06 \approx 1$ and has formed a disc with a weak outflow. The intermediary phase μ05–M10–r001 has $\varepsilon = 1.6$ which corresponds, as expected, to a disrupted pseudo–disc. These values are compatible with those obtained for lower Mach numbers, *e.g.* μ05–M01 and μ05–M03 have $\varepsilon = 0.26 < 1$ and $\varepsilon = 2.4 \approx 1$ respectively (identical values are necessarily obtained for μ10–M01, *etc.*).

Comparing the outflow velocities between the earlier laminar cores, the sub–sonic cores in section VI.5 and the transonic cores in this section we find a steady decrease in the outflow speed, $|v_z|$, as the conditions become more complicated. For example, a laminar core with a fully aligned magnetic field can produce an outflow with $|v_z| = 8$ km $\cdot$ s^{-1}, a sub–sonic core where $\varepsilon = 2.4$ produces a slower and less collimated outflow, but the transonic core with $\varepsilon = 1.06$ only produces $|v_z| = 0.5$ km $\cdot$ s^{-1}.

Figure VI.xiii shows the same poloidal–toroidal decomposition as in figure VI.x but for the three $\mathscr{M} = 1$ calculations discussed in this section. The change between no outflow when $\varepsilon = 26$ and a collimated jet when $\varepsilon = 1.06$ is again shown in this analysis. There is also the hint of a weak outflow in the highly distrupted pseudo–disc when $\varepsilon = 1.6$, however, the lack of a disc structure to collimate this suppresses a jet structure from being formed. This highlights how the formation of a disc is necessary to produce a jet–like outflow around a first hydrostatic core.

VI.7 Discussion and Comparison to Observations

We observe that the ratio of the total magnetic, turbulent and rotational kinetic energies to the gravitational self-potential in the $\mathscr{M} = 1$ cores is very close to unity. Consequently, these cores are on the limit of boundedness and would become unbound with only a small increase in the turbulent velocities. This is consistent with the observed average velocities seen in cluster scale simulations, where cores (or comparable regions) undergoing a Jeans collapse are often sub–sonic, notwithstanding the initial highly super–sonic velocities in the progenitor cloud Klessen, Heitsch, and Mac Low (2000), and compatible with observed star formation regions, *e.g.* in Ophiuchus Pattle *et al.* (2015).

A large value of ε in these highly turbulent (and weakly bound) cores is comparable to the strongly misaligned magnetic field and rotation axes that we explored in chapters IV and V. In those cases, values of the parameter $\vartheta \geq 60°$ produced highly disrupted discs — with correspondingly slower rotation profiles — and this was fatal to the production

of an outflow. The production of a bipolar jet from a first hydrostatic core is therefore linked to both having a suitable field strength and geometry (turbulence can not make a weaker field more able to produce the necessary poloidal components to form a jet) to generate the outflow at all, combined with an environment conducive to the formation of a sub–Keplerian pseudo–disc. This former requirement is satisfied by having $\mu \geq 10$ and $\vartheta < 60°$, whilst the latter requires $\varepsilon \lesssim 1$ which implies either a sufficently weak turbulent velocity field *or* a sufficiently strong rotational velocity field.

Observations of potential first hydrostatic core outflows (*e.g.* Dunham *et al.* 2011) report outflow speeds of around $|v_z| = 5\text{km} \cdot \text{s}^{-1}$. These are consistent with the observed $|v_z|$ values seen for very weakly turbulent and laminar cores, where $\varepsilon \gg 1$ but in these configurations the total kinetic energy is actually relatively low. Outflows are produced with much higher initial kinetic energies, *i.e.* when $\mathscr{M} = 1$, provided that $\varepsilon \gtrsim 1$. However, the outflow produced in this scenario — transonic turbulence coupled with additional angular momentum — is much slower. This has an important implication for observations, *viz.* that faster outflows are the result of less 'dynamic' initial conditions. Conversely it also indicates that a slower outflow speed implies *either* a reduction in angular momentum (although not discussed in this chapter this conclusion follows from the discussion about the formation mechanism of the jet) *or* a reduction in ε. This allows a limited degree of re–winding of the evolution of very young protostellar objects to predict the conditions in the Jeans unstable core from which they formed. The size of the first hydrostatic core provides a limit on the maximum outflow and jet velocity (see D. J. Price, Pringle, and King 2003). Therefore, simply trying to increase ε to obtain faster jets is not possible, and objects such as `MMS-6/OMC-3` found by Takahashi and Ho (2012) or the Herbig–Haro object `HH 1165` found by Riaz *et al.* (2017) are more evolved than the first core phase.

We noted earlier that our results are broadly comparable with Matsumoto, Machida, and Inutsuka (2017). For example, in the initial phase of the collapse we obtain a similar link between oblateness and field strength, and disruption of the collapsing core by higher Mach numbers (see also Matsumoto and Hanawa 2011). However, Matsumoto, Machida, and Inutsuka (2017) use significantly stronger magnetic fields ($1.12 \leq \mu \leq 2.81$). The core mass used there was also higher than our work ($M_{\text{core}} = 2.51\ \text{M}_\odot$ as opposed to $1\ \text{M}_\odot$) so this implies a much stronger magnetic field is present. We obtain a similar reduction in the radius of the pseudo–disc as μ is reduced as in that paper, however, because we also probe much weaker field strengths — $\mu \leq 20$ — we also find that we also find that once magnetic effects are reduced further the disc size again decreases due to reduced angular momentum transport (see sections V.5 and V.6). The difference in magnetic field strengths also explains the lack of any magnetic pressure induced 'cavity' in our calculations. We also note that our calculations include a radiative transfer scheme and begin with uniform density, not Bonnor–Ebert, spheres.

We find a strong, but not perfect, alignment between our pseudo–discs and the outflow produced. This is likely due to the way we super–impose a random turbulent velocity

and a solid body rotation profile together. This guarantees that the angular momentum vector of the system will be very closely aligned to the z–axis (which is also the magnetic field axis). In comparison, an approach whereby the random seed used to generate the turbulence is used to produce angular momentum will result in a more complicated angular momentum vector. Consequently, in such a system misalignements between the discs and outflows are more likely to occur. However, our approach has the advantage that it is possible to separate linear and rotational effects more easily. Keeping the rotational component of the velocity field separate would also allow the effect of varying ϑ to be more readily explored. We note, however, that the partially asymmetrical appearance of the outflow when $\mathscr{M} = 1$ and $\varepsilon \gg 1$ is compatible with the complex structure of HH 1165 (Riaz *et al.* 2017), and in particular the asymmetrical nature of the outflow seen in that system. This indicates that the combination of rotational effects — to create a disc and outflows — and turbulence is necessary to explain the complex structures seen in protostars.

CHAPTER VII

Helical Outflows and Binaries from Rapidly Rotating Centrally Condensed Cores

Into what dangers would you lead me, Cassius,
That you would have me seek into myself
For that which is not in me?

Marcus Junius Brutus 'the Younger'

Men at some time are masters of their fates:
The fault, dear Brutus, is not in our stars,
But in ourselves, that we are underlings.

Gaius Cassius Longinus
Scene II, Act I, Julius Cæsar
William Shakespeare (1599)

VII.1 Initial Conditions

We again use the radiative magnetohydrodynamic scheme used in chapter VI and set out in chapter II. However, we switch from using an initial uniform density distribution to using a Bonnor–Ebert (Bonnor 1956; Ebert 1955) sphere as our initial density profile. This has two principal advantages. Firstly that this is a more realistic initial configuration for a molecular cloud core. Secondly, it allows a greater degree of angular momentum to be introduced into the core before effects such as 'ring fragmentation' occur. We discuss how the initial density profile is set up in sub–section VII.1.1 and the application of a rotational velocity field in sub–section VII.1.2. Otherwise we use the same initial conditions are before, *e.g.* the initial magnetic field is defined via the mass–to–flux ratio, μ and the angle between the field and rotation axes, ϑ. This chapter uses $\mu = 5$ and $\vartheta = 0°$ throughout. Since the purpose of the work in this chapter is to compare the effect of changing the angular momentum in the core, we set the critical density for sink particle insertion to $\rho_{\text{crit}} = 10^{-5}\,\text{g}\cdot\text{cm}^{-3}$ for the reasons identified in section VI.2. We find that when we increase the initial angular momentum of the core that even a strong $\mu = 5$ magnetic field will not prevent fragmentation and the formation of a binary system. This provides a route to binary formation in strong field configurations (*cf.* the formation of binaries when $\mu = 20$ *only* in chapter V).

VII.1.1 The Bonnor–Ebert Sphere

A Bonnor–Ebert sphere is a density profile derived from two observations. The first of these is the inner boundary condition that

$$\rho\left(r = 0\right) = \rho_{\text{max}}, \tag{VII.1}$$

$$\partial_r \rho\big|_{r=0} = 0. \tag{VII.2}$$

This is simply a statement that the central density of the density distribution, $\rho\left(r\right)$ is finite and continuous — the former is true in all fluids, and the latter is a reasonable statement for a molecular cloud core. The second observation is that a centrally condensed region of a molecular cloud (*i.e.* a cloud core) should be in pressure equilibrium with the surrounding cloud at the boundary. This criterion was present in our earlier uniform density profiles, and is a reasonable statement given the fluid forms a continuum between the containing cloud and the core. This outer boundary condition can be expressed in a number of ways, one being that[1] the

$$P\left(r = r_{\text{core}}\right) = P_{\text{ext}} = c_{s,\text{ext}}^2 \rho_{\text{ext}}. \tag{VII.3}$$

1. assuming the equation of state for an ideal gas is used

Alternatively, one could imagine this as simply the radius at which the pressure of the sphere becomes equal to the container medium. The solution to the Lane–Emden (Emden 1907; Lane 1870) equation which satisfies these boundary conditions is the Bonnor–Ebert sphere. The Lane–Emden equation is the differential equation given by

$$\frac{1}{\xi^2}\partial_\xi \left[\xi^2 \partial_\xi \Phi(\xi)\right] = \exp\left[-\Phi(\xi)\right], \tag{VII.4}$$

where $\xi(r) = r/r_0$ is a dimensionless 'radius' expressed in terms of a characteristic radius, r_0. This is given by

$$r_0 = \frac{c_s}{\sqrt{4\pi G \rho_0}}. \tag{VII.5}$$

We then set the density profile according to a polytrope–like equation of the form

$$\rho(r) = \rho_0 \exp\left[-\Phi(\xi)\right], \tag{VII.6}$$

The function $\Phi(\xi)$ is defined to have the boundary conditions(see, *e.g.*, Banerjee, Pudritz, and Holmes 2004)

$$\Phi(\xi = 0) = 0, \tag{VII.7}$$

$$\partial_\xi \Phi(\xi = 0) = 0. \tag{VII.8}$$

From this, it follows that the ρ_0 in equation VII.6 represents the central density (*i.e.* the density where $r = 0$ and consequently $\xi = 0$). This then leads to the observation that the mass contained within $r = \xi$ is given by

$$M(r = \xi) = \frac{c^3}{\sqrt{4\pi G^3 \rho_0}}\varsigma, \tag{VII.9}$$

where the dimensionless 'mass' is given by (McLaughlin and Pudritz 1996)

$$\varsigma = \xi^2 \partial_\xi \Phi(r). \tag{VII.10}$$

The second boundary condition (equation VII.8) combined with this equation for the mass implies that a sphere where the adimensional radius, $\xi = 0$, will correspondly have zero mass.

An equilibrium is obtained when $\xi \leq 6.451$ (Bonnor 1956), *i.e.* for the density profile obtained for

$$\rho(r) = \rho_0 \exp\left[-\Phi(\xi \leq 6.451)\right] \tag{VII.11}$$

will have sufficent pressure support to prevent a gravitational collapse[2].

2. this again assumes an ideal gas equation of state, and also assumes no other processes of mass transfer,

We wish to obtain initial density profiles that, although centrally condensed, will inevitably collapse due to the Jeans (1902) instability. Consequently throughout this chapter we use $\xi = 7.45$, *i.e.* $^{15}/_{100}{}^{\text{th}}$ higher than the 'critical value'. By exceeding the critical value to such an extent, we ensure that support from magnetic or thermal pressure will not act to hold the core against a gravitational collapse. In the previous chapters we used a uniform sphere with a 30:1 density contrast between the core and the container medium. In this chapter, we again begin by setting $1\,{}^1/_2$ million S.P.H. particles[3] into an uniform sphere with a radius of $r_{\text{core}} = 4 \times 10^{16}$ cm. This means than the initial density of the container medium is $\rho = 1 \times 10^{-19}\,\text{g}\cdot\text{cm}^{-3}$ and the initial density throughout the core is $\rho = 3\times10^{-18}\,\text{g}\cdot\text{cm}^{-3}$. We the re–arrange the S.P.H. particles so that the sphere is centrally condensed (*i.e.* we reduce the particle separation as $r \rightarrow 0$) following an $\xi = 7.45$ Bonnor–Ebert density profile. This increases the central density to $\rho = 5.5\times10^{-17}\,\text{g}\cdot\text{cm}^{-3}$, as shown in figure VII.i. We note here that this shifting of the particle does not introduce random noise into the particle lattice, and is not therefore a source of the kinds of error discussed in sub–section III.1.2. As before the edge of the core is placed in pressure equilibrium with the container medium, satisfying the boundary condition given by equation VII.3. The core has a uniform temperature of $T_{\text{fl}} = 13.8\,\text{K}$ throughout. Consequently, because of the equation of state used (*vide* equation VI.8 *supra*), the pressure ranges from approximately[4] 1.5×10^{-9} barye at the interface between the core and the container medium to 2.6×10^{-8} barye at the centre of the core.

VII.1.2 Angular Momentum

A centrally condensed sphere can be given a higher initial rotation rate (Ω_0) before 'ring fragmentation' occurs (see, *e.g.*, Bate 2011; Larson 1972; Norman and Wilson 1978). Consequently, we perform calculations with a range of initial rotation rates. As in previous chapters, we measure the initial rotation speed by way of the dimensionless number β_{rot}. In chapters IV and V we used $\beta_{\text{rot}} = 0.005$, corresponding to $\Omega_0 = 1.77\times10^{-13}\,\text{rad}\cdot\text{s}^{-1}$. Although in two calculations in chapter VI we also explored $\beta_{\text{rot}} = 0.01$ and 0.02 (corresponding to $\Omega_0 = 3.54\times10^{-13}$ and $7.08\times10^{-13}\,\text{rad}\cdot\text{s}^{-1}$) in this chapter we go further, and also begin with initial rotation speeds up to sixteen times that used in chapters IV and V. In a uniform sphere this would result in catastrophic fragmentation of the core due to the accumulation of a large amount of angular momentum in the centre as $t \rightarrow t_{\text{ff}}$. However, if we compare the initial angular momentum for a uniform sphere compared to a Bonnor–Ebert sphere

---

e.g. gravity–driven ambipolar–diffusion, are present and neither are additional support mechanisms, *e.g.* magnetic pressure or a non–zero velocity field, are present

3. the calculations presented here do no use a turbulent velocity field as in chapter VI so we revert to using the same numerical resolution as in chapters IV and V

4. the barye is the centimetre–gramme–second unit of pressure, equivalent to $1\,\text{dyn}\cdot\text{cm}^{-2} = 1\,\mu\text{bar} = 0.7501\,\mu\text{mHg}$

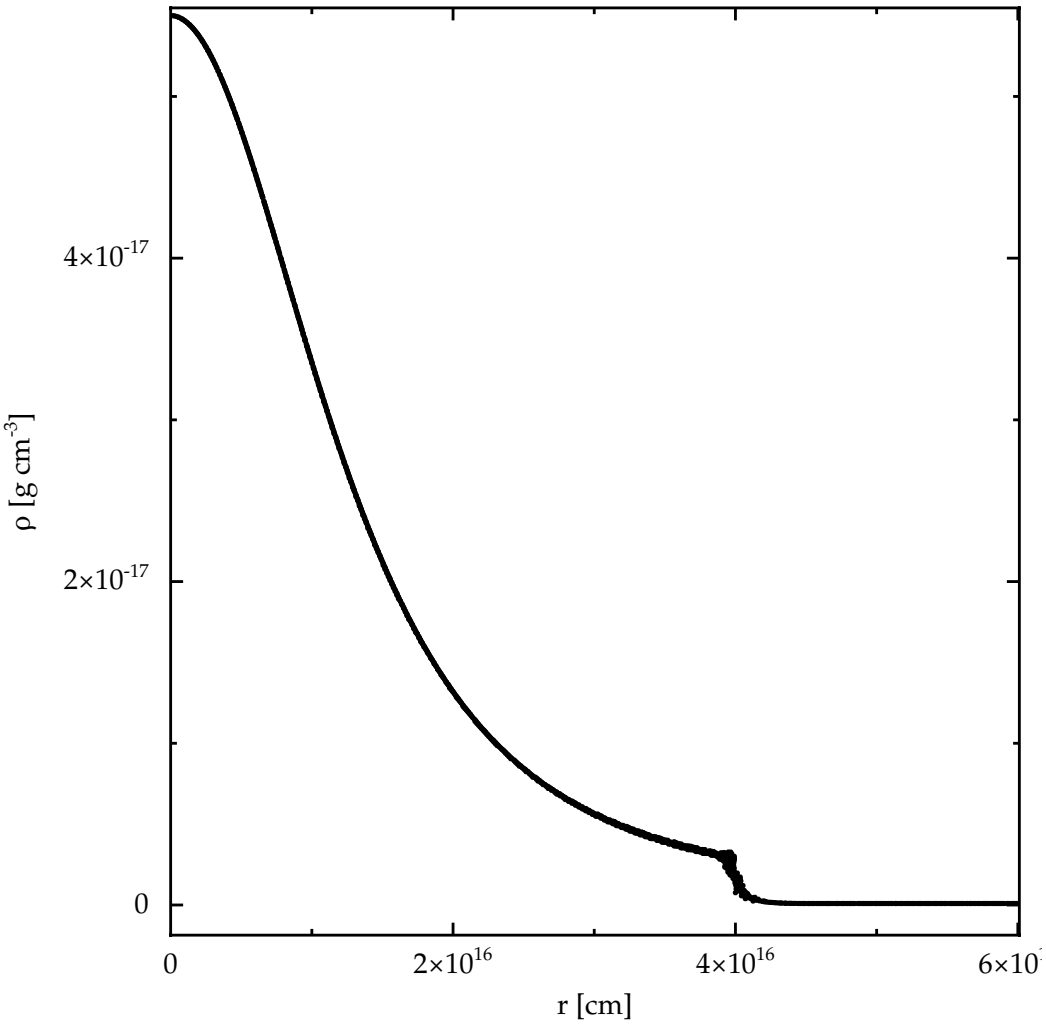

Figure VII.i. Plot of fluid density, ρ, as a function of radius, r, for a Bonnor–Ebert sphere density profile with $\xi = 7.45$ placed in pressure equilibrium within a container medium with a 30:1 density contrast between the medium and the sphere edge.

at each initial rotation rate we find that the total momentum is reduced in the Bonnor–Ebert configuration. For example, for an initial rotation rate of $\Omega_0 = 1.77 \times 10^{-13}\,\mathrm{rad}\cdot\mathrm{s}^{-1}$ produces an initial total angular momentum of $|L_0| = 2.25 \times 10^{53}\,\mathrm{dyn}\cdot\mathrm{cm}\cdot\mathrm{s}$ for a uniform sphere and $|L_0| = 1.51 \times 10^{53}\,\mathrm{dyn}\cdot\mathrm{cm}\cdot\mathrm{s}$ for the Bonnor–Ebert density distribution. Although this is apparently a small reduction, it is actually a reduction of $\approx 1/3$, and it is important to bear in mind that the majority of the mass in the system is not contained in the most centrally condensed region.

Consequently, in this chapter we use initial solid body rotation profiles corresponding to $\beta_{\mathrm{rot}} \in [0.005, 0.02, 0.04, 0.08]$, corresponding to $\Omega_0 \in [1.77, 7.08, 14.16, 28.32] \times 10^{-13}\,\mathrm{rad}\cdot\mathrm{s}^{-1}$ and $|L_0| \in [1.51, 6.06, 12.11, 24.24] \times 10^{53}\,\mathrm{dyn}\cdot\mathrm{cm}\cdot\mathrm{s}$. An alternative way of comparing rotation rates is to consider the quantity Ωt_{ff}, and for this we obtain values of $\Omega t_{\mathrm{ff}} \in [0.136, 0.545, 1.09, 2.18]$; this means we are probing the regime identified by Banerjee, Pudritz, and Holmes (2004) where binaries are not formed ($\Omega t_{\mathrm{ff}} = 0.1$), a regime where they are ($\Omega t_{\mathrm{ff}} \geq 0.2$) and configurations much more rapidly rotating than this. Although this well exceeds the limit ($\Omega t_{\mathrm{ff}} \simeq 0.3$) for ring–mode fragmentation observed by Matsumoto and Hanawa (2003), the incorporation of a reasonably strong, $\mu = 5$, magnetic field in these calculations mitigates against this by transporting angular momentum by magnetic braking and an outflow.

VII.2 Outflows

A Bonnor–Ebert sphere appears to collapse more rapidly than the free–fall time obtained from its mean density would suggest (and compared to a uniform sphere with that density). This is actually an artefact of its centrally condensed nature: in effect the core is partially pre–collapsed. Consequently, the central density reaches 'interesting' values more rapidly than a uniform sphere, as we show in figure VII.ii. The initial process of the collapse occurs comparably to the uniform spheres presented in previous chapters, albeit markedly quicker. As before, once the core reaches an 'interesting' density, a pseudo–disc forms and this then drives an outflow. Changing the initial rotation rate does have an effect similar to increasing the mass–to–flux ratio, however, as faster rotating cores become more ellipsoidal. In a similar way to figure VI.vi, we show this effect in figure VII.iii, where higher values of β_{rot} clearly cause flatter and larger density profiles. This is caused by a combination of the centripetal accelerations in the faster rotating cores coupled with the lack of any magnetic pressure parallel to the z–axis (which is the magnetic field axis). This effect is significantly more marked for $\beta_{\mathrm{rot}} = 0.04$ and (in particular) 0.08, but a slight increase in eccentricity can be seen between $\beta_{\mathrm{rot}} = 0.005$ and 0.02. This change in overall mass distribution does not affect how much fluid ultimately ends up within the centre of the collapsed core (although the increased rotation rate does slow the collapse rate down).

Once the core has collapsed so that the maximum density exceeds $\rho \approx 1 \times 10^{-10}\,\mathrm{g}\cdot\mathrm{cm}^{-3}$ a dense pseudo–disc forms. This disc is then able to produce a bipolar outflow

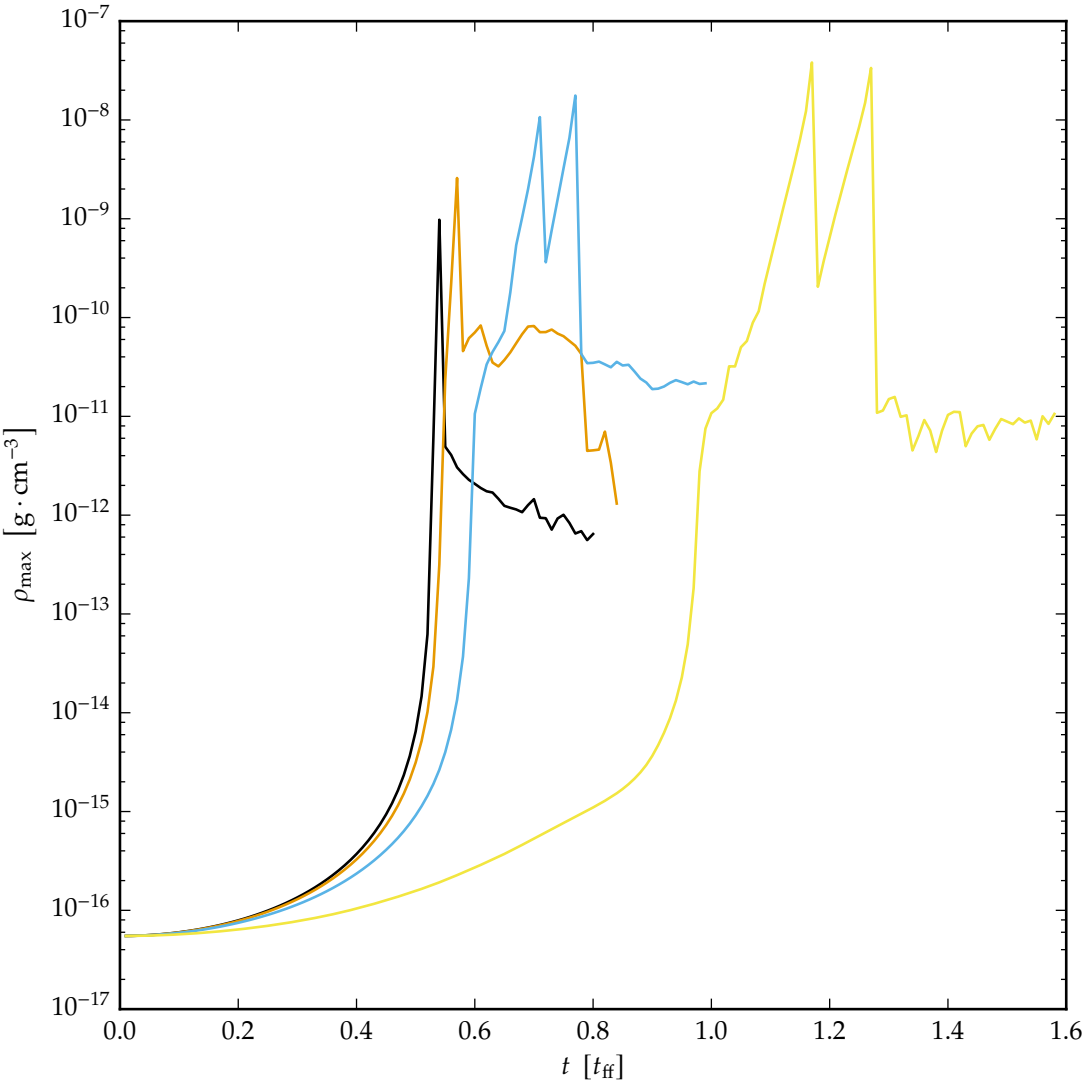

Figure VII.ii. Graph of maximum fluid density, $\rho_{\max}$ against time, t, for $\beta_{\rm rot} = 0.005$ (black line), 0.02 (orange), 0.04 (blue), and 0.08 (yellow). Higher rotation rates clearly cause a slower collapse, although even at $\beta_{\rm rot} = 0.08$ the centrally condensed Bonnor–Ebert spheres collapse to high densities in less than a free–fall time. The critical density for sink insertion is 10^{-5} g · cm^{-3} which provides a maximum density. Unlike for lower critical densities, this appears not to be reached due to the rapid nature of the second collapse phase. The 'double bumps' seen for higher values of $\beta_{\rm rot}$ are caused by a pair of second collapses happening as a binary system is formed.

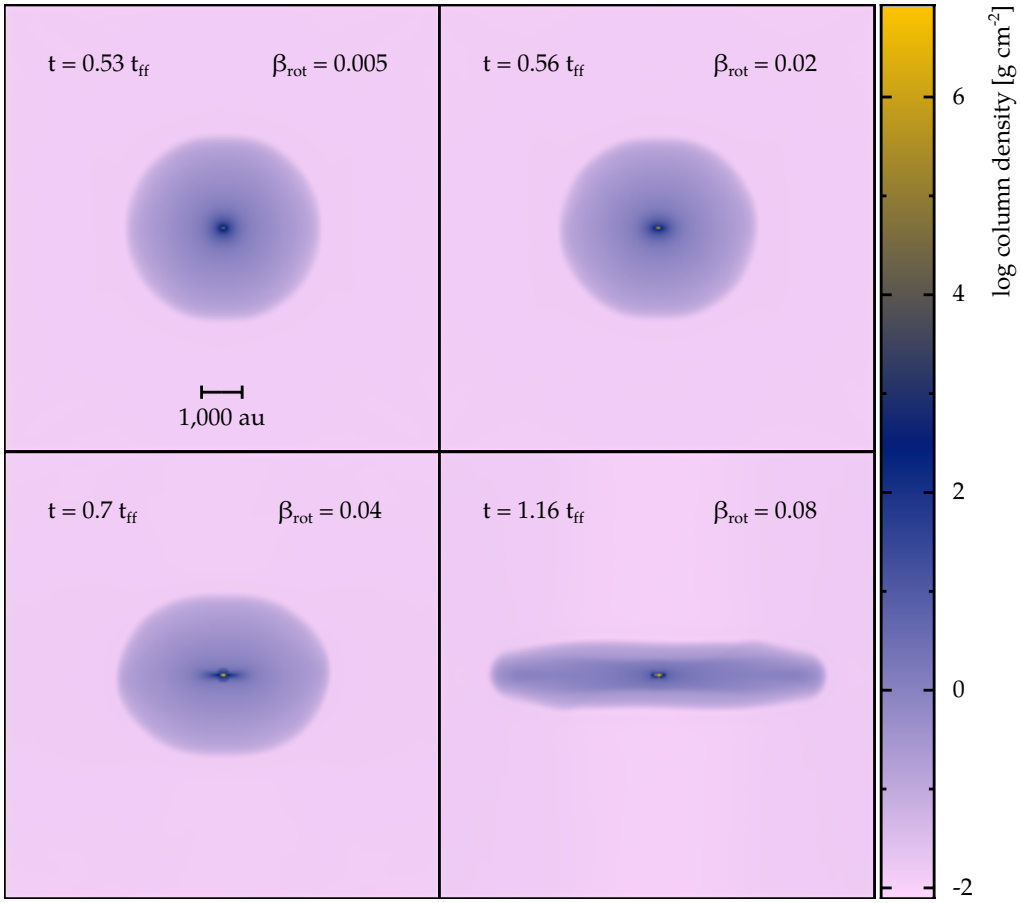

Figure VII.iii. Column density projections in y–direction for four $\mu = 5$ calculations with $\beta_{\rm rot} \in [0.005, 0.02, 0.04, 0.08]$ showing the increase in ellipsoidality as $\beta_{\rm rot}$ increases. A combination of centripetal forces and the absence of magnetic pressure parallel to the field axis (*i.e.* in the z–direction) result in a flattened and wider profile for higher rotation rates.

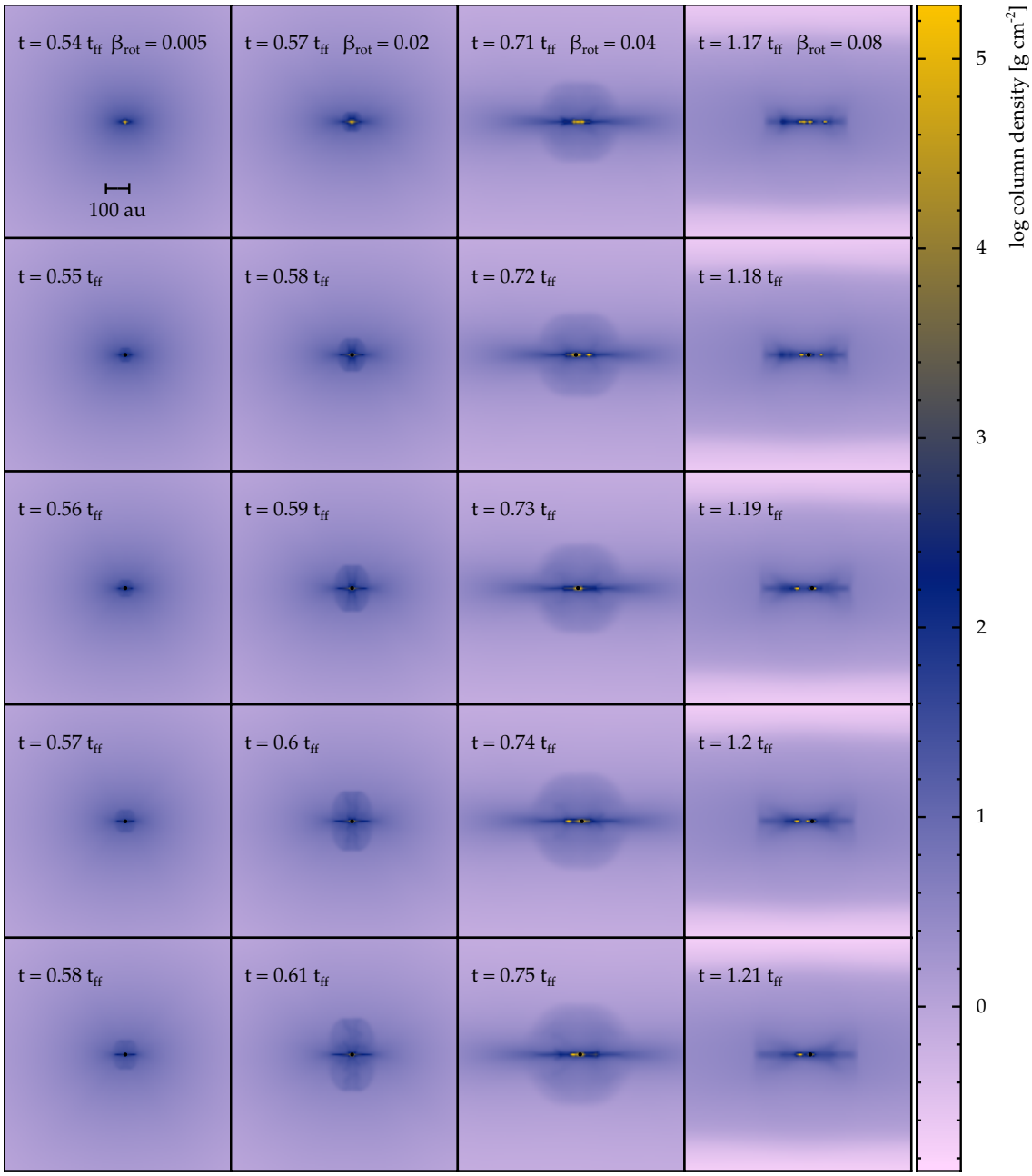

Figure VII.iv. Column density projections in y–direction for four $\mu = 5$ calculations with $\beta_{\rm rot} \in [0.005, 0.02, 0.04, 0.08]$ (columns, left–to–right) at five equally spaced time–steps. The first row is $^1/_{100}\, t_{\rm ff}$ before the insertion of the first sink particle, the second row and subsequent rows are then steps of $^1/_{100}\, t_{\rm ff}$ later. All four calculations produce an outflow notwithstanding the fragmentation into binaries for $\beta_{\rm rot} \geq 0.02$, and the velocity of this outflow increases as the rotation rate increases, however, at higher values of $\beta_{\rm rot}$ the opening angle of the outflow increases and it becomes more diffuse.

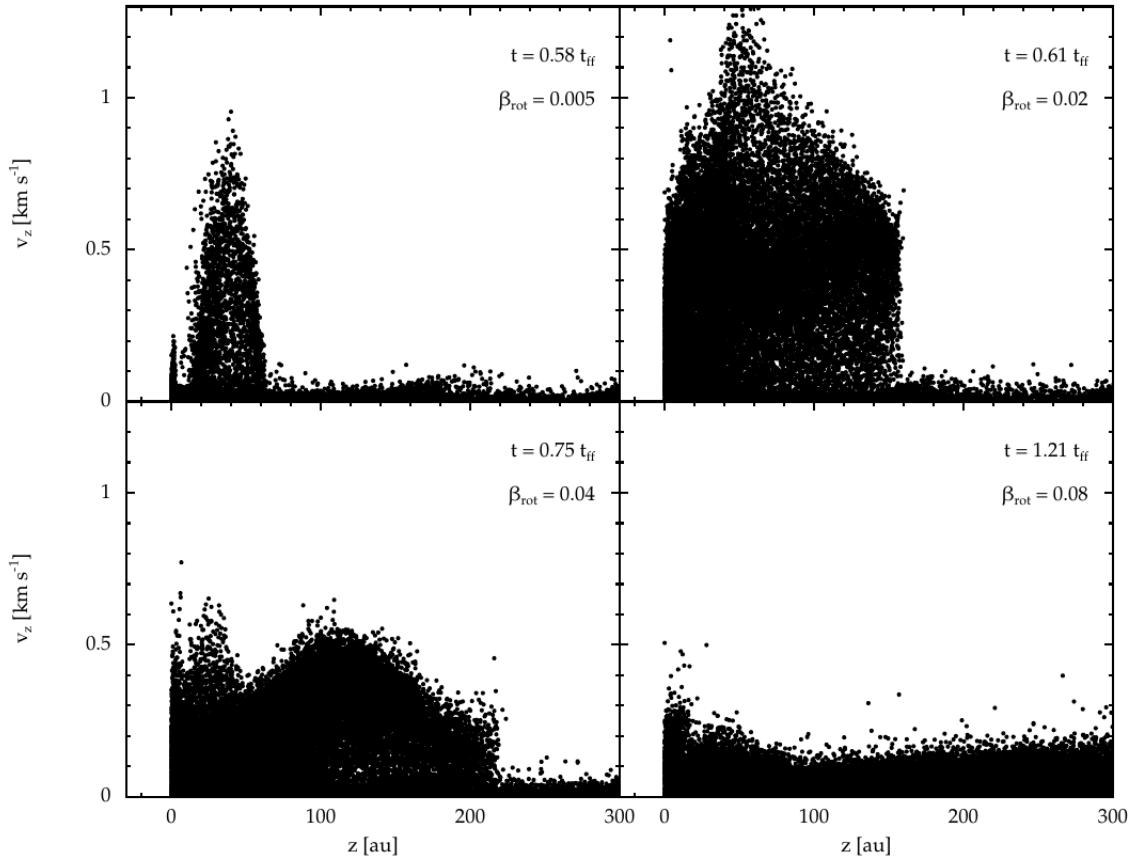

Figure VII.v. S.P.H. particle velocities in the z–direction for all particles with both $z > 0\,\mathrm{au}$ and $v_z > 0\,\mathrm{km \cdot s^{-1}}$ (*i.e.* the upper half of the outflow) at the same dynamical time as the bottom row of figure VII.iv. The upper–row shows $\beta_{\rm rot} = 0.005$ and 0.02, both of which do not fragment and produce a bipolar jet outflow, which increases in velocity as the rotation rate increases. In contrast, the lower–row shows $\beta_{\rm rot} = 0.04$ and 0.08 which do form binary systems, and exhibit slower outflow velocities than the non–fragmenting cores.

due to the combination of the disc winding up a toroidal magnetic field and then this azimuthal field being lifted out of the disc by a strong poloidal field (see the discussion in section V.5 on outflow and jet formation). As indicated in in figure VII.iv, the velocities of these outflows are proportional to $\beta_{\rm rot}$ when a bipolar outflow and no binary system is produced. This is consistent with our observations in the previous chapter, in particular section VI.6, that quantity of angular momentum contained in the core is directly related to the velocity of the outflow. Unlike the turbulent cores presented in section VI.6 *supra*, the cores here are laminar and this produces a comparably faster outflow lack of disc disruption by turbulence. However, the outflow velocities obtained here — $|v_z| \approx 1\,\mathrm{km{\cdot}s^{-1}}$ for $\beta_{\rm rot} \leq 0.02$ as shown on the top row of figure VII.v — are in general significantly slower than those obtained from uniform spheres. This is unsurprising, however, if we consider the fact that these Bonnor–Ebert density profiles contain less angular momentum for a given rotation rate than a comparable uniform density core. Interestingly, $|v_z| \approx 1\,\mathrm{km \cdot s^{-1}}$ is comparable to the result obtained in section VI.6 when $\varepsilon > 1$. This may imply that when using more realistic initial conditions than a laminar uniform sphere, the maximum outflow speed from a first hydrostatic core is somewhat lower than the more idealised analysis presented in chapters IV and V would suggest. When $\beta_{\rm rot} > 0.02$ the core fragments, and as this supresses the formation of a bipolar outflow. Consequently, as seen on the bottom row of figure VII.v the outflow velocities are reduced. We observe below that increasing $\beta_{\rm rot}$ in a binary system causes an increased binary separation. The outflow velocity for a binary system is reduced as the binary separation is increased: $\beta_{\rm rot} = 0.04$ has an outflow with a velocity of $|v_z| \approx 0.5\,\mathrm{km \cdot s^{-1}}$ but this falls to $|v_z| \approx 0.3\,\mathrm{km \cdot s^{-1}}$ for $\beta_{\rm rot} = 0.08$.

VII.3 Binaries

Figure VII.vi shows the change in column density for each calculation as a function of time from just before the first sink particle is inserted until $1/25\,t_{\rm ff}$ after. We find that rotation rates corresponding to $\beta_{\rm rot} \leq 0.02$ are resistant to fragmentation, and conversely the faster rotators are susceptible to fragmentation. We observed in section V.6 that at high mass–to–flux ratios (in that section, $\mu = 20$) an excess of angular momentum in the core could cause fragmentation and the formation of a close binary or ternary system. Here we find that simply adding additional angular momentum to a lower mass–to–flux ratio calculation ($\mu = 5$) can also cause fragmentation. Importantly, unlike in the preceding chapter, this fragmentation is not at the expense of an outflow, *cf.* figure VII.iv *supra*. In chapter V, the cause of the fragmentation was the lack of any outflow to transport angular momentum away from the protostar and pseudo–disc; here we find instead that the outflow produced from the pseudo–disc around a first hydrostatic core can be of insufficent magnitude to remove 'enough' angular momentum in some situations.

Figure VII.vii follows the evolution of the two calculations which have fragmented

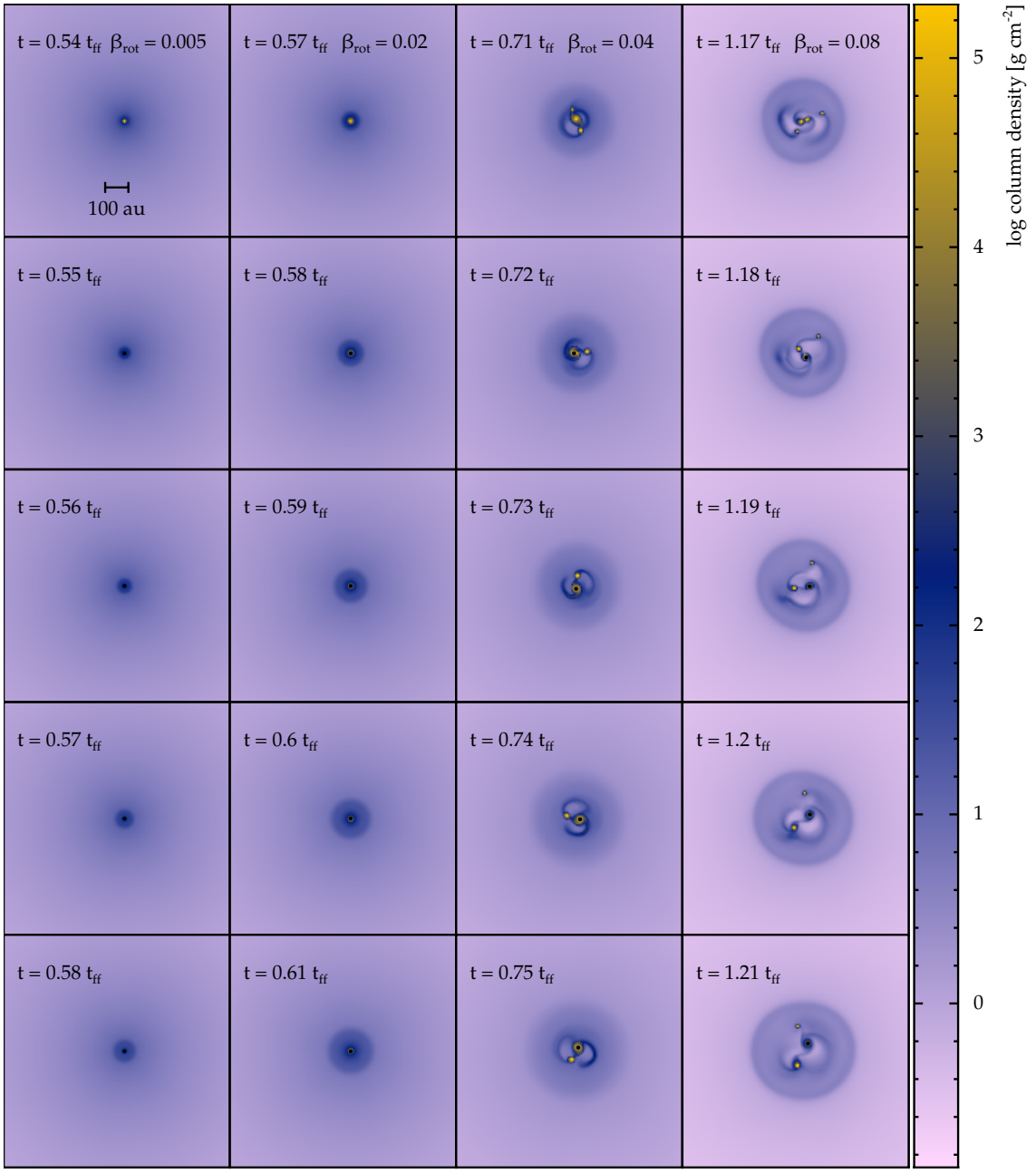

Figure VII.vi. Column density projections in z–direction for four $\mu = 5$ calculations with $\beta_{\rm rot} \in [0.005, 0.02, 0.04, 0.08]$ (columns, left–to–right) at five equally spaced time–steps, similar to figure VII.iv. As before the first row is $1/100\, t_{\rm ff}$ before the insertion of the first sink, and then each subsequent row is $1/100\, t_{\rm ff}$ more evolved. $\beta_{\rm rot} \leq 0.02$ form unary systems, whilst the two fastest rotation speeds have fragmented into multiple systems (although the second sink particle has not yet been inserted).

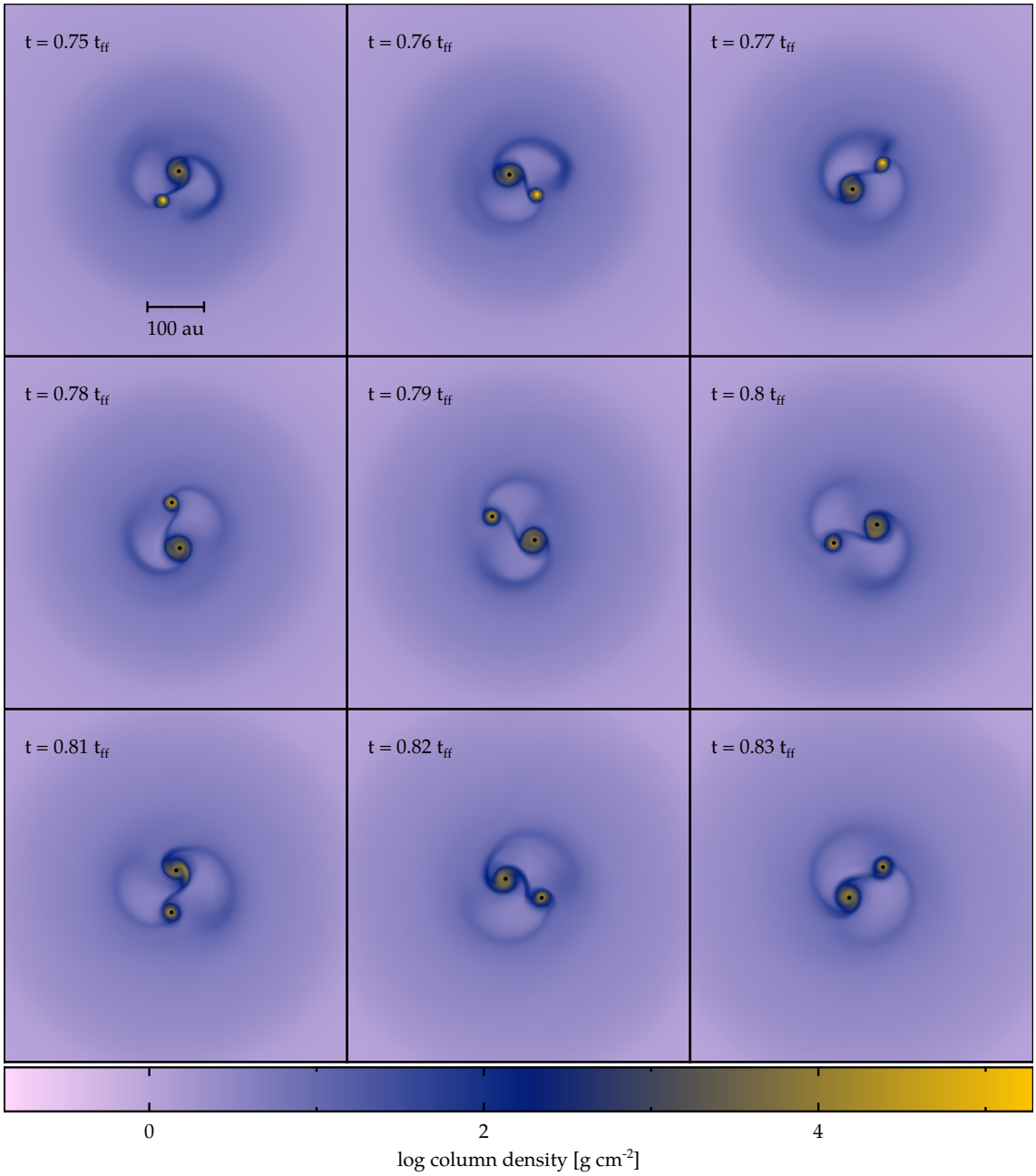

VII.vii.a. $\beta_{\rm rot} = 0.04$

Figure VII.vii. continued below

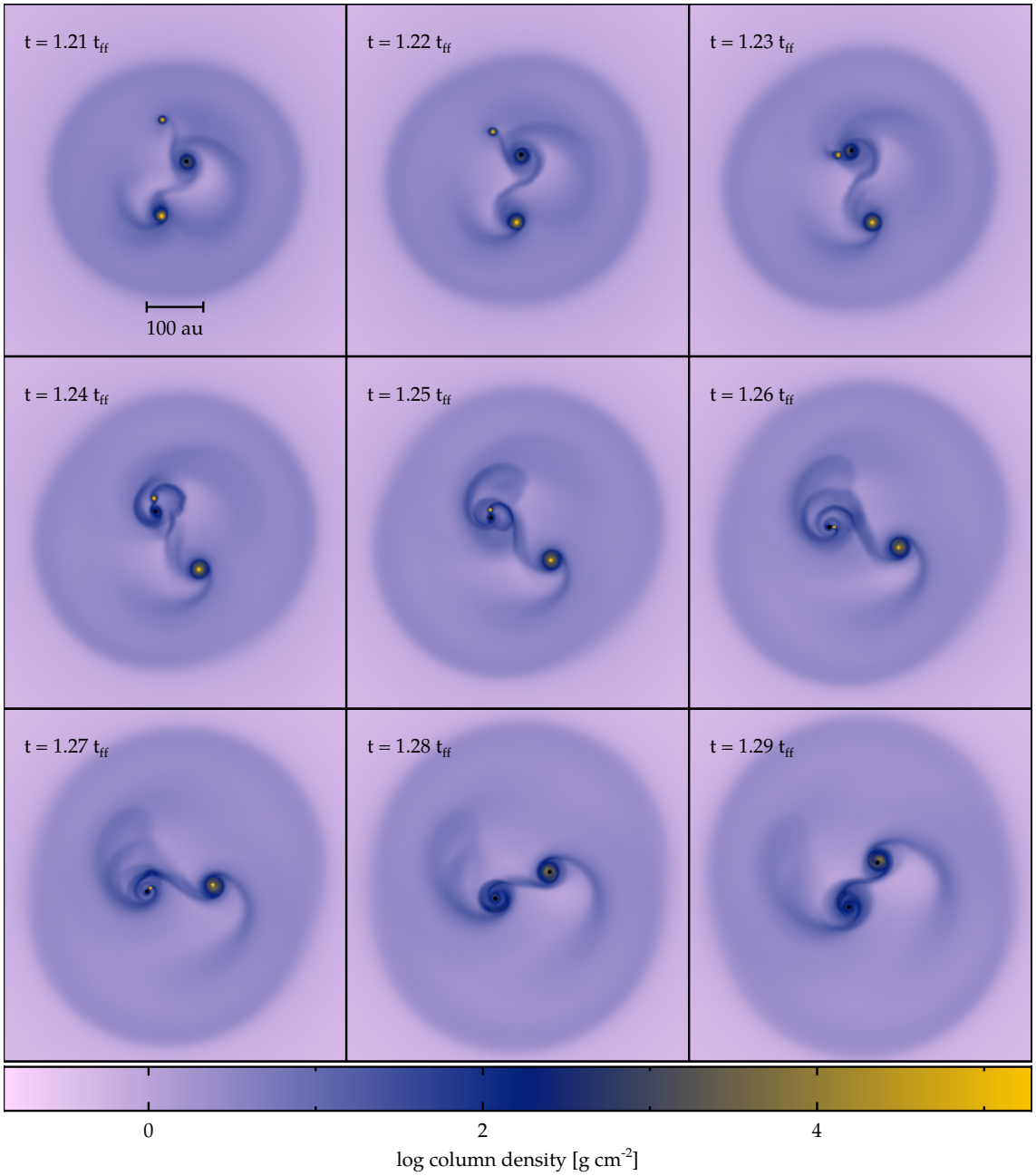

VII.vii.b. $\beta_{rot} = 0.08$

Figure VII.vii. Column density projections in the z–directions for the $\mu = 5$, $\beta_{rot} = 0.04$ (sub–figure VII.vii.a) and $\beta_{rot} = 0.08$ (sub–figure VII.vii.b) calculations. These projections begin at the same dynamical time that figure VII.vi ends, *i.e.* $1/25\ t_{ff}$ after the first sink particle is inserted and continued for a further $2/25\ t_{ff}$. Both calculations produce stable binary systems with the separation between the binaries increasing in the faster rotating calculation.

for a further $2/25\, t_{\rm ff}$ after figure VII.vi. Both calculations form clear and stable binary systems with each protostar being embedded in an individual pseudo–disc. An interesting evolutionary effect is seen in sub–figure VII.vii.a. We saw in the final panels of the $\beta_{\rm rot} = 0.08$ calculation in figure VII.vi that this calculation had fragmented into *three* dense regions, however, the smaller of these regions ultimately merges with the first sink particle, in contrast to a similar evolutionary process in section V.6 where a ternary system was formed (following a comparable evolutionary path to that described in Tobin *et al.* (2016)). A clue to the different nature of this calculation is seen at $t = 1.17\, t_{\rm ff}$ in figure VII.vi, where this calculation has actually fragmented symmetrically into four dense regions. Two larger regions closer to the barycentre and then two smaller ones formed further out. The first of these rapidly merges with an inner dense region, which then forms a sink particle. This now more massive protostar and disc combination then gravitationally attracts the second outer dense region and merges with it. The fragmentation seen for $\beta_{\rm rot} = 0.04$ is simpler although even then, initially at $t = 0.71\, t_{\rm ff}$ three dense regions are formed. Importantly, the fragmentation seen here is — to the limits of our numerical method — rotationally symmetrical, as expected given the lack of any rotational anisotropies in the initial density profile. This may well be similar to the 'satellite' fragmentation mode and similar effects seen in Matsumoto and Hanawa (2003) when $0.1 \lesssim \Omega t_{\rm ff} \lesssim 0.3$ albeit at a *much* faster initial rotation speed; additional stability against more dramatic fragmentation being provided by transporting angular momentum away in the helical outflow. That the $\beta_{\rm rot} = 0.02$ calculations, which have $\Omega t_{\rm ff} \approx 0.5$, do not even form a bar instability, let alone a binary system, echoes this analysis. We also note that unlike Banerjee, Pudritz, and Holmes (2004), when a binary does form this happens from the pseudo–disc transforming directly into a bar–mode rather than proceeding via a ring–mode instability, which again is likely the result of enhanced angular momentum transport. Although Banerjee and Pudritz (2006) in an M.H.D. calculation found that the ring–mode remained even for $\Omega t_{\rm ff} = 0.4$, we note that the calculations presented there used both a comparably weaker field[5] of $3.4\,\mu{\rm G} \leq |B_0| \leq 14\,\mu{\rm G}$ and also included ambipolar diffusion effects which will act to reduce this field further. We observed in chapter V that weak magnetic fields can allow fragmentation even at low rotation speeds. The calculation in this chapter have an initial magnetic field strength of $|B_0| = 163\ \mu{\rm G}$ which is significantly higher, and explains this variance.

In figure VII.viii we show the radially averaged tangential velocity as a function of radius compared to the Keplerian velocity at the same radii for each calculation. For simplicity, the results for the two fragmenting calculations are only shown for the first sink particle. From this we notice two things, firstly that the $\beta_{\rm rot} = 0.005$ calculation is clearly sub–Keplerian (in a manner comparable to the results obtained in earlier chapters).

5. the initial mass of the core was also $M{\rm core} = 2.1\,{\rm M}_\odot$ so the effective mass–to–flux ratio would be *even higher* than this weaker field would initially suggest

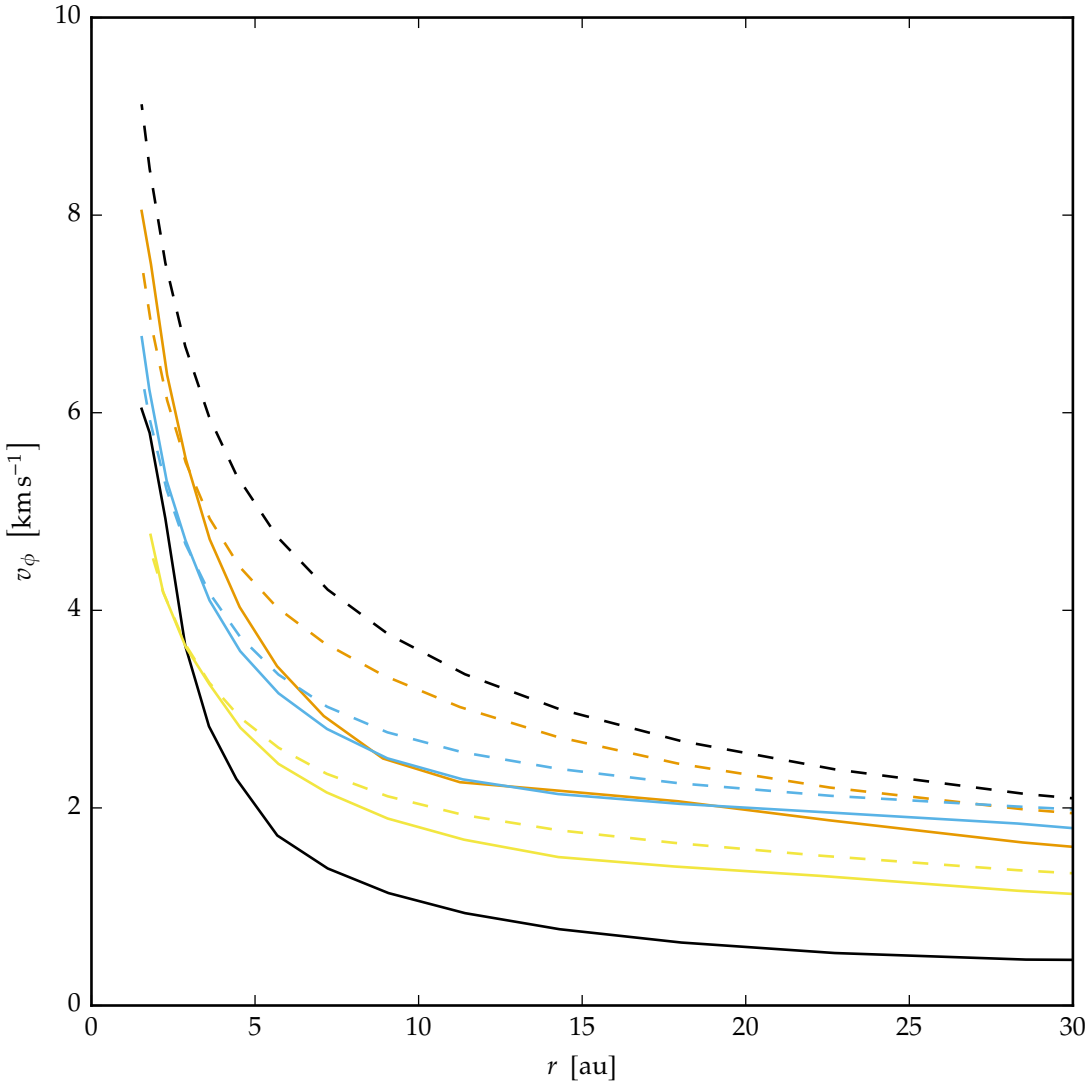

Figure VII.viii. Radially averaged tangential velocity, v_ϕ, as a function of radius, r, for $\beta_{\rm rot} = 0.005$ (solid black line), 0.02 (solid orange line), 0.04 (solid blue line) and 0.08 (solid yellow line) compared to the corresponding Keplerian velocities (dashed lines). These velocities were calculated $1/100\, t_{\rm ff}$ after a sink particle is inserted in each calculation.

However, all three of the remaining calculations become Keplerian. . From this we can infer two things: firstly, as expected increasing the initial rotation rate significantly still results in a disc limited by the Keplerian velocity (faster rotation speeds will not be bound into a disc structure). Secondly, and more interestingly, it indicates that fragmentation is not necessarily related to being in Keplerian rotation or not nor is it related to absolute velocity of the pseudo–disc. Instead it is more closely related — like the outflow — to the quantity of angular momentum available in the system. This analysis is echoed by comparing the rotation speed at somewhat higher radii. Between radii of 10 au and $\approx$ 30 au the two fragmenting calculations — $\beta_{\rm rot} = 0.04$ and 0.08 — have rotation profiles markedly closer to the Keplerian velocity at those larger radii than other calculations.

Figure VII.ix shows the change in separation between the two sink particles (which represent protostars) over time. Although both calculations exhibit some variation in the separation, the faster rotating $\beta_{\rm rot} = 0.08$ calculation has a consistently higher separation between the two sink particles compared to the $\beta_{\rm rot} = 0.04$. This also shows that the system is essentially stable and that the two sink particles — and hence protostars — are unlikely to merge.

VII.3.1 Outflows from Binaries

Formation of two stable binary systems, both with outflows, allows an analysis of the nature of first hydrostatic core outflows in binary as opposed to unary systems. The same magnetohydrodynamical phenomena are present notwithstanding these systems are binaries rather than single systems. However, the motion of a pair of protostars around a common barycentre produces a unique scenario. Figure VII.x shows the z–direction velocity for the $\beta_{\rm rot} = 0.08$ calculation. An unusual approach to showing the velocity is taken to show how the outflow is formed. We only consider the fluid velocity for S.P.H. particles above $z = 0$, *i.e.* above the orbital plane of the protostellar system. This is necessary because the outflow is symmetrical and otherwise positive average z–components of the velocity would be offset by negative average velocities below the plane, hiding or obscuring the outflow. We find that a helical outflow is produced, as shown by the blue regions in figure VII.x. Two hydrodynamic pseudo–discs rotating around a common barycentre would naturally lose some material due to centrifugal effects. This material, however, would only have velocities in the x–y plane[6] and consequently would not have an appreciable z–component of its velocity. That the motion see in figure VII.x *does* have a velocity out of the orbital plane indicates that these outflows are magnetically driven and are traveling, like outflows from unary systems, parallel to the magnetic field and rotation axis.

This magnetic origin is confirmed by looking at the density weighted average of the

6. technically the orbital plane of the system, which is by definition the x–y plane due to our initial conditions

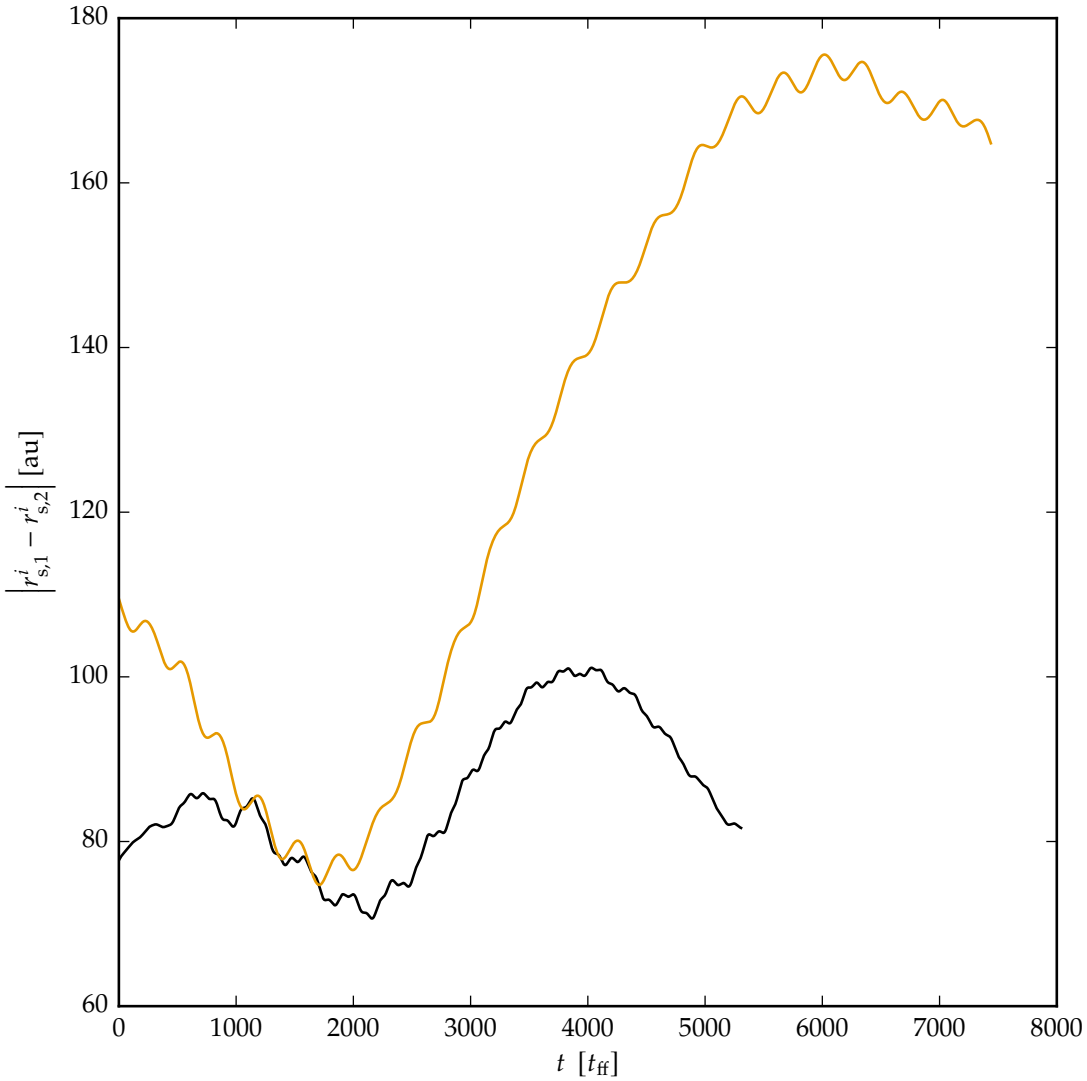

Figure VII.ix. Plot of sink particle separation, *i.e.* $\left|r^i_{s,1} - r^i_{s,2}\right|$ where $r^i_{s,1}$ represents the position vector to the first sink particle, *etc.*, against time since the second sink particle was inserted, t, for the $\beta_{rot} = 0.04$ (black line) and $\beta_{rot} = 0.08$ (orange line). Although both calculations exhibit some variation in the separation over time, both sink particles are stable and are not spiralling in or being ejected.

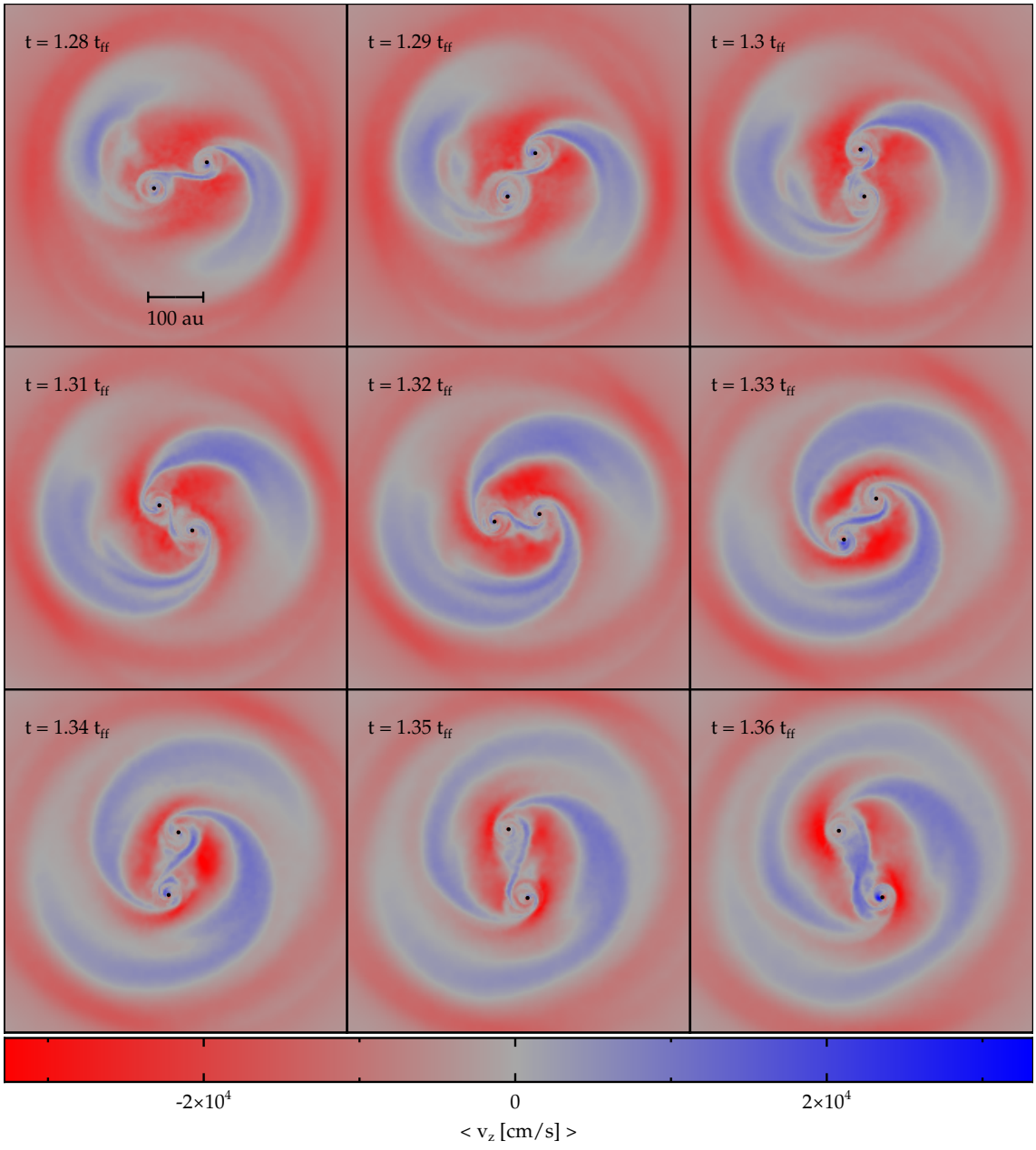

Figure VII.x. Density weighted average of the z–velocity of the fluid, $\langle v_z \rangle$, for all S.P.H. particles with $z > 0$ projected in the z–direction. Red indicates regions where fluid is traveling towards the plane of the protostellar system, conversely blue indicates fluid moving away from that plane. Two 'helical' outflow structures can be seen, emenating from each pseudo–disc

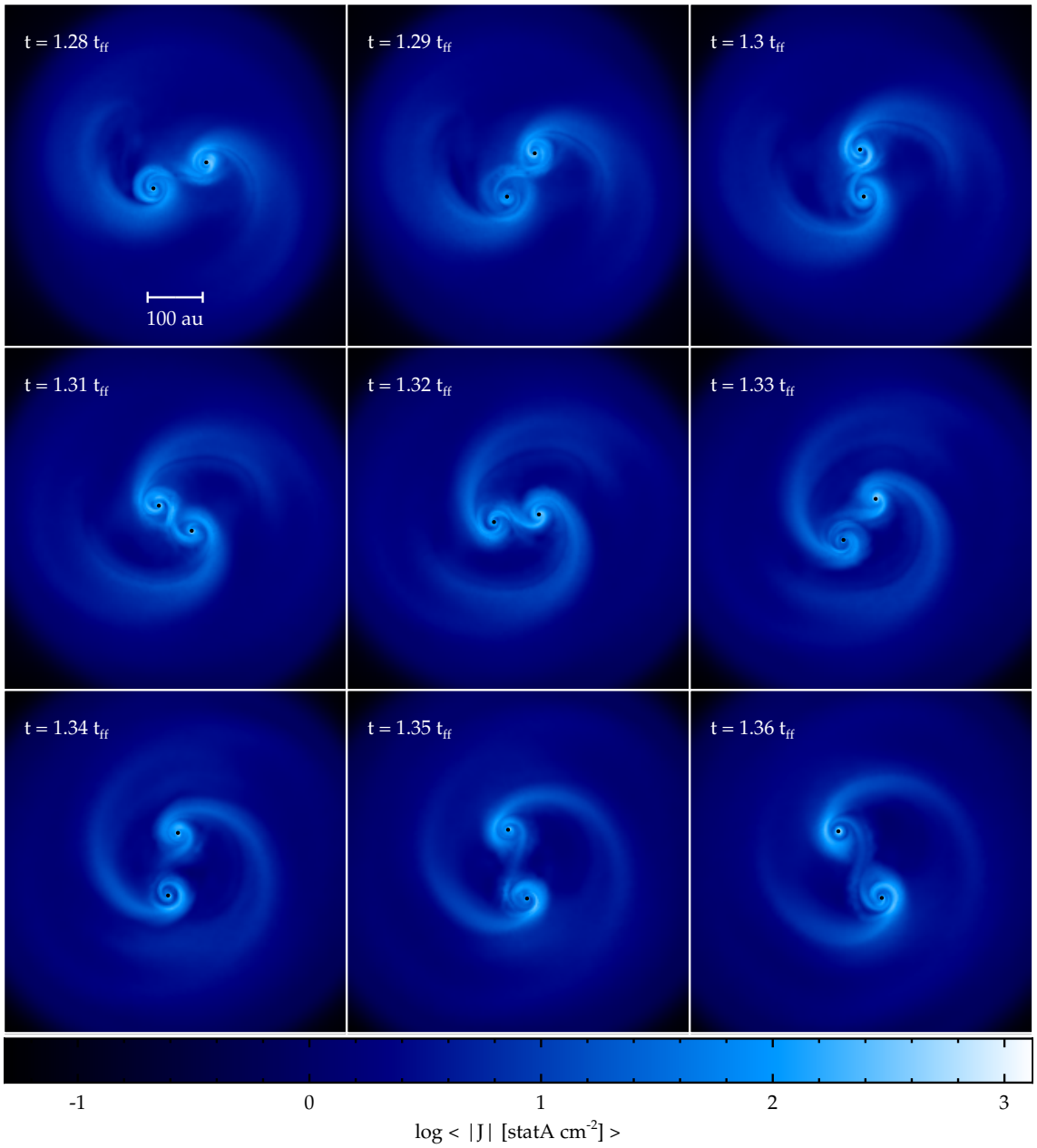

Figure VII.xi. Density weighted average of the magnitude of the current density, $\langle |J^i| \rangle$, for all S.P.H. particles with $z > 0$ projected in the z–direction for $\mu = 5$, $\beta_{\rm rot} = 0.08$. A region with an elevated current density is produced in both pseudo–discs and in an arm structure corresponding to the initial part of the outflow seen in figure VII.x, demonstrating the magnetic origin, and the origin within the pseudo–disc, of these structures

magnitude of the current density[7] (*cf.* sub–section IV.3.1, although in that sub–section we used a cross–section as opposed to an average here, necessary to incorporate the z–dimensional effects of the helical outflow) shown in figure VII.xi. There is a clear correlation between an elevated current density, *i.e.* a elevated motion of charges, and the helical outflow seen in the velocity plot in figure VII.x, showing the magnetised nature of these outflows. Figure VII.xi also shows how these outflows are magnetically linked to the pseudo–discs, which also demonstrate an elevated current density compared to the surrounding fluid. The larger scale regions of the outflow do not, however, show an elevated current density, which indicates that — as expected — once these structures are magnetically produced they are no longer driven by magnetohydrodynamical effects.

VII.4 Comparison of Sink Particle Size

The insertion of a sink particle into these calculations essentially punches a hole with a diameter of 2 au into each pseudo–disc. Since the discs themselves have diameters only an order–of–magnitude larger, we re–ran the $\beta_{\text{rot}} = 0.08$ calculation from $1/100\, t_{\text{ff}}$ before a sink particle is inserted, but with the accretion radius of the new sink particle set to $r_{\text{crit}} = 1/10$ au as opposed to 1 au. Figure VII.xii shows a representative sample for this pair of calculations . In terms of the evolution of the pseudo–discs, no qualitative differences can be observed. This implies that physical processes[8] occuring at sub–astronomical unit scales has a limited impact on the wider disc. The variation that is seen is likely caused by gravitational potential energy being liberated as radiation in the region $1/10\,\text{au} \leq r \leq 1\,\text{au}$ which will change the temperature of the fluid, and hence the structure slightly. This analysis is confirmed by comparing the shape of the outflow produced from the $\beta_{\text{rot}} = 0.08$ calculation in figure VII.xiii.

We would not necessarily expect this result to be as consistent in a non–fragmenting system, since there the maximum jet velocity must be related to the maximum Keplerian velocity, *i.e.* the minimum radius, obtainable. However, we note that decreasing the critical radius from $r_{\text{crit}} = 5\,\text{au}$ (as used in D. J. Price, Tricco, and Bate 2012) to 1 au only increased the jet velocity by a maximum of $3\,\text{km}\cdot\text{s}^{-1}$. These calculations were performed using uniform spheres, not centrally condensed density profiles, and we observe above that the latter set of initial conditions produce markedly slower outflows in any event. There is limited benefit in exploring the use of sink particles smaller than $1/10$ au unless the size is set sufficently small to capture the whole second core phase (see Larson 1969). These small cores have already been observed to produce significantly faster outflows (Bate, Tricco, and D. J. Price 2014) than first hydrostatic cores, and it appears that any radius larger than this which still contains most of the first core is sufficent if the additional

7. $J^i = \epsilon^{ijk}\nabla^j B^k$

8. at least insofar as radiation *ideal* magnetohydrodynamics is concerned

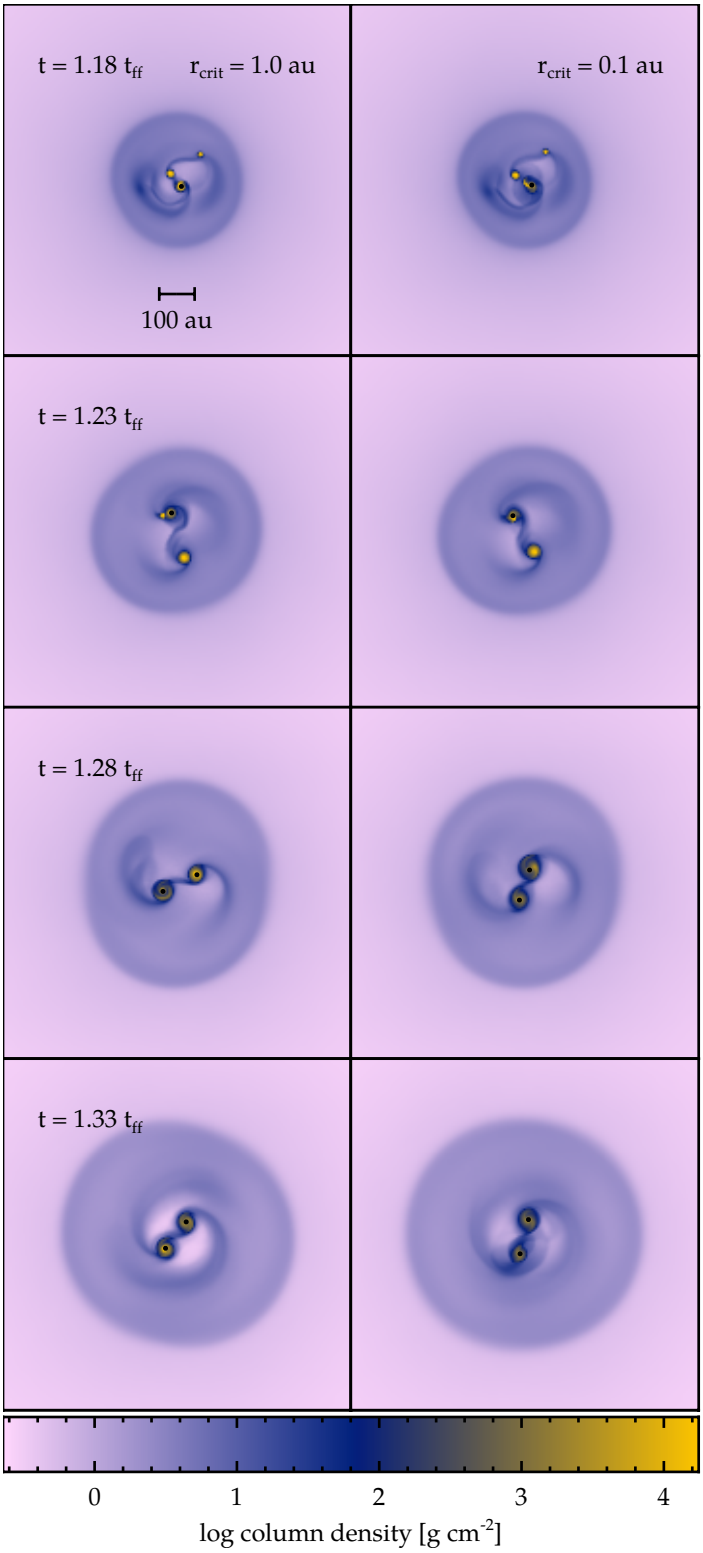

Figure VII.xii. Column density projections in the z–direction for the $\beta_{\rm rot} = 0.08$ comparing our usual sink particle radius, $r_{\rm crit} = 1$ au (left column) and $r_{\rm crit} = 1/10$ au (right column). We note that few qualitative differences are observed between the two accretion radii, and those that are present are likely effects of the gravity tree rather than additional physical processes from within $r < 1$ au.

computational expense of following the collapse that far is not desired.

Consequently, we conclude that — at least for the initial conditions we use throughout this thesis — a sink particle size of 1 au is qualitatively converged.

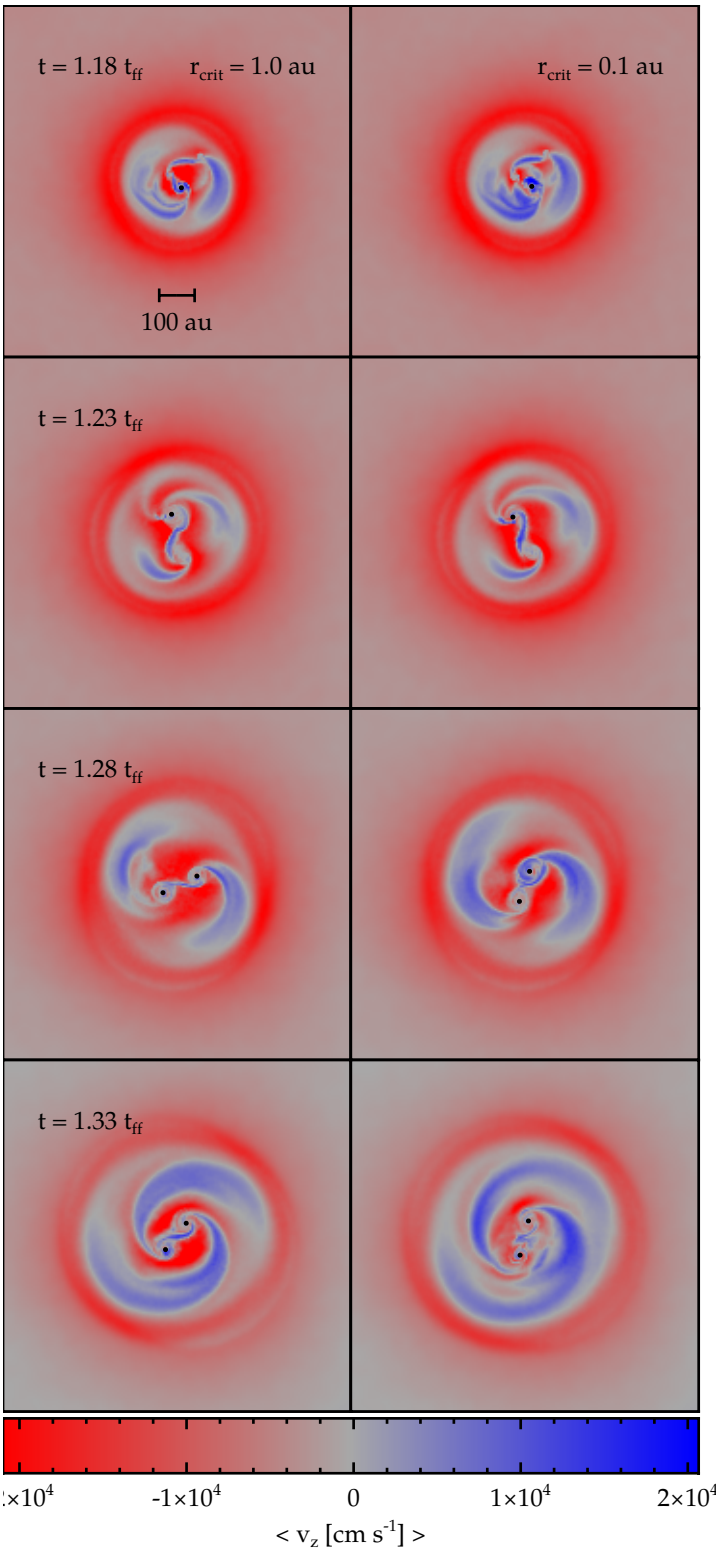

Figure VII.xiii. Density weighted average of the z–component of the velocity, $\langle v_z \rangle$, for all S.P.H. particles with $z > 0$, projected in the z–direction for the $\beta_{\rm rot} = 0.08$ comparing our usual sink particle radius, $r_{\rm crit} = 1$ au (left column) and $r_{\rm crit} = 1/10$ au (right column). The outflows produced are qualitatively similar with both sink radii.

CHAPTER VIII

Summary and Conclusion

Leb' wohl, du kühnes,
herrliches Kind!
Du meines Herzens
heiligster Stolz!
Leb' wohl! Leb' wohl! Leb' wohl!

Flammende Glut
umglühe den Fels;
mit zehrenden Schrecken
scheuch' es den Zagen;
der Feige fliehe
Brünnhildes Fels! —
Denn einer nur freie die Braut,
der freier als ich, der Gott!

Dritte Szene, Dritte Aufzug, Die Walküre,
Erster Tag des Bühnenfestspiels: Der Ring des Nibelungen,
Richard Wagner (1856)

VIII.1 The formation of first hydrostatic cores

Clearly, the wide diversity of initial conditions for a molecular cloud core produce a comparably wide range of evolutionary outcomes. In the preceding four chapters we considered a range of these configurations. Changes in the initial magnetic (sub–sections VIII.1.1 and VIII.1.2 *infra*), velocity (sub–section VIII.1.3 *infra*), or density (sub–section VIII.1.4 *infra*) fields can change the resulting protostar markedly. These effects can range from producing a strong collimated outflow to none at all and between forming a solitary protostar or a binary or ternary system.

Observations of molecular cloud cores provide a wide range of possible initial conditions. Similarly, observations of Y.S.Os. demonstrate that the star formation process can produce a extensive variety of objects. Our exploration of the parameter space shows that the configuration of a molecular cloud core prior to the collapse beginning can produce a variety of outcomes, and this may explain some of the variation in protostars and Y.S.Os. observed. Although we have only followed the collapse to the length scales of the first hydrostatic core phase[1], which is a comparatively early evolutionary point, many of the variations seen are significant and would be expected to impact the subsequent evolution of the protostar.a

VIII.1.1 Magnetic field: geometry

We began in chapter IV by first considering how the geometry of the initial magnetic field influences the collapse and ultimately the final protostar. We found that the shape of the molecular cloud core mid–collapse is influenced by the inclination of the field with the respect to the rotation axis, denoted by ϑ. A magnetic field that is aligned with the rotation axis produces a core which is oblate and with the semi–major axis perpendicular to the axes. However, when the magnetic field is perpendicular to the rotation axis a prolate core is formed. At intermediary inclination angles the core is triaxial, but in all cases the semi–major axis remains perpendicular to the magnetic field. This also affects the psuedo–disc which forms late in the collapse: this forms perpendicular to the magnetic field axis on all but the shortest length scales.

Since any outflow that is produced is a result of motion in the pseudo–disc, a change in the orientation of this disc changes the nature of the outflow produced. We find that the outflow velocity is reduced as ϑ is increased, ranging from $|v_z| \simeq 8\,\mathrm{km}\cdot\mathrm{s}^{-1}$ when $\vartheta = 0°$ to effectively no outflow when the field is completely misaligned, *i.e.* when $\vartheta = 90°$. In addition, only initial fields where $\vartheta < 45°$ produce a bipolar collimated jet. As well as providing an observational constraint — it is unlikely that any observed first hydrostatic core outflow originates from a molecular core where $\vartheta \gtrsim 45°$ — this also has implications

1. although some calculations do continue beyond the timescale on which a first hydrostatic core is expected to exist.

for angular momentum transport. Magnetic braking in cores with a field strength high enough to produce an outflow appears to be capable of prevent fragmentation even when no jet is produced. However, a jet is a very efficent mode of angular momentum transport (*cf.* Lynden–Bell 1996) and therefore a highly misaligned system will progress to the second collapse phase with a very different angular momentum configuration than the aligned situation.

VIII.1.2 Magnetic field: magnitude

In chapter V, we then considered how changing the initial magnetic field strength influenced this evolution. We found that contrary to what may have been initially suspected, the velocity of the jet actually *increased* when the initial field was weakened from $\mu = 5$ to $\mu = 10$. This increase in velocity was accompanied by an increase in the size and rotation speed of the pseudo–disc surrounding the protostar. The cause of the larger disc is a reduction in magnetic braking as a method of angular momentum transport. This allows both a larger disc and a faster rotating one but unlike hydrodynamic discs the combination of *some* magnetic braking is sufficent to prevent fragmentation (since no fragmentation is observed when $\mu = 10$ and $\vartheta \geq 45°$ at which point the jets are suppressed). As the maximum outflow velocity is closely linked to the rotation speed of the disc (D. J. Price, Pringle, and King 2003) this necessarily produces a faster outflow.

This is an important result as it effectively places an upper limit on the velocity of a first hydrostatic core outflow. Any observations of an outflow faster than $|v_z| \simeq 10\,\mathrm{km\cdot s^{-1}}$ are likely to be more evolved objects that the first core phase. Since 'fast' outflow velocities only occur when the field and rotation axes are closely aligned, and there is observational evidence that misalignement is not uncommon, this upper limit may itself be quite high. In the regime between $\vartheta = 0°$ and $45°$ the jets become progressively slower.

However, we found that by reducing the field still further, to $\mu = 20$, prevented the formation of an outflow at all. As a result, the now essentially Keplerian disc becomes unstable to fragmentation and the formation of binary or ternary systems. This is caused by the combination of no angular momentum transport by a jet combined with reduced transport from magnetic braking. Changes in the inclination angle, ϑ, do not change this. Consequently, one route to the formation of binary and multiple star systems may be a weak initial magnetic field (but not so weak as to cause prolific fragmentation) but *not* changed field geometries alone. This fragmentation mode occurs at a reasonably low initial rotation rate ($\beta_{\mathrm{rot}} = 0.005$) and does not form systems with extreme multiplicity in the way that a gravitationally unstable hydrodynamic disc does. We note, however, that including radiative transfer but not magnetic fields can also reduce fragmentation in pseudo–discs.

A poloidal–toroidal decomposition of the magnetic field structure gives an insight into these very different morphologies. We find that the key combination required to drive the collimated jet outflow mode is a poloidal magnetic field to lift material out of

the plane of the pseudo–disc coupled with a strong toroidal field to collimate the jet. When the magnetic field is weaker, *i.e.* in the $\mu = 20$ calculations, the poloidal field is insufficent and a weak 'bulk' outflow is produced. A torodially dominated disc remains, however, but without the poloidal field to move material this can not drive a jet. Misaligned calculations have weaker (or for the most misaligned *no*) collimated outflow due to the reduced impact of the torodial field caused by the shape of the pseudo–disc not being perpendicular to the rotation axis.

VIII.1.3 Velocity Field

We then returned to an aligned magnetic field configuration, but explored the impact of changing the velocity field in the core in chapter VI. In the preceding paragraphs, we used a laminar core with only a solid–body rotation profile as a source of kinetic energy. Here, we applied a Gaussian divergence–free turbulent velocity field to the core. Cores with an initial turbulent Mach number of $\mathscr{M} = 1$ (*i.e.* transonic cores) at at the limit of boundness. In addition, cores with this degree of turbulence are too disrupted to form a pseudo–disc and hence an outflow (they are, however, resistant to fragmentation). Sub–sonic cores are somewhat disrupted, with outflows produced with $\mathscr{M} = 1/10$ for both $\mu = 5$ and $\mu = 10$. At $\mathscr{M} = 3/10$ only a $\mu = 5$ core produces an outflow and this has a reduced velocity. This again implies that the upper limit identified in the preceding sub–section may only apply to idealised initial conditions.

If we add additional angular momentum to a $\mathscr{M} = 1$ transonic core we can produce an outflow again. The important parameter is the ratio between the initial turbulent kinetic and rotational kinetic energies, ε. When $\varepsilon \gtrsim 1$ a pseudo–disc can be formed and hence and outflow and *vice versa*. From this, we find that a core with $\mu = 5$, $\mathscr{M} = 1$ and $\beta_{\rm rot} = 0.02$ *does* produce a bipolar outflow. This outflow is comparably slow — $|v_z| \approx 1\,\mathrm{km\cdot s^{-1}}$ — and somewhat asymmetrical. We therefore note that in more realistic initial conditions first hydrostatic core outflows may be much slower than idealised configurations would tend to imply. In addition, angular momentum transport by an outflow is closely linked to the balance between linear and angular momentum in the core when it begins collapsing.

A disrupted psuedo–disc results in a suppressed outflow. This occurs at all field strengths for transonic turbulence and at all but the weakest (*i.e.* closest to laminar) sub–sonic turbulence for stronger field strengths. This effect is again seen in the ratio of poloidal and toroidal field components. The disrupted pseudo–discs without a collimated outflow have a qualitively similar appearance to a misaligned laminar calculation. However, when $\varepsilon \gtrsim 1$, the pseudo–disc produced by the additional angular momentum contains a strongly toroidal field. This can generate a collimated outflow in a calculation that with a lower amount of angular momentum would not.

VIII.1.4 Density Field

Finally, we switch in chapter VII from a uniform density distribution to a Bonnor–Ebert sphere profile. This allows significantly more angular momentum to be included in a core before effects such as ring fragmentation occur. From this, we observe as expected that when $\beta_{\rm rot} \leq 0.02$ (in a laminar core with $\mu = 5$, $\vartheta = 0°$) the outflow velocity increases with increasing $\beta_{\rm rot}$. For $\beta_{\rm rot} \geq 0.04$ the core fragments into a binary pair which acts to substantially reduce the outflow velocity. The outflow velocity in any case in a collapsed Bonnor–Ebert sphere is much lower than for an uniform sphere, with $|v_z| \approx 1\,{\rm km}\cdot{\rm s}^{-1}$ for $\beta_{\rm rot} \leq 0.02$.

The binary systems produced in this configuration do transport angular momentum by an outflow. This, however, takes the form of an helical structure with one arm emanating from each of the psuedo–discs in the binary pair. Additionally, the velocity of this helical outflow is less than $|v_z| \simeq 0.5\,{\rm km}\cdot{\rm s}^{-1}$. We have followed these binary systems for many orbits and they are stable and unlikely to merge. In addition to binary formation by a weak magnetic field, this provides a route to binary formation in a stronger field configuration — provided sufficent angular momentum can be provided.

Echoing the earlier observation that idealised initial conditions may produce excessively high outflow velocities, we find a similar effect when switching from a uniform sphere to a Bonnor–Ebert sphere. Clearly the binaries discussed above produce slower outflows. However, at lower rotation rates the outflow produced is still slower than for a comparable uniform sphere calculation. For example, when $\beta_{\rm rot} = 0.005$ (which is comparable with the calculations in chapter IV) the outflow velocity, $|v_z| \approx 1\,{\rm km}\cdot{\rm s}^{-1}$, is markedly reduced. A Bonnor–Ebert density profile, being a centrally condensed distribution, is a better approximation of a 'real' molecular cloud core. This implies that even for aligned, laminar configurations the maximum outflow velocity may be much lower than earlier work would indicate.

VIII.2 Towards a stable smoothed particle magnetohydrodynamics

We have analysed the troublesome nature of implementing magnetohydrodynamics in a discrete Lagrangian particle scheme. The principal overall conclusion is that disorder in the particle lattice as a source of error is more problematic than the inherent truncation error caused by floating point operations. In particular, test problems may not expose this error since, by design, they do not create the *combination* of a disordered lattice, a complex and comparably strong magnetic field, and strong density gradients. However, real scientific problems — in particular the collapse of a molecular cloud core — do create all three circumstances.

These circumstances leave quandary: the equations of smoothed particle magnetohydrodynamics derived from the Lagrangian are inherently perfectly conservative. However, they are unstable when the plasma β is less than unity. When this happens the fluid

pressure is insufficent to suppress the spurious force parallel to the magnetic field lines caused by (effectively) errors in maintaining $\nabla^i B^i = 0$. However, we show that any attempt to correct this is problematic. Firstly, because it moves S.P.M.H.D. away from a Lagrangian formulation and therefore is inherently non–conservative. However, in addition we show that the successful Børve, Omang, and Trulsen (2001) source term correction scheme is broadly equivalent to removing the first order error from the anisotropic S.P.M.H.D. momentum equation. This prevents particles annealing into a 'low energy' state (*vide* D. J. Price 2012) and consequently causes inexorable deteroration in momentum conservation. The fundamental issue is that a conservative *or* a correct formulation of M.H.D. in S.P.H. is possible with the current state–of–the–art.

As an aside, we also discuss the impact of different choices of average in the kernel function in S.P.H.. Although we use an S.P.H. formalism — setting the smoothing length and fluid density self–consistently — which does not use an average like this, many S.P.H. schemes still do. However, hitherto discussion of this point has been quite limited. We show that any reasonable choice of average produces converged results in a test problem designed to cause issues with gradients in ρ (and hence h). This is a particularly challenging numerical calculation so this demonstrates the robustness of each choice of average.

VIII.3 Final Notes

This thesis makes extensive use of the `NumPy` (van der Walt, Colbert, and Varoquaux 2011) and `Matplotlib` (J. D. Hunter 2007) `Python` modules[2]. All rendered figures were produced using the `splash` programme[3] (D. J. Price 2007, 2011b).

Most calculations were performed on the University of Exeter Supercomputer[4], a 'Distributed Research utilising Advanced Computing' (Di.R.A.C.) Facility jointly funded by the Science and Technology Facilities Council (S.T.F.C.), the Large Facilities Capital Fund of Department for Business, Energy, and Industrial Strategy (B.E.I.S.) and the University of Exeter.

Some calculations used the Di.R.A.C. `Complexity` system[5], operated by the University of Leicester I.T. Services, which forms part of the S.T.F.C. Di.R.A.C. H.P.C. Facility. This equipment is funded by the B.E.I.S. National E.–Infrastructure capital grant no. `ST/K000373/1` and S.T.F.C. Di.R.A.C. Operations grant no. `ST/K0003259/1`.

A small number of calculations used the `Isca` supercomputer[6], funded and operated

2. see `http://www.numpy.org/` and `https://matplotlib.org/`

3. see `http://users.monash.edu.au/~dprice/splash/`

4. further details can be found at `https://wiki.astro.ex.ac.uk/bin/view/Zen/WebHome`

5. see `http://www2.le.ac.uk/offices/itservices/ithelp/services/hpc/dirac` and `https://www.dirac.ac.uk/`

6. further details can be found at `http://www.exeter.ac.uk/research/hpc/about/`

by the University of Exeter.

Like almost every astronomical publication, this thesis makes use of the bibliographic services of N.A.S.A.'s Astrophysics Data System[7] (Eichhorn 1994).

7. http://adswww.harvard.edu/

CHAPTER IX

Further Work

Sed Cæsar in omnia præceps,
nil actum credens, cum quid superesset agendum.

Liber II, Pharsalia seu De Bello Civili,
Marcus Annæus Lucanus (*ca.* A.D. 61)

IX.1 Non–Ideal magnetohydrodynamics

Throughout this thesis we have assumed that the ideal magnetohydrodynamics approximation (that the flux is 'frozen in' to the fluid) holds. Eliminating this assumption, *i.e.* moving to a non–ideal M.H.D. scheme (see sub–section I.3.2) provides the most obvious avenue for further work. Masson *et al.* (2016), Wurster, D. J. Price, and Ayliffe (2014), and Wurster, D. J. Price, and Bate (2016) have already considered this for certain cases. However, these have been generally limited to laminar velocity profiles and do not always include radiation. The `NICIL` library (Wurster 2016a,b) has already been implemented in both the `sphNG` and `Phantom` codes, so running a comparable suite of calculations to those presented in chapter VI is possible. However, the time–stepping required to fully evolve all three non–ideal M.H.D. phenomena is considerably shorter than for idea M.H.D. which causes marked increases in run times. This effect, whilst reducing the throughput of calculations, seems to be tractable for laminar cores, however, the additional density anisotropies and the consequently larger region of the calculation requiring a shorter time–step in a turbulent fluid may challenge this.

Non–ideal M.H.D. effects, particularly effects which provide for magnetic diffusion such as Ohmic resistivity and ambipolar diffusion will act to reduce the field strength. Firstly, this would allow mass–to–flux ratios of $\mu < 5$ to be explored more readily. For example, it would be possible to approach the 'average' value of $\mu \approx 2 \sim 3$ found by Crutcher (1999). Secondly, we found in chapter V that each field strength considered produced a different outflow morphology. Incorporating dissipative M.H.D. effects may move stronger fields towards weaker fields, *e.g.* it may act to decrease the degree of angular momentum transport by magnetic braking when $\mu = 5$ producing a faster outflow, or it may decrease the minimum value of μ required to cause fragmentation into a binary system.

In addition, Tsukamoto *et al.* (2015a), Wurster, D. J. Price, and Bate (2016) and Bai and Stone (2017) have found that the *non–dissipative* Hall effect can significantly change the morphology of the discs around protostars. Given that we have shown that the nature of a protostellar outflow has strong dependence on disc structure it would be instructive to consider how the Hall effect changes this. Due to the way the Hall effect can transform the magnetic field it will be particularly interesting to consider the impact of this M.H.D. phenomenon on the disordered magnetic field in a turbulent calculation.

IX.2 The Density Field

In chapter VII we showed that a centrally condensed Bonnor–Ebert density profile changes the velocity of an outflow at lower angular momenta, whilst at higher momenta binary systems are formed. This should be extended to cover the same range of field geometries — $0° \leq \vartheta \leq 90°$ — and field strengths — $5 \leq \mu \leq 20$ — explored in chapters IV and V.

Importantly it would allow a comparison between the binary formation mode when $\mu = 20$ in a uniform density sphere and that seen for stronger fields in a rapidly rotating Bonnor–Ebert sphere to be made. This will provide further insights into whether binary formation is possible before or during the first hydrostatic core phase. In a similar vein, the turbulent calculations in chapter VI can be extended to Bonnor–Ebert spheres. *Inter alia*, this may allow super–sonic turbulence to be studied without unbinding the core due to the centrally condensed nature of a Bonnor–Ebert sphere. Similarly, the non–ideal M.H.D. schemes discussed in the previous paragraph can be applied to the same

IX.3 A Distance Ladder?

Turning to larger scales, throughout this thesis we have chosen initial conditions loosely based on observations but which are always approximately uniform and simplified. A more nuanced approach would be to perform a calculation of the evolution of a complete molecular cloud and then use this to set the initial conditions. Out of computational necessity a molecular cloud calculation will have a significantly reduced mass resolution compared to our calculations in this thesis. However, if Jeans unstable regions can be identified, these can be used to set the initial conditions for a calculation like that performed in this work. Most simply, this could be done by just measuring the 'average' values of the magnetic, velocity, and density fields in the Jeans unstable region and then setting up an idealised molecular core based on these. In effect, we could use the results of a calculation like Bate (2009) to select regions of the parameter space to explore.

A more advanced method would be to 'zoom' in on regions of the molecular cloud (see, albeit at a larger scale, *e.g.*, Rey-Raposo *et al.* 2017; Rey-Raposo, Dobbs, and Duarte-Cabral 2015) and then by using an S.P.H. particle splitting scheme create a higher mass resolution calculation. This allows complex and asymmetrical field structures (in all three of the magnetic, velocity and density fields) to be used as initial conditions and may provide a more realistic starting point. Either approach will also indicate if there are regions of our idealised parameter space which are unrealistic or which do not occur in simulated molecular clouds. In principle this process could be extended further in both directions: our first hydrostatic cores could be used to seed calculations of more evolved protostars and molecular cloud calculations could be derived from galactic scale simulation. In effect, this would the computational astronomy analogue to the cosmological 'distance ladder'.

Ceterum censeo magnetismum esse delendam

With apologies to Cato the Elder *et al.*

The Bibliography

Adams, Douglas Noel (1979).
The Hitchhiker's Guide to the Galaxy.
Pan Books: London, United Kingdom.

Adams, F. C., C. J. Lada, and F. H. Shu (1987).
'Spectral evolution of young stellar objects'.
Astrophys. J. v. 312, pp. 788–806. i.s.s.n.: 0004–637X, 1538–4357.
d.o.i.: 10.1086/164924.

Alexander, D. R. (1975).
'Low–Temperature Rosseland Opacity Tables'.
Astrophys. J. Suppl. S. v. 29, p. 363. i.s.s.n.: 0067-0049.
d.o.i.: 10.1086/190349.

Alfvén, H. (1942).
'Existence of Electromagnetic–Hydrodynamic Waves'.
Nature v. 150, pp. 405–406. i.s.s.n.: 0028–0836, 1476–4687.
d.o.i.: 10.1038/150405d0.

Alighieri, Dante (1320).
Divina Commedia. Paradiso. (The Divine Comedy: Paradise). Italian.

Allen, A., Z.-Y. Li, and F. H. Shu (2003).
'Collapse of Magnetized Singular Isothermal Toroids — ii. Rotation and Magnetic Braking'.
Astrophys. J. v. 599, pp. 363–379. i.s.s.n.: 0004–637X, 1538–4357.
d.o.i.: 10.1086/379243. arxiv: astro-ph/0311377.

André, P., A. Men'shchikov, S. Bontemps, V. Könyves, F. Motte, N. Schneider, P. Didelon, V. Minier, P. Saraceno, D. Ward-Thompson, J. di Francesco, G. White, S. Molinari, L. Testi, *et al.* (2010).
'From filamentary clouds to prestellar cores to the stellar IMF: Initial highlights from the Herschel Gould Belt Survey'.
Astron. Astrophys. v. 518, p. L102. i.s.s.n.: 0004–6361, 1432–0746.
d.o.i.: 10.1051/0004-6361/201014666. arxiv: 1005.2618.

Apollodorus (*ca.* 100 B.C.–200 B.C.).
Βιβλιοθήκη. (The Library). Trans. from the Ancient Greek by Sir James George Frazer.
Harvard University Press: Cambridge, M.A., United States. i.s.b.n.: 978–0–67–499135–4.

Archimedes of Syracuse (*ca.* 250 B.C.).
Περὶ τῶν ἐπιπλεόντων σωμάτων. (On Floating Bodies). Ancient Greek. v. 1.

Armitage, P. J. (2011).
'Dynamics of Protoplanetary Disks'.

Ann. Rev. Astron. Astr. v. 49, pp. 195–236. i.s.s.n.: 0066–4146.
d.o.i.: 10.1146/annurev-astro-081710-102521. arxiv: 1011.1496.

Arouet, François-Marie (Voltaire) (1764).
Dictionnaire philosophique. (Philosophical Dictionary). French.

Athanassoula, E., E. Fady, J. C. Lambert, and A. Bosma (2000).
'Optimal softening for force calculations in collisionless *N*-body simulations'.
Mon. Not. R. Astron. Soc. v. 314, pp. 475–488. i.s.s.n.: 0035–8711, 1365–2966.
d.o.i.: 10.1046/j.1365-8711.2000.03316.x. arxiv: astro-ph/9912467.

Bai, X.-N. and J. M. Stone (2017).
'Hall Effect–Mediated Magnetic Flux Transport in Protoplanetary Disks'.
Astrophys. J. v. 836, p. 46. i.s.s.n.: 0004–637X, 1538–4357.
d.o.i.: 10.3847/1538-4357/836/1/46. arxiv: 1612.03912.

Balbus, S. A. and C. Terquem (2001).
'Linear Analysis of the Hall Effect in Protostellar Disks'.
Astrophys. J. v. 552, pp. 235–247. i.s.s.n.: 0004–637X, 1538–4357.
d.o.i.: 10.1086/320452. arxiv: astro-ph/0010229.

Ballesteros–Paredes, J., R. S. Klessen, M.-M. Mac Low, and E. Vazquez-Semadeni (2007).
'Molecular Cloud Turbulence and Star Formation'.
in: *Protostars and Planets v*. Ed. by B. Reipurth, D. Jewitt, and Keil K. Space Science Series.
University of Arizona Press: Tucson, A.Z., United States, pp. 63–80. i.s.b.n.: 978-0-8165-2654-3.
arxiv: astro-ph/0603357.

Banerjee, R. and R. E. Pudritz (2006).
'Outflows and Jets from Collapsing Magnetized Cloud Cores'.
Astrophys. J. v. 641, pp. 949–960. i.s.s.n.: 0004–637X, 1538–4357.
d.o.i.: 10.1086/500496. arxiv: astro-ph/0508374.

Banerjee, R., R. E. Pudritz, and L. Holmes (2004).
'The formation and evolution of protostellar discs; three–dimensional adaptive mesh refinement hydrosimulations of collapsing, rotating Bonnor–Ebert spheres'.
Mon. Not. R. Astron. Soc. v. 355, pp. 248–272. i.s.s.n.: 0035–8711, 1365–2966.
d.o.i.: 10.1111/j.1365-2966.2004.08316.x. arxiv: astro-ph/0408277.

Baraffe, I. and M. F. El Eid (1991).
'Evolution of massive stars with variable initial compositions'.
Astron. Astrophys. v. 245, pp. 548–560. i.s.s.n.: 0004–6361, 1432–0746.

Barnes, J. E. (1992).
'Transformations of galaxies. i. Mergers of equal-mass stellar disks'.
Astrophys. J. v. 393, pp. 484–507. i.s.s.n.: 0004–637X, 1538–4357.
d.o.i.: 10.1086/171522.

Barnes, J. E. and L. Hernquist (1992).
'Dynamics of interacting galaxies'.
Ann. Rev. Astron. Astr. v. 30, pp. 705–742. i.s.s.n.: 0066–4146.
d.o.i.: 10.1146/annurev.aa.30.090192.003421.

— (1996).
'Transformations of Galaxies. ii. Gasdynamics in Merging Disk Galaxies'.
Astrophys. J. v. 471, p. 115. i.s.s.n.: 0004–637X, 1538–4357.
d.o.i.: 10.1086/177957.

Barnes, J. E. and P. Hut (1986).
'A hierarchical $\mathcal{O}\left(N \log N\right)$ force-calculation algorithm'.
Nature v. 324, pp. 446–449. i.s.s.n.: 0028–0836, 1476–4687.
d.o.i.: 10.1038/324446a0.

Bastian, N., K. R. Covey, and M. R. Meyer (2010).
'A Universal Stellar Initial Mass Function? A Critical Look at Variations'.
Ann. Rev. Astron. Astr. v. 48, pp. 339–389. I.S.S.N.: 0066–4146.
D.O.I.: 10.1146/annurev-astro-082708-101642. ARXIV: 1001.2965.

Basu, S. and T. C. Mouschovias (1994).
'Magnetic braking, ambipolar diffusion, and the formation of cloud cores and protostars. I — Axisymmetric solutions'.
Astrophys. J. v. 432, pp. 720–741. I.S.S.N.: 0004–637X, 1538–4357.
D.O.I.: 10.1086/174611.

Bate, M. R. (2009).
'Stellar, brown dwarf and multiple star properties from hydrodynamical simulations of star cluster formation'.
Mon. Not. R. Astron. Soc. v. 392, pp. 590–616. I.S.S.N.: 0035–8711, 1365–2966.
D.O.I.: 10.1111/j.1365-2966.2008.14106.x. ARXIV: 0811.0163.

— (2011).
'Collapse of a molecular cloud core to stellar densities: the formation and evolution of pre-stellar discs'.
Mon. Not. R. Astron. Soc. v. 417, pp. 2036–2056. I.S.S.N.: 0035–8711, 1365–2966.
D.O.I.: 10.1111/j.1365-2966.2011.19386.x. ARXIV: 1108.0009.

— (2012).
'Stellar, brown dwarf and multiple star properties from a radiation hydrodynamical simulation of star cluster formation'.
Mon. Not. R. Astron. Soc. v. 419, pp. 3115–3146. I.S.S.N.: 0035–8711, 1365–2966.
D.O.I.: 10.1111/j.1365-2966.2011.19955.x. ARXIV: 1110.1092.

Bate, M. R., I. A. Bonnell, and V. Bromm (2003).
'The formation of a star cluster: predicting the properties of stars and brown dwarfs'.
Mon. Not. R. Astron. Soc. v. 339, pp. 577–599.
D.O.I.: 10.1046/j.1365-8711.2003.06210.x. ARXIV: astro-ph/0212380.

Bate, M. R., I. A. Bonnell, and N. M. Price (1995).
'Modelling accretion in protobinary systems'.
Mon. Not. R. Astron. Soc. v. 277, pp. 362–376. I.S.S.N.: 0035–8711, 1365–2966.
D.O.I.: 10.1093/mnras/277.2.362. ARXIV: astro-ph/9510149.

Bate, M. R. and A. Burkert (1997).
'Resolution requirements for smoothed particle hydrodynamics calculations with self-gravity'.
Mon. Not. R. Astron. Soc. v. 288, pp. 1060–1072. I.S.S.N.: 0035–8711, 1365–2966.

Bate, M. R., T. S. Tricco, and D. J. Price (2014).
'Collapse of a molecular cloud core to stellar densities: stellar–core and outflow formation in radiation magnetohydrodynamic simulations'.
Mon. Not. R. Astron. Soc. v. 437, pp. 77–95. I.S.S.N.: 0035–8711, 1365–2966.
D.O.I.: 10.1093/mnras/stt1865. ARXIV: 1310.1092.

Beck, R. (2005).
'Observations of Magnetic Fields in Galaxies'.
IN: *Magnetic Fields in the Universe: From Laboratory and Stars to Primordial Structures.* Ed. by E. M. de Gouveia dal Pino, G. Lugones, and A. Lazarian. v. 784. A.I.P. Conference Series. American Institute of Physics, pp. 343–353. I.S.B.N.: 978-0735402737.
D.O.I.: 10.1063/1.2077197.

Benz, W. (1988).
'Applications of smooth particle hydrodynamics (S.P.H.) to astrophysical problems.'
Comput. Phys. Commun. v. 48, pp. 97–105. I.S.S.N.: 0010–4655.
D.O.I.: 10.1016/0010-4655(88)90027-6.

Benz, W. (1990).
'Smooth Particle Hydrodynamics: A Review'.
IN: *Numerical Modelling of Nonlinear Stellar Pulsations Problems and Prospects*. Ed. by J. R. Buchler. V. 302. N.A.T.O. A.S.I. Series.
Kluwer: Dordrecht, The Netherlands. CAP. 16, PP. 269–288. I.S.B.N.: 978–94–010–6720–1.

Benz, W., A. G. W. Cameron, W. H. Press, and R. L. Bowers (1990).
'Dynamic mass exchange in doubly degenerate binaries. I — 0.9 and 1.2 solar mass stars'.
Astrophys. J. V. 348, PP. 647–667. I.S.S.N.: 0004–637X, 1538–4357.
D.O.I.: 10.1086/168273.

Beuther, H., W. H. T. Vlemmings, R. Rao, and F. F. S. van der Tak (2010).
'Magnetic Field Structure in a High-mass Outflow/Disk System'.
Astrophys. J. Lett. V. 724, PP. L113–L117. I.S.S.N.: 2041–8205.
D.O.I.: 10.1088/2041-8205/724/1/L113. ARXIV: 1010.3635.

Black, D. C. and P. Bodenheimer (1975).
'Evolution of rotating interstellar clouds. I — Numerical techniques'.
Astrophys. J. V. 199, PP. 619–632. I.S.S.N.: 0004–637X, 1538–4357.
D.O.I.: 10.1086/153729.

Blair, Eric Arthur (George Orwell) (1946).
Politics and the English Language.

Blandford, R. D. and D. G. Payne (1982).
'Hydromagnetic flows from accretion discs and the production of radio jets'.
Mon. Not. R. Astron. Soc. V. 199, PP. 883–903. I.S.S.N.: 0035–8711, 1365–2966.
D.O.I.: 10.1093/mnras/199.4.883.

Bogovalov, S. and K. Tsinganos (1999).
'On the magnetic acceleration and collimation of astrophysical outflows'.
Mon. Not. R. Astron. Soc. V. 305, PP. 211–224. I.S.S.N.: 0035–8711, 1365–2966.
D.O.I.: 10.1046/j.1365-8711.1999.02413.x. EPRINT: astro-ph/9901081.

Bok, B. J. and E. F. Reilly (1947).
'Small Dark Nebulae.'
Astrophys. J. V. 105, P. 255. I.S.S.N.: 0004–637X, 1538–4357.
D.O.I.: 10.1086/144901.

Bonnell, I. A. and M. R. Bate (1994).
'The Formation of Close Binary Systems'.
Mon. Not. R. Astron. Soc. V. 271, PP. 999–1004. I.S.S.N.: 0035–8711, 1365–2966.
ARXIV: astro-ph/9411081.

Bonnor, W. B. (1956).
'Boyle's Law and gravitational instability'.
Mon. Not. R. Astron. Soc. V. 116, P. 351. I.S.S.N.: 0035–8711, 1365–2966.
D.O.I.: 10.1093/mnras/116.3.351.

Børve, S., M. Omang, and J. Trulsen (2001).
'Regularized Smoothed Particle Hydrodynamics: A New Approach to Simulating Magnetohydrodynamic Shocks'.
Astrophys. J. V. 561, PP. 82–93. I.S.S.N.: 0004–637X, 1538–4357.
D.O.I.: 10.1086/323228.

Bourke, T. L., J. J. Tobin, A. Gusdorf, H. G. Arce, and M. Tafalla (2017).
'Revealing the Jets in the BHR 71 Protostellar System'.
IN: *American Astronomical Society Meeting Abstracts #229*. V. 49. *B. Am. Astron. Soc.* American Astronomical Society, P. 432.01.

Boyle, Robert (1662).
A Defence of the Doctrine Touching the Spring and Weight of the Air.
Thomas Robinson: London, England.

Brahe, Tycho (1573).
De nova et nullius ævi memoria prius visa stella. (Concerning the Star, new and never before seen in the life or memory of anyone). Latin.

Brookshaw, L. (1994).
'Solving the Heat Diffusion Equation in S.P.H. (Invited paper)'.
Mem. Soc. Astron. Italiana v. 65, p. 1033. I.S.S.N.: 1824-016X.

Burkert, A. and P. Bodenheimer (2000).
'Turbulent Molecular Cloud Cores: Rotational Properties'.
Astrophys. J. v. 543, pp. 822–830. I.S.S.N.: 0004–637X, 1538–4357.
D.O.I.: 10.1086/317122. ARXIV: astro-ph/0006010.

Burnham, S. W. (1890).
'Note on Hind's Variable Nebula in Taurus'.
Mon. Not. R. Astron. Soc. v. 51, p. 94. I.S.S.N.: 0035–8711, 1365–2966.
D.O.I.: 10.1093/mnras/51.2.94.

Butcher, J. C. (1964).
'Implicit Runge–Kutta Processes'.
Math. Comput. v. 18, n. 85, pp. 50–64. I.S.S.N.: 0025–5718, 1088–6842.
D.O.I.: 10.2307/2003405.

Calpeyron, Benoît Paul Émile (1834).
'Mémoire sur la puissance motrice de la chaleur'. (Memoire on the power of heat). French.
J. École Polytech. v. 14, pp. 153–190.

Caswell, J. L. (1976).
'A map of the northern sky at 10 MHz'.
Mon. Not. R. Astron. Soc. v. 177, pp. 601–616. I.S.S.N.: 0035–8711, 1365–2966.
D.O.I.: 10.1093/mnras/177.3.601.

Cauchy, Augustin-Louis (1827).
'De la pression ou tension dans un corps solide'. (On the pressure or tension in a solid body). French.
IN: *Exercices d'analyse et de physique mathematique*. v. 2, p. 42.

Chabrier, G. (2003).
'Galactic Stellar and Substellar Initial Mass Function'.
Publ. Astron. Soc. Pac. v. 115, pp. 763–795.
D.O.I.: 10.1086/376392. EPRINT: astro-ph/0304382.

Chabrier, G. and I. Baraffe (1997).
'Structure and evolution of low-mass stars'.
Astron. Astrophys. v. 327, pp. 1039–1053. I.S.S.N.: 0004–6361, 1432–0746.
ARXIV: astro-ph/9704118.

Chandrasekhar, S. and E. Fermi (1953a).
'Magnetic Fields in Spiral Arms.'
Astrophys. J. v. 118, p. 113. I.S.S.N.: 0004–637X, 1538–4357.
D.O.I.: 10.1086/145731.

— (1953b).
'Problems of Gravitational Stability in the Presence of a Magnetic Field.'
Astrophys. J. v. 118, p. 116. I.S.S.N.: 0004–637X, 1538–4357.
D.O.I.: 10.1086/145732.

Chapman, N. L., P. F. Goldsmith, J. L. Pineda, D. P. Clemens, D. Li, and M. Krčo (2011).
'The Magnetic Field in Taurus Probed by Infrared Polarization'.

Astrophys. J. v. 741, p. 21. I.S.S.N.: 0004–637X, 1538–4357.
D.O.I.: 10.1088/0004-637X/741/1/21. ARXIV: 1108.0410.

Chaussonnet, G., S. Braun, L. Wieth, R. Koch, and H.-J. Bauer (2015).
'Influence of particle disorder and smoothing length on S.P.H. operator accuracy'.
IN: *Proceedings of the 10th. international S.P.H.E.R.I.C. workshop*. Ed. by Renato Vacondio. S.P.H. European Research Interest Community.
Università degli Studi di Parma: Parma, Repubblica Italiana. I.S.B.N.: 978–88–7847–487–1.

Chen, X., H. G. Arce, Q. Zhang, T. L. Bourke, R. Launhardt, M. Schmalzl, and T. Henning (2010).
'L1448 IRS2E: A Candidate First Hydrostatic Core'.
Astrophys. J. v. 715, pp. 1344–1351. I.S.S.N.: 0004–637X, 1538–4357.
D.O.I.: 10.1088/0004-637X/715/2/1344. ARXIV: 1004.2443.

Ching, T.-C., S.-P. Lai, Q. Zhang, L. Yang, J. M. Girart, and R. Rao (2016).
'Helical Magnetic Fields in the NGC 1333 IRAS 4A Protostellar Outflows'.
Astrophys. J. v. 819, p. 159. I.S.S.N.: 0004–637X, 1538–4357.
D.O.I.: 10.3847/0004-637X/819/2/159. ARXIV: 1601.05229.

Cho, J. and A. Lazarian (2005).
'Grain Alignment by Radiation in Dark Clouds and Cores'.
Astrophys. J. v. 631, pp. 361–370. I.S.S.N.: 0004–637X, 1538–4357.
D.O.I.: 10.1086/432528. ARXIV: astro-ph/0505571.

Chow, E. and J. J. Monaghan (1997).
'Ultrarelativistic S.P.H.'
J. Comput. Phys. v. 134, pp. 296–305. I.S.S.N.: 0021-9991.
D.O.I.: 10.1006/jcph.1997.5708.

Ciardi, A. and P. Hennebelle (2010).
'Outflows and mass accretion in collapsing dense cores with misaligned rotation axis and magnetic field'.
Mon. Not. R. Astron. Soc. v. 409, pp. L39–L43. I.S.S.N.: 0035–8711, 1365–2966.
D.O.I.: 10.1111/j.1745-3933.2010.00942.x. ARXIV: 1009.0453.

Cicero, Marcus Tullius (*ca.* 45 B.C.).
De Finibus Bonorum Et Malorum. (On the ends of good and evil). Latin.

Clausius, R. J. E. (1870).
'On a Mechanical Theorem Applicable to Heat.'
Philos. Mag. SER. 4th. v. 40, pp. 122–127. I.S.S.N.: 0031–8086.

Cohen, E. R. and B. N. Taylor (1987).
'The 1986 CODATA Recommended Values of the Fundamental Physical Constants.'
J. Res. Natl. Inst. Stan. v. 85-95, N. 2. I.S.S.N.: 0091–0635.

Cohen, R. S., H. Cong, T. M. Dame, and P. Thaddeus (1980).
'Molecular clouds and galactic spiral structure'.
Astrophys. J. Lett. v. 239, pp. L53–L56. I.S.S.N.: 2041–8205.
D.O.I.: 10.1086/183290.

Colagrossi, A., M. Antuono, and D. Le Touzé (2009).
'Theoretical considerations on the free–surface role in the smoothed particle hydrodynamics model'.
Phys. Rev. SER. 3rd. (*E*) v. 79 (5), p. 056701. I.S.S.N.: 2470–0045, 2470–0053.
D.O.I.: 10.1103/PhysRevE.79.056701.

Courant, R., K. Friedrichs, and H. Lewy (1928).
'Über die partiellen Differenzengleichungen der mathematischen Physik'. (On the partial difference equations of mathematical physics). Trans. from the German by International Business Machines.
Math. Ann. v. 100 (1), pp. 32–74. I.S.S.N.: 0025–5831, 1432–1807.
D.O.I.: 10.1007/BF01448839.

Crapsi, A., P. Caselli, C. M. Walmsley, P. C. Myers, M. Tafalla, C. W. Lee, and T. L. Bourke (2005).
'Probing the Evolutionary Status of Starless Cores through N_2H^+ and N_2D^+ Observations'.
Astrophys. J. v. 619, pp. 379–406. I.S.S.N.: 0004–637X, 1538–4357.
D.O.I.: 10.1086/426472. ARXIV: astro-ph/0409529.

Crutcher, R. M. (1999).
'Magnetic Fields in Molecular Clouds: Observations Confront Theory'.
Astrophys. J. v. 520, pp. 706–713. I.S.S.N.: 0004–637X, 1538–4357.
D.O.I.: 10.1086/307483.

— (2005).
'Magnetic fields and massive star formation'.
IN: *Massive Star Birth: A Crossroads of Astrophysics*. Ed. by R. Cesaroni, M. Felli, E. Churchwell, and M. Walmsley. v. S227. Proceedings of the I.A.U. Symposia and Colloquia. International Astronomical Union. Cambridge University Press: Cambridge, United Kingdom, pp. 98–107. I.S.B.N.: 978-0521851985.
D.O.I.: 10.1017/S1743921305004412.

— (2012).
'Magnetic Fields in Molecular Clouds'.
Ann. Rev. Astron. Astr. v. 50, pp. 29–63. I.S.S.N.: 0066–4146.
D.O.I.: 10.1146/annurev-astro-081811-125514.

Crutcher, R. M., N. Hakobian, and T. H. Troland (2010).
'Self-consistent analysis of OH Zeeman observations'.
Mon. Not. R. Astron. Soc. v. 402, pp. L64–L66. I.S.S.N.: 0035–8711, 1365–2966.
D.O.I.: 10.1111/j.1745-3933.2009.00802.x. ARXIV: 0912.3024.

Crutcher, R. M. and I. Kazes (1983).
'The magnetic field of the NGC 2024 molecular cloud — Detection of OH line Zeeman splitting'.
Astron. Astrophys. v. 125, pp. L23–L26. I.S.S.N.: 0004–6361, 1432–0746.

Crutcher, R. M. and T. H. Troland (2008).
'Testing Faraday Rotation Estimates of Magnetic Field Strengths toward Dark Clouds'.
Astrophys. J. v. 685, pp. 281–284. I.S.S.N.: 0004–637X, 1538–4357.
D.O.I.: 10.1086/590404.

Crutcher, R. M., T. H. Troland, A. A. Goodman, C. E. Heiles, I. Kazes, and P. C. Myers (1993).
'OH Zeeman observations of dark clouds'.
Astrophys. J. v. 407, pp. 175–184. I.S.S.N.: 0004–637X, 1538–4357.
D.O.I.: 10.1086/172503.

Crutcher, R. M., T. H. Troland, and C. E. Heiles (1981).
'Magnetic fields in molecular clouds — OH Zeeman observations'.
Astrophys. J. v. 249, pp. 134–137. I.S.S.N.: 0004–637X, 1538–4357.
D.O.I.: 10.1086/159268.

Crutcher, R. M., T. H. Troland, and I. Kazes (1987).
'Magnetic field strengths in molecular clouds'.
Astron. Astrophys. v. 181, pp. 119–126. I.S.S.N.: 0004–6361, 1432–0746.

Crutcher, R. M., B. Wandelt, C. E. Heiles, E. Falgarone, and T. H. Troland (2010).
'Magnetic Fields in Interstellar Clouds from Zeeman Observations: Inference of Total Field Strengths by Bayesian Analysis'.
Astrophys. J. v. 725, pp. 466–479. I.S.S.N.: 0004–637X, 1538–4357.
D.O.I.: 10.1088/0004-637X/725/1/466.

Cudlip, W., I. Furniss, K. J. King, and R. E. Jennings (1982).
'Far infrared polarimetry of W51A and M42'.
Mon. Not. R. Astron. Soc. v. 200, pp. 1169–1173. I.S.S.N.: 0035–8711, 1365–2966.

Dalgarno, A. and W. G. Roberge (1979).
'Collision-induced dissociation of interstellar molecules'.
Astrophys. J. Lett. v. 233, pp. L25–L27. I.S.S.N.: 2041–8205.
D.O.I.: 10.1086/183069.

Dalrymple, R.A. and B.D. Rogers (2006).
'Numerical modeling of water waves with the S.P.H. method'.
Coast. Eng. v. 53, n. 2–3, pp. 141–147. I.S.S.N.: 0378–3839.
D.O.I.: 10.1016/j.coastaleng.2005.10.004.

Dame, T. M., H. Ungerechts, R. S. Cohen, E. J. de Geus, I. A. Grenier, J. May, D. C. Murphy, L.-A. Nyman, and P. Thaddeus (1987).
'A composite CO survey of the entire Milky Way'.
Astrophys. J. v. 322, pp. 706–720. I.S.S.N.: 0004–637X, 1538–4357.
D.O.I.: 10.1086/165766.

de Coulomb, Charles–Augustin (1785).
'Second Mémoire sur l'Électricité et le Magnétisme'. (Second Memorial on Electricity and Magnetism). French.
Mémoires de l'Académie Royale des Sciences.

Dedner, A., F. Kemm, D. Kröner, C.-D. Munz, T. Schnitzer, and M. Wesenberg (2002).
'Hyperbolic Divergence Cleaning for the M.H.D. Equations'.
J. Comput. Phys. v. 175, pp. 645–673. I.S.S.N.: 0021-9991.
D.O.I.: 10.1006/jcph.2001.6961.

Dehnen, W. (2001).
'Towards optimal softening in three-dimensional N-body codes - I. Minimizing the force error'.
Mon. Not. R. Astron. Soc. v. 324, pp. 273–291. I.S.S.N.: 0035–8711, 1365–2966.
D.O.I.: 10.1046/j.1365-8711.2001.04237.x. ARXIV: astro-ph/0011568.

Dehnen, W. and H. Aly (2012).
'Improving convergence in smoothed particle hydrodynamics simulations without pairing instability'.
Mon. Not. R. Astron. Soc. v. 425, pp. 1068–1082. I.S.S.N.: 0035–8711, 1365–2966.
D.O.I.: 10.1111/j.1365-2966.2012.21439.x. ARXIV: 1204.2471.

Digel, S. W., D. A. Lyder, A. J. Philbrick, D. Puche, and P. Thaddeus (1996).
'A Large–Scale CO Survey toward W3, W4, and W5'.
Astrophys. J. v. 458, p. 561. I.S.S.N.: 0004–637X, 1538–4357.
D.O.I.: 10.1086/176839.

Diodorus Siculus (*ca.* 36 B.C.).
Βιβλιοθήκη ἱστορική. (The Historical Library). Trans. from the Ancient Greek by C. H. Oldfather.
Harvard University Press: Cambridge, M.A., United States. I.S.B.N.: 978-06–7499–334–1.

Donati, J.-F., M. B. Skelly, J. Bouvier, S. G. Gregory, K. N. Grankin, M. M. Jardine, G. A. J. Hussain, F. Ménard, C. Dougados, Y. Unruh, S. Mohanty, M. Aurière, J. Morin, R. Farès, and MAPP Collaboration (2010).
'Magnetospheric accretion and spin-down of the prototypical classical T Tauri star AA Tau'.
Mon. Not. R. Astron. Soc. v. 409, pp. 1347–1361. I.S.S.N.: 0035–8711, 1365–2966.
D.O.I.: 10.1111/j.1365-2966.2010.17409.x. ARXIV: 1007.4407.

Dunham, M. M., X. Chen, H. G. Arce, T. L. Bourke, S. Schnee, and M. L. Enoch (2011).
'Detection of a Bipolar Molecular Outflow Driven by a Candidate First Hydrostatic Core'.
Astrophys. J. v. 742, p. 1. I.S.S.N.: 0004–637X, 1538–4357.
D.O.I.: 10.1088/0004-637X/742/1/1. ARXIV: 1108.1342.

Dyer, C. C. and P. S. S. Ip (1993).
'Softening in N-body simulations of collisionless systems'.
Astrophys. J. v. 409, pp. 60–67. I.S.S.N.: 0004–637X, 1538–4357.
D.O.I.: 10.1086/172641.

Ebert, R. (1955).
'Über die Verdichtung von H I–Gebieten. Mit 5 Textabbildungen'. German.
Z. Astrophys. v. 37, p. 217. I.S.S.N.: 0372–8331.

Eggen, O. J., D. Lynden–Bell, and A. R. Sandage (1962).
'Evidence from the motions of old stars that the Galaxy collapsed.'
Astrophys. J. v. 136, p. 748. I.S.S.N.: 0004–637X, 1538–4357.
D.O.I.: 10.1086/147433.

Eichhorn, G. (1994).
'An Overview of the Astrophysics Data System'.
Exp. Astron. v. 5, pp. 205–220. I.S.S.N.: 0922–6435, 1572–9508.
D.O.I.: 10.1007/BF01583697.

Ellis, G. R. A. and P. A. Hamilton (1966).
'Ionized Hydrogen in the Plane of the Galaxy'.
Astrophys. J. v. 146, p. 78. I.S.S.N.: 0004–637X, 1538–4357.
D.O.I.: 10.1086/148860.

Elmegreen, B. G. (1987).
'Supercloud formation by nonaxisymmetric gravitational instabilities in sheared magnetic galaxy disks'.
Astrophys. J. v. 312, pp. 626–639. I.S.S.N.: 0004–637X, 1538–4357.
D.O.I.: 10.1086/164907.

— (1993a).
'Star Formation at Compressed Interfaces in Turbulent Self–gravitating Clouds'.
Astrophys. J. Lett. v. 419, p. L29. I.S.S.N.: 2041–8205.
D.O.I.: 10.1086/187129.

— (1993b).
'The H to H2 transition in galaxies - Totally molecular galaxies'.
Astrophys. J. v. 411, pp. 170–177. I.S.S.N.: 0004–637X, 1538–4357.
D.O.I.: 10.1086/172816.

Emden, Jacob Robert (1907).
Gaskugeln: Anwendungen der mechanischen Wärmetheorie auf kosmologische und meteorologische Probleme. German.
Nabu Press: Charleston, S.C., United States. I.S.B.N.: 978–114–78–9710–4.

Euler, L. (1769).
Institutionum Calculi Integralis. In quo methodus inveniendi functiones unius variabilis ex data relatione differentialium secundi altiorisve gradus pertractatur. (The Foundations of the Integral Calculus. In which the method of finding functions of one variable from a given relation of the differentials of the second or higher order are treated of). Latin. ED. 3rd. v. 2.
Academiæ Imperialis Scientiarium: Санкт-Петербург, Россійская Имперія (St. Petersburg, Russian Empire).

Falgarone, E., T. H. Troland, R. M. Crutcher, and G. Paubert (2008).
'CN Zeeman measurements in star formation regions'.
Astron. Astrophys. v. 487, pp. 247–252. I.S.S.N.: 0004–6361, 1432–0746.
D.O.I.: 10.1051/0004-6361:200809577.

Faraday, M. (1832).
'Experimental Researches in Electricity'.
Phil. Trans. R. Soc. v. 122, pp. 125–162.
D.O.I.: 10.1098/rstl.1832.0006.

Federrath, C. (2015).
'Inefficient star formation through turbulence, magnetic fields and feedback'.
Mon. Not. R. Astron. Soc. v. 450, pp. 4035–4042. I.S.S.N.: 0035–8711, 1365–2966.
D.O.I.: 10.1093/mnras/stv941. ARXIV: 1504.03690.

Federrath, C. and R. S. Klessen (2012).
'The Star Formation Rate of Turbulent Magnetized Clouds: Comparing Theory, Simulations, and Observations'.
Astrophys. J. v. 761, p. 156. I.S.S.N.: 0004–637X, 1538–4357.
D.O.I.: 10.1088/0004-637X/761/2/156. ARXIV: 1209.2856.

Federrath, C., J. Roman-Duval, R. S. Klessen, W. Schmidt, and M.-M. Mac Low (2010).
'Comparing the statistics of interstellar turbulence in simulations and observations. Solenoidal versus compressive turbulence forcing'.
Astron. Astrophys. v. 512, A81.
D.O.I.: 10.1051/0004-6361/200912437. ARXIV: 0905.1060.

Fehlberg, E. (1969).
'Low–order classical Runge–Kutta formulas with stepsize control and their application to some heat transfer problems'.
N.A.S.A. Tech. Rep. v. R-315.

— (1970).
'Klassische Runge–Kutta–Formeln vierter und niedrigerer Ordnung mit Schrittweiten–Kontrolle und ihre Anwendung auf Wärmeleitungsprobleme'.
Comput. v. 6, pp. 61–71. I.S.S.N.: 0010–485X, 1436–5057.

Ferrière, K. M. (2001).
'The interstellar environment of our galaxy'.
Rev. Mod. Phys. v. 73, pp. 1031–1066. I.S.S.N.: 0034–6861, 1539–0756.
D.O.I.: 10.1103/RevModPhys.73.1031. ARXIV: astro-ph/0106359.

Fick, A. (1855).
'Über Diffusion'.
Ann. Phys. v. 170, N. 1, pp. 59–86. I.S.S.N.: 1521-3889.
D.O.I.: 10.1002/andp.18551700105.

Field, G. B., D. W. Goldsmith, and H. J. Habing (1969).
'Cosmic–Ray Heating of the Interstellar Gas'.
Astrophys. J. Lett. v. 155, p. L149. I.S.S.N.: 2041–8205.
D.O.I.: 10.1086/180324.

Fleck Jr., R. C. and F. O. Clark (1981).
'A turbulent origin for the rotation of molecular clouds'.
Astrophys. J. v. 245, pp. 898–902. I.S.S.N.: 0004–637X, 1538–4357.
D.O.I.: 10.1086/158866.

Fleming, Iain Lancaster (1958).
Dr. No.
Jonathan Cape: London, United Kingdom.

Foster, P. N. and R. A. Chevalier (1993).
'Gravitational Collapse of an Isothermal Sphere'.
Astrophys. J. v. 416, p. 303. I.S.S.N.: 0004–637X, 1538–4357.
D.O.I.: 10.1086/173236.

Freitag, M. and W. Benz (2001).
'A new Monte Carlo code for star cluster simulations. I. Relaxation'.
Astron. Astrophys. v. 375, pp. 711–738. I.S.S.N.: 0004–6361, 1432–0746.
D.O.I.: 10.1051/0004-6361:20010706. ARXIV: astro-ph/0102139.

Galli, D., S. Lizano, F. H. Shu, and A. Allen (2006).
'Gravitational Collapse of Magnetized Clouds — I. Ideal Magnetohydrodynamic Accretion Flow'.
Astrophys. J. v. 647, pp. 374–381. I.S.S.N.: 0004–637X, 1538–4357.
D.O.I.: 10.1086/505257. EPRINT: astro-ph/0604573.

Galli, D. and F. H. Shu (1993).
'Collapse of Magnetized Molecular Cloud Cores. II. Numerical Results'.
Astrophys. J. v. 417, p. 243. I.S.S.N.: 0004–637X, 1538–4357.
D.O.I.: 10.1086/173306.

Gaustad, J. E. (1963).
'The Opacity of Diffuse Cosmic Matter and the Early Stages of Star Formation.'
Astrophys. J. v. 138, p. 1050. I.S.S.N.: 0004–637X, 1538–4357.
D.O.I.: 10.1086/147705.

Geha, M., T. M. Brown, J. Tumlinson, J. S. Kalirai, J. D. Simon, E. N. Kirby, D. A. VandenBerg, R. R. Muñoz, R. J. Avila, P. Guhathakurta, and H. C. Ferguson (2013).
'The Stellar Initial Mass Function of Ultra-faint Dwarf Galaxies: Evidence for IMF Variations with Galactic Environment'.
Astrophys. J. v. 771, p. 29. I.S.S.N.: 0004–637X, 1538–4357.
D.O.I.: 10.1088/0004-637X/771/1/29. ARXIV: 1304.7769.

Ghosh, P. and F. K. Lamb (1978).
'Disk accretion by magnetic neutron stars'.
Astrophys. J. Lett. v. 223, pp. L83–L87. I.S.S.N.: 2041–8205.
D.O.I.: 10.1086/182734.

Giannetti, A., J. Brand, Á. Sánchez-Monge, F. Fontani, R. Cesaroni, M. T. Beltrán, S. Molinari, R. Dodson, and M. J. Rioja (2013).
'Physical properties of high-mass clumps in different stages of evolution'.
Astron. Astrophys. v. 556, A16. I.S.S.N.: 0004–6361, 1432–0746.
D.O.I.: 10.1051/0004-6361/201321456. ARXIV: 1307.4932.

Gilbert, William Schwenck (1882).
Iolanthe. Or the Peer and the Peri.
Chappell & Co.: London, United Kingdom.

Gillmon, K. and J. M. Shull (2006).
'Molecular Hydrogen in Infrared Cirrus'.
Astrophys. J. v. 636, pp. 908–915. I.S.S.N.: 0004–637X, 1538–4357.
D.O.I.: 10.1086/498055. ARXIV: astro-ph/0507587.

Gingold, R. A. and J. J. Monaghan (1982).
'Kernel estimates as a basis for general particle methods in hydrodynamics'.
J. Comput. Phys. v. 46, pp. 429–453. I.S.S.N.: 0021-9991.
D.O.I.: 10.1016/0021-9991(82)90025-0.

Godunov, S. K. (1959).
'Разностный метод численного расчета разрывных решений уравнений гидродинамики'. (A Difference Scheme for Numerical Solution of Discontinuous Solution of Hydrodynamic Equations). Trans. from the Russian by U.S. Joint Publications Research Service (J.P.R.S. 7225).
Mat. Sb. v. 47(89), N. 3, pp. 271–306.

Goodman, A. A., P. Bastien, F. Menard, and P. C. Myers (1990).
'Optical polarization maps of star–forming regions in Perseus, Taurus, and Ophiuchus'.
Astrophys. J. v. 359, pp. 363–377. I.S.S.N.: 0004–637X, 1538–4357.
D.O.I.: 10.1086/169070.

Goodman, A. A., P. J. Benson, G. A. Fuller, and P. C. Myers (1993).
'Dense cores in dark clouds. VIII - Velocity gradients'.
Astrophys. J. v. 406, pp. 528–547. I.S.S.N.: 0004–637X, 1538–4357.
D.O.I.: 10.1086/172465.

Goodman, A. A. and C. E. Heiles (1994).
'The magnetic field in the Ophiuchus dark cloud complex'.

Astrophys. J. v. 424, pp. 208–221. i.s.s.n.: 0004–637X, 1538–4357.
d.o.i.: 10.1086/173884.

Guertler, J., T. Henning, and J. Dorschner (1989).
'Properties of circumstellar silicate dust (Review)'.
Astron. Nachr. v. 310, pp. 319–327. i.s.s.n.: 0004–6337, 1521–3994.
d.o.i.: 10.1002/asna.2113100419.

Haro, G. (1952).
'Herbig's Nebulous Objects Near NGC 1999.'
Astrophys. J. v. 115, p. 572. i.s.s.n.: 0004–637X, 1538–4357.
d.o.i.: 10.1086/145576.

Hartmann, L., R. Hewett, S. Stahler, and R. D. Mathieu (1986).
'Rotational and radial velocities of T Tauri stars'.
Astrophys. J. v. 309, pp. 275–293. i.s.s.n.: 0004–637X, 1538–4357.
d.o.i.: 10.1086/164599.

Hayashi, C. (1961).
'Stellar evolution in early phases of gravitational contraction.'
Publ. Astron. Soc. Jpn. v. 13, pp. 450–452. i.s.s.n.: 0004–6264.

Hayashi, C. and R. Hoshi (1961).
'The Outer Envelope of Giant Stars with Surface Convection Zone'.
Publ. Astron. Soc. Jpn. v. 13, pp. 442–449. i.s.s.n.: 0004–6264.

Heaviside, O. (1889).
'On the Electromagnetic Effects due to the Motion of Electrification through a Dielectric'.
Philos. Mag. ser. 5th. v. 27, pp. 324–339. i.s.s.n.: 0031–8086.

Heiles, C. E., A. A. Goodman, C. F. McKee, and E. G. Zweibel (1993).
'Magnetic fields in star-forming regions — Observations'.
in: *Protostars and Planets iv*. Ed. by E. H. Levy and J. I. Lunine. Space Science Series.
University of Arizona Press: Tucson, A.Z., United States, pp. 279–326. i.s.b.n.: 978-0816513345.

Hennebelle, P., B. Commerçon, G. Chabrier, and P. Marchand (2016).
'Magnetically Self–regulated Formation of Early Protoplanetary Disks'.
Astrophys. J. Lett. v. 830, p. L8. i.s.s.n.: 2041–8205.
d.o.i.: 10.3847/2041-8205/830/1/L8. arxiv: 1608.02525.

Hennebelle, P. and E. Falgarone (2012).
'Turbulent molecular clouds'.
Astron. Astrophys. Rev. v. 20, p. 55. i.s.s.n.: ????–????
d.o.i.: 10.1007/s00159-012-0055-y. arxiv: 1211.0637.

Hennebelle, P. and S. Fromang (2008).
'Magnetic processes in a collapsing dense core. i — Accretion and ejection'.
Astron. Astrophys. v. 477, pp. 9–24. i.s.s.n.: 0004–6361, 1432–0746.
d.o.i.: 10.1051/0004-6361:20078309. arxiv: 0709.2886.

Herbig, G. H. (1951).
'The Spectra of Two Nebulous Objects Near NGC 1999.'
Astrophys. J. v. 113, pp. 697–699. i.s.s.n.: 0004–637X, 1538–4357.
d.o.i.: 10.1086/145440.

Hernquist, L. (1989).
'Tidal triggering of starbursts and nuclear activity in galaxies'.
Nature v. 340, pp. 687–691. i.s.s.n.: 0028–0836, 1476–4687.
d.o.i.: 10.1038/340687a0.

Hernquist, L. and N. Katz (1989).
'TREESPH – A unification of S.P.H. with the hierarchical tree method'.

Astrophys. J. Suppl. S. v. 70, pp. 419–446. i.s.s.n.: 0067-0049.
d.o.i.: 10.1086/191344.

Heyer, M. H. and C. M. Brunt (2004).
'The Universality of Turbulence in Galactic Molecular Clouds'.
Astrophys. J. Lett. v. 615, pp. L45–L48. i.s.s.n.: 2041–8205.
d.o.i.: 10.1086/425978. arxiv: astro-ph/0409420.

Heyer, M. H. and T. M. Dame (2015).
'Molecular Clouds in the Milky Way'.
Ann. Rev. Astron. Astr. v. 53, pp. 583–629. i.s.s.n.: 0066–4146.
d.o.i.: 10.1146/annurev-astro-082214-122324.

Hibbard, J. E. (1997).
'Mergers, interactions, and the fueling of starbursts'.
in: *American Institute of Physics Conference Series*. Ed. by S. S. Holt and L. G. Mundy. v. 393. American Institute of Physics Conference Series, pp. 259–270.
d.o.i.: 10.1063/1.52790. arxiv: astro-ph/9701130.

Hildebrand, R. H., L. Kirby, J. L. Dotson, M. Houde, and J. E. Vaillancourt (2009).
'Dispersion of Magnetic Fields in Molecular Clouds. i.'
Astrophys. J. v. 696, pp. 567–573. i.s.s.n.: 0004–637X, 1538–4357.
d.o.i.: 10.1088/0004-637X/696/1/567. arxiv: 0811.0813.

Hily-Blant, P., D. Teyssier, S. Philipp, and R. Güsten (2005).
'Velocity field and star formation in the Horsehead nebula'.
Astron. Astrophys. v. 440, pp. 909–919. i.s.s.n.: 0004–6361, 1432–0746.
d.o.i.: 10.1051/0004-6361:20041733. arxiv: astro-ph/0601605.

Hipparchus (*ca.* 160 B.C.–120 B.C.).
Τῶν Ἀράτου καὶ Εὐδόξου φαινομένων ἐξήγησις. (Commentary on the Phenomena of Aratus and Eudoxus). Ancient Greek.

Holmberg, E. (1941).
'On the Clustering Tendencies among the Nebulae. ii — a Study of Encounters Between Laboratory Models of Stellar Systems by a New Integration Procedure.'
Astrophys. J. v. 94, p. 385. i.s.s.n.: 0004–637X, 1538–4357.
d.o.i.: 10.1086/144344.

Homer (760 B.C.–710 B.C.).
Ἰλιάς. (The Illiad). ancientgreek.

Hopkins, P. F. (2015).
'A new class of accurate, mesh–free hydrodynamic simulation methods'.
Mon. Not. R. Astron. Soc. v. 450, pp. 53–110. i.s.s.n.: 0035–8711, 1365–2966.
d.o.i.: 10.1093/mnras/stv195. arxiv: 1409.7395.

Hopkins, P. F. and M. J. Raives (2016).
'Accurate, meshless methods for magnetohydrodynamics'.
Mon. Not. R. Astron. Soc. v. 455, pp. 51–88. i.s.s.n.: 0035–8711, 1365–2966.
d.o.i.: 10.1093/mnras/stv2180. arxiv: 1505.02783.

Houde, M., R. Rao, J. E. Vaillancourt, and R. H. Hildebrand (2011).
'Dispersion of Magnetic Fields in Molecular Clouds. iii.'
Astrophys. J. v. 733, p. 109. i.s.s.n.: 0004–637X, 1538–4357.
d.o.i.: 10.1088/0004-637X/733/2/109. arxiv: 1103.4772.

Houde, M., J. E. Vaillancourt, R. H. Hildebrand, S. Chitsazzadeh, and L. Kirby (2009).
'Dispersion of Magnetic Fields in Molecular Clouds. ii.'
Astrophys. J. v. 706, pp. 1504–1516. i.s.s.n.: 0004–637X, 1538–4357.
d.o.i.: 10.1088/0004-637X/706/2/1504. arxiv: 0909.5227.

Hoyle, F. (1953).
'On the Fragmentation of Gas Clouds Into Galaxies and Stars.'
Astrophys. J. v. 118, p. 513. I.S.S.N.: 0004–637X, 1538–4357.
D.O.I.: 10.1086/145780.

Hull, C. L. H., R. L. Plambeck, A. D. Bolatto, G. C. Bower, J. M. Carpenter, R. M. Crutcher, J. D. Fiege, E. Franzmann, N. S. Hakobian, and C. E. Heiles (2013a).
'Misalignment of Magnetic Fields and Outflows in Protostellar Cores'.
Astrophys. J. v. 768, p. 159. I.S.S.N.: 0004–637X, 1538–4357.
D.O.I.: 10.1088/0004-637X/768/2/159. ARXIV: 1212.0540.

Hull, C. L. H., R. L. Plambeck, A. D. Bolatto, G. C. Bower, J. M. Carpenter, R. M. Crutcher, J. D. Fiege, E. Franzmann, N. S. Hakobian, C. E. Heiles, and M. Houde (2013b).
'The Distribution of Angles Between Outflows and Magnetic Fields in Low–mass Protostellar Cores'.
IN: *American Astronomical Society Meeting Abstracts #221*. v. 45. *B. Am. Astron. Soc.* American Astronomical Society, p. 426.04.

Hunter, C. (1977).
'The collapse of unstable isothermal spheres'.
Astrophys. J. v. 218, pp. 834–845. I.S.S.N.: 0004–637X, 1538–4357.
D.O.I.: 10.1086/155739.

Hunter, J. D. (2007).
'Matplotlib: A 2–D graphics environment'.
Comput. Sci. Eng. v. 9, n. 3, pp. 90–95.
D.O.I.: 10.1109/MCSE.2007.55.

Işık, E., D. Schmitt, and M. Schüssler (2011).
'Magnetic flux generation and transport in cool stars'.
Astron. Astrophys. v. 528, A135. I.S.S.N.: 0004–6361, 1432–0746.
D.O.I.: 10.1051/0004-6361/201014501. ARXIV: 1102.0569.

Jeans, J. H. (1902).
'The Stability of a Spherical Nebula'.
Phil. Trans. R. Soc. SER. *A* v. 199, pp. 1–53. I.S.S.N.: 1364–503X.
D.O.I.: 10.1098/rsta.1902.0012.

Joos, M., P. Hennebelle, and A. Ciardi (2012).
'Protostellar disk formation and transport of angular momentum during magnetized core collapse'.
Astron. Astrophys. v. 543, A128. I.S.S.N.: 0004–6361, 1432–0746.
D.O.I.: 10.1051/0004-6361/201118730. ARXIV: 1203.1193.

Kanipe, J. (1989).
'Inside Orion's stellar nursery.'
Astron. v. 17, pp. 40–43. I.S.S.N.: 0091–6358.

Kauffmann, J., F. Bertoldi, N. J. Evans II, and C2D Collaboration (2005).
'Spitzer discovery of very low luminosity objects'.
Astron. Nachr. v. 326, pp. 878–881. I.S.S.N.: 0004–6337, 1521–3994.
D.O.I.: 10.1002/asna.200310446. ARXIV: astro-ph/0510501.

Kepler, Johannes (1606).
De Stella nova in pede Serpentarii. (On the new star in Ophiuchus' foot). Latin.

Kim, W.-T., E. C. Ostriker, and J. M. Stone (2003).
'Magnetorotationally Driven Galactic Turbulence and the Formation of Giant Molecular Clouds'.
Astrophys. J. v. 599, pp. 1157–1172. I.S.S.N.: 0004–637X, 1538–4357.
D.O.I.: 10.1086/379367. ARXIV: astro-ph/0309080.

Klessen, R. S., F. Heitsch, and M.-M. Mac Low (2000).
'Gravitational Collapse in Turbulent Molecular Clouds. I. Gasdynamical Turbulence'.

Astrophys. J. v. 535, pp. 887–906. i.s.s.n.: 0004–637X, 1538–4357.
d.o.i.: 10.1086/308891. arxiv: astro-ph/9911068.

Knuth, Donald Ervin (1968).
The Art of Computer Programming. ed. 3rd. v. 1.
Addison–Wesley: Boston, M.A., United States. i.s.b.n.: 0-201-03801-3.

Kroupa, P. (2001).
'On the variation of the initial mass function'.
Mon. Not. R. Astron. Soc. v. 322, pp. 231–246. i.s.s.n.: 0035–8711, 1365–2966.
d.o.i.: 10.1046/j.1365-8711.2001.04022.x. eprint: astro-ph/0009005.

Kutta, Martin Wilhelm (1901).
'Beitrag zur näherungsweisen Integration totaler Differentialgleichungen'.
Z. Math. Phys. v. 46, pp. 435–453.

Lane, Jonathan Homer (1870).
'On the Theoretical Temperature of the Sun under the Hypothesis of a Gaseous Mass Maintaining its Volume by its Internal Heat and Depending on the Laws of Gases Known to Terrestrial Experiment'.
Am. J. Sci. v. 50 (2), pp. 57–74. i.s.s.n.: 0002–9599, 1945–452X.

Langer, N., M. F. El Eid, and I. Baraffe (1989).
'Blue supergiant supernova progenitors'.
Astron. Astrophys. v. 224, pp. L17–L20. i.s.s.n.: 0004–6361, 1432–0746.

Larson, R. B. (1969).
'Numerical calculations of the dynamics of collapsing proto–star'.
Mon. Not. R. Astron. Soc. v. 145, p. 271. i.s.s.n.: 0035–8711, 1365–2966.

— (1972).
'The Collapse of a Rotating Cloud'.
Mon. Not. R. Astron. Soc. v. 156, p. 437. i.s.s.n.: 0035–8711, 1365–2966.
d.o.i.: 10.1093/mnras/156.4.437.

— (1981).
'Turbulence and star formation in molecular clouds'.
Mon. Not. R. Astron. Soc. v. 194, pp. 809–826. i.s.s.n.: 0035–8711, 1365–2966.

Lattanzio, J. C., J. J. Monaghan, H. Pongracic, and M. P. Schwarz (1986).
'Controlling Penetration'.
S.I.A.M. J. Sci. Stat. Comp. v. 7, n. 2, pp. 591–598. i.s.s.n.: 0196-5204.
d.o.i.: 10.1137/0907039.

Lepp, S. and J. M. Shull (1983).
'The kinetic theory of H_2 dissociation'.
Astrophys. J. v. 270, pp. 578–582. i.s.s.n.: 0004–637X, 1538–4357.
d.o.i.: 10.1086/161149.

Levermore, C. D. and G. C. Pomraning (1981).
'A flux–limited diffusion theory'.
Astrophys. J. v. 248, pp. 321–334. i.s.s.n.: 0004–637X, 1538–4357.
d.o.i.: 10.1086/159157.

Lewis, B. T. and M. R. Bate (2017).
'The dependence of protostar formation on the geometry and strength of the initial magnetic field'.
Mon. Not. R. Astron. Soc. v. 467, pp. 3324–3337. i.s.s.n.: 0035–8711, 1365–2966.
d.o.i.: 10.1093/mnras/stx271. arxiv: 1701.08741.

Lewis, B. T., M. R. Bate, J. J. Monaghan, and D. J. Price (2015).
'Stable smoothed particle magnetohydrodynamics in very steep density gradients'.
in: *Proceedings of the 10th. international S.P.H.E.R.I.C. workshop*. S.P.H. European Research Interest Commu-

nity.
Università degli Studi di Parma: Parma, Repubblica Italiana. I.S.B.N.: 978–88–7847–487–1.

Lewis, B. T., M. R. Bate, and D. J. Price (2015).
'Smoothed particle magnetohydrodynamic simulations of protostellar outflows with misaligned magnetic field and rotation axes'.
Mon. Not. R. Astron. Soc. V. 451, PP. 4807–4818. I.S.S.N.: 0035–8711, 1365–2966.
D.O.I.: 10.1093/mnras/stv957. ARXIV: 1504.08322.

— (2017).
'Erratum and Addendum: Smoothed particle magnetohydrodynamic simulations of protostellar outflows with misaligned magnetic field and rotation axes'.
Mon. Not. R. Astron. Soc. V. 464, PP. 2499–2501. I.S.S.N.: 0035–8711, 1365–2966.
D.O.I.: 10.1093/mnras/stw2474.

Lewis, B. T., M. R. Bate, and T. S. Tricco (2016).
'Smoothed Particle Magnetohydrodynamics: A State of the Union'.
IN: *Proceedings of the 11th. international S.P.H.E.R.I.C. workshop*. Ed. by Xiangyu Hu. S.P.H. European Research Interest Community.
Technische Universität München: München, Bundesrepublik Deutschland. I.S.B.N.: 978–30–0053–358–7.

Li, Z.-Y., R. Krasnopolsky, and H. Shang (2013).
'Does Magnetic–field–Rotation Misalignment Solve the Magnetic Braking Catastrophe in Protostellar Disk Formation?'
Astrophys. J. V. 774, P. 82. I.S.S.N.: 0004–637X, 1538–4357.
D.O.I.: 10.1088/0004-637X/774/1/82. ARXIV: 1301.6545.

Libersky, L. D. and A. G. Petschek (1990).
'Smooth Particle Hydrodynamics with Strength of Materials, Advances in the Free Lagrange Method'.
IN: *Advances in the Free–Lagrange Method Including Contributions on Adaptive Gridding and the Smooth Particle Hydrodynamics Method*. Ed. by H. E. Trease, M. F. Fritts, and P. Crowley. V. 395. *Lect. Notes. Phys.*
Springer: Heidelberg, Bundesrepublik Deutschland, PP. 248–257. I.S.B.N.: 978-3-540-54960-4.
D.O.I.: 10.1007/3-540-54960-9_58.

Lo, E. Y. M. and S. Shao (2002).
'Simulation of near–shore solitary wave mechanics by an incompressible S.P.H. method'.
Appl. Ocean. Res. V. 24, N. 5, PP. 275–286. I.S.S.N.: 0141–1187.
D.O.I.: 10.1016/S0141-1187(03)00002-6.

Lorentz, H. A. (1892).
'La Théorie electromagnétique de Maxwell et son application aux corps mouvants'. (The electromagnetic theory of Maxwell and its application to the movement of particles).
Archives néerlandaises des sciences exactes et naturelles V. 25, PP. 363–552.

Lucanus, Marcus Annæus (*ca.* 61 A.D.).
Pharsalia. De Bello Civili. (Pharsalus. The Civil War). Latin.

Lucy, L. B. (1977).
'A numerical approach to the testing of the fission hypothesis'.
Astron. J. V. 82, PP. 1013–1024. I.S.S.N.: 0004–6256, 1538–3881.
D.O.I.: 10.1086/112164.

— (1999).
'Computing radiative equilibria with Monte Carlo techniques'.
Astron. Astrophys. V. 344, PP. 282–288. I.S.S.N.: 0004–6361, 1432–0746.

Luzum, B., N. Capitaine, A. Fienga, W. Folkner, T. Fukushima, J. Hilton, C. Hohenkerk, G. Krasinsky, G. Petit, E. Pitjeva, M. Soffel, and P. Wallace (2011).
'The I.A.U. 2009 system of astronomical constants: the report of the I.A.U. working group on numerical standards for Fundamental Astronomy'.

Celest. Mech. Dyn. Astr. v. 110, pp. 293–304. i.s.s.n.: 0923–2958, 1572–9478.
d.o.i.: 10.1007/s10569-011-9352-4.

Lynden–Bell, D. (1996).
'Magnetic collimation by accretion discs of quasars and stars'.
Mon. Not. R. Astron. Soc. v. 279, pp. 389–401. i.s.s.n.: 0035–8711, 1365–2966.
d.o.i.: 10.1093/mnras/279.2.389.

— (2001).
'Why Do Disks Form Jets?'
in: *The Central Kiloparsec of Starbursts and A.G.N.: The La Palma Connection*. Ed. by J. H. Knapen, J. E. Beckman, I. Shlosman, and T. J. Mahoney. v. 249. Astronomical Society of the Pacific Conference Series, pp. 212–229. i.s.b.n.: 1-58381-089-7.
arxiv: astro-ph/0203480.

Mac Low, M.-M. and R. S. Klessen (2004).
'Control of star formation by supersonic turbulence'.
Rev. Mod. Phys. v. 76, pp. 125–194. i.s.s.n.: 0034–6861, 1539–0756.
d.o.i.: 10.1103/RevModPhys.76.125. arxiv: astro-ph/0301093.

Machida, M. N., S.-i. Inutsuka, and T. Matsumoto (2006).
'Second Core Formation and High-Speed Jets: Resistive Magnetohydrodynamic Nested Grid Simulations'.
Astrophys. J. Lett. v. 647, pp. L151–L154. i.s.s.n.: 2041–8205.
d.o.i.: 10.1086/507179. arxiv: astro-ph/0603456.

— (2008).
'High– and Low–Velocity Magnetized Outflows in the Star Formation Process in a Gravitationally Collapsing Cloud'.
Astrophys. J. v. 676, pp. 1088–1108. i.s.s.n.: 0004–637X, 1538–4357.
d.o.i.: 10.1086/528364.

Machida, M. N., T. Matsumoto, T. Hanawa, and K. Tomisaka (2005).
'Collapse and fragmentation of rotating magnetized clouds — ii. Binary formation and fragmentation of first cores'.
Mon. Not. R. Astron. Soc. v. 362, pp. 382–402. i.s.s.n.: 0035–8711, 1365–2966.
d.o.i.: 10.1111/j.1365-2966.2005.09327.x. arxiv: astro-ph/0506440.

Malinen, J., L. Montier, J. Montillaud, M. Juvela, I. Ristorcelli, S. E. Clark, O. Berné, J.-P. Bernard, V.-M. Pelkonen, and D. C. Collins (2016).
'Matching dust emission structures and magnetic field in high–latitude cloud L1642: comparing Herschel and Planck maps'.
Mon. Not. R. Astron. Soc. v. 460, pp. 1934–1945. i.s.s.n.: 0035–8711, 1365–2966.
d.o.i.: 10.1093/mnras/stw1061. arxiv: 1512.03775.

Mariotte, Edmé (1679).
'Second essai. De la nature de l'air'. (Second essay. On the nature of the air). French.
in: *Essais de Physique, ou mémoires pour servir à la science des choses naturelles*.
E. Michallet: Paris, Royaume de France.

Masson, J., G. Chabrier, P. Hennebelle, N. Vaytet, and B. Commerçon (2016).
'Ambipolar diffusion in low–mass star formation — i. General comparison with the ideal magnetohydrodynamic case'.
Astron. Astrophys. v. 587, A32. i.s.s.n.: 0004–6361, 1432–0746.
d.o.i.: 10.1051/0004-6361/201526371. arxiv: 1509.05630.

Mathis, J. S., W. Rumpl, and K. H. Nordsieck (1977).
'The size distribution of interstellar grains'.

Astrophys. J. v. 217, pp. 425–433. I.S.S.N.: 0004–637X, 1538–4357.
D.O.I.: 10.1086/155591.

Matsumoto, T. and T. Hanawa (2003).
'Fragmentation of a Molecular Cloud Core versus Fragmentation of the Massive Protoplanetary Disk in the Main Accretion Phase'.
Astrophys. J. v. 595, pp. 913–934.
D.O.I.: 10.1086/377367. EPRINT: astro-ph/0306121.

— (2011).
'Protostellar Collapse of Magneto–turbulent Cloud Cores: Shape During Collapse and Outflow Formation'.
Astrophys. J. v. 728, p. 47. I.S.S.N.: 0004–637X, 1538–4357.
D.O.I.: 10.1088/0004-637X/728/1/47. ARXIV: 1008.3984.

Matsumoto, T., M. N. Machida, and S.-i. Inutsuka (2017).
'Circumstellar Disks and Outflows in Turbulent Molecular Cloud Cores: Possible Formation Mechanism for Misaligned Systems'.
Astrophys. J. v. 839, p. 69. I.S.S.N.: 0004–637X, 1538–4357.
D.O.I.: 10.3847/1538-4357/aa6a1c. ARXIV: 1703.09139.

Matsumoto, T. and K. Tomisaka (2004).
'Directions of Outflows, Disks, Magnetic Fields, and Rotation of Young Stellar Objects in Collapsing Molecular Cloud Cores'.
Astrophys. J. v. 616, pp. 266–282. I.S.S.N.: 0004–637X, 1538–4357.
D.O.I.: 10.1086/424897. ARXIV: astro-ph/0408086.

Maxwell, J. C. (1861).
'On the physical lines of force'.
Philos. Mag. SER. 4th. v. 90, pp. 11–23. I.S.S.N.: 0031–8086.
D.O.I.: 10.1080/14786431003659180.

McKee, C. F. (1989).
'Photoionization-regulated star formation and the structure of molecular clouds'.
Astrophys. J. v. 345, pp. 782–801. I.S.S.N.: 0004–637X, 1538–4357.
D.O.I.: 10.1086/167950.

McKee, C. F. and E. C. Ostriker (2007).
'Theory of Star Formation'.
Ann. Rev. Astron. Astr. v. 45, pp. 565–687. I.S.S.N.: 0066–4146.
D.O.I.: 10.1146/annurev.astro.45.051806.110602. ARXIV: 0707.3514.

McKee, C. F. and J. P. Ostriker (1977).
'A theory of the interstellar medium — Three components regulated by supernova explosions in an inhomogeneous substrate'.
Astrophys. J. v. 218, pp. 148–169. I.S.S.N.: 0004–637X, 1538–4357.
D.O.I.: 10.1086/155667.

McLaughlin, D. E. and R. E. Pudritz (1996).
'The Formation of Globular Cluster Systems. I. The Luminosity Function'.
Astrophys. J. v. 457, p. 578. I.S.S.N.: 0004–637X, 1538–4357.
D.O.I.: 10.1086/176754.

Mellon, R. R. and Z.-Y. Li (2008).
'Magnetic Braking and Protostellar Disk Formation: The Ideal M.H.D. Limit'.
Astrophys. J. v. 681, pp. 1356–1376. I.S.S.N.: 0004–637X, 1538–4357.
D.O.I.: 10.1086/587542. ARXIV: 0709.0445.

Men'shchikov, A., P. André, P. Didelon, V. Könyves, N. Schneider, F. Motte, S. Bontemps, D. Arzoumanian, M. Attard, A. Abergel, J.-P. Baluteau, J.-P. Bernard, L. Cambrésy, P. Cox, *et al.* (2010).

'Filamentary structures and compact objects in the Aquila and Polaris clouds observed by Herschel'. *Astron. Astrophys.* v. 518, p. L103. I.S.S.N.: 0004–6361, 1432–0746. D.O.I.: 10.1051/0004-6361/201014668. ARXIV: 1005.3115.

Merritt, D. (1996).
'Optimal Smoothing for N–Body Codes'. *Astron. J.* v. 111, p. 2462. I.S.S.N.: 0004–6256, 1538–3881. D.O.I.: 10.1086/117980. ARXIV: astro-ph/9511146.

Milton, John (1667–1674).
Paradise Lost. A Poem in Ten Books.

Milton, K. A. (2006).
'Theoretical and experimental status of magnetic monopoles'. *Rep. Prog. Phys.* v. 69, PP. 1637–1711. I.S.S.N.: 0034–4885, 1361–6633. D.O.I.: 10.1088/0034-4885/69/6/R02. ARXIV: hep-ex/0602040.

Monaghan, J. J. (1988).
'An introduction to S.P.H.' *Comput. Phys. Commun.* v. 48, PP. 89–96. I.S.S.N.: 0010–4655. D.O.I.: 10.1016/0010-4655(88)90026-4.

— (1997).
'S.P.H. and Riemann Solvers'. *J. Comput. Phys.* v. 136, PP. 298–307. I.S.S.N.: 0021-9991. D.O.I.: 10.1006/jcph.1997.5732.

Morris, J. P. (1996).
'Analysis of smoothed particle hydrodynamics with applications'. PhD thesis. Monash University.

Morris, J. P. and J. J. Monaghan (1997).
'A Switch to Reduce S.P.H. Viscosity'. *J. Comput. Phys.* v. 136, PP. 41–50. I.S.S.N.: 0021-9991. D.O.I.: 10.1006/jcph.1997.5690.

Motte, F. and P. André (2001).
'The circumstellar environment of low-mass protostars: A millimeter continuum mapping survey'. *Astron. Astrophys.* v. 365, PP. 440–464. I.S.S.N.: 0004–6361, 1432–0746. D.O.I.: 10.1051/0004-6361:20000072.

Mouschovias, T. C. and L. Spitzer Jr. (1976).
'Note on the collapse of magnetic interstellar clouds'. *Astrophys. J.* v. 210, p. 326. I.S.S.N.: 0004–637X, 1538–4357. D.O.I.: 10.1086/154835.

MPI–2 (2003).
Extensions to the Message–Passing Interface. Message Passing Interface Forum.

Myers, P. C. (2009).
'Filamentary Structure of Star–forming Complexes'. *Astrophys. J.* v. 700, PP. 1609–1625. I.S.S.N.: 0004–637X, 1538–4357. D.O.I.: 10.1088/0004-637X/700/2/1609. ARXIV: 0906.2005.

Myers, P. C., T. L. Bourke, T. L. Huard, N. J. Evans II, J. Kauffmann, M. M. Dunham, T. Y. Brooke, C. H. Young, and c2d Team (2005).
'Spitzer Discovery of Very Low Luminosity Objects in Dense Cores'. IN: *American Astronomical Society Meeting Abstracts #207*. v. 37. *B. Am. Astron. Soc.* American Astronomical Society, p. 1256.

Nagasawa, M. and S. M. Miyama (1987).
'Three–Dimensional Numerical Simulation of Interstellar Cloud–Cloud Collisions and Triggered Star Formation. I. Head–On Collisions'.

Prog. Theor. Phys. v. 78, pp. 1250–1272. i.s.s.n.: 0033–068X, 1347–4081.
d.o.i.: 10.1143/PTP.78.1250.

Nakano, T. and T. Nakamura (1978).
'Gravitational Instability of Magnetized Gaseous Disks 6'.
Publ. Astron. Soc. Jpn. v. 30, pp. 671–680. i.s.s.n.: 0004–6264.

Navier, Claude–Louis Marie Henri (1823).
'Mémoire sur les lois du mouvement des fluides'. (Memoire on the law of the movement of fluid). French.
Mémoires de l'Académie Royale des Sciences v. 6, pp. 389–440.

Neff, S. G. and J. S. Ulvestad (2000).
'V.L.A. Observations of the Nearby Merger NGC 4038/4039: H II Regions and Supernova Remnants in the "Antennae"'.
Astron. J. v. 120, pp. 670–696. i.s.s.n.: 0004–6256, 1538–3881.
d.o.i.: 10.1086/301503.

Neininger, N. (1992).
'The magnetic field structure of M51'.
Astron. Astrophys. v. 263, pp. 30–36. i.s.s.n.: 0004–6361, 1432–0746.

Nejad-Asghar, M. (2010).
'Non–similar collapse of singular isothermal spherical molecular cloud cores with nonzero initial velocities'.
Res. Astron. Astrophys. v. 10, pp. 1275–1286. i.s.s.n.: 1674–4527.
d.o.i.: 10.1088/1674-4527/10/12/008. arxiv: 1007.0625.

Newton, Sir Isaac (1669).
De analysi per æquationes numero terminorum infinitas. (On the Analysis by means of equations of an infinite number of terms). Latin.

— (1687).
Philosophiæ Naturalis Principia Mathematica. (Mathematical Principles of Natural Philosophy). Latin. ed. 1st.
The President, Council and Fellows of the Royal Society of London for Improving Natural Knowledge: London, United Kingdom.

— (1704–1718).
Opticks. Or, a Treatise of the Reflexions, Refractions, Inflexions and Colours of Light.

Norman, M. L. and J. R. Wilson (1978).
'The fragmentation of isothermal rings and star formation'.
Astrophys. J. v. 224, pp. 497–511. i.s.s.n.: 0004–637X, 1538–4357.
d.o.i.: 10.1086/156397.

Ohm, Georg Simon (1827).
'Die galvanische Kette, mathematisch bearbeitet'. (The Galvanic Circuit Investigated Mathematically). German.

openMP v. 2.5 (2005).
Application Programming Interface. OpenMP Architecture Review Board.

Orszag, S. A. and C.-M. Tang (1979).
'Small–scale structure of two–dimensional magnetohydrodynamic turbulence'.
J. Fluid. Mech. v. 90, pp. 129–143. i.s.s.n.: 0022–1120, 1469–7645.
d.o.i.: 10.1017/S002211207900210X.

Ostriker, E. C., J. M. Stone, and C. F. Gammie (2001).
'Density, Velocity, and Magnetic Field Structure in Turbulent Molecular Cloud Models'.
Astrophys. J. v. 546, pp. 980–1005. i.s.s.n.: 0004–637X, 1538–4357.
d.o.i.: 10.1086/318290. arxiv: astro-ph/0008454.

Padoan, P. and Å. Nordlund (2002).
'The Stellar Initial Mass Function from Turbulent Fragmentation'.
Astrophys. J. v. 576, pp. 870–879. I.S.S.N.: 0004–637X, 1538–4357.
D.O.I.: 10.1086/341790. ARXIV: astro-ph/0011465.

Pandey, B. P. and M. Wardle (2008).
'Hall magnetohydrodynamics of partially ionized plasmas'.
Mon. Not. R. Astron. Soc. v. 385, pp. 2269–2278. I.S.S.N.: 0035–8711, 1365–2966.
D.O.I.: 10.1111/j.1365-2966.2008.12998.x. ARXIV: 0707.2688.

Parker, E. N. (1955).
'Hydromagnetic Dynamo Models.'
Astrophys. J. v. 122, p. 293. I.S.S.N.: 0004–637X, 1538–4357.
D.O.I.: 10.1086/146087.

— (1966).
'The Dynamical State of the Interstellar Gas and Field'.
Astrophys. J. v. 145, p. 811. I.S.S.N.: 0004–637X, 1538–4357.
D.O.I.: 10.1086/148828.

— (1970).
'The Generation of Magnetic Fields in Astrophysical Bodies. I. The Dynamo Equations'.
Astrophys. J. v. 162, p. 665. I.S.S.N.: 0004–637X, 1538–4357.
D.O.I.: 10.1086/150697.

— (1971a).
'The Generation of Magnetic Fields in Astrophysical Bodies. II. The Galactic Field'.
Astrophys. J. v. 163, p. 255. I.S.S.N.: 0004–637X, 1538–4357.
D.O.I.: 10.1086/150765.

— (1971b).
'The Generation of Magnetic Fields in Astrophysical Bodies. III. Turbulent Diffusion of Fields and Efficient Dynamos'.
Astrophys. J. v. 163, p. 279. I.S.S.N.: 0004–637X, 1538–4357.
D.O.I.: 10.1086/150766.

Pattle, K., D. Ward-Thompson, J. M. Kirk, G. J. White, E. Drabek-Maunder, J. Buckle, S. F. Beaulieu, D. S. Berry, H. Broekhoven-Fiene, M. J. Currie, M. Fich, J. Hatchell, H. Kirk, T. Jenness, *et al.* (2015).
'The JCMT Gould Belt Survey: first results from the SCUBA-2 observations of the Ophiuchus molecular cloud and a virial analysis of its prestellar core population'.
Mon. Not. R. Astron. Soc. v. 450, pp. 1094–1122. I.S.S.N.: 0035–8711, 1365–2966.
D.O.I.: 10.1093/mnras/stv376. ARXIV: 1502.05858.

Phillips, G. J. and J. J. Monaghan (1985).
'A numerical method for three–dimensional simulations of collapsing, isothermal, magnetic gas clouds'.
Mon. Not. R. Astron. Soc. v. 216, pp. 883–895. I.S.S.N.: 0035–8711, 1365–2966.

Pineda, J. E., H. G. Arce, S. Schnee, A. A. Goodman, T. Bourke, J. B. Foster, T. Robitaille, J. Tanner, J. Kauffmann, M. Tafalla, P. Caselli, and G. Anglada (2011).
'The Enigmatic Core L1451-mm: A First Hydrostatic Core? Or a Hidden Ve.L.L.O.?'
Astrophys. J. v. 743, p. 201. I.S.S.N.: 0004–637X, 1538–4357.
D.O.I.: 10.1088/0004-637X/743/2/201. ARXIV: 1109.1207.

Planck Collaboration, P. A. R. Ade, N. Aghanim, M. I. R. Alves, M. Arnaud, D. Arzoumanian, M. Ashdown, J. Aumont, C. Baccigalupi, A. J. Banday, R. B. Barreiro, N. Bartolo, E. Battaner, K. Benabed, *et al.* (2016a).
'Planck intermediate results. XXXV. Probing the role of the magnetic field in the formation of structure in molecular clouds'.
Astron. Astrophys. v. 586, A138. I.S.S.N.: 0004–6361, 1432–0746.
D.O.I.: 10.1051/0004-6361/201525896. ARXIV: 1502.04123.

Planck Collaboration, N. Aghanim, M. I. R. Alves, D. Arzoumanian, J. Aumont, C. Baccigalupi, M. Ballardini, A. J. Banday, R. B. Barreiro, N. Bartolo, S. Basak, K. Benabed, J.-P. Bernard, M. Bersanelli, *et al.* (2016b).
'Planck intermediate results. XLIV — Structure of the Galactic magnetic field from dust polarization maps of the southern Galactic cap'.
Astron. Astrophys. V. 596, A105. I.S.S.N.: 0004–6361, 1432–0746.
D.O.I.: 10.1051/0004-6361/201628636. ARXIV: 1604.01029.

Planck, M. K. E. L. (1914).
Vorlesungen über die Theorie der Wärmestrahlung. (The Theory of Heat Radiation). Trans. from the German by Morton Masius.
Courier Corporation: North Chelmsford, M.A., United States.

Plummer, H. C. (1911).
'On the problem of distribution in globular star clusters'.
Mon. Not. R. Astron. Soc. V. 71, PP. 460–470. I.S.S.N.: 0035–8711, 1365–2966.
D.O.I.: 10.1093/mnras/71.5.460.

Pollack, J. B., C. P. McKay, and B. M. Christofferson (1985).
'A calculation of the Rosseland mean opacity of dust grains in primordial solar system nebulae'.
Icarus V. 64, PP. 471–492. I.S.S.N.: 0019–1035.
D.O.I.: 10.1016/0019-1035(85)90069-7.

Pound, M. W., B. Reipurth, and J. Bally (2003).
'Looking into the Horsehead'.
Astron. J. V. 125, PP. 2108–2122. I.S.S.N.: 0004–6256, 1538–3881.
D.O.I.: 10.1086/368138.

Press, W. H. (1986).
'Techniques and tricks for N–body computation'.
IN: *The Use of Supercomputers in Stellar Dynamics*. Ed. by P. Hut and S. L. McMillan. V. 267. *Lect. Notes. Phys.*
Springer: Heidelberg, Bundesrepublik Deutschland, PP. 184–192. I.S.B.N.: 978-3-540-17196-6.
D.O.I.: 10.1007/BFb0116411.

Price, D. J. (2004).
'Magnetic fields in Astrophysics'. PhD thesis. University of Cambridge.

— (2007).
'splash: An Interactive Visualisation Tool for Smoothed Particle Hydrodynamics Simulations'.
Publ. Astron. Soc. Aust. V. 24, PP. 159–173.
D.O.I.: 10.1071/AS07022. ARXIV: 0709.0832.

— (2010).
'Smoothed Particle Magnetohydrodynamics — IV. Using the vector potential'.
Mon. Not. R. Astron. Soc. V. 401, PP. 1475–1499. I.S.S.N.: 0035–8711, 1365–2966.
D.O.I.: 10.1111/j.1365-2966.2009.15763.x. ARXIV: 0909.2469.

— (2011a).
'ndspmhd— Smoothed Particle Magnetohydrodynamics Code'.
Astrophysics Source Code Library.
ASCL: 1101.002.

— (2011b).
'SPLASH: An Interactive Visualization Tool for Smoothed Particle Hydrodynamics Simulations'.
Astrophysics Source Code Library.
ASCL: 1103.004.

— (2012).
'Smoothed particle hydrodynamics and magnetohydrodynamics'.
J. Comput. Phys. V. 231, PP. 759–794. I.S.S.N.: 0021-9991.
D.O.I.: 10.1016/j.jcp.2010.12.011. ARXIV: 1012.1885.

Price, D. J. and M. R. Bate (2007).
'The impact of magnetic fields on single and binary star formation'.
Mon. Not. R. Astron. Soc. v. 377, pp. 77–90. I.S.S.N.: 0035–8711, 1365–2966.
D.O.I.: 10.1111/j.1365-2966.2007.11621.x. ARXIV: astro-ph/0702410.

— (2008).
'The effect of magnetic fields on star cluster formation'.
Mon. Not. R. Astron. Soc. v. 385, pp. 1820–1834. I.S.S.N.: 0035–8711, 1365–2966.
D.O.I.: 10.1111/j.1365-2966.2008.12976.x. ARXIV: 0801.3293.

— (2009).
'Inefficient star formation: the combined effects of magnetic fields and radiative feedback'.
Mon. Not. R. Astron. Soc. v. 398, pp. 33–46. I.S.S.N.: 0035–8711, 1365–2966.
D.O.I.: 10.1111/j.1365-2966.2009.14969.x. ARXIV: 0904.4071.

Price, D. J. and J. J. Monaghan (2004a).
'Smoothed Particle Magnetohydrodynamics — I. Algorithm and tests in one dimension'.
Mon. Not. R. Astron. Soc. v. 348, pp. 123–138. I.S.S.N.: 0035–8711, 1365–2966.
D.O.I.: 10.1111/j.1365-2966.2004.07345.x. ARXIV: astro-ph/0310789.

— (2004b).
'Smoothed Particle Magnetohydrodynamics — II. Variational principles and variable smoothing–length terms'.
Mon. Not. R. Astron. Soc. v. 348, pp. 139–152. I.S.S.N.: 0035–8711, 1365–2966.
D.O.I.: 10.1111/j.1365-2966.2004.07346.x. ARXIV: astro-ph/0310790.

— (2005).
'Smoothed Particle Magnetohydrodynamics - III. Multidimensional tests and the $\nabla \cdot \boldsymbol{B} = 0$ constraint'.
Mon. Not. R. Astron. Soc. v. 364, pp. 384–406. I.S.S.N.: 0035–8711, 1365–2966.
D.O.I.: 10.1111/j.1365-2966.2005.09576.x. ARXIV: astro-ph/0509083.

— (2007).
'An energy–conserving formalism for adaptive gravitational force softening in smoothed particle hydrodynamics and N–body codes'.
Mon. Not. R. Astron. Soc. v. 374, pp. 1347–1358. I.S.S.N.: 0035–8711, 1365–2966.
D.O.I.: 10.1111/j.1365-2966.2006.11241.x. ARXIV: astro-ph/0610872.

Price, D. J., J. E. Pringle, and A. R. King (2003).
'A comparison of the acceleration mechanisms in young stellar objects and active galactic nuclei jets'.
Mon. Not. R. Astron. Soc. v. 339, pp. 1223–1236. I.S.S.N.: 0035–8711, 1365–2966.
D.O.I.: 10.1046/j.1365-8711.2003.06278.x. ARXIV: astro-ph/0211330.

Price, D. J., T. S. Tricco, and M. R. Bate (2012).
'Collimated jets from the first core'.
Mon. Not. R. Astron. Soc. v. 423, pp. L45–L49. I.S.S.N.: 0035–8711, 1365–2966.
D.O.I.: 10.1111/j.1745-3933.2012.01254.x. ARXIV: 1203.2933.

Price, D. J., J. Wurster, C. Nixon, T. S. Tricco, S. Toupin, A. Pettitt, C. Chan, G. Laibe, S. Glover, C. Dobbs, R. Nealon, D. Liptai, H. Worpel, C. Bonnerot, *et al.* (2017).
'Phantom: A smoothed particle hydrodynamics and magnetohydrodynamics code for astrophysics'.
ArXiv e-prints.
ARXIV: 1702.03930.

Pringle, J. E. (1989).
'On the formation of binary stars'.
Mon. Not. R. Astron. Soc. v. 239, pp. 361–370. I.S.S.N.: 0035–8711, 1365–2966.
D.O.I.: 10.1093/mnras/239.2.361.

Procopiu, Ștefan (1913).
'Determining the Molecular Magnetic Moment by M. Planck's Quantum Theory'.
Bull. Sci. Acad. Roum. v. 1, p. 151.

Ptolemy, Claudius (*ca.* 150 A.D.–170 A.D.).
Almagest. (Μαθηματικὴ Σύνταξις). Trans. from the Ancient Greek with corrections from the Arabic by G. J. Toomer. With a forew. by Owen Gingerich.
Princeton University Press: Princeton, N.J., United States. I.S.B.N.: 978-06–9100–260–6.

Raphson, J. (1690).
Analysis Æquationum Universalis. (Universal Equation Analysis). Latin.

Rappaport, S., F. Verbunt, and P. C. Joss (1983).
'A new technique for calculations of binary stellar evolution, with application to magnetic braking'.
Astrophys. J. v. 275, pp. 713–731. I.S.S.N.: 0004–637X, 1538–4357.
D.O.I.: 10.1086/161569.

Reipurth, B., S. Heathcote, and F. Vrba (1992).
'Star formation in Bok globules and low–mass clouds. IV. Herbig–Haro objects in B335'.
Astron. Astrophys. v. 256, pp. 225–230. I.S.S.N.: 0004–6361, 1432–0746.

Reynolds, O. (1883).
'An experimental investigation of the circumstances which determine whether the motion of water shall be direct or sinuous, and of the law of resistance in parallel channels'.
Phil. Trans. R. Soc. v. 174, pp. 935–982.
D.O.I.: 10.1098/rstl.1883.0029.

Reynolds, S. P., K. J. Borkowski, D. A. Green, U. Hwang, I. Harrus, and R. Petre (2008).
'The Youngest Galactic Supernova Remnant: G1.9+0.3'.
Astrophys. J. Lett. v. 680, p. L41. I.S.S.N.: 2041–8205.
D.O.I.: 10.1086/589570. ARXIV: 0803.1487.

Rey-Raposo, R., C. Dobbs, O. Agertz, and C. Alig (2017).
'The roles of stellar feedback and galactic environment in star–forming molecular clouds'.
Mon. Not. R. Astron. Soc. v. 464, pp. 3536–3551. I.S.S.N.: 0035–8711, 1365–2966.
D.O.I.: 10.1093/mnras/stw2607. ARXIV: 1610.01371.

Rey-Raposo, R., C. Dobbs, and A. Duarte-Cabral (2015).
'Are turbulent spheres suitable initial conditions for star–forming clouds?'
Mon. Not. R. Astron. Soc. v. 446, pp. L46–L50. I.S.S.N.: 0035–8711, 1365–2966.
D.O.I.: 10.1093/mnrasl/slu167. ARXIV: 1410.1351.

Riaz, B., C. Briceno, E. Whelan, and S. Heathcote (2017).
'First large scale Herbig–Haro jet driven by a proto-brown dwarf'.
ArXiv e-prints.
ARXIV: 1705.01170.

Richtmyer, R. D., J. Pasta, and S. Ulam (1947).
'Statistical Methods in Neutron Diffusion'.
L.A.N.L. reports v. L.A.M.S.–551.

Roberts, W. W. (1969).
'Large–Scale Shock Formation in Spiral Galaxies and its Implications on Star Formation'.
Astrophys. J. v. 158, p. 123. I.S.S.N.: 0004–637X, 1538–4357.
D.O.I.: 10.1086/150177.

Robishaw, T., J. Green, G. Surcis, W. H. T. Vlemmings, A. M. S. Richards, S. Etoka, T. Bourke, V. Fish, M. D. Gray, H. Imai, B. Kramer, J. McBride, E. Momjian, A. P. Sarma, and A. A. Zijlstra (2015).
'Measuring Magnetic Fields Near and Far with the S.K.A. *via* the Zeeman Effect'.
IN: *Advancing Astrophysics with the Square Kilometre Array (A.A.S.K.A.14.)* Square Kilometre Array Organisation.

Dolman Scott Ltd.: Thatcham, United Kingdom, P. 110. I.S.B.N.: 978-1-909204-70-6.
ARXIV: 1503.01779.

Robitaille, T. P. and B. A. Whitney (2010).
'The Present–Day Star Formation Rate of the Milky Way Determined from Spitzer–Detected Young Stellar Objects'.
Astrophys. J. Lett. V. 710, PP. L11–L15. I.S.S.N.: 2041–8205.
D.O.I.: 10.1088/2041-8205/710/1/L11. ARXIV: 1001.3672.

Rodionov, S. A. and N. Y. Sotnikova (2005).
'Optimal Choice of the Softening Length and Time Step in N–body Simulations'.
Астрон. ж. V. 49, PP. 470–476. I.S.S.N.: 1063–7729, 1562–6881.
D.O.I.: 10.1134/1.1941489. ARXIV: astro-ph/0504573.

Rosseland, S. (1924).
'Note on the absorption of radiation within a star'.
Mon. Not. R. Astron. Soc. V. 84, PP. 525–528. I.S.S.N.: 0035–8711, 1365–2966.
D.O.I.: 10.1093/mnras/84.7.525.

Rosswog, S. and D. J. Price (2007).
'MAGMA: a three-dimensional, Lagrangian magnetohydrodynamics code for merger applications'.
Mon. Not. R. Astron. Soc. V. 379, PP. 915–931. I.S.S.N.: 0035–8711, 1365–2966.
D.O.I.: 10.1111/j.1365-2966.2007.11984.x. ARXIV: 0705.1441.

Runge, Carl David Tolmé (1895).
'Über die numerische Auflösung von Differentialgleichungen'.
Math. Ann. V. 46, PP. 167–178. I.S.S.N.: 0025–5831, 1432–1807.

Salpeter, E. E. (1955).
'The Luminosity Function and Stellar Evolution.'
Astrophys. J. V. 121, P. 161. I.S.S.N.: 0004–637X, 1538–4357.
D.O.I.: 10.1086/145971.

— (1977).
'Formation and destruction of dust grains'.
Ann. Rev. Astron. Astr. V. 15, PP. 267–293. I.S.S.N.: 0066–4146.
D.O.I.: 10.1146/annurev.aa.15.090177.001411.

Sandstrom, K. M. and A. A. Goodman (2001).
'Estimating Magnetic Field Strength in Molecular Clouds with the Chandrasekhar–Fermi Method'.
IN: *American Astronomical Society Meeting Abstracts #199*. V. 33. *B. Am. Astron. Soc.* American Astronomical Society, P. 1528.

Santos, F. P., G. A. P. Franco, A. Roman-Lopes, W. Reis, and C. G. Román-Zúñiga (2014).
'Optical/Near-infrared Polarization Survey of Sh 2-29: Magnetic Fields, Dense Cloud Fragmentations, and Anomalous Dust Grain Sizes'.
Astrophys. J. V. 783, P. 1.
D.O.I.: 10.1088/0004-637X/783/1/1. ARXIV: 1310.7037.

Santos-Lima, R., E. M. de Gouveia Dal Pino, and A. Lazarian (2012).
'The Role of Turbulent Magnetic Reconnection in the Formation of Rotationally Supported Protostellar Disks'.
Astrophys. J. V. 747, P. 21. I.S.S.N.: 0004–637X, 1538–4357.
D.O.I.: 10.1088/0004-637X/747/1/21. ARXIV: 1109.3716.

Sargent, A. I. (1977).
'Molecular clouds and star formation. I. Observations of the Cepheus OB3 molecular cloud'.
Astrophys. J. V. 218, PP. 736–748. I.S.S.N.: 0004–637X, 1538–4357.
D.O.I.: 10.1086/155729.

Sargent, A. I. (1979).
'Molecular clouds and star formation. II. Star formation in the Cepheus OB3 and Perseus OB2 molecular clouds'.
Astrophys. J. V. 233, PP. 163–181. I.S.S.N.: 0004–637X, 1538–4357.
D.O.I.: 10.1086/157378.

Schaye, J., R. A. Crain, R. G. Bower, M. Furlong, M. Schaller, T. Theuns, C. Dalla Vecchia, C. S. Frenk, I. G. McCarthy, J. C. Helly, A. Jenkins, Y. M. Rosas-Guevara, S. D. M. White, M. Baes, *et al.* (2015).
'The EAGLE project: simulating the evolution and assembly of galaxies and their environments'.
Mon. Not. R. Astron. Soc. V. 446, PP. 521–554. I.S.S.N.: 0035–8711, 1365–2966.
D.O.I.: 10.1093/mnras/stu2058. ARXIV: 1407.7040.

Searle, L. and R. Zinn (1978).
'Compositions of halo clusters and the formation of the galactic halo'.
Astrophys. J. V. 225, PP. 357–379. I.S.S.N.: 0004–637X, 1538–4357.
D.O.I.: 10.1086/156499.

Seifried, D., R. Banerjee, R. E. Pudritz, and R. S. Klessen (2012).
'Disc formation in turbulent massive cores: circumventing the magnetic braking catastrophe'.
Mon. Not. R. Astron. Soc. V. 423, PP. L40–L44. I.S.S.N.: 0035–8711, 1365–2966.
D.O.I.: 10.1111/j.1745-3933.2012.01253.x. ARXIV: 1201.5302.

Seneca, Lucius Annæus (*ca.* 65 A.D.).
Epistulæ Morales ad Lucilium. (Moral Letters to Lucilius). Latin.

Shakespeare, William (1599).
The Tragedy of Julius Cæsar.

Shao, S. and E. Y. M. Lo (2003).
'Incompressible S.P.H. method for simulating Newtonian and non–Newtonian flows with a free surface'.
Adv. Water. Resour. V. 26, N. 7, PP. 787–800. I.S.S.N.: 0309–1708.

Shu, F. H. (1977).
'Self-similar collapse of isothermal spheres and star formation'.
Astrophys. J. V. 214, PP. 488–497. I.S.S.N.: 0004–637X, 1538–4357.
D.O.I.: 10.1086/155274.

Simon, A. (1955).
'Ambipolar Diffusion in a Magnetic Field'.
Phys. Rev. SER. 2nd. V. 98, PP. 317–318.
D.O.I.: 10.1103/PhysRev.98.317.

Springel, V. (2011).
'Moving–mesh hydrodynamics with the AREPO code'.
IN: *Computational Star Formation*. Ed. by J. Alves, B. G. Elmegreen, J. M. Girart, and V. Trimble. V. 270. I.A.U. Symposium, PP. 203–206.
D.O.I.: 10.1017/S1743921311000378.

Stasyszyn, F. A. and D. Elstner (2015).
'A vector potential implementation for smoothed particle magnetohydrodynamics'.
J. Comput. Phys. V. 282, PP. 148–156. I.S.S.N.: *J. Comput. Phys.*
D.O.I.: 10.1016/j.jcp.2014.11.011. ARXIV: 1411.3290.

Stephens, I. W., L. W. Looney, W. Kwon, M. Fernández-López, A. M. Hughes, L. G. Mundy, R. M. Crutcher, Z.-Y. Li, and R. Rao (2014).
'Spatially resolved magnetic field structure in the disk of a T Tauri star'.
Nature V. 514, PP. 597–599. I.S.S.N.: 0028–0836, 1476–4687.
D.O.I.: 10.1038/nature13850. ARXIV: 1409.2878.

Stokes, G. G. (1851).
'On the Effect of the Internal Friction of Fluids on the Motion of Pendulums'.
Trans. Cambridge Philos. Soc. v. 9, pp. 8–106.

— (1854).
'On the Theories of the Internal Friction of Fluids in Motion and of the Equilibrium and Motion of Elastic Solids'.
Trans. Cambridge Philos. Soc. v. 8, pp. 287–319.

Sugimoto, D., Y. Chikada, J. Makino, T. Ito, T. Ebisuzaki, and M. Umemura (1990).
'A special–purpose computer for gravitational many–body problems'.
Nature v. 345, pp. 33–35. i.s.s.n.: 0028–0836, 1476–4687.
d.o.i.: 10.1038/345033a0.

Takahashi, S. and P. T. P. Ho (2012).
'The Discovery of the Youngest Molecular Outflow Associated with an Intermediate–mass Protostellar Core, MMS-6/OMC-3'.
Astrophys. J. Lett. v. 745, p. L10. i.s.s.n.: 2041–8205.
d.o.i.: 10.1088/2041-8205/745/1/L10. arxiv: 1112.4596.

Terebey, S., F. H. Shu, and P. Cassen (1984).
'The collapse of the cores of slowly rotating isothermal clouds'.
Astrophys. J. v. 286, pp. 529–551. i.s.s.n.: 0004–637X, 1538–4357.
d.o.i.: 10.1086/162628.

Tobin, J. J., K. M. Kratter, M. V. Persson, L. W. Looney, M. M. Dunham, D. Segura-Cox, Z.-Y. Li, C. J. Chandler, S. I. Sadavoy, R. J. Harris, C. Melis, and L. M. Pérez (2016).
'A triple protostar system formed via fragmentation of a gravitationally unstable disk'.
Nature v. 538, pp. 483–486. i.s.s.n.: 0028–0836, 1476–4687.
d.o.i.: 10.1038/nature20094. arxiv: 1610.08524.

Tomida, K., K. Tomisaka, T. Matsumoto, Y. Hori, S. Okuzumi, M. N. Machida, and K. Saigo (2013).
'Radiation Magnetohydrodynamic Simulations of Protostellar Collapse: Protostellar Core Formation'.
Astrophys. J. v. 763, p. 6. i.s.s.n.: 0004–637X, 1538–4357.
d.o.i.: 10.1088/0004-637X/763/1/6. arxiv: 1206.3567.

Tomisaka, K. (2002).
'Collapse of Rotating Magnetized Molecular Cloud Cores and Mass Outflows'.
Astrophys. J. v. 575, pp. 306–326. i.s.s.n.: 0004–637X, 1538–4357.
d.o.i.: 10.1086/341133. arxiv: astro-ph/0105527.

Tóth, G. (2000).
'The $\nabla \cdot \boldsymbol{B} = 0$ Constraint in Shock-Capturing Magnetohydrodynamics Codes'.
J. Comput. Phys. v. 161, pp. 605–652. i.s.s.n.: 0021-9991.
d.o.i.: 10.1006/jcph.2000.6519.

Tricco, T. S. (2015).
'Simulating Astrophysical Magnetic Fields with Smoothed Particle Magnetohydrodynamics'. PhD thesis. Monash University.
arxiv: 1505.04494.

Tricco, T. S. and D. J. Price (2012).
'Constrained hyperbolic divergence cleaning for smoothed particle magnetohydrodynamics'.
J. Comput. Phys. v. 231, pp. 7214–7236. i.s.s.n.: 0021-9991.
d.o.i.: 10.1016/j.jcp.2012.06.039. arxiv: 1206.6159.

— (2013a).
'A Switch for Artificial Resistivity and Other Dissipation Terms'.
in: *Proceedings of the 8th. international S.P.H.E.R.I.C. workshop*. S.P.H. European Research Interest Community.

Stiftelsen for Industriell og Teknisk Forskning: Trondheim, Kongeriket Norge.
ARXIV: 1310.4260.

Tricco, T. S. and D. J. Price (2013b).
'A switch to reduce resistivity in smoothed particle magnetohydrodynamics'.
Mon. Not. R. Astron. Soc. V. 436, PP. 2810–2817. I.S.S.N.: 0035–8711, 1365–2966.
D.O.I.: 10.1093/mnras/stt1776. ARXIV: 1309.5437.

Tricco, T. S., D. J. Price, and M. R. Bate (2016).
'Constrained hyperbolic divergence cleaning in smoothed particle magnetohydrodynamics with variable cleaning speeds'.
J. Comput. Phys. V. 322, PP. 326–344. I.S.S.N.: 0021-9991.
D.O.I.: 10.1016/j.jcp.2016.06.053. ARXIV: 1607.02394.

Troland, T. H. and R. M. Crutcher (2008).
'Magnetic Fields in Dark Cloud Cores: Arecibo OH Zeeman Observations'.
Astrophys. J. V. 680, PP. 457–465. I.S.S.N.: 0004–637X, 1538–4357.
D.O.I.: 10.1086/587546. ARXIV: 0802.2253.

Tsukamoto, Y., K. Iwasaki, S. Okuzumi, M. N. Machida, and S.-i. Inutsuka (2015a).
'Bimodality of Circumstellar Disk Evolution Induced by the Hall Current'.
Astrophys. J. Lett. V. 810, P. L26. I.S.S.N.: 2041–8205.
D.O.I.: 10.1088/2041-8205/810/2/L26. ARXIV: 1506.07242.

— (2015b).
'Effects of Ohmic and ambipolar diffusion on formation and evolution of first cores, protostars, and circumstellar discs'.
Mon. Not. R. Astron. Soc. V. 452, PP. 278–288. I.S.S.N.: 0035–8711, 1365–2966.
D.O.I.: 10.1093/mnras/stv1290. ARXIV: 1503.04901.

Tyndall, John (1894).
Faraday as a Discoverer.
Cambridge University Press: Cambridge, United Kingdom. I.S.B.N.: 978-110-72-6223-2.

Vacondio, R, BD Rogers, PK Stansby, P Mignosa, and J Feldman (2013).
'Variable resolution for S.P.H.: a dynamic particle coalescing and splitting scheme'.
Comput. Method. Appl. M. V. 256, PP. 132–148. I.S.S.N.: 0045–7825.

van der Walt, S., S. C. Colbert, and G. Varoquaux (2011).
'The NumPy array: a structure for efficient numerical computation'.
Comput. Sci. Eng. V. 13, N. 2, PP. 22–30.
D.O.I.: 10.1109/MCSE.2011.37.

Vázquez-Semadeni, E., J. Kim, M. Shadmehri, and J. Ballesteros-Paredes (2005).
'The Lifetimes and Evolution of Molecular Cloud Cores'.
Astrophys. J. V. 618, PP. 344–359. I.S.S.N.: 0004–637X, 1538–4357.
D.O.I.: 10.1086/425951. EPRINT: astro-ph/0409247.

von Goethe, Johann Wolfgang (1787).
'Ein andres'. (Another). German.
IN: *Gesellige Lieder*. (Convivial Songs).

von Neumann, J. and R. D. Richtmyer (1950).
'A method for the numerical calculation of hydrodynamic shocks'.
J. Appl. Phys. V. 21, PP. 232–237. I.S.S.N.: 0021–8979, 1089–7550.

Wagner, Wilhelm Richard (1856).
Die Walküre. Erster Tag des Bühnenfestspiels: Der Ring des Nibelungen. (The Valkyrie. First Day of the Festival Play for the Stage: The Ring of the Nibelung). German.

Wardle, M. (2007).
'Magnetic fields in protoplanetary disks'.

Astrophys. Space. Sci. v. 311, pp. 35–45. i.s.s.n.: 0004–640X, 1572–946X.
d.o.i.: 10.1007/s10509-007-9575-8. arxiv: 0704.0970.

Wardle, M. and C. Ng (1999).
'The conductivity of dense molecular gas'.
Mon. Not. R. Astron. Soc. v. 303, pp. 239–246. i.s.s.n.: 0035–8711, 1365–2966.
d.o.i.: 10.1046/j.1365-8711.1999.02211.x. arxiv: astro-ph/9810468.

Ward-Thompson, D., J. M. Kirk, P. André, P. Saraceno, P. Didelon, V. Könyves, N. Schneider, A. Abergel, J.-P. Baluteau, J.-P. Bernard, S. Bontemps, L. Cambrésy, P. Cox, J. di Francesco, *et al.* (2010).
'A Herschel study of the properties of starless cores in the Polaris Flare dark cloud region using PACS and SPIRE'.
Astron. Astrophys. v. 518, p. L92. i.s.s.n.: 0004–6361, 1432–0746.
d.o.i.: 10.1051/0004-6361/201014618. arxiv: 1005.2519.

Ward-Thompson, D., J. M. Kirk, R. M. Crutcher, J. S. Greaves, W. S. Holland, and P. André (2000).
'First Observations of the Magnetic Field Geometry in Prestellar Cores'.
Astrophys. J. Lett. v. 537, pp. L135–L138. i.s.s.n.: 2041–8205.
d.o.i.: 10.1086/312764. arxiv: astro-ph/0006069.

Wendland, Holger (1995).
'Piecewise polynomial, positive definite and compactly supported radial functions of minimal degree'.
Adv. Comput. Math. v. 4, n. 1, pp. 389–396. i.s.s.n.: 1019–7168, 1572–9044.

Weyl, Hermann Klaus Hugo (1918).
Das Kontinuum. (The Continuum: A Critical Examination of the Foundation of Analysis). Trans. from the German by Stephen Pollard and Thomas Bole.
Dover Publications Inc.: Mineola, New York. i.s.b.n.: 978–04–8667–982–2.

White, S. D. M. and M. J. Rees (1978).
'Core condensation in heavy halos — A two-stage theory for galaxy formation and clustering'.
Mon. Not. R. Astron. Soc. v. 183, pp. 341–358. i.s.s.n.: 0035–8711, 1365–2966.
d.o.i.: 10.1093/mnras/183.3.341.

Whitehouse, S. C. and M. R. Bate (2004).
'Smoothed particle hydrodynamics with radiative transfer in the flux-limited diffusion approximation'.
Mon. Not. R. Astron. Soc. v. 353, pp. 1078–1094. i.s.s.n.: 0035–8711, 1365–2966.
d.o.i.: 10.1111/j.1365-2966.2004.08131.x. arxiv: astro-ph/0406392.

— (2006).
'The thermodynamics of collapsing molecular cloud cores using smoothed particle hydrodynamics with radiative transfer'.
Mon. Not. R. Astron. Soc. v. 367, pp. 32–38. i.s.s.n.: 0035–8711, 1365–2966.
d.o.i.: 10.1111/j.1365-2966.2005.09950.x. arxiv: astro-ph/0511671.

Whitehouse, S. C., M. R. Bate, and J. J. Monaghan (2005).
'A faster algorithm for smoothed particle hydrodynamics with radiative transfer in the flux–limited diffusion approximation'.
Mon. Not. R. Astron. Soc. v. 364, pp. 1367–1377. i.s.s.n.: 0035–8711, 1365–2966.
d.o.i.: 10.1111/j.1365-2966.2005.09683.x. arxiv: astro-ph/0509837.

Williams, J. P., L. Blitz, and C. F. McKee (2000).
'The Structure and Evolution of Molecular Clouds: from Clumps to Cores to the IMF'.
in: *Protostars and Planets iv*. Ed. by V. Mannings, A. P. Boss, and S. S. Russell. Space Science Series.
University of Arizona Press: Tucson, A.Z., United States, pp. 97–120. i.s.b.n.: 9780816520596.
arxiv: astro-ph/9902246.

Wurster, J. (2016a).
'NICIL: A Stand Alone Library to Self–Consistently Calculate Non–Ideal Magnetohydrodynamic Coefficients in Molecular Cloud Cores'.

Publ. Astron. Soc. Aust. v. 33, e041.
d.o.i.: 10.1017/pasa.2016.34. arxiv: 1608.00983.

Wurster, J. (2016b).
'NICIL: Non–Ideal magnetohydrodynamics Coefficients and Ionisation Library'.
Astrophysics Source Code Library.
ascl: 1608.016.

Wurster, J., D. J. Price, and B. Ayliffe (2014).
'Ambipolar diffusion in smoothed particle magnetohydrodynamics'.
Mon. Not. R. Astron. Soc. v. 444, pp. 1104–1112. i.s.s.n.: 0035–8711, 1365–2966.
d.o.i.: 10.1093/mnras/stu1524. arxiv: 1408.1807.

Wurster, J., D. J. Price, and M. R. Bate (2016).
'Can non–ideal magnetohydrodynamics solve the magnetic braking catastrophe?'
Mon. Not. R. Astron. Soc. v. 457, pp. 1037–1061. i.s.s.n.: 0035–8711, 1365–2966.
d.o.i.: 10.1093/mnras/stw013. arxiv: 1512.01597.

— (2017).
'The impact of non–ideal magnetohydrodynamics on binary star formation'.
Mon. Not. R. Astron. Soc. v. 466, pp. 1788–1804. i.s.s.n.: 0035–8711, 1365–2966.
d.o.i.: 10.1093/mnras/stw3181. arxiv: 1612.02016.

Zeeman, P. (1897).
'The Effect of Magnetisation on the Nature of Light Emitted by a Substance'.
Nature v. 55, p. 347. i.s.s.n.: 0028–0836, 1476–4687.
d.o.i.: 10.1038/055347a0.

Translations of the Epigraphs

Chapter I — The Introduction

'*Omnium rerum principia parva sunt.*' (Marcus Tullius Cicero) —

'Everything has a small beginning.'

'*Poca favilla gran fiamma seconda.*' (Dante Aligheri) —

'A great flame follows a small spark.'

Chapter II — The Smoothed Particle Radiation Magnetohydrodynamics Method

'*Omnis ars naturæ imitatio est.*' (Seneca the Younger) —

'All art is but an imitation of nature.'

Chapter III — Pushing the Limits of Smoothed Particle Magnetohydrodynamics

'*καὶ σὲ γέρον τὸ πρὶν μὲν ἀκούομεν ὄλβιον εἶναι.*' (Homer) —

'Old sir, we are told that once you prospered.'

Chapter IV — The Evolution of Protostellar Cores with Misaligned Magnetic Fields and Rotation axes

'*Qu'est-ce que la tolérance ? C'est l'apanage de l'humanité. Nous sommes tous pétris de faiblesses et d'erreurs ; pardonnons-nous réciproquement nos sottises, c'est la première loi de la nature.*' (Voltaire) —

'What is tolerance? It is the consequence of humanity. We are all formed of frailty and error; let us pardon reciprocally each other's folly — that is the first law of nature.'

Chapter V — The Dependence of Protostar Evolution on the Magnitude and Geometry of the Initial Magnetic Field

'*Du mußt steigen oder sinken.*
Du mußt herrschen und gewinnen,
Oder dienen und verlieren,
Leiden oder triumphieren,
Amboß oder Hammer sein.' (Johann Wolfgang von Goethe) —

You must either ascend or sink.
You must either conquer and rule,
Or serve and lose,
suffer or triumph,
the anvil or the hammer be.

Chapter VIII — Summary and Conclusion

'Leb' wohl, du kühnes,
herrliches Kind!
Du meines Herzens
heiligster Stolz!
Leb' wohl! Leb' wohl! Leb' wohl!

Flammende Glut
umglühe den Fels;
mit zehrenden Schrecken
scheuch' es den Zagen;
der Feige fliehe
Brünnhildes Fels! —
Denn einer nur freie die Braut,
der freier als ich, der Gott!'
(Richard Wagner) —

'Farewell, you bold,
wonderful child!
You, my heart's
holiest pride.
Farewell, farewell, farewell!

A blaze of flame
shall burn round the rock;
with devouring terror
let it scare the fainthearted;
let cowards run away
from Brünnhilde's rock!
For only one shall win the bride,
one freer than I, the God!'

Chapter IX — Further Work

'*Sed Cæsar in omnia præceps,*
nil actum credens, cum quid superesset agendum.' (Marcus Annæus Lucanus) —

'But Caesar, headlong in all his designs,
thought nothing done while anything remained to do.'

Post–Script to Chapter IX

'*Ceterum censeo magnetismum esse delendam.*' (following Cato the Elder) —

'Moreover I declare that magnetisum must be destroyed.'

The Indicies

Using Smoothed Particle Radiation Magnetohydrodynamics to Explore How Protostars are Formed

There is no easy route from the Earth to the Stars

Benjamin T. Lewis